



BALTICA VII

Life Management and Maintenance
for Power Plants
Vol. 1

VTT SYMPOSIUM 246

Keywords:

power plant, maintenance, boilers,
machinery, equipment, inspection,
monitoring, condition, life, performance,
risk, reliability

BALTICA VII
Life Management and Maintenance
for Power Plants
Vol. 1

Helsinki–Stockholm–Helsinki
12–14 June, 2007

Edited by

Juha Veivo & Pertti Auerkari

Organised by

VTT



ISBN 978-951-38-6315-9 (soft back ed.)

ISSN 0357-9387 (soft back ed.)

ISBN 978-951-38-6316-6 (URL: <http://www.vtt.fi/publications/index.jsp>)

ISSN 1455-0873 (URL: <http://www.vtt.fi/publications/index.jsp>)

Copyright © VTT Technical Research Centre of Finland 2007

JULKAISIJA – UTGIVARE – PUBLISHER

VTT, Vuorimiehentie 3, PL 1000, 02044 VTT
puh. vaihde 020 722 111, faksi 020 722 4374

VTT, Bergsmansvägen 3, PB 1000, 02044 VTT
tel. växel 020 722 111, fax 020 722 4374

VTT Technical Research Centre of Finland
Vuorimiehentie 3, P.O.Box 1000, FI-02044 VTT, Finland
phone internat. +358 20 722 111, fax + 358 20 722 4374

VTT, Kemistintie 3, PL 1000, 02044 VTT
puh. vaihde 020 722 111, faksi 020 722 7002

VTT, Kemistvägen 3, PB 1000, 02044 VTT
tel. växel 020 722 111, fax 020 722 7002

VTT, Kemistintie 3, P.O. Box 1000, FI-02044 VTT, Finland
phone internat. +358 20 722 111, fax + 358 20 722 7002

Preface

The drivers in power technology, production and business are again shifting, this time towards zero carbon and other new solutions that aim to simultaneously answer the age-old questions on cost, availability and acceptability of different fuels and conversion processes. Only a part of the answer implies completely new technology, and much of the rest is likely to mean evolutionary development of existing principles. Even then, the common awareness on global warming is unprecedented and will have large scale consequences in decisions on investment. Tightly on the heels of new investment must follow the effort required for life management and maintenance, which need to take into account the peculiarities of new technology that may be very specific and suffer from lacking prior experience. However, the changes will also affect existing plant that may face new fuels, operational modes, and upgrading in some aspects at least.

The dash for biomass and other renewable fuels will not easily cover all power consumption any time soon, and also the base load plants will be affected by the change. It remains to be seen to what extent this implies e.g. ultrasupercritical efficiency, carbon sequestration, coal gasification, and/or new nuclear concepts. However, no single technology will cover all needs, and we probably have to live with an array of solutions that all need to be served and maintained for best performance. The BALTICA VII Conference aims to provide an updated and state-of-the-art experience on the essentials for life management and maintenance of power plants, and the conference papers of these proceedings will offer an excellent review on the current issues and solutions.

The editors wish to express their sincere gratitude to the authors, referees, organisers and the Board of the Conference for their invaluable contribution in preparing for the event and the proceedings. Financial and other contributions by the supporting and sponsoring organisations are also gratefully acknowledged.

Espoo, June 2007

Juha Veivo Pertti Auerkari

Editors

Contents

Contents of Volume 1

Preface	3
Session 1. New technology for competitive plant	
Maintenance of industrial plants as a part of corporate social responsibility <i>A. Jovanovic, D. Brukmajster</i> <i>ZIRN – University of Stuttgart, Germany</i>	7
Life management of creep strengthened ferritic steels in boilers and piping <i>J. Parker</i> <i>Structural Integrity Associates, Inc., Canada</i>	20
Interrelationship between toughness parameters determined from the Charpy-V impact test <i>K. Wallin</i> <i>Academy of Finland, Helsinki, Finland</i>	37
Session 2. Developments and experience – boilers and steam systems	
UK experience with modified 9Cr (grade 91) steel <i>S. J. Brett</i> <i>RWE npower, UK</i>	48
Life extension of hot steam piping after 200 000 h of service <i>J. Rantala, J. Salonen, P. Auerkari, S. Holmström, O. Lehtinen*, M. Pitkänen**, R. Nikkarila***</i> <i>VTT Technical Research Centre of Finland, Espoo, Finland</i> <i>*Fortum Power and Heat, Naantali, Finland</i> <i>**Fortum Power and Heat, Espoo, Finland</i> <i>***Inspecta, Espoo, Finland</i>	61
Predicting lifetimes of components in power station engineering plant <i>A. Morris, A. Puri*, C. Maharaj*, M. Kourmpetis*, M. Sjö Dahl **, J.P. Dear*</i> <i>E.ON UK</i> <i>*Imperial College, London, UK</i> <i>**Luleå University of Technology, Sweden</i>	70

Structural analysis and lifetime assessment of outlet headers <i>K. Calonius, O. Cronvall, P. Junninen</i> <i>VTT Technical Research Centre of Finland, Espoo, Finland</i>	83
Remaining life assessment of steam turbine boilers <i>V. Mentl, V. Liska</i> <i>SKODA Research Ltd., Pilsen, Czech republic</i>	106
Typical failures of reheater coils <i>E. Zbroińska-Szczuchura, J. Dobosiewicz, F. Klepacki</i> <i>Pro Novum, Katowice, Poland</i>	113
Reheat cracking susceptibility of new generation 2%CrMo(W)V P23 steel multipass welds made using matching and mis-matching filler metals <i>P. Nevasmaa, J. Salonen, S. Holmström</i> <i>VTT Technical Research Centre of Finland, Espoo, Finland</i>	128
Long-term creep testing and microstructure evaluation of P91 steel weld joints <i>D. Jandová, J. Kasl, V. Kanta</i> <i>ŠKODA VÝZKUM s.r.o., Plzeň, Czech Republic</i>	143
A hardness-based creep rupture model for new and service aged P91 steel <i>D.J. Allen, S.T. Fenton</i> <i>E.ON UK plc, UK</i>	156
Impurity effects on heat-to-heat variation in creep life for some heat resistant steels <i>F. Abe, H. Tanaka, M. Murata</i> <i>National Institute for Materials Science</i> <i>Tsukuba, Japan</i>	171
Predicting creep strain response from rupture data and a robust creep curve model <i>S. Holmström, P. Auerkari, S. Holdsworth*</i> <i>VTT Technical Research Centre of Finland, Espoo, Finland</i> <i>*EMPA, Dübendorf, Switzerland</i>	185
A new methodology for long term creep data generation for power plant components <i>B. Wilshire, P.J. Scharning, R. Hurst*</i> <i>University of Wales Swansea, UK</i> <i>*EC JRC Petten, The Netherlands</i>	196

Session 5. Conceptual and materials aspects for novel base load plant

VTT technology strategy in novel base load concepts <i>P. Aaltonen, L. Heikinheimo, T. Vanttola, J. Hämäläinen</i> <i>VTT Technical Research Centre of Finland, Espoo, Finland</i>	208
Generation IV material issues <i>L. Heikinheimo, P. Aaltonen, A. Toivonen</i> <i>VTT Technical Research Centre of Finland, Espoo, Finland</i>	212
Oxyfuel concept development <i>T. Pikkarainen, A. Tourunen, J. Hämäläinen</i> <i>VTT Technical Research Centre of Finland, Jyväskylä, Finland</i>	224
Modelling of supercritical conditions in the safety analysis codes <i>T. Vanttola, M. Hänninen, A. Daavittila</i> <i>VTT Technical Research Centre of Finland, Espoo, Finland</i>	235
NULIFE – Network of excellence for harmonised nuclear plant life management methods <i>R. Rintamaa, I. Aho-Mantila, N. Taylor*</i> <i>VTT Technical Research Centre of Finland, Espoo, Finland</i> <i>*JRC Petten, The Netherlands</i>	236
High temperature oxidation and corrosion of boiler materials <i>S. Tuurna, S. Yli-Olli, S. Holmström, L. Heikinheimo</i> <i>VTT Technical Research Centre of Finland, Espoo, Finland</i>	244

Maintenance of industrial plants as a part of corporate social responsibility

A. Jovanovic and D. Brukmajster

ZIRN – Interdisciplinary Research Unit on Risk Governance and Sustainable Technology Development, University of Stuttgart, Germany

Abstract

The paper deals with the change of role of maintenance of industrial plant along the corresponding change of priorities in the operation of plants. It looks at the role of maintenance in the actual concepts of operation in which the highest priority is often not any more at the technical and engineering aspects (“the plant must run and produce...”), or the economic aspects (“... yes, but at an affordable price and costs”), but at the “socially responsible production”. Taking the currently accepted “measures” like KPI’s and indices like GRI or those proposed in the EU project like NEEDS as the basis for the analysis, the paper shows how, where and how much maintenance can contribute to better performance of a plant according to the above “measures”. In particular, the paper highlights those KPI’s and indices which can be of a particular interest for the maintenance of the fossil fuel power plants.

1. Introduction – CSR, KPI, Integrated Risk Management

1.1 Corporate Social Responsibility (CSR)

Corporate Social Responsibility (CSR) continues to steadily grow in importance. Especially in the EU sustainable development and responsible business behavior and ethics are high on the policy agenda. Through the debate initiated by the Commission Green Paper «Promoting a European Framework for Corporate Social Responsibility» of July 2001 and the subsequent Communication «Corporate Social Responsibility A Business Contribution to Sustainable Development» of July 2002, the interest for and understanding of CSR and all its multiple facets has increased rapidly.

In 2002 The Commission introduced a European Multistakeholder Forum on Corporate Social Responsibility as a part of its strategy for promoting innovation, transparency and convergence of CSR practices and instruments. Recent years have witnessed a proliferation of CSR instruments: codes, reporting standards and guidelines, labeling schemes, management systems, screening methodologies for socially responsible investment. Not all these tools are comparable in scope,

intent, origin, implementation or applicability to particular businesses or sectors. As expectations on CSR become more defined, there is a strong case for greater transparency, credibility and coherence between standards, practices and measurement of performance.

1.2 Measuring CSR – Key Performance Indicators (KPIs)

As concern about the broad impacts of business on society has increased, there has been an explosion in the development of instruments to measure, evaluate, improve and communicate corporate performance in relation to social, environmental and ethical criteria. While there is little available data to put an exact figure on the number of companies that have taken on these instruments it is clear that they are becoming a significant part of the business environment.

The above concern is usually expressed in practice through the key performance indicators (KPI) as financial and non-financial metrics used to quantify objectives to reflect strategic performance of an organization. KPIs are frequently used to “value” difficult to measure activities such as the benefits of leadership development, engagement, service, and satisfaction. KPIs are, thus, tools for measuring and monitoring of the goals set up by the organization in the particular area of the company’s activities, or at the level of the company as whole.

The KPIs differ depending on the nature of the organization and the organization’s strategy. They help an organization to measure progress towards their organizational goals, especially toward those difficult to quantify. KPIs should be a part of a measurable objective. As such they can well fit the need to “measure CSR”. On the other hand, in the promotion of CSR one must have clear understanding of CSR instruments, their use, merits and limits.

1.3 CSR, industrial safety and KPIs

Industrial plants appear as the source of the industrial risk on all steps of their life cycle (Fig. 1). For large plants (e.g. power plants, refineries, process plants, etc.) with the design life of often more than several decades and with their age advancing towards and beyond the design limits, proper, i.e. “responsible”, inspection and maintenance may become key factors of safety of these plants, i.e. of the risks related to them. One can therefore say, that “the risk management is a major measure of the corporate responsibility of a plant owner” and that, especially for the plants in advanced age “inspection and maintenance are the major factors of risk”. The two premises yield the conclusion that the “inspection and maintenance, for a given class of plants, may become the main measure of the CSR of the company”. Practical aspects of this assertion are discussed below.

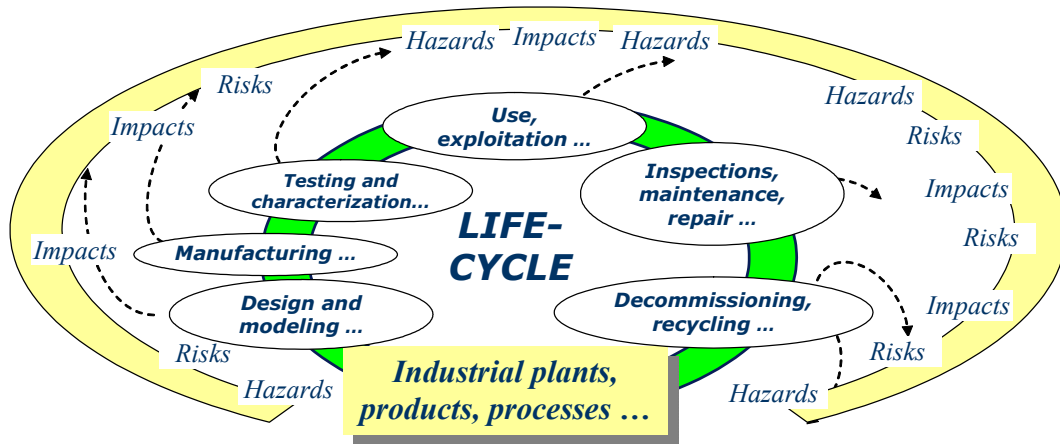


Figure 1. Industrial plants as source of industrial risks.

The above reasoning allows examining the role of maintenance of industrial plants along the corresponding change of priorities in the modern operation of plants: the concepts in which the highest priority is often not any more at the technical and engineering aspects (“the plant must run and produce...”), or the economic aspects (“... yes, but at an affordable price and costs”), but at the “socially responsible production”. Taking the currently accepted “measures” like KPI’s and indices like GRI or those proposed in the EU project like NEEDS as the basis for the analysis, the paper shows how, where and how much maintenance can contribute to better performance of a plant according to the above “measures”. In particular, the paper highlights those KPI’s and indices which can be of a particular interest for the maintenance of the fossil fuel power plants.

2. CSR Instruments

The problem today is not lack of instruments: there are many of them now available. The problem is their consistency and overall acceptance.

2.1 Available CSR instruments

The useful survey of available CSR instruments can be found on several source, like for instance:

- ILO Business and Social Initiatives Database¹ provides an exhaustive database of documents relating to CSR including instruments, searchable by sector, country and type of initiative
- Maquila Solidarity Network Codes Resources² compares major multi-stakeholder labor codes

¹ <http://oracle02.ilo.org:6060/vpi/vpisearch.first>

² www.maquilasolidarity.org/resources/codes/index.htm

- OECD Codes of Corporate Conduct Inventory³ looks at 233 voluntary codes
- Global Look, ILO⁴ reviews 215 codes and instruments in relation to labor issues
- U.S. Council for International Business Compendium of Corporate Responsibility Initiatives outlines approx. 20 the major international instruments⁵.

2.2 GRI – A common framework for sustainability reporting

The Global Reporting Initiative's (GRI) is a global initiative providing global reporting on economic, environmental, and social performance, within its international network of thousands from business, civil society, labor, and professional institutions. GRI accomplishes this vision in a consensus-seeking process primarily by means of its Sustainability Reporting Framework (<http://www.globalreporting.org/Home>, Fig. 2).

The reporting system is well developed for the generic aspects of CSR and covers the following main aspects (“CSR categories”):

- Economic aspects
- Environmental aspects
- Social aspects: Labor Practices and Decent Work
- Human Rights aspects
- Society related aspects
- Product Responsibility aspects.

Detailed guidelines are provided for each of the aspects and they include the assessment details. The assessment can be both based on self-declared items and on the GRI-checked ones (Fig. 3).

³ <http://www.oecd.org/ech/act/codes.htm>

⁴ <http://www.unglobalcompact.org/un/gc/unweb.nsf/content/ilostudy.htm>

⁵ www.uscib.org/docs/01_10_24_cr_compendium.pdf

Report Application Level	C	C+	B	B+	A	A+
Standard Disclosures	<p>Report on:</p> <ul style="list-style-type: none"> 1.1 2.1 - 2.10 3.1 - 3.8, 3.10 - 3.12 4.1 - 4.4, 4.14 - 4.15 	<p>Report on all criteria listed for Level C plus:</p> <ul style="list-style-type: none"> 1.2 3.9, 3.13 4.5 - 4.13, 4.16 - 4.17 	<p>Same as requirement for Level B</p>	<p>Report Externally Assured</p>	<p>Report Externally Assured</p>	<p>Report Externally Assured</p>
	<p>Not Required</p>	<p>Management Approach Disclosures for each Indicator Category</p>	<p>Management Approach disclosed for each Indicator Category</p>	<p>Report Externally Assured</p>	<p>Management Approach disclosed for each Indicator Category</p>	<p>Report Externally Assured</p>
	<p>Report on a minimum of 10 Performance Indicators, including at least one from each of: social, economic, and environment.</p>	<p>Report on a minimum of 20 Performance Indicators, at least one from each of: economic, environment, human rights, labor, society, product responsibility.</p>	<p>Respond on each core G3 and Sector Supplement* indicator with due regard to the materiality Principle by either: a) reporting on the indicator or b) explaining the reason for its omission.</p>	<p>Report Externally Assured</p>	<p>Respond on each core G3 and Sector Supplement* indicator with due regard to the materiality Principle by either: a) reporting on the indicator or b) explaining the reason for its omission.</p>	<p>Report Externally Assured</p>

*Sector supplement in final version

Figure 2. GRI reporting system and its (key) Performance Indicators and Sector Supplement performance Indicators.


		2002 In Accordance	C	C+	B	B+	A	A+
Mandatory	Self Declared			Report Externally Assured	✓	Report Externally Assured		Report Externally Assured
	Third Party Checked			Report Externally Assured	✓	Report Externally Assured		Report Externally Assured
Optional	GRI Checked			Report Externally Assured		Report Externally Assured		Report Externally Assured

Figure 3. Self-assessment vs. “GRI-checked”: The example illustrates that a report maker self-declared the B level and a third party checked the declaration and the GRI checked the declaration.

2.3 Economy and environment – main CSR-related issues of maintenance of aged plants

Although maintenance of aged plants could be put in the relationship to all six CSR categories mentioned above, and environment are certainly of a particular interest. Examples of indicators to look at for the definition of the KPIs are given below, as considered in the NEEDS project⁶ of the EU.

2.3.1 Economy

Examples of indicators (put in relationship to maintenance):

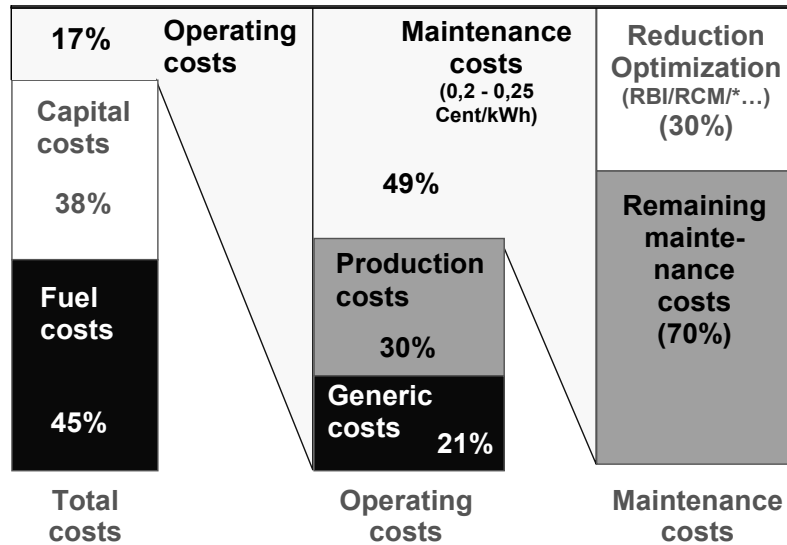
- Impact on customers / electricity price (indicator: production/maintenance cost, in €/kWh)
- Technical availability of the plant (indicator: plant availability, in %)
- Predictability of resource availability (indicator: possibility to predict resource availability day/week/month in advance, on ordinal scale).

2.3.2 Environment

Examples of indicators (put in relationship to maintenance):

- Impacts from accidents through release of effluents (indicator: release, in t/kWh)
- Impacts from accidents through land contamination (indicator: surface contaminated, in km²/kWh)
- Acidification and eutrophication (indicator: size of ecosystems affected by the air pollution from the plant).

⁶ <http://www.needs-project.org/>



* Other methods/tools:

- ⇒ Business Re-engineering
- ⇒ Lean Management, Lean Maintenance
- ⇒ Total Productive Maintenance, Total Quality Management
- ⇒ Outsourcing
- ⇒ ...

Figure 4. Maintenance cost in the economy of the plant (Source: E.ON VGB PowerTech 1/2001 / RWE).

3. KPIs in Inspection and Maintenance

KPI selection should be done in that way that they serve the purpose, i.e. they define the target. When selecting a KPI, the following rules should be applied:

- 1 up to 5 indicators per target
- Relevance: the indicator must be relevant for the target
- Operability: indicator must be influence able by the management
- Cost – Benefit – Ratio: to get the indicator must be easy.

The indicators can be

- Absolute Indicators: number of events, values in Euro....
- classification Indicators: quotas, percentages ...
- Index Indicators: test points.

Each KPI is linked to a measurement. The measurement has to have:

- the target value of the indicator
- the interval of measurement
- the threshold values.

Examples of the KPIs that could be interesting for maintenance are given in the tables below.

3.1 KPIs: corporate perspective

Objective	KPI
1. Improve Safety and Environmental Conditions	Number of overall safety and environmental incidents
2. Increase Asset Utilization	Overall equipment effectiveness, utilization
3. Increase Return on Investment (ROI)	Return on Capital Employed
4. Increase Revenue from Assets	Production Throughput
5. Minimize Safety and Environmental Incidents	Accident by type, time of day, craft, personnel age, training hours attended, supervisor, unit, area
6. Reduce Production Unit Costs	Cost Per Unit
7. Reduction of Controllable Lost Profit	Lost Profit Opportunity Cost
8. Reduction of Maintenance Expenses	Annual Maintenance Cost / Asset Replacement Cost / Maintenance Cost / Unplanned cost as a % total maintenance cost

3.2 KPIs: asset perspective

Objective	KPI
1. Improve System Availability	Unit Availability / Uptime
2. Increase Equipment Reliability	Average Cost Per Repair
3. Increase Equipment Reliability	MTBR ⁷ / MTBF ⁸
4. Minimize Unscheduled Equipment Downtime	Number of Lost Profit Opportunity Events
5. Reduce Equipment Failure Time	Equipment Failure Downtime
6. Reduce Non-Equipment Downtime	Downtime due to quality, feedstock, production scheduling
7. Reduce Scheduled Maintenance Downtime	Turnaround Downtime
8. Reduce Unscheduled Repairs	Number of Failures

⁷ Man Time Between Repairs

⁸ Mean Time Between Failures

3.3 KPIs: work practices perspective

Objective	KPI
1. Improve Labor Efficiency	Labor Cost of Repairs
2. Improve Maintenance Planning and Scheduling	% of Emergency (break in) work orders
3. Optimize Time-Based Maintenance	% of Critical Equipment Optimized
4. Perform Criticality and Risk Assessments	Number of failures on critical and high risk equipment
5. Perform Reliability Studies	Number of new work orders generated from Reliability Analysis
6. Reduce Maintenance Material Inefficiencies	Average Parts Wait Time

3.4 KPIs: knowledge and experience

Objective	KPI
1. Improve Operations Communications	Number of defects observed from operators
2. Improve Historical Equipment Data Collection	% of populated required fields in work order history
3. Train Maintenance and Operations Personnel	Hours of training per employee / Euros spent on training per employee

Examples of the key software features are shown in the figures below (screen shots from a system currently under development at Steinbeis Advanced Risk Technologies). The software will include the KPI monitoring (balanced score-card) as also shown in Fig. 5.

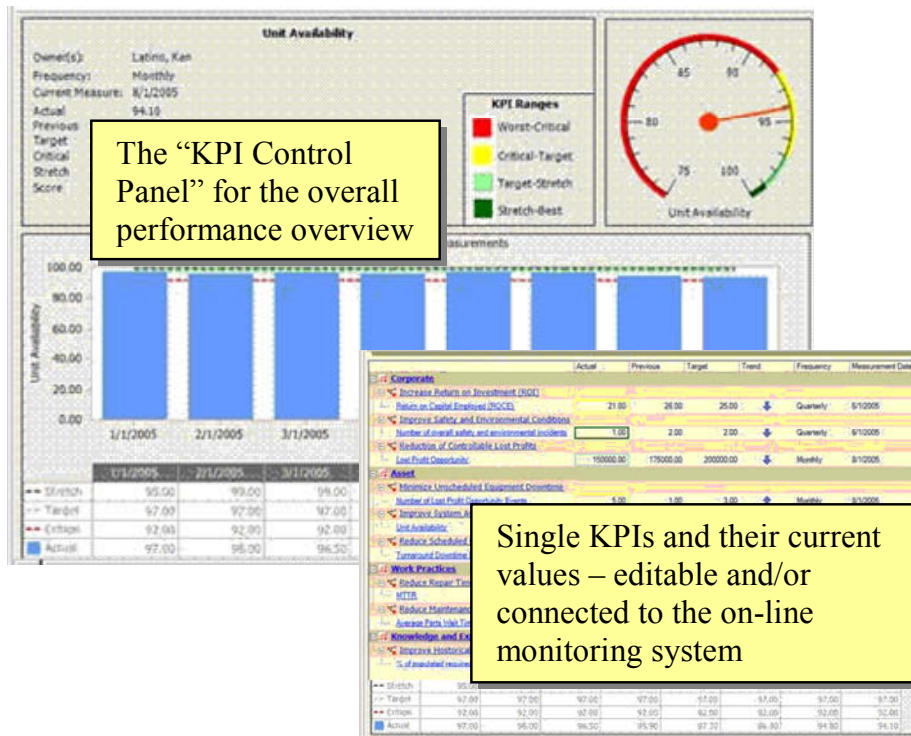


Figure 5. Sample sheets for monitoring KPI development.

4. Performance review: Using the RBI and RCM related KPIs for assessing the CSR performance

An example of using the RBI and RCM related KPIs for assessing the CSR performance is given in RIMAP CEN WA 24 [1]. The purpose of the evaluation of the risk-based decision-making process is to assess its effectiveness and impact in establishing the inspection and maintenance programs. This allows the identification of areas where modifications and improvements are needed. Specifically, evaluation consists of:

- Assessment of the effectiveness of the risk-based decision-making process at achieving the intended goals (assessment of effectiveness)
- Updating the risk-based decision-making process by taking into account possible plant changes and available new knowledge (reassessment of the risk).

4.1 Requirements

The evaluation process involves both internal and external assessment conducted by the operating organization and by independent external experts, respectively. The internal evaluation by the plant organization is an integral part of RBIM activity and should be considered as a living process within the overall risk decision-making process. Internal evaluation can take place in any moment of RBIM, especially when:

- discrepancy from expectation is found
- new knowledge is available or plant changes occur.

In both cases, a detailed analysis of the importance of the involved item (discrepancy or new knowledge/plant change) has to be conducted in order to assess whether it has a significant impact on the RBIM process, and some corrective action should be undertaken. In these cases a thorough analysis of the causes to discrepancy or of the effects of the new knowledge/plant changes has to be performed.

External evaluation can be executed through independent reviews by external or regulatory organizations (e.g., audits). Independent reviews provide an opportunity to complement the internal evaluation with a different and neutral perspective. A point to note is that the value of information provided by the independent review is directly proportional to the openness and collaboration that the external experts will find in the audited organization. The integration of independent reviews with internal evaluation allows the identification of necessary actions for improvement.

4.2 Inputs

For assessment of effectiveness:

- Definition of risk decision-making process goals (risk may be expressed in one or more of the following terms: safety, health, environment and business impact)
- Definition of Performance Indicators as a measure of the RBM/RBLM process achievements against the above goals. (Note that in order to enable a meaningful evaluation of the performance, consideration should be given to the appropriate time frame applied for the various performance indicators. Especially when a relation should be identified between the performance and potential causes, it may be more meaningful when certain quantities are assessed for a longer period of time. For example, the cost of inspection and maintenance in year X affects the availability in a certain period of time after year X.)
- Reference to existing standards
- Benchmarking with similar operating organizations.

For reassessment of risk:

A) Plant information

- Changes in design
- Changes in plant operation (mission, operational regime, production rate, capacity, internal & external environment)

- Time dependent operating conditions (e.g., fatigue, cracks)
- Changes in plant management
- Change in level of personnel training
- Feedback from industry-wide operational experience
- Inspection results (rate of relevant damage/degradation mechanisms)
- Maintenance records.

B) New knowledge:

- Applicable research and development results
- Newly improved risk processes
- Advanced inspection methods
- Failure history of actual systems/components
- Newly discovered degradation mechanisms (absence/presence of unanticipated degradation mechanisms)
- New data on inspection and testing effectiveness.

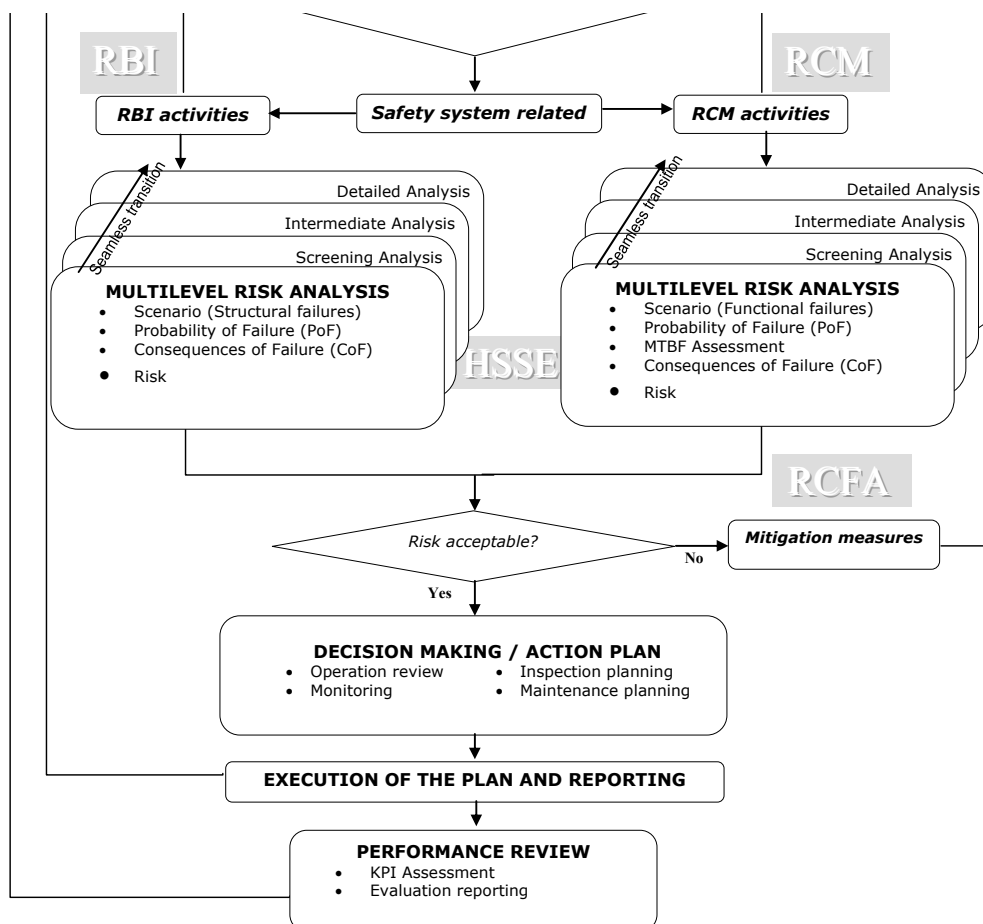


Figure 6. Position of the performance review in the framework of RIMAP procedure of CEN WA 24.

4.3 Procedure

Assessment of efficiency is a combination of good reporting including the aspects with respect to the business targets, and external audit of the plant (Figure 6). This audit can be done by internal resources (typical for large organizations), by the owner, or by an independent third party.

4.4 Reporting of Key Performance Indicators

Key Performance Indicators (KPIs) are in this context used for measurement of the business performance of a plant. The KPIs should reflect important goals for the plant, company or owner, and may change with time. For example, a plant in its run-in period may focus on availability and at a later stage more on maintenance cost.

5. Conclusions

The changes in the role of maintenance of industrial plant result in the corresponding changes of priorities in plant operation. Regarding the role of maintenance in the concepts of operation the highest priority is often no more in the technical, engineering or even in the economic aspects, but rather at the “socially responsible production”. Taking the currently accepted “measures” like KPI’s, indices like GRI, or those proposed in the EU project NEEDS as the basis for the analysis, it has been shown above how maintenance can contribute to better performance of a plant according to these “measures”.

As for the most other measures and indices of performance, also for those related to inspection and maintenance the major problems remaining are:

- Global (“universal”) acceptance
- Coherence of measures and their weights, needed for the comparability of different plants (How to combine different KPIS?)
- Right balance between the specific and general aspects covered (the too specific measures not broadly applicable, the too generic ones often meaningless).

References

- [1] RIMAP CEN Workshop Document, CEN Workshop 24 “Risk-Based Inspection and Maintenance Procedures for European Industry”, Jovanovic A., Main Editor, Final Draft Document in 60 days public discussion at CEN, April 2007.
- [2] RIMAP D.4.2: Benchmarking indicators, GROWTH project GIRD-CT-2001-03008 “RIMAP”, RIMAP RTD Consortium, 2002.

Life management of creep strengthened ferritic steels in boilers and piping

Jonathan Parker

Structural Integrity Associates, Inc., Oakville, Canada

Abstract

The advantages offered by creep strengthened ferritic steels can only be realized with careful control of fabrication methods. Effort will be needed during service to evaluate component performance. Direct life assessment methods can provide useful information for condition assessment provided that the methods are properly matched to the potential damage mechanisms and locations.

1. Introduction

Grade 91 steels (9Cr-1Mo-V steel) were accepted by ASTM for tubing applications in 1983 and for headers and piping in 1984. Subsequently, alloys based on 9 to 12% Cr have been used in a wide range of applications in both new construction and existing plant. (e.g. 1, 2, 3) Due to the importance of these steels to the global power generation industry, major research efforts have been undertaken in the USA, in Europe and in Japan and other Pacific Rim countries. These efforts have been aimed at understanding and quantifying the factors affecting microstructure and properties to optimize the use of Grade 91 and to develop further advanced steels.

The improvements in performance offered by Grade 91 can only be realised when manufacturing parameters and operating conditions are carefully controlled within defined limits. These issues include careful control of alloy composition, fabrication and welding practices and associated heat treatment. Indeed, one recent development is renewed interest in the use of longitudinally seam welded piping. Seam welded piping fabricated from CrMo steels are well known to be at high risk of catastrophic creep failure and in most cases the use of seamless alternatives is preferred. There are several power-related projects in North America and elsewhere that either are in progress or have been completed in which seam-welded piping fabricated from Grade 91 material will represent a significant portion of either the main or hot reheat steamline piping circuit.

The present paper reviews key information regarding the high temperature performance of creep strengthened ferritic steels and highlights key methods

which should be adopted for quality assurance during construction and for subsequent in-service assessment of performance.

2. Creep behaviour

At the design stage it is necessary to assess the expected long term creep strength. Establishing allowable stresses for a given alloy thus involves analysis and extrapolation of available shorter term data. In setting allowable stresses the various design codes require:

- That different numbers of material casts and types are tested
- Extrapolation of data using an accepted methodology with a requirement for some ‘long term’ data to be included in the available data set.

Frequently parametric methods are used for data extrapolation. One of the most common is the Larson Miller method which is based on the premise that stress rupture results generated over a range of stresses and temperatures can be superimposed on a single master curve. In any material data set there will be variation due to scatter in results and so, in most cases, codes seek to ensure that allowables are based on conservative methods of extrapolation and include factors of safety. Consideration of the situation regarding Grade 91 steel illustrates the problems which can occur using parametric methods for excessive levels of extrapolation. The stress rupture behaviour of traditional boiler steels is described using the Larson Miller equation using the equation:

$$LMP = T (\text{constant} + \log t) \quad (1)$$

Where t is the rupture life and the constant normally has a value of 20. This value is typically determined by best fit curve fitting the available data. However, the number obtained is related to the activation energy for creep fracture. Thus, if the data set assessed involves failure from a common mechanism then a reasonable fit will be obtained. The typical value of 20 for low alloy steels is thus derived from the relevant activation energy. Moreover, if the failure mechanism in the laboratory tests is relevant to the long term service behavior analysis of the results will be relevant to in-service performance. In the case of tests on Grade 91, a very wide range of “constant values” has been reported, but in general the most used value is close to 30. This is because in most cases the tests used in the analysis were relatively short term under conditions not representative of service. The relatively rapid tests were described with a relatively high value of activation energy thus giving a high value of the constant. The traditional view has been challenged (4) on the basis that when considering tests with relevant damage to long-term service the data are best described with a constant of 20. Since the data analysis is required for extrapolation of results, it should be appreciated that use

of the lower constant significantly reduces the predicted long-term creep lives. Thus, the 'right' value' is not simply a matter for academic interest.

The previous comments should not be taken as a specific criticism of the Larson Miller method in isolation. It is clearly the case that if the short term data are generated under conditions or microstructures that are fundamentally different from those in service, problems with extrapolation will occur. As more rupture results become available it appears that the long term performance of Grade 91 steel is falling below earlier predictions. The data presented in Fig. 1 show recent results reported for different test temperatures (5). The curves through the actual results at 550°C and 600°C are below the level predicted some 10 years before. This behavior can be explained by microstructural changes which only occur in the long term and variations in damage development.

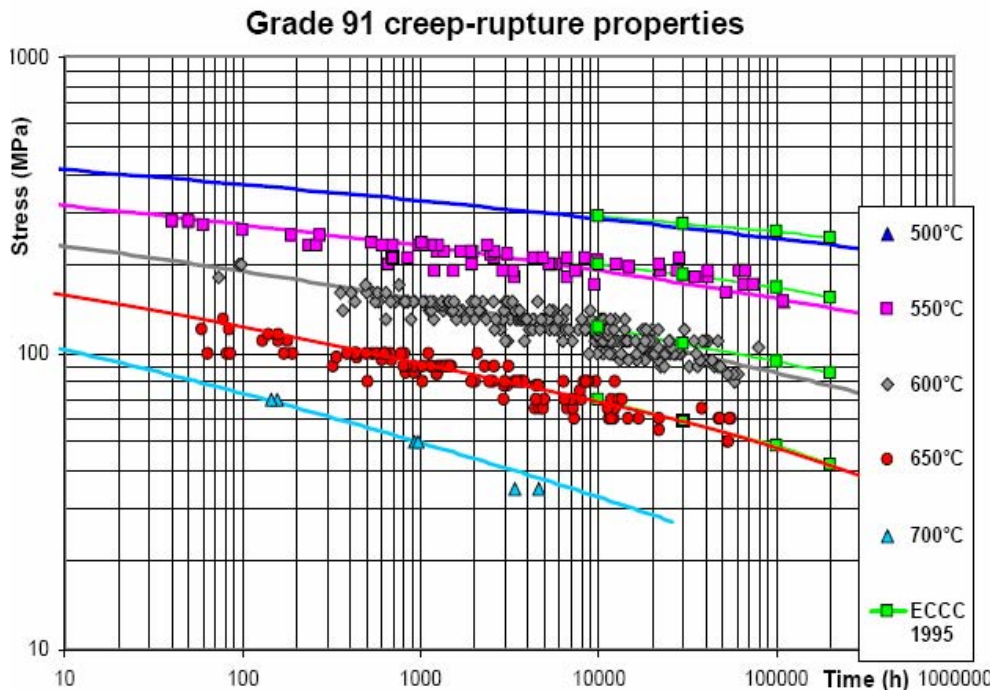


Figure 1. Comparison of long term stress rupture behavior for Grade 91 steels with predictions made in 1995 (5).

3. Component manufacture

Fabrication of fittings bends etc requires that multiple heat treatment cycles are applied. The excellent properties for Grade 91 recorded under laboratory conditions are achieved with strict control of composition and heat treatment. Thus, the more fabrication steps are involved during the manufacturing process, the greater is the opportunity for error.

‘After fabrication’ quality assurance normally consists of looking for macroscopic defects e.g. inaccurate dimensions or cracks. Testing of this type is important for Grade 91 steel. Indeed, cracking has been found in parent metal sections either before or very soon after service (6). It thus appears that the Quality Assurance approaches used following fabrication do not always find the defects present.

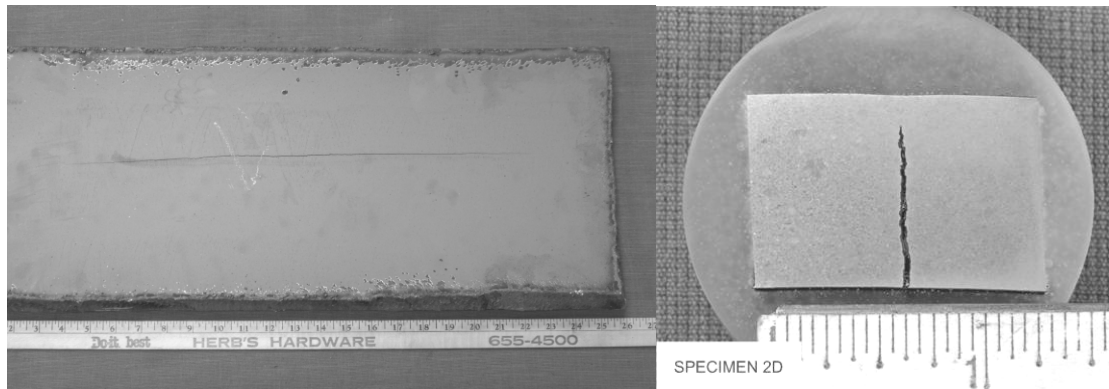


Figure 2. Example of cracking found shortly after service in the parent metal of a Grade 91 piping component (6).

It is now also apparent that a proper QA evaluation requires an assessment of metallurgical condition. The metallurgical tests typically seek to assess whether the material has been fabricated to produce the necessary balance of high strength and toughness. Brittleness has traditionally been assessed in steel structures by looking for untempered martensite. Since these structures are hard as well as brittle, hardness testing was both a reasonable and practical approach to use. Thus, much of the shop and field QA testing of Grade 91 components to date has involved hardness testing. Application of portable hardness equipment requires use of proper procedures, staff training etc because errors in data can result from variations in surface preparation, user technique, calibration issues etc. However, consideration of results of properly conducted test programs shows that component fabricated from Grade 91 have been found entering service with hardness values from 150 HV to over 300 HV. Certainly values over 300 HV would normally be considered above the acceptable range and because of low toughness concerns, these components would be candidates for additional tempering. At the bottom end of the range, the concerns are with material with unacceptably low creep strength. Where ‘soft’ material has been found metallographic evaluation has shown that the microstructures are predominantly ferrite and coarse carbides, see for example Fig. 3. In this condition the creep strength may be over an order of magnitude lower than that expected.

In a similar manner to in-service experience with CrMoV low alloy steel and X20 where in-service damage has been found, bending of Grade 91 can result in reduced creep life. These problems can occur in either cold bent or hot bent components. However, it appears the reasons for the problems are different.

Experimental programs have shown that cold work induced bending does have a significant adverse effect on the creep rupture strength of Grade 91 material (7, 8). It appears that damage increases as the level of cold strain increases. Moreover, application of a subcritical heat treatment provides no significant benefit in restoring creep properties. The increased rates of creep may be related to the influence of cold work in accelerating recovery and recrystallization processes or because the cold strain can promote creep cavity formation thus causing more creep voids to initiate early in life. Both of these effects have been found to accelerate creep damage in previous studies examining the influence of prestraining on creep behavior of pure metals and commercial alloys.

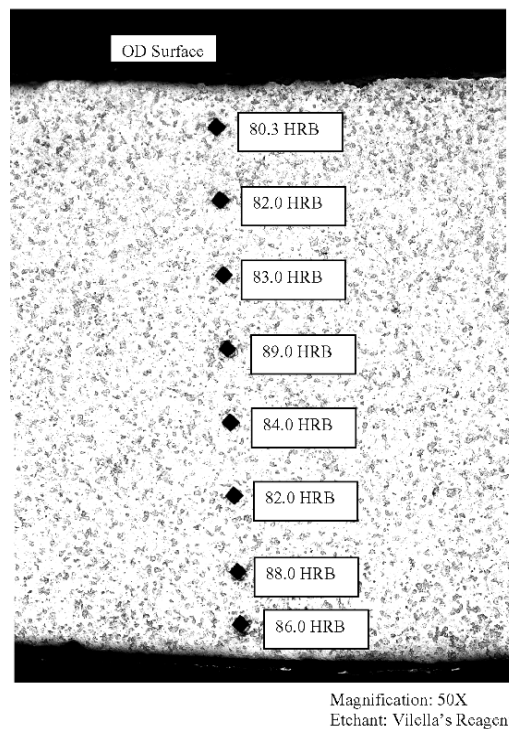


Figure 3. An example of a material sample removed from a component soon after the start of service showing a ferritic rather than the normal martensitic microstructure in Grade 91 piping. (9).

Hot forming is normally performed by induction bending. This process should allow close control of both the deformation and the temperature profiles. However, it is generally recommended that a full normalized and tempering treatment must follow all hot forming operations. It is important that the heat treatment is performed on the entire piece to avoid local microstructural transitions, and that the specified temperature conditions are applied. Proper instrumentation in the form of thermocouples should be used to monitor temperature distributions through both the normalizing and tempering operations. Post heat treatment quality assurance should include review of the temperature records and hardness testing. In situations where hardness data are below 200 HV further evaluation should be performed.

4. Weldment performance

Strength of the weldment is a critical consideration in determining the long-term integrity of the component or system. While room temperature strength is important, the long-term strength of the weldment at elevated temperatures is crucial. Weldments manufactured from advanced steels are particularly susceptible to creep cracking at the outer edge of the heat-affected zone (HAZ) known as Type IV cracking, Fig. 4.

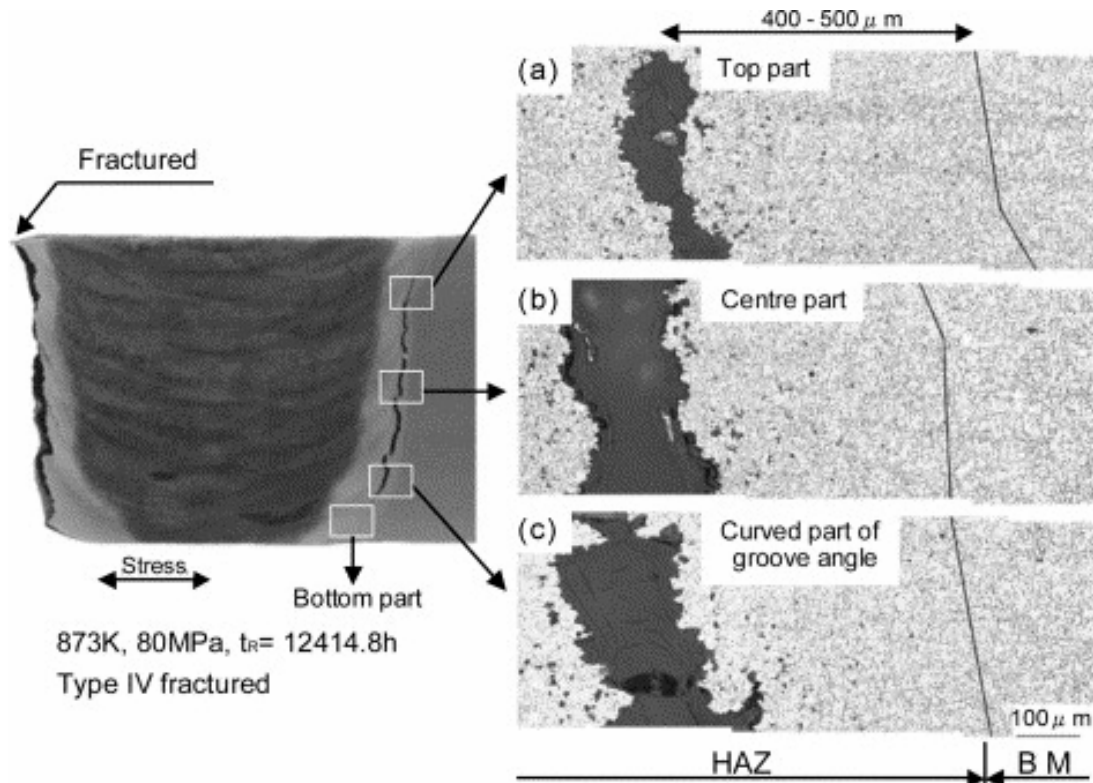


Figure 4. An example of Type IV cracking in an advanced steel weld (10).

It has been shown that welds fabricated from advanced steels exhibit a relatively high susceptibility to Type IV cracking. This occurs because the excellent creep strength of the parent is achieved by ensuring that a uniform distribution of fine carbide and carbonitrides precipitates is developed. The thermal cycles involved with welding cause the normal precipitate distribution to be modified so that a relatively narrow band of low strength material is developed. In the presence of a suitable creep stress, accelerated creep damage is developed within this zone.

Because of the catastrophic nature of the failures associated with seam welded piping for some time now there has been a trend to replace low alloy steel longitudinal seam welds in main steam and hot reheat piping. It is therefore particularly interesting to note that recently seam welded hot reheat piping has been used in the design and fabrication of advanced fossil plant. These

components fabricated predominantly from Grade 91 martensitic steel have been shown to be susceptible to the development of creep damage and cracking much more rapidly than would be expected from consideration of parent metal properties. In welds fabricated with a double vee profile the macroscopic features of the crack path seem similar to those in low alloy steels, see for example Fig. 5 from a full sized component test on a double seam welded Grade 91 bend. Detailed evaluation shows, however, that although damage again initiates at or very close to the cusp region, in this case cavitation and cracking is in the HAZ. This damage thus appears very similar to Type IV cracking observed in ‘U’ preparation welds. It appears that the very high susceptibility of Grade 91 steels to Type IV cracking is likely to be a significant problem with seam welded pipe for either relatively thick section, e.g. geometries in main steam lines or relatively thin section, e.g. geometries typical of hot reheat lines.

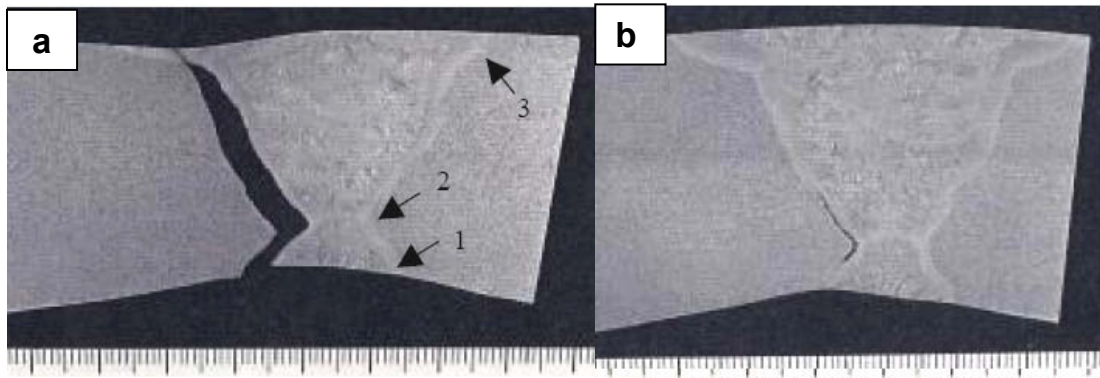


Figure 5. Crack path through the heat affected zone of a Grade 91 longitudinal seam weld (a), and a region of damage initiation in the weld cusp region (b) (11).

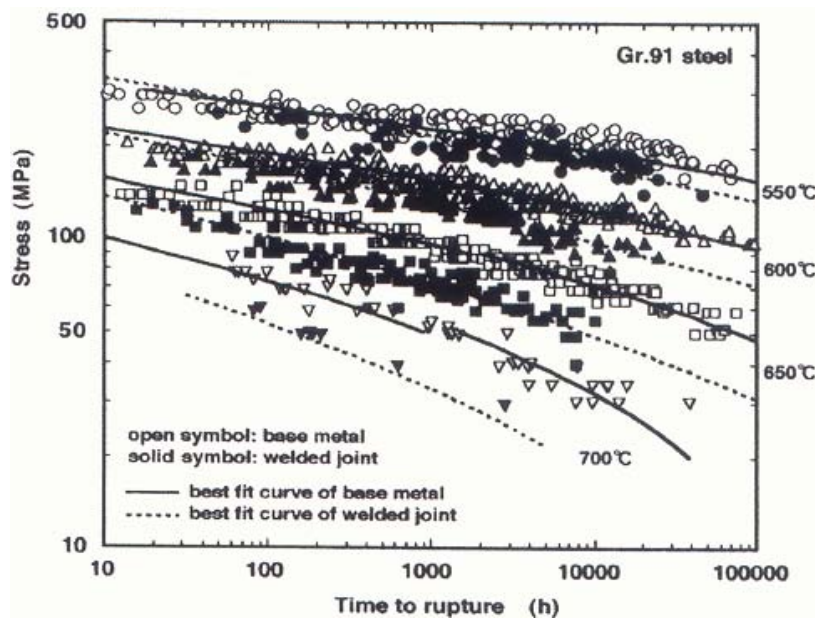


Figure 6. Comparison between creep rupture data of welded joints and base metals for Gr.91 steel (12).

Consideration of the results of long term testing on cross weld samples shows that as the test duration increases the failure location changes from being in the parent metal to the Type IV location. Thus, as was discussed earlier it is again the case that only long term laboratory tests give failure modes typical of service. Analysis of a very wide range of parent and cross weld data (12) shows that the decrease in life for welds compared to parent increases with increasing temperature, Fig. 6. As shown there is a significantly lower life for welds at temperatures relevant to service thus it is considered necessary that weld strength reduction factors should be included both in design and performance assessment calculations. There is still discussion regarding the specific value that should be adopted as a strength reduction factor for CSF steels. In general, the most widely quoted value for a Weld Strength Reduction factor for Grade 91 is in the range 0.65 to 0.75 of the base metal allowable stress.

5. Service experience

A series of plant failures have been reported in Grade 91 components. One of the first which occurred after 20 000 hrs was attributed to incorrect heat treatment. Others in header end plate welds occurred after 36 500 hrs (with 469 hot and 72 cold starts). Damage in both cases was identified as Type IV cracking, Fig. 7 (13). Key information related to the damage included, nominal operating conditions for the headers were 568°C 1055°F, and 160 bar, and the failed weld had been inspected using manual UT and found clear 8 663 hrs prior to failure. Following the failure, high sensitivity UT was carried out on the three other modified 9 Cr headers on the affected unit and the equivalent headers on another unit. This led to the discovery of further damaged end plate welds. Failures in other end cap welds have occurred and these locations are increasingly being earmarked for on site component inspection using advanced techniques such as Linear Array UT.

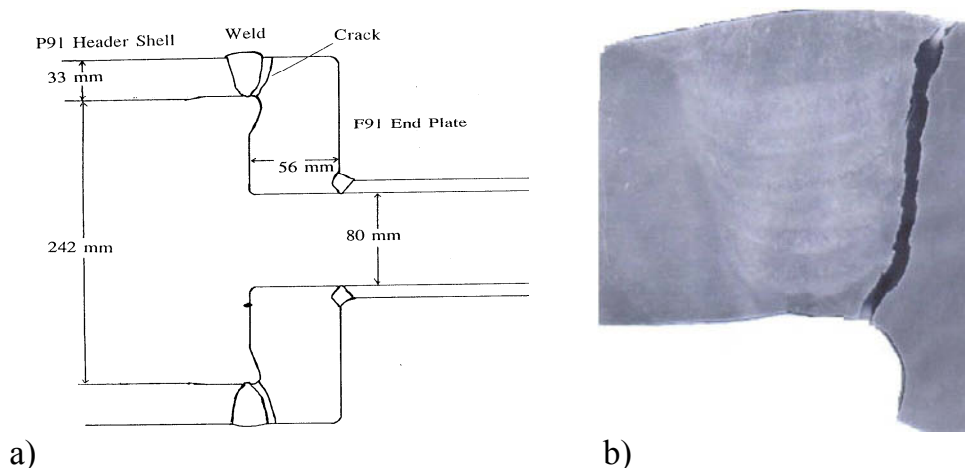


Figure 7. Schematic diagram showing the component geometry and the crack (a) (13), and a metallographic section showing Type IV cracking (b) (14).

A key finding in the cause investigation was that the casualty materials had entered service in an over-tempered condition. It did not however prove possible to confirm this from the manufacturing heat-treatment records available. Two factors identified metallographically were: low hardness and high aluminium to nitrogen (Al:N) ratio. Subsequent examination of a wider range of components has found that further creep damaged Grade 91 welds have occurred in service in situations where the parent exhibited high Al:N ratios (15). In this case metallurgical analysis of material samples removed from the in-service components alerted the utility to the increased risk of damage. The inspections performed identified a significant number of welds with Type IV cracking, e.g. Fig. 8, and it was possible to undertake the necessary remedial action without the need for numerous forced outages.



Fig. 4. Type IV crack on the header side toe of a large branch

Figure 8. Examples of type IV cracking observed in header welds (15).

It is apparent that the influence of High Al levels will not be limited to influences on creep strength. It has been clearly demonstrated that high levels of fine inclusions in a steel can reduce ductility with high aluminum (16) and reductions in ductility with Al:N ratios have been reported. This reduction occurs particularly in steels with a fine grain size because in this case the large number of inclusions on grain boundaries act to initiate creep voids and cracks (17). In the present case the high levels of Al will promote Type IV cracking both by reducing the strength and by facilitating damage nucleation.

The low hardness values measured in these components were consistent with an over-tempered condition and poor creep strength. The poor creep strength at low N: Al ratio occurs because the formation of aluminium nitride will leave less nitrogen available to form the creep resisting nitrides and carbonitrides. The creep strength of modified 9Cr is critically dependent on these precipitates. Indeed, study of 9–12%Cr martensitic alloys has shown that there is a significant effect of the level of Al present on creep strength. Reductions in creep strength

have been measured for 12%Cr steel irrespective of the Nb content of the steel (18). This acceleration appears to be direct consequence of reduced vanadium nitrides. In addition, the additional amount of aluminium nitrides formed at high aluminium content appears to reduced creep ductility Fig. 9 (18). This reduction is a consequence of easier void nucleation when fine inclusions are present.

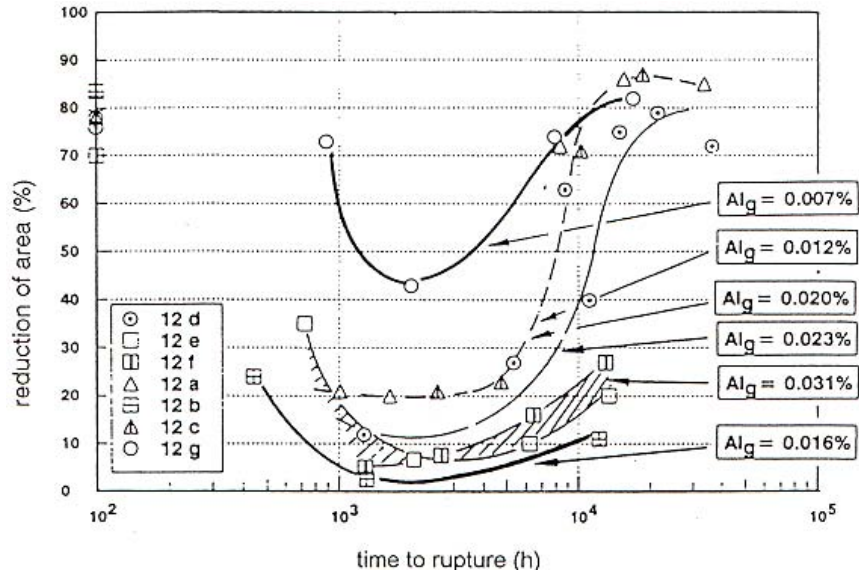


Figure 9. Reductions in the creep ductility of X19CrMoVNbN 11.1 steel as a result of increased aluminum content (18).

6. In – service monitoring

Coarse screening using portable hardness testing at room temperature has value in identification of components with poor strength or toughness. However, this type of testing will not be sufficiently accurate to differentiate between all the expected ranges of creep strength. Thus, additional developments associated with material sampling and testing are clearly required to properly assess creep strength. The following sections highlight information from hardness, from sampling and specialist testing and from strain monitoring. In each case the benefit to performance evaluation is high lighted. Detailed discussion of the advanced NDE techniques used to assess damage developments in welds is not presented. It must be emphasized that proper application of NDE is a key aspect of an integrated assessment program.

6.1 Hardness testing

It has been suggested that hardness measurements made under ambient conditions can be used to reflect the development of damage in service

components. However, measurements of hardness undertaken under plant conditions are susceptible to wide scatter making accurate life assessment difficult if not impossible. The scatter in plant data may be explained in part by work which shows that surface preparation affects hardness particularly at low loads for softer microstructural forms. The following have been suggested as factors, which, for a given material, will influence hardness values: surface preparation, number of measurements, wall thickness, degree of surface “flatness”, measuring orientation, type of tester, indenter load, and oxidation /decarburization of the surface.

Provided proper care is taken in surface preparation and in making the measurements, it is apparent that hardness data can be used to:

- Identify areas where fabrication ‘irregularities’ have occurred, Fig. 10,
- Allow a reasonable estimate of the equivalent operating temperature in cases where repeat measurements have been taken at different times at a given location, and
- Provide one input into relationships seeking to link hardness changes to creep life.

To utilize such measurements for estimating remaining life, it is typical to ignore the well-known fact that hardness will be affected by other factors other than precipitate size and distribution, e.g. grain size, and for CSF steels composition and dislocation density and arrangement. Where large databases have been developed for traditional alloys, analysis indicates that trends in behavior can be identified. Thus, for 2¼Cr1Mo steel, it appears that it is possible to apply a lower bound criterion to provide a realistic minimum remaining life indicator.

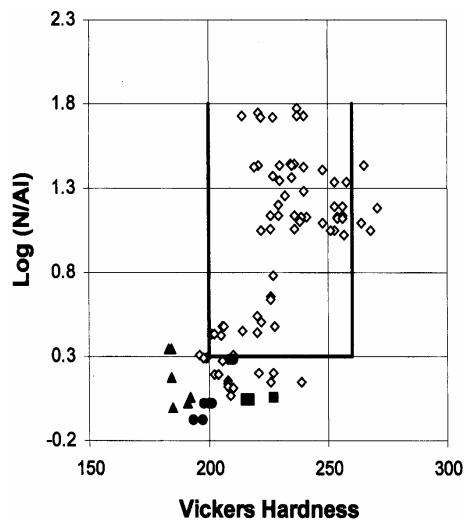


Figure 10. Materials confirmed to have low creep strength, either by in-service failure (triangles) or creep testing (circles small scale, square uniaxial), plotted as $N: A_I$ ratio and hardness (15).

6.2 Sampling and specialist testing

Techniques are available which allow sample removal to be undertaken in an effectively non-destructive manner (e.g. 19). Even small sections of material are of benefit since application of laboratory techniques allows actual composition to be determined. For complex alloys such as CSF steels this is an advantage because it permits accurate determination of all elements. In addition, a number of specialist small sample techniques have been developed which allow measurement of properties. For example, performing punch tests under controlled high temperature conditions has permitted detail of materials creep behavior to be established. Work in this area has predominantly been undertaken in Europe and Japan with information obtained on a range of pure metals and engineering alloys including aluminium, copper, low alloy steels, austenitic steels and Grade 91 martensitic steel (e.g. 20, 21).

In addition, creep data have been measured using indentation creep. This approach monitors strain time behaviour for a given load and temperature. The creep curves developed allow the minimum creep rate to be determined so that a direct measure of strength is available, for example Fig. 11 (22, 23). These data can be used to assess component behaviour as part of a parallel analysis program or through knowledge of Monkman Grant used to estimate actual life.

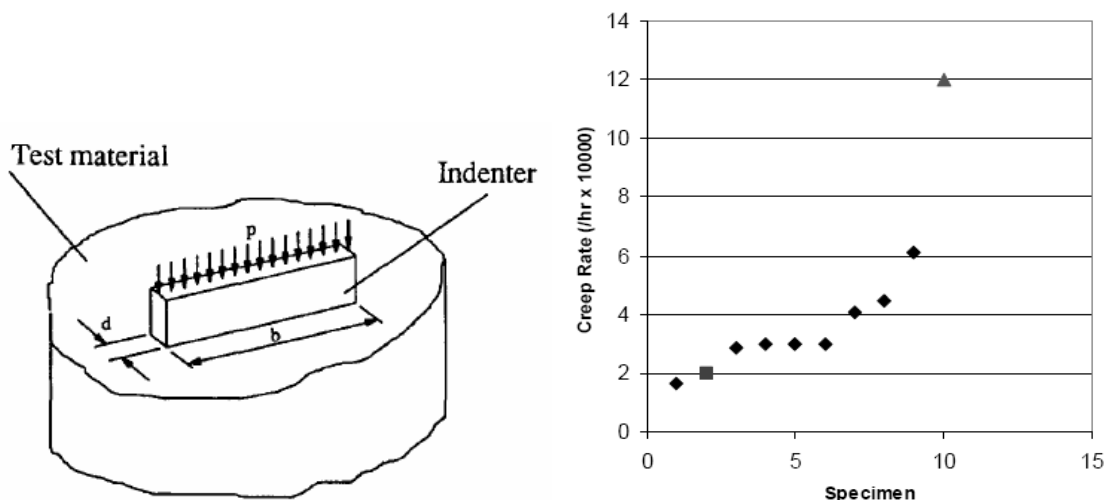


Figure 11. Schematic diagram showing the indentation creep arrangement (a)(22) and results from a series of tests showing the measured variation in creep strength(b). The measured strength values were in agreement with other data obtained using standard techniques (23).

The specialist test techniques are therefore of benefit to condition assessment of CSF steel components because data provide:

- Measurement of the creep strength of components, and
- Estimates of the levels of in-service creep damage.

These capabilities offer advantages to component assessment since the estimates of performance are based on actual not assumed properties, With CSF steels since the possible variability is large this is of particular advantage.

6.3 Strain monitoring

On-line displacement measurements at elevated temperatures are typically undertaken using capacitance devices. The trend in strain accumulation under multiaxial conditions is similar to uniaxial i.e. the rate decreases during primary creep before accelerating in a tertiary stage.

Because of the uncertainty with initial creep strength one option for the assessment of the “as fabricated” strength is to utilize in service strain measurements. This method has been widely used as a direct measurement of performance both in laboratory experiments, in full size pressure vessel tests and for in-service monitoring. A recent application has described the use of capacitance gauges for the assessment of an X 20 steam line bend. The gauges, shown in Fig. 12, with typical output showing displacement: time behaviour presented in Fig. 13. This application demonstrated that output was reliable and it was possible to take readings from a location of known damage (24).



Figure 12. Capacitance strain gauges shown installed on an X20 steam pipe component (24).

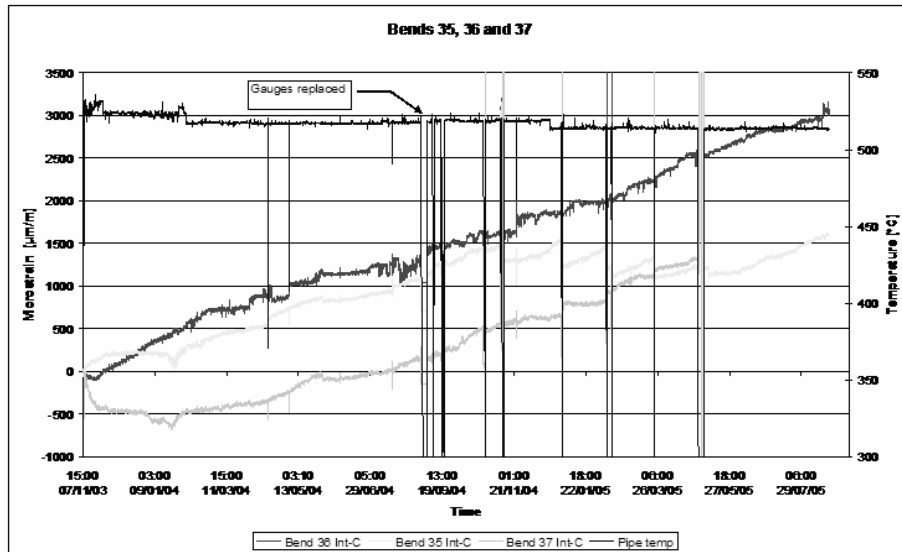


Figure 13. Output from 3 X20 piping components showing the increase in displacement with time (24).

Strain monitoring is an attractive remanent assessment method since it can be carried out non-destructively either at ambient conditions or on-line. The simplest strain based approach is the application of a strain limit. In this context a value of 1% strain has been suggested as indicating that the frequency of inspections should be increased. Detailed modeling of strain accumulation with time allows creep curves to be developed for any applied stress conditions. This approach has been used to develop relationships between creep strain and remaining life. The curves developed for selected stresses are shown in Fig. 14. Consideration of Fig. 14 indicates that for service stresses the proposed strain limit occurs at approximately 70% of the creep life. This in agreement with the strain limit approach suggested following evaluation of plant experience.

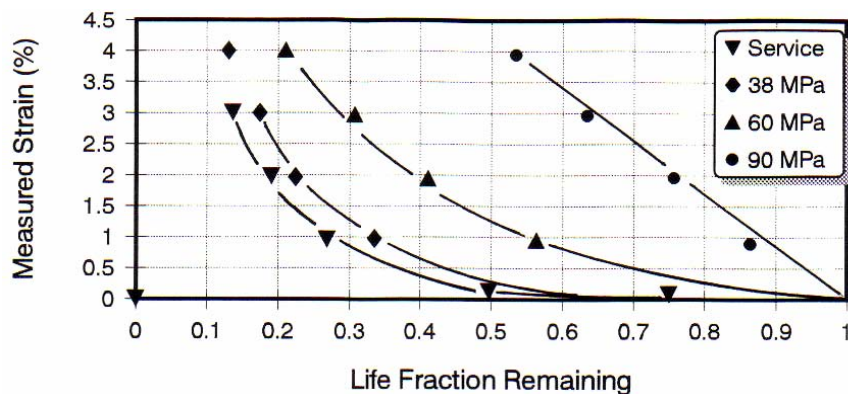


Figure 14. The variation of hoop creep strain with remaining life fraction (25).

The results shown in Fig. 14 are consistent with the semi quantitative strain limits recommended in European assessment approaches such TRD 508. Here

the recommended limits where further detailed assessment and lifing are 1% to 2% hoop strain. The analysis in Fig. 14 indicates that for typical in service conditions in pipes these limits occur at between 75 and 85% life fraction.

Whilst long term damage development in weld heat affected zones, for example Type IV, occurs with low overall deformation there are relatively high levels of local strain. Thus, provided sufficiently accurate strain monitoring takes place, assessment of deformation can provide a means of evaluation of condition. Since in some cases HAZ damage develops in the body of the component evaluation of surface cavitation using replica techniques may prove non-conservative.

7. Concluding remarks

The advantages offered by creep strengthened ferritic steels can only be realized with careful control of fabrication methods. Appropriate quality assurance checks must be performed to ensure that properties meet specification. Where these tests indicate that properties are marginal or below, follow up programs must be carried out for underpin analysis of long term performance. Because of concerns over accelerated damage in welds there are significant benefits to using advanced NDE techniques to identify and characterize defects.

References

1. Viswanathan, R. and Bakker, W. "Materials for Boilers in Ultra Supercritical Power Plants", International Joint Power Generation Conference, IJPG2000 _ 15049, Florida, 2000.
2. Hahn, B., Baumhoff, V. and Zschau, M. "Use of Grade 91 steel in Power Plant retrofitting applications – experience and application potential", Proc. Conf. Advanced Heat Resistant Steels for Power Generation, Spain, 1998.
3. Haarmann, K., Vaillant, J.C., Vandenberghe, B., Bendick, W. and Arbab, A. The T91 / P91 Book Vallourec Mannesmann Tubes, 2002.
4. Kimura, K., Sawada, K., Kubo, K. and Kushima, H. "Stress dependence of recovery processes and long term life prediction of 9Cr-1Mo-V-Nb steel", Int. Conf. on High Temperature Plant Integrity, Cambridge, UK, 2004.
5. Cipola, L., Di Gianfrancesco, A., Cumino, G. and Caminada, S. "Long term creep behavior of grade 91 steel", Creep and Fracture in High Temperature Components – Design and Life assessment, ECCO Conference, London, 2005.
6. Sims, M. EPRI Int. Conf. on "Weld Repair", Destine, Florida, (June 2003).

7. Arav, F., Lentferink, H.J.M., Etienne, C.F. and van Wortel, J.C. "Effect of Fabrication Processes on the Creep Behavior of 9–12% Chromium Steels, Proc Fifth Int. Conf. on Creep, Orlando, Florida, 1992.
8. Henry, J.F., Zhou, G., Ward, C.T. and Price, R.L. "Effects of Cold work and Heat Treatment on the stress –rupture behavior of Grade 91 material", EPRI Int. Conf. on Materials and corrosion experience for fossil power plants, Isle of Palms, SC, 2003.
9. Rapkin, K. Presentation to the EEI Materials Working group, 2006.
10. Watanabe, T., Tabuchi, M., Yamazaki, M., Hongo, H. and Tanabe, T. "Creep damage evaluation of 9Cr–1Mo–V–Nb steel welded joints showing Type IV fracture", Int. J. Pres. Vessel and Piping, 2006, 83, pp. 63–71.
11. Nonaka, I., Ito, T., Takemasa, F., Saitou, K., Miyashi, Y. and Fujita, A. "Full Size Internal Pressure Creep Test for Welded P91 Hot Reheat Elbow", Int. Conf. on High Temperature Plant Integrity, Cambridge, UK, 2004.
12. Tabuchi, M. and Takahashi, Y. "Evaluation of Creep Strength Reduction Factors for Welded Joints of Modified 9CR-1Mo Steel (P91)," Conf. Proc.s of PVP2006 ASME Pressure Vessels and Piping Division Conference, Vancouver, Can. 2006.
13. Brett, S.J. "Innogy's approach to identifying in-service modified 9Cr Forgings with low creep strength", EPRI / DOE Conf. on advances in life assessment and optimization of fossil power plants, Orlando, Fl. 2002.
14. Fleming, A. "New Materials for High-temperature Service in Power Generation", OMMI, Vol. 1, Issue 2, 2002, pp. 1–8.
15. Brett, S.J., Oates, D.L. and Johnston, C. "In service Type IV cracking of a modified Grade 91 header", Creep and fracture in high-temperature Components – design and Life assessment, ECCC conference, London, 2005.
16. Sawada, K., Taneike, M., Kimura, K. and Abe, F. "Effect of Nitrogen Content on Microstructural Aspects and Creep Behaviour in Extremely Low Carbon 9Cr Heat-resistant Steel", ISIJ International, Vol. 44, 2004, pp. 1243–1249.
17. Parker, J. and Parsons, A.W.J. "Fracture Behaviour of Low Alloy Steel Weldments" ASME, P V P Conf., Minneapolis, 1994, Vol. 288, pp. 423–428.
18. Foldyna, V. and Kubon, Z. "Consideration of the Role of Nb, Al and Trace Elements in Creep Resistance and Embrittlement Susceptibility of 9–12% Cr Steel," Conf. Proc., York, UK. Paper 13, 1994. Pp. 175–187.

19. Bisbee, L.H., Parker, J.D. and Mercaldi, D. "SSAM – a system for non-destructive material removal", *Condition Monitoring and Diagnostic Engineering Management*, Adam Hilger, 1991. Pp. 520–524.
20. Parker, J.D. and James, J.D. 'Creep Behavior of Miniature Disc Specimens of Low Alloy Steel', *Int. Conf. Developments in Progressing Technology*, American Society for Mechanical Engineers, Vol. 279, 1994, pp. 167–172.
21. Parker, J.D., Stratford, G.C., Shaw, N., Spink, G. and Metcalfe, H. 'The Application of Miniature Disc Testing for the Assessment of Creep Damage in CrMoV Rotor Steels, BALTICA IV – Plant Maintenance, 1998. Pp. 477–488.
22. Hyde, T.H., Sun, W. and Becker, A.A. 'Analysis of the Impression Creep Test Method Using a Rectangular Indenter for Determining the Creep Properties in Welds', *Int. J. Mech. Sci.*, Vol. 38, No 10, 1996, pp. 1089–1102.
23. Brett, S.J. "Identification of Weak thick Section Modified 9Chrome forgings in Service", 3rd EPRI Conf. on Advances in Materials Technology for Fossil Power Plants, Swansea, (Ed. by R. Viswanathan, W. Bakke and J. Parker), 2001.
24. Newby, M. "Remote Monitoring of Strain Rates on Steam pipework", EPRI Conference on Remaining Life Assessment of Fossil Plants, Louisville, 2006
25. Parker, J.D. 'Life prediction of cylindrical components operating under high temperature creep conditions', *Assessment of fossil power plants* (Eds. by R.B. Dooley and R. Viswanathan), EPRI Report CS-5208, 1987.

Interrelationship between toughness parameters determined from the Charpy-V impact test

Kim Wallin
Academy Professor
Academy of Finland
Helsinki, Finland

Historical background

Sometimes, it may be impossible or impractical to perform actual fracture toughness tests on a material. There may be insufficient material available for testing or the cost, in relation to the structure, may be too high. In such cases, the fracture toughness may sometimes be estimated indirectly from some simpler test. One example of such a simple test is the Charpy impact test. Today still, the Charpy impact test is the most commonly used standard test to evaluate a materials fracture properties. The test is quick and simple to perform and requires small specimens. Nearly all materials and manufacturing standards apply requirements based on the Charpy impact test. The development of the Charpy impact test was led by A.E.A. Charpy, at the beginning of the 20th century. Depending on viewpoints, the introduction of the test is attributed to 1898 or 1901 [1, 2]. Thus the test is more than a 100 years old. In the beginning, the test was not clearly standardised and several different specimen and notch configurations were introduced. Many of these early configurations have disappeared, but still there are many different specimen versions left.

The main parameter determined in the Charpy test is the energy required to fracture the specimen. The principle of the test is presented in Fig. 1. In the test, effectively a certain potential energy, defined by mass of striker and height of fall, is transformed into kinetic energy, part of which is used to fracture the test specimen and remaining kinetic energy being transformed back to potential energy, defined by mass of striker and height of rise. The height difference, of the striker, between start and end of test gives thus the energy used to break the specimen (CV, CU₅. etc.). The test is ingenious in its simplicity, in that the only instrumentation needed is an angle transducer dial, giving the beginning and end of test angles, from which the spent energy can simply be calculated, when the length of arm and striker mass are known.

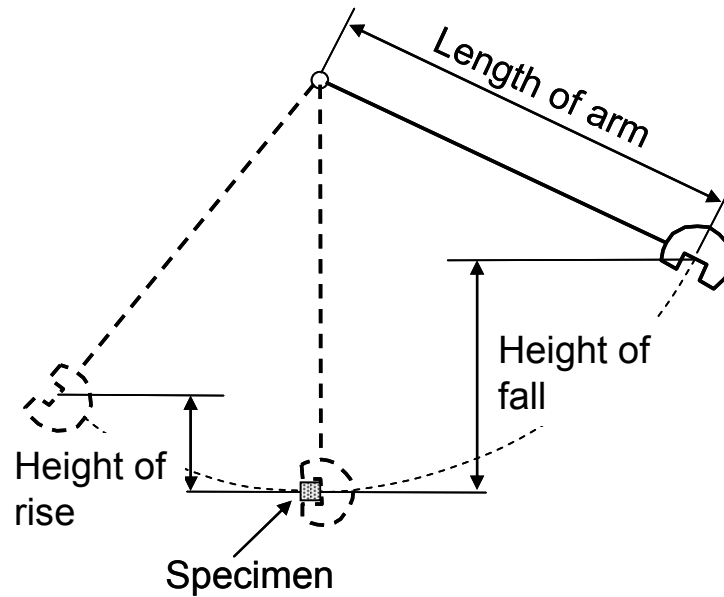


Figure 1. Principle of the Charpy pendulum impact test.

Besides impact energy, the Charpy test allows the definition of two additional parameters. Lateral expansion (LE), which describes the specimen deformation and fracture appearance (SA), which describes the test temperature location with respect to the ductile-to-brittle transition region.

One problem with the Charpy test is that it does not distinguish between different events related to the fracture process. Part of the absorbed energy goes into the initiation of fracture from the notch, part of the energy goes into the propagation of the crack and part goes into the plastic deformation of the specimen. The part of the energy going into crack propagation is exceptionally complex since the propagation of the crack can occur either with a ductile or brittle micro-mechanism or a combination of both.

Fig. 2 shows two possible fracture surfaces. Fig. 2a is typical for ferritic structural steels tested in the ductile to brittle transition region. The zone termed “dcg” denotes ductile crack growth, i.e. crack propagation through void growth and coalescence or ductile grain boundary fracture. The zone “c” denotes trans-crystalline cleavage fracture and zone “s” shear lips that have fractured in mode II with a ductile mechanism. The individual proportion of the different fracture modes depend on material and test temperature. Part of the ductile fracture can occur prior to cleavage (dcg I) and part can occur after crack arrest (dcg II). For some materials, there may even be several cleavage arrest and re-initiations, with some ductile crack growth in between. The significance of such test results can be difficult to assess with respect to fracture toughness. At temperatures where cleavage fracture cannot initiate or for materials where cleavage fracture does not occur, the fracture surface has the features of Fig. 2b.

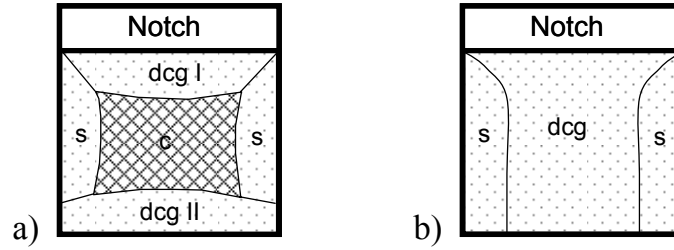


Figure 2. Schematic presentation of possible fracture surfaces in a Charpy test: a) material showing a ductile to brittle transition, b) material without cleavage fracture.

Energy is absorbed in the development of zones dcg and s. The cleavage fracture zone develops essentially during constant displacement, and does not affect markedly the total absorbed energy. The size of the shear lip zones is mainly a function of the materials tearing resistance properties and the materials strain hardening. The higher the tearing resistance is, the bigger the shear lips become. Interestingly, the fracture of the shear lips absorbs less energy than the ductile tearing. This phenomenon leads to a size effect on impact energy in the upper shelf region, when testing specimens of different thickness.

1. Fracture appearance

The fracture appearance (SA) in a Charpy test is determined based on the proportional amount of ductile crack growth (dcg) and shear fracture (s) areas on the fracture surface as schematically shown in Fig. 2a. Expressed in equation form, the fracture appearance can be expressed in the form of Eq. 1.

$$SA[\%] = \frac{\sum A_{dcg} + \sum A_s}{\sum A_{dcg} + \sum A_s + \sum A_c} \cdot 100\% \quad (1)$$

The fracture appearance is a sensible parameter only for metals that undergo a transition from cleavage fracture to ductile fracture with increasing temperature. It is thus mainly used for ferritic structural steels. The fracture appearance gives information as to where in the ductile-to-brittle transition region the test result corresponds to. A value close to 100% indicates that the impact energy relates nearly to upper shelf and an increase in temperature will not significantly change the test result. However, SA values in the range 30% to 60% indicates that the test temperature is in the midrange of the transition region and the impact energy may be strongly dependent on even small temperature changes. The ASTM E23 testing standard includes a calibration fracture surface set, based on which one can visually estimate the specimens fracture appearance, with a “resolution” of 10%. However, the calibration set is ideally applicable only for standard structural steels, where the fracture surface follows the trend shown in Fig. 2a.

Sometimes the fracture surface may include splits, perpendicular to the fracture surface and sometimes the fracture surface may contain multiple cleavage regions. Also, especially TMCP steels may sometimes show cleavage fracture areas with approximately a 45° angle to the crack lane. These fractures can be difficult to visually distinguish from shear fractures and in such cases the fracture surface should be examined by SEM. In the case of austenite-ferrite duplex steels, where the ferrite constituent becomes brittle with decreasing temperature, but the austenitic constituent remains ductile, the unambiguous definition of fracture appearance is difficult.

Since the fracture appearance shows a similar transition with temperature as does the impact energy it is only natural that also fracture appearance transition temperatures have been suggested and are in fact used for several elevated temperature and pipe line steels.

2. Relation between fracture appearance and impact energy

Since impact energy and fracture appearance are parameters relating to the behaviour of the same specimen, one could assume that there might exist a relation between the two parameters. Until now, no such general relation has been established. Most of the energy in an impact test is usually absorbed in the primary ductile crack growth (dcg I, in Fig. 2a), before cleavage initiation and fracture of shear lips. In the case of a deep cracked specimen, the ductile tearing would normally be related to the fracture mechanical driving force (J-integral, etc.) by approximately a power law expression (Eq. 2), describing the materials tearing resistance curve.

$$J = J_1 \cdot \Delta a^m \quad (2)$$

In the case of a bend specimen, it is possible to develop an analytical expression, combining the measured total energy with the materials tearing resistance curve in the form of Eq. 3.

$$E_{TOT} = \int_0^{\Delta} P \cdot \partial \Delta = \frac{B \cdot J_1}{\eta} \cdot \left[(W - a_0) \cdot \Delta a^m + \frac{1-m}{1+m} \cdot \Delta a^{m+1} \right] \quad (3)$$

Eq. 3 is not exactly valid for estimation of the Charpy-V impact energy, since Eq. 3 does not consider that the Charpy specimen has a blunt shallow notch, which will affect the initial part of the tearing resistance curve. It also does not consider that the energy parts absorbed by the dcg II and s regions do not follow Eq. 3. However, since the major part of energy is absorbed in the dcg I region, the equation should still be able to provide an approximate relation between impact

energy and fracture appearance. When the total energy corresponding to an arbitrary crack extension Δa , is divided with the total energy for $\Delta a = W - a_0$, one can get an estimate between impact energy and upper shelf energy (Eq. 4).

$$\frac{C_V}{C_{V-US}} \approx \frac{1+m}{2} \cdot \left[\left(\frac{\Delta a}{W - a_0} \right)^m + \frac{1-m}{1+m} \left(\frac{\Delta a}{W - a_0} \right)^{1+m} \right] \quad (4)$$

Eq. 4 is expressed in terms of crack extension (Δa) but if it is assumed that the region dcg I dominate, the equation can be re-written as Eq. 5.

$$\frac{C_V}{C_{V-US}} \approx \frac{1+m}{2} \cdot \left[\left(\frac{SA}{100\%} \right)^m + \frac{1-m}{1+m} \left(\frac{SA}{100\%} \right)^{1+m} \right] \cdot 100\% \quad (5)$$

The outcome of Eq. 5 is dependent on the power m , which describes the steepness of the tearing resistance curve, but it is independent of the materials strength properties. For most ductile metals, the power varies in the range 0.3–0.7. Therefore one can usually, with sufficient accuracy, approximate m as being 0.5. The prediction from Eq. 5 is compared to actual experimental data in Fig. 3. The data comes from a variety of sources, but they all represent ferritic structural steels. The steels used have varying yield strengths and their upper shelf energies range from 100 J to 295 J. Eq. 5 is seen to describe the mean behaviour of the data quite well. The scatter of the data is due to several factors. Firstly, some scatter is due to variations in m . Second, some scatter is due to the simplified assumptions made in neglecting the effect of shallow blunt notch and effect of regions dcg II and s, which will vary from material to material. Third, some scatter is due to the rather crude measurement accuracy of the fracture appearance when it is made visually using calibration figures and to the uncertainty related to the definition of the upper shelf energy. Overall, the accuracy of the relation is still $\pm 15\%$, which must be considered quite satisfactory, since it is of the same order as the scatter in upper shelf energy.

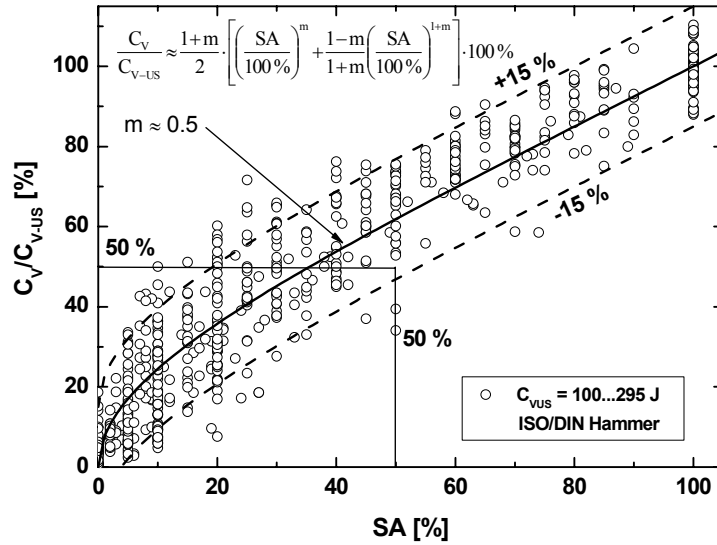


Figure 3. Approximate relation between Charpy-V fracture appearance and impact energy for ferritic structural steels.

An example of the typical uncertainty related to fracture appearance measurements is presented in Fig. 4, where data for a single steel from a European round-robin exercise [3] is collected. For this material the exponent m is close to 0.7, but the overall scatter is actually nearly identical to the one seen in Fig. 3. It should be kept in mind that the fracture appearance is more a qualitative than quantitative parameter. Fracture appearance is the Charpy-V parameter susceptible to human judgement and systematic differences arising from human interpretations of the fracture surface are quite common. Because of this, transition temperatures based on fracture appearance are more prone to human errors than energy or lateral expansion.

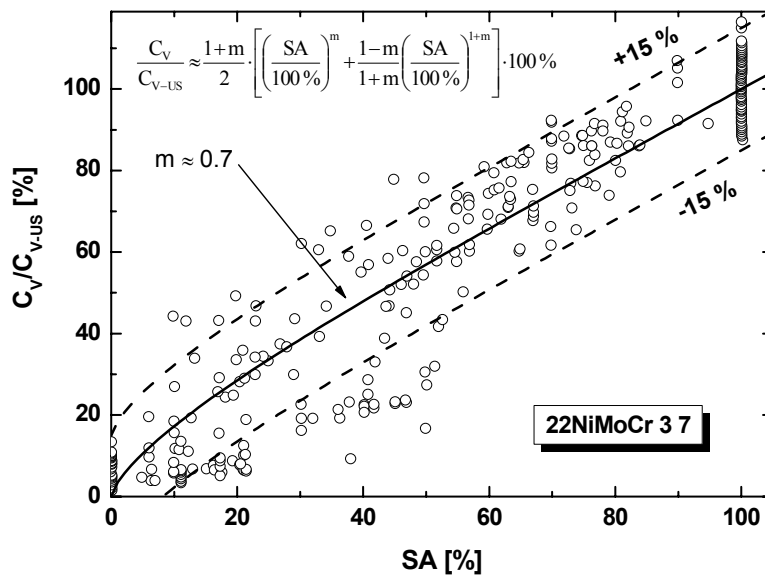


Figure 4. Uncertainty in relation between impact energy and fracture appearance for a single steel based on round-robin testing [3].

The above equations are not valid for austenite-ferrite duplex steels. For such steels, in the ductile-to-brittle transition region, it is more difficult to define the region c on the fracture surface, since the region will be a mixture of cleavage in ferrite grains and ductile tearing in austenite grains. The relation between impact energy and fracture appearance does not in this case allow a simple theoretical description. Based on a somewhat limited data base, the fully empirical Eq. 6 was developed (Fig. 5). Partly due to the difficulty in estimating SA for duplex steels, the scatter is somewhat larger than for ferritic structural steels.

$$\frac{C_v}{C_{v-US}} \approx 5\% + 95\% \cdot \left(\frac{SA}{100\%} \right)^2 \quad (6)$$

Since the fracture appearance parameter was originally developed specifically for ferritic low and medium strength structural steels, its use and relevance to other more exotic materials should always be carefully contemplated. If the cleavage region c cannot be clearly defined on the fracture surface the fracture appearance parameter should not be determined, nor used as a criterion. This is the case for e.g. the austenite-ferrite duplex steels, maraging steels and cast irons.

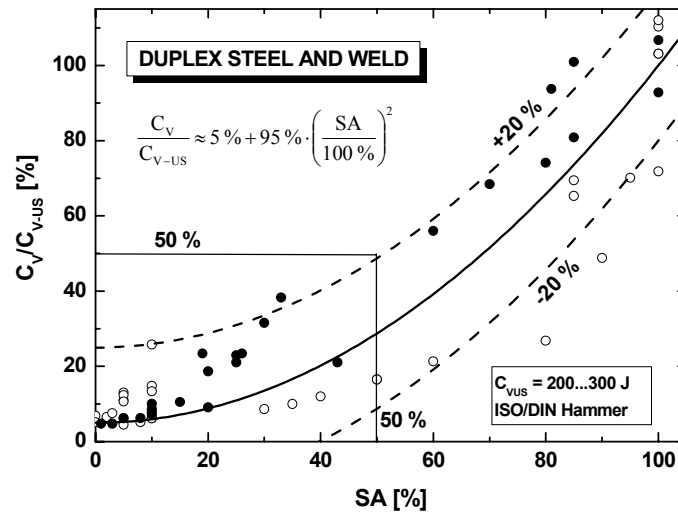


Figure 5. Approximate relation between Charpy-V fracture appearance and impact energy for austenite-ferrite duplex steels.

3. Relation between fracture appearance and impact energy transition temperatures

The relation between the fracture appearance and impact energy, also means that there is a comparatively simple dependence between transition temperatures corresponding to similar definitions for these two parameters. This means that for the impact energy an energy level proportional to the upper shelf energy should

be used. An example of such a correlation is presented in Fig. 6, where the 50% fracture appearance transition temperature ($FATT_{50\%}$) is correlated with the 50% upper shelf energy transition temperature ($TC_{V50\%US}$). This is the simplest correlation possible, since both temperatures refer to the location in the middle of the transition curve. Because, impact energy generally reaches the mid-point earlier than fracture appearance (Fig. 3), the $TC_{V50\%US}$ temperature is on the average 8°C lower than $FATT_{50\%}$. The exact difference will depend on the materials tearing resistance properties, but the standard deviation for 103 different data sets is only 8.2°C [4]. The data covers ferritic structural steels with yield strength in the range 300–1200 MPa and upper shelf energies between 35–300 J. The materials, for which fracture appearance is not a good parameter, also the use of the relation in Fig. 6 should not be attempted. This is, as earlier stated, the case for e.g. the austenite-ferrite duplex steels, maraging steels and cast irons.

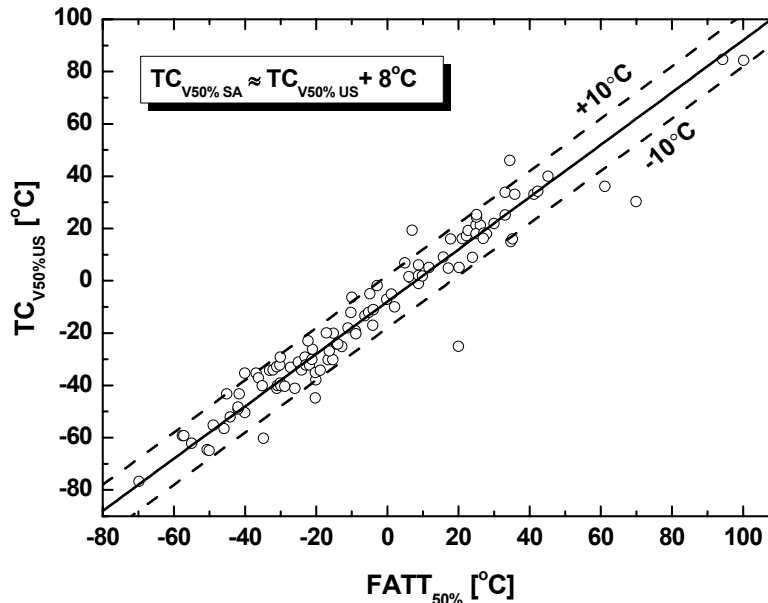


Figure 6. Approximate relation between Charpy-V 50% fracture appearance temperature and 50% of upper shelf energy temperature for ferritic structural steels [4].

In the case of comparison of transition temperatures, where one is based on a fixed energy level (like 41 J) and the other is based on a fixed fracture appearance percentage, the correlation will be function of the materials upper shelf energy and the steepness of the transition curve. The lower the materials upper shelf energy is, the less conservative the fracture appearance transition criterion will be. Often the material may degrade as function of time, due e.g. to thermal ageing or neutron irradiation. If the degradation affects both the materials transition behaviour as well as the upper shelf toughness, a fracture appearance based transition criterion will indicate slightly lesser embrittlement than a constant energy based transition criterion would do.

4. Lateral expansion

The third Charpy parameter recognized in test standards is the lateral expansion (LE). Because the specimen is loaded in bending, the bottom part will be in compression and plastic deformation will cause the base of the specimen to widen (Fig. 7). At the same time as the specimen expands laterally at the base, it also contracts laterally at the notch root. Earlier, this lateral contraction (LC) has also been used as a toughness parameter [5], but the measurement of the contraction is so laborious, that the lateral expansion parameter has become the standard parameter. The lateral contraction was normally measured at the notch root by means of an optical eyepiece equipped with a stage micrometer and this made the measurement susceptible to measuring uncertainties. The lateral expansion gives a measure of the materials capacity to sustain deformation. The lateral expansion parameter shows, a similar transition behaviour, as does impact energy and fracture appearance for ferritic structural steels.

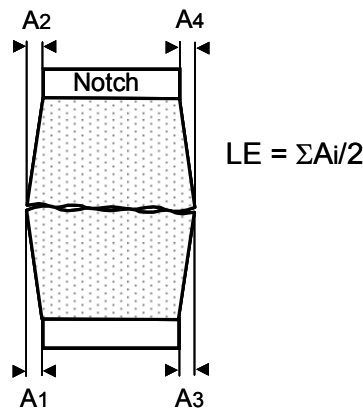


Figure 7. Definition of lateral expansion LE.

5. Relation between lateral expansion and impact energy

Since lateral expansion is due to plastic deformation, energy is required to produce the plastic deformation. This indicates a direct relation between lateral expansion and impact energy. However, as for fracture appearance, a general relation between the parameters has not until now been suggested. The energy required to produce plasticity in the specimen is dependent on the materials flow stress. Thus, theoretically, lateral expansion should be related to impact energy divided by the materials dynamic flow stress. As a simplification, the dynamic flow stress can be approximated by the static ultimate stress. Fig. 8 shows the resulting dependence between impact energy and lateral expansion (Eq. 7), established for the steels shown in the figure.

$$C_V / \sigma_U \left[\text{mm}^3 \right] \approx 5 + 80 \cdot LE[\text{mm}] + 4.5 \cdot LE[\text{mm}]^4 \quad (7)$$

The relation contains an offset parameter, which accounts for the energy absorption prior to plastic deformation of the specimen. It contains a linear portion connecting energy with plastic work and it contains a non-linear portion. The non-linear portion stems from the fact that close to the upper shelf, ductile tearing of the specimen causes the bending stresses of the specimen to decrease to a level where further plastic deformation of the specimen no longer affects the lateral expansion, whereas the ductile tearing still absorbs energy. This causes lateral expansion to reach an apparent upper shelf slightly earlier than impact energy or fracture appearance.

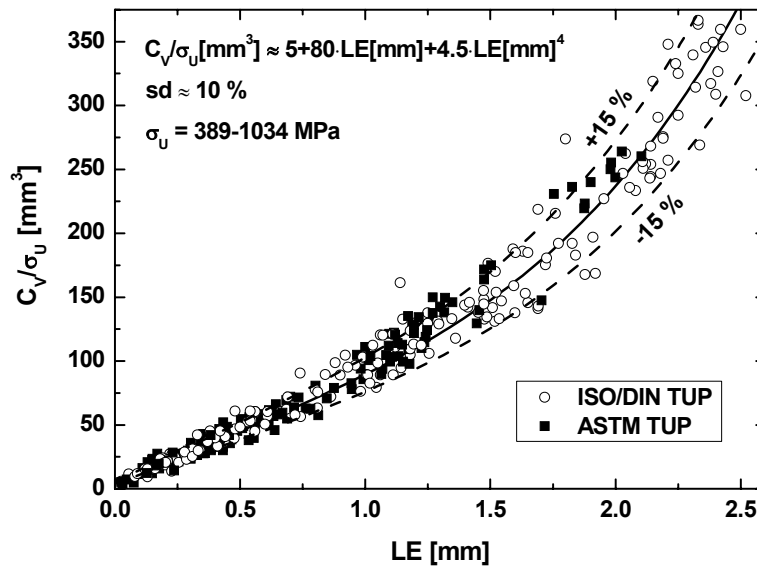


Figure 8. Relation between Charpy-V impact energy and lateral expansion [6, 7, 8, 9].

In the case of comparison of transition temperatures, where one is based on a fixed energy level (like 68 J) and the other is based on a fixed lateral expansion (like 0.89 mm), the correlation will be function of the materials ultimate strength (or dynamic flow strength) and the steepness of the transition curve. The higher the materials ultimate strength is, the more conservative the lateral expansion transition criterion will be. Often, when the material degrade as function of time due e.g. to thermal ageing or neutron irradiation, also the materials ultimate strength increases. This causes a constant lateral expansion based transition criterion to indicate slightly more embrittlement than a constant energy based transition criterion.

Acknowledgements

This manuscript has been written as a part of the project “Micromechanism Based Modelling of Fracture with Emphasis on Structural Integrity Assessment”, funded by the Academy of Finland, Decision No. 117700.

References

1. Siewert, T.A., Manahan, M.P., McCowan, C.N., Holt, J.M., Marsh, F.J. and Ruth, E.A. The History and Importance of Impact Testing. Pendulum Impact Testing: A Century of Progress, ASTM STP 1380, T. A. Siewert and M.P. Manahan, Sr., Eds. American Society for Testing and Materials, West Conshohocken, PA, 1999. Pp. 3–16.
2. Tóth, L., Rossmann, H.-P. and Siewert, T.A. Historical Background and Development of the Charpy Test. From Charpy to Present Impact Testing, ESIS Publication 30, D. François and A. Pineau, Eds. Elsevier, 2002. Pp. 3–19.
3. Böhme, W. Experience with Instrumented Charpy Tests Obtained by a DVM Round-Robin and Further Developments. Evaluating Material Properties by Dynamic Testing, ESIS 20, E. van Walle, Ed. Mechanical Engineering Publications, London, 1996. Pp. 1–23.
4. Wallin, K. Fracture toughness correlations. Research Reports 428. Technical Research Centre of Finland. Espoo 1986. 31 p. + app. 33 p. (In Finnish.)
5. Puzak, P.P. and Pellini, W.S. Evaluation of Notch-Bend Specimens. The Welding Journal Research Supplement, 33, 1954, pp. 187s – 192s.
6. Nanstad, R.K. and Sokolov, M.A. Charpy Impact Test Results on Five Materials and NIST Verification Specimens Using Instrumented 2-mm and 8-mm Strikers. Pendulum Impact Machines: Procedures and Specimens for Verification, ASTM STP 1248, T. A. Siewert and A. K. Schmieder, Eds. American Society for Testing and Materials, Philadelphia, 1995. Pp. 111–139.
7. Gross, J.H. and Stout, R.D. Ductility and Energy Relations in Charpy Tests of Structural Steels. The Welding Journal Research Supplement, 37, 1958, pp. 151s–159s.
8. Wallin, K., Nevasmaa, P., Planman, T. and Valo, M. Evolution of the Charpy-V Test from a Quality Control Test to a Materials Evaluation Tool for structural Integrity Assessment. From Charpy to Present Impact Testing. ESIS Publication 30. D. François and A. Pineau, Eds. Elsevier, 2002. Pp. 57–68.
9. Pawelski, O., Gopinathan, V. and Hagedorn, K. Relation Between Impact Strength and Lateral Expansion of Steels With About 400 to 800 N/mm² Yield Point. Archiv für das Eisenhüttenwesen, 51, 1980, pp. 435–437.

UK experience with modified 9Cr (grade 91) steel

S.J. Brett

RWE npower, Swindon, UK

Abstract

Following its introduction in the late 1980s, modified 9Cr (grade 91) steel has found widespread use for retrofit and new build applications in the UK power industry. Although it has only been in service for a relatively short period of time, currently approximately 80 000 hours, a number of problems have arisen. Some have been related to incorrect processing or heat treatment at the manufacturing stage. However examples have also occurred of material apparently correctly heat treated having lower than expected creep strength, particularly in the Type IV zone at the outer edge of the weld heat affected zone. This paper discusses the types of problems which have been encountered by UK generating companies using thick section grade 91 steel and the options available for identifying material vulnerable to early cracking in service.

1. Introduction

Grade 91 steel is designed to enter service in a tempered fully martensitic condition, typically with normalisation (austenitisation) in the temperature range 1040–1090°C and tempering in the range 730–780°C. It presents a greater challenge to fabricators than the earlier low alloy steels formerly used in high temperature power plant applications. Failure to adhere to the correct processing requirements may result in material with inadequate strength [1].

However experience has also shown that even grade 91 material which has been successfully produced in a fully martensitic condition, and apparently correctly tempered, can fail relatively early in service at welds by Type IV cracking in the fine grained region towards the parent side edge of the heat affected zone [2–4]. This can be a more difficult problem to detect and prevent. In some cases however such material has been successfully identified by a combination of hardness testing and compositional surveys. A number of in-service failures of this type in components fabricated in thick section have been shown to be associated with a common compositional factor, low nitrogen to aluminium ratio, resulting in weak parent creep strength [2]. The weak creep strength has been attributed to the formation of coarse aluminium nitride precipitates with a consequential reduction of the fine vanadium nitride population [5].

2. Fabrication Issues

The fabrication-related problems can be broadly divided between failure to produce the correct fully martensitic structure, resulting in a non martensitic or partially martensitic material with very low parent creep strength, or the production of a fully martensitic but inadequately tempered structure, resulting in material with low ductility prone to a number of early cracking mechanisms. The former condition is difficult, but unfortunately not impossible, to achieve if the material is cooled very slowly from the normalisation temperature. The latter condition can occur if the material is not cooled after normalisation to a temperature low enough to produce complete transformation to martensite, in which case subsequent tempering will only temper the existing martensite. Any untransformed material present will then transform to untempered martensite when the material is subsequently cooled to ambient.

Similar considerations apply to the welding and post weld heat treatment (PWHT) of grade 91 steel. If the weld is not cooled after welding and before PWHT sufficiently to ensure complete transformation to martensite, the untransformed regions will transform to hard untempered martensite when the weld is cooled after PWHT. One way to ensure that the weld is cooled sufficiently after welding is to require ultrasonic inspection of the weld prior to PWHT. This has the additional advantage that any defects in the as-welded condition which will require further remedial welding are identified before the cost of PWHT is incurred.

3. Longer Term Cracking

The earliest use of grade 91 in the UK, for retrofit headers on large coal-fired plant, occurred at a time when electricity in England and Wales was supplied by the Central Electricity Generating Board and, possibly because of the depth of technical expertise available within that organisation, early problems arising from incorrect welding and heat treatment were rare. Subsequent experience however has demonstrated that even grade 91 components produced with the correct tempered martensitic structure and correctly fabricated, can still fail unexpectedly early in service.

The earliest failure of this grade of steel in the UK occurred on a transition joint “bottle” forging in 1994 after only 20 000 hours operation, nominally at 568°C [2, 3]. Failure occurred by Type IV cracking near the outer edge of the forged F91 side heat affected zone on the weld joining the bottle forging to the T91 tubing. It was followed by further bottle failures at periodic intervals over the next 10 years. Although they were boiler tube components the bottles had been machined from thick forged bar and must therefore be classified as thick section

in terms of their production route. In 1996 an explosive failure of a forged header F91 endplate, also operating at 568°C occurred after 36 000 hours operation, by Type IV cracking on the endplate side of the weld joining it to the main header body [3]. The weld failed completely, ejecting the endplate into the boiler dead space and depressurising the boiler. The next significant event occurred in 2004, when extensive Type IV cracking was found on the P91 main barrel sections of a header during a planned outage after 58 000 hours operation at 568°C [4].

An example of Type IV cracking in a failed transition bottle is shown in Fig. 1. Damage at the crack tip in a partly cracked bottle is shown in Fig. 2. The damage mechanism appears to be primarily intergranular cavitation with only very limited evidence of other mechanisms such as grain boundary decohesion. In this respect the failure mode is largely indistinguishable from Type IV cracking in low alloy steels.

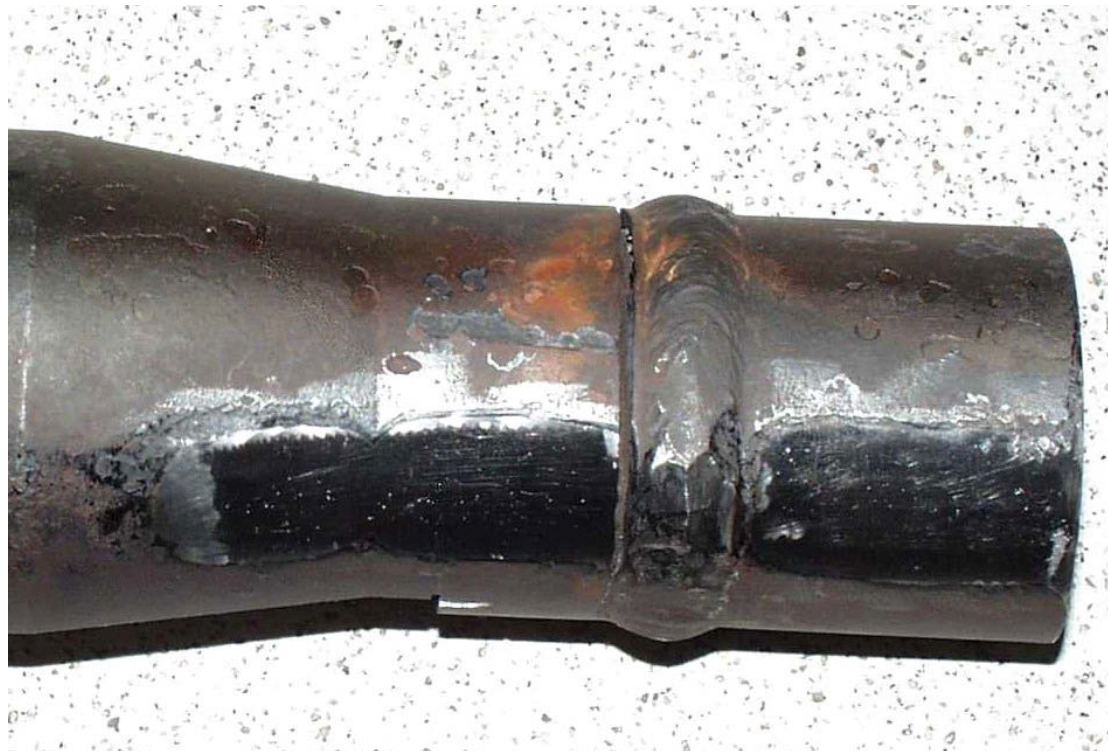


Figure 1. Type IV cracking on the F91 side of a weld between an F91 forged transition bottle and a T91 tube (48 mm OD) taken from Ref. [2].

The earliest failures led, during this period, to renewed interest in the creep strength of grade 91 steel, particularly in relation to its Type IV properties. In the case of one of the bottle failures the opportunity was taken to obtain a comparison of the post service creep rupture life of the grade 91 Type IV zone adjacent to the unfailed central Inconel transition weld with that of the grade 91 parent. The results showed a large shortfall in Type IV life, by approximately a factor of 5 in the test range adopted [6]. While testing ex-service material in this

way can be a valid means of investigating the ratio of the remanent lives of the Type IV zone and parent, it should be noted that it will exaggerate the ratio of their original lives. In addition the presence of the relatively strong Inconel weld metal may have shortened the Type IV life in the grade 91 material. However, even allowing for these factors, the results indicated that the Type IV zone could be substantially weaker than the parent, even in a weak parent.

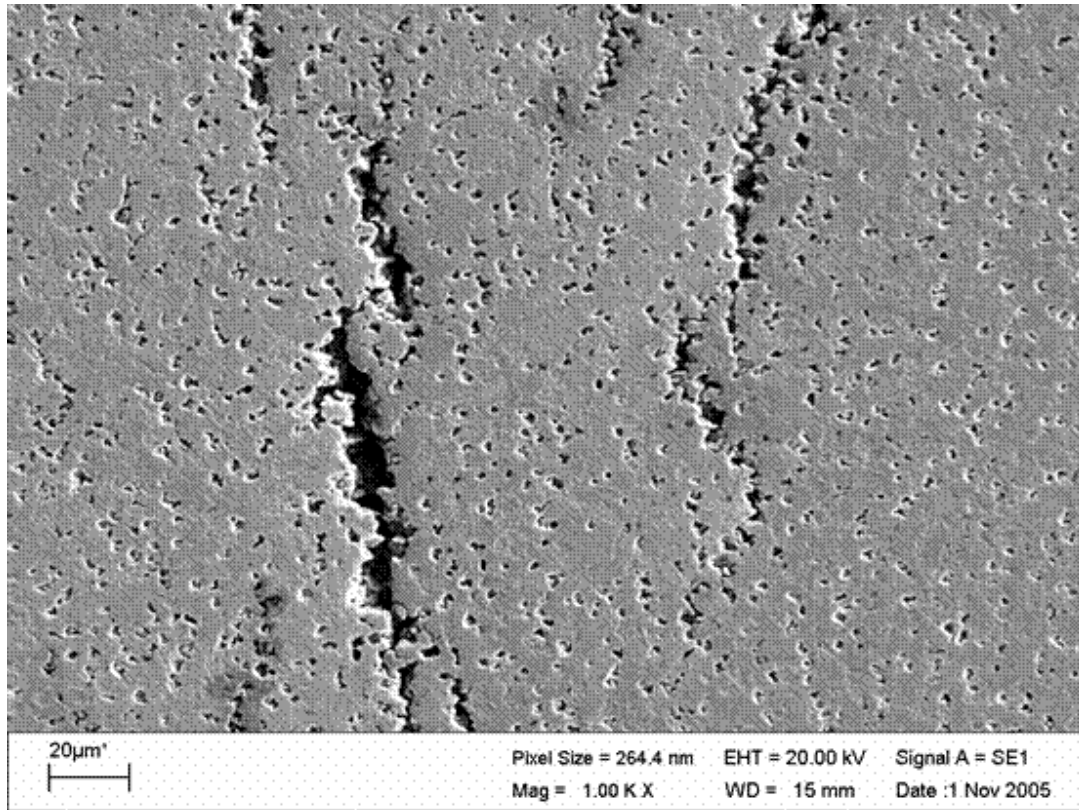


Figure 2. Damage ahead of the Type IV crack tip in a cracked transition bottle.

In order to investigate the Type IV shortfall in terms of original strength it was necessary to investigate weak parent material welded in the as-received condition with matching weld metal. A length of 257 mm diameter cylindrical bar, surplus to a header installation contract, and therefore representative of material which had entered service, was obtained from a manufacturer and studied in a number of collaborative exercises. This material, designated as Bar 257, was demonstrated, even in the as-received condition to have a parent creep strength lower than the expected mean-20% value for grade 91. It was available in sufficient quantity to manufacture a test weld and investigate the Type IV strength, which was shown to be substantially lower than that of the parent, as illustrated in Fig. 3 [7, 8].

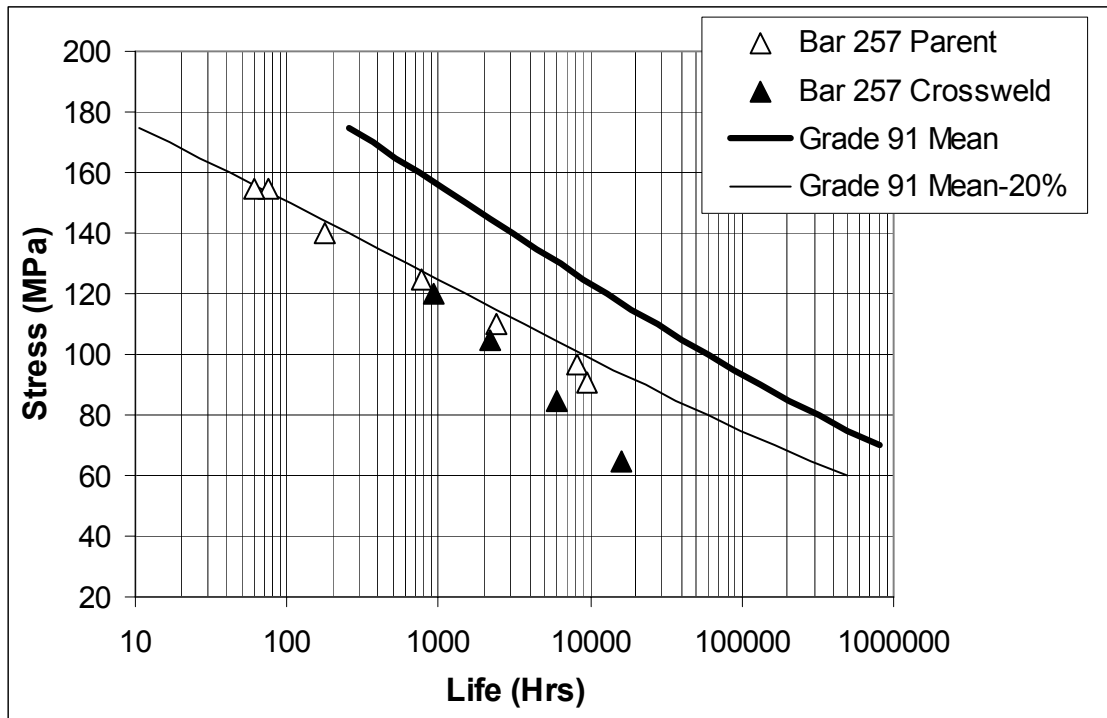


Figure 3. Bar 257 parent and Type IV rupture life at 600°C, taken from Ref. [8].

4. Aluminium Nitride

In considering the casualty materials, i.e. those which have cracked or failed in service, along with the extensively investigated weak Bar 257 material, a number of factors arise. All these materials when investigated either by sampling or metallurgical replication, were found to be fully martensitic with no obvious evidence, on the basis of optical microscopy, of anything indicating abnormal properties. The transition bottles investigated, and the failed endplate, were found to have lower hardness than expected for grade 91 material which had been in service for such short times (180–190 VHN). The Bar 257 material, in the as-received condition, and the cracked header barrels had hardness in the range 200–210 VHN which, while still relatively low, is not exceptional. Indirect evidence of extended tempering time was found for the transition bottles, but not for the header barrels. Tempering times for the endplate and bar, while relatively long, were commensurate with the thickness of the sections involved.

In terms of operating conditions again the evidence is inconclusive. There is no evidence of abnormally high operating temperature associated with any of the in-service examples. The operating stress acting on the failed endplate was shown to be high as a result of the geometry of the flat endplate to header body weld, but evidence of high stress could not be found in the cases of the transition bottles or the header barrels.

The only factor identified which is common to all the materials is compositional. While the individual chemical compositions were within the required specification all were found to have nitrogen levels in the lower half, and aluminium levels in the upper half, of the respective ranges. It was postulated that this combination could promote the formation of aluminium nitride precipitates at the expense of the vanadium nitride type precipitates which play a key role in providing the high creep strength of this grade of steel. A series of electron microscopy studies carried out at Loughborough University eventually demonstrated the presence of coarse (0.5–1.0 μm) AlN particles in transition bottles, the failed endplate and the as-received bar [5, 9, 10]. A typical example of an AlN needle is shown in Fig. 4. The cracked header barrels have not yet been investigated in detail.



Figure 4. Example of an AlN needle (0.5 μm long) taken from Ref. [5].

In order to minimise this potential problem a relatively high nitrogen: aluminium ratio is desirable and this can be achieved if aluminium is limited. RWE npower currently specifies a maximum aluminium level of 0.015 wt%, compared to the standard maximum of 0.04 wt%, e.g. [11]. This can be relaxed for particular plant items if it is clear that they are going to experience relatively low loads in service. The effect on the nitrogen: aluminium ratio as shown in material test certificates is illustrated in Fig. 5, which compares components purchased before and after the modification.

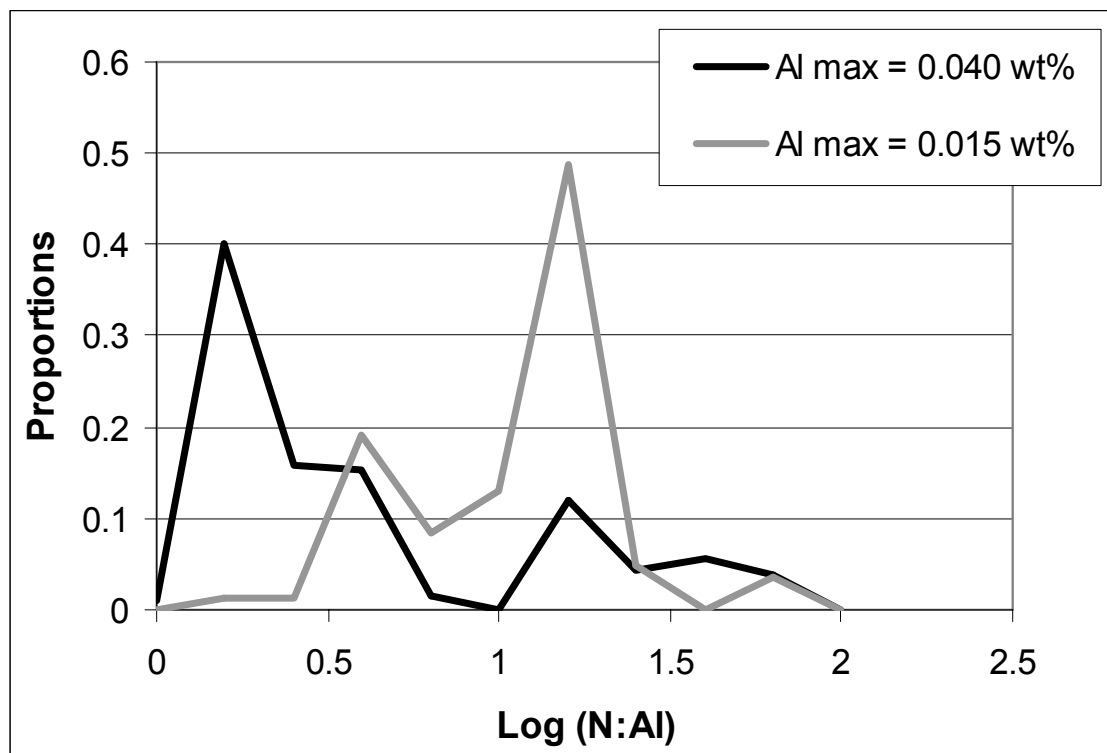


Figure 5. Effect of lowering maximum aluminium level on the distribution of nitrogen: aluminium ratio for RWE npower grade 91 items entering service.

5. Investigation Techniques

In the light of the experience to date a number of comments can be made about the techniques available for detecting in-service problems.

5.1 Standard Non Destructive Testing

In general the techniques used on low alloy components and welds are equally effective on grade 91. Particular care must however be taken when looking for internal cracking on complex geometries. The header barrel cracking referred to above, which was on the outside surface of the header was found easily, whereas the internal cracking on the failed endplate was not. Only once the failure had occurred and the detailed orientation of the cracking revealed by subsequent metallurgical investigation was an effective ultrasonic procedure developed for use on other endplates of the same geometry. It should be noted that a number of different endplate designs are currently in service. Some, such as those incorporating unwelded lands as part of the design, present great difficulty to the NDT operator.

Complementary investigation techniques such as metallurgical replication are useful for identifying aberrant microstructure but will not necessarily provide early warning of the failure of a correctly martensitic, but weak, structure. As a class of steel, grade 91 appears to exhibit far less cavitation during the process of creep deformation [12]. This adds difficulty to the quantitative assessment of its proximity to failure. In addition, of course, external replication of a component is not likely to identify internally initiating damage.

5.2 Hardness Surveys

Hardness surveys provide an indication of potential in-service problems. High hardness values may indicate inadequate tempering during fabrication or post weld heat treatment. Very low hardness values may, in extreme cases, indicate a lack of full martensitic structure. A fully martensitic structure with low hardness is likely to have low creep strength. While there is no general fundamental relationship between hardness and creep strength, a reasonable empirical correlation has been found between hardness and creep strength in short term laboratory tests for grade 91 materials in the as-received condition or having experienced only limited service [13]. The correlation between hardness and longer term creep life remains to be demonstrated.

A limitation to the use of hardness data is the accuracy of the hardness testing procedure used. The results obtained may be influenced by the testing technique chosen, the operator and the individual testing device. Care must be taken in choice of hardness technique and procedure and in correlating the results obtained, ideally against laboratory hardness tests. Examples have been encountered of very low hardness found on plant components which, following laboratory hardness testing of samples taken, have been shown to be erroneous.

5.3 Compositional Checks

A survey of chemical composition from the manufacturers material test certificates can be useful in identifying components from casts with high aluminium content and/or low nitrogen to aluminium ratio. In fact the cracked header barrels referred to above were discovered by these means. The process is not however always simple. Examples have been found of wide variation between ladle (melt) analyses and the product check analyses for aluminium, indicating either segregation effects or inconsistencies in the measurement of this element. This is illustrated in Fig. 6 which compares the material test certificate ladle and product aluminium levels for two stations.

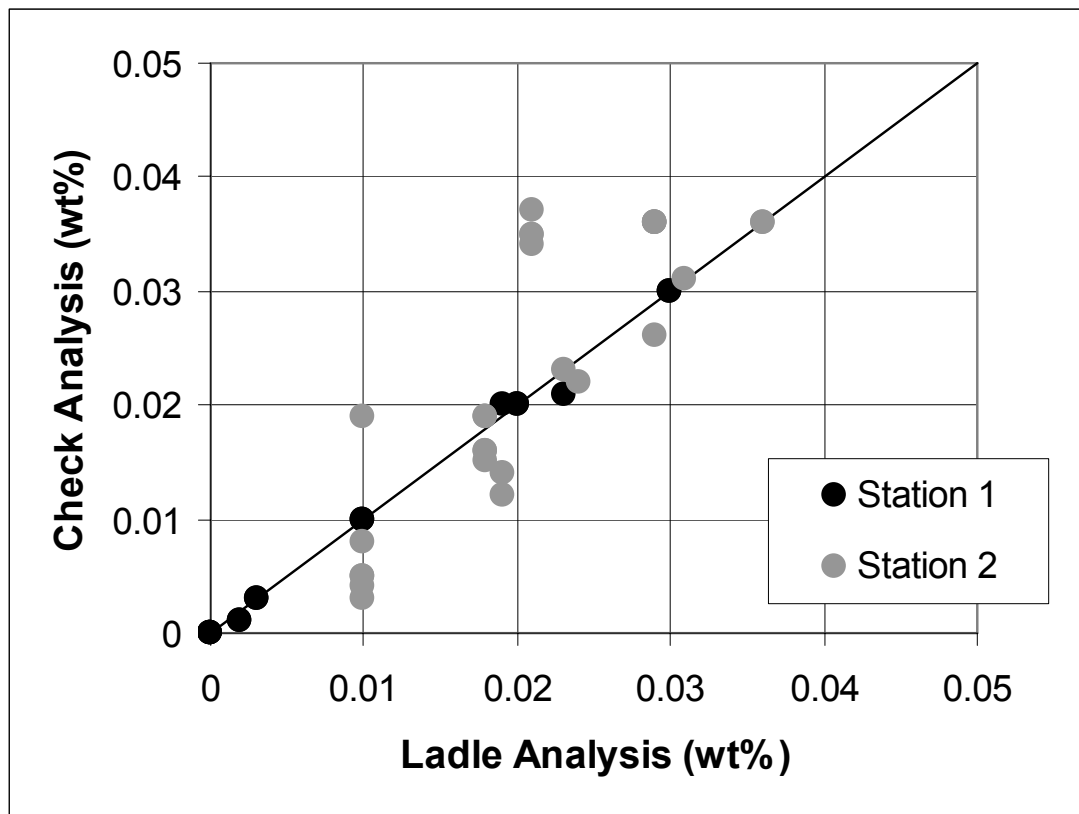


Figure 6. A comparison between cast and product aluminium levels for two stations.

In some cases it may prove necessary to carry out additional analyses to confirm the levels of nitrogen and aluminium present. These can be obtained by means of shallow surface drillings without impairing the structural integrity of the in-service component. Chemical analysis requires 1 g of material for nitrogen and 0.5 g for aluminium. RWE npower experience is that, while nitrogen levels are generally consistent with the original test certificate values, aluminium levels can differ significantly. It is of course important to define whether the aluminium measured is soluble or total, the value of interest being the soluble aluminium level. However, even taking this into account the results obtained can differ from the values shown on the original test certificates. One series of grade 91 forgings in service sampled in-situ, for example, gave aluminium levels which conflicted with both ladle and product analyses (Fig. 7).

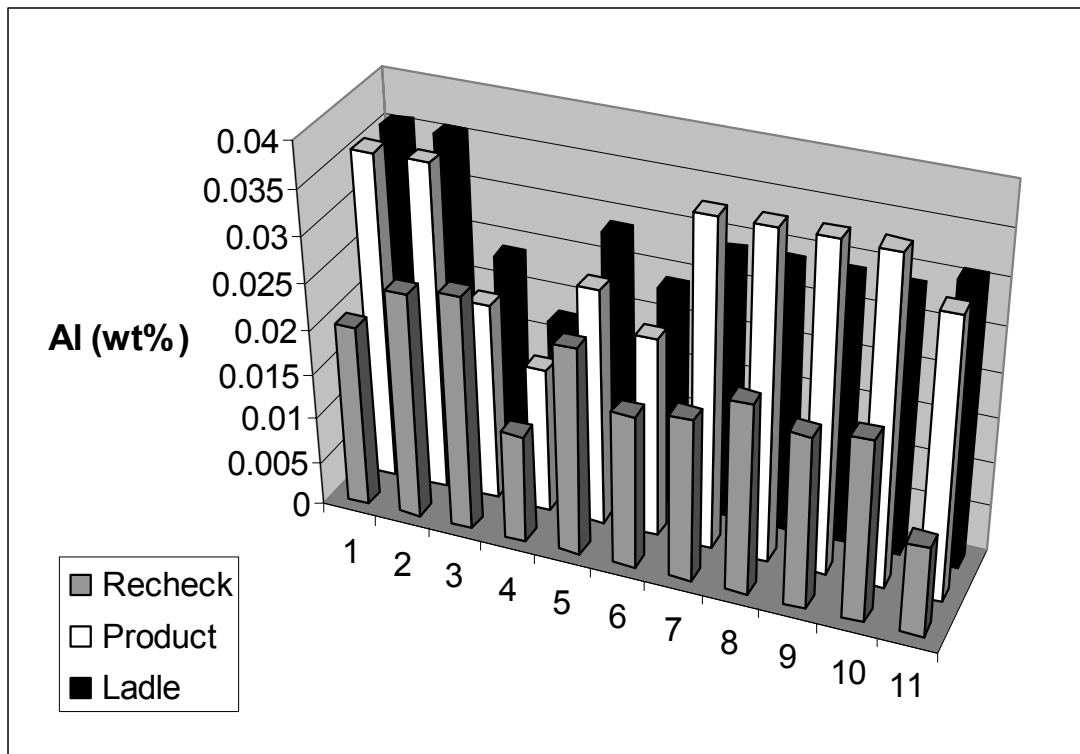


Figure 7. Comparison between test certificate ladle and product aluminium levels in a series of grade 91 forgings with values obtained subsequently by in-situ sampling.

5.4 Mechanical Testing

In those cases where component items with potentially poor creep properties have been identified in-service it may be necessary to carry out some method of establishing that such fears are justified before deciding on replacement or repair options. Where sufficient material is available standard creep tests can be used, but in general this unlikely to be an option.

An alternative approach is the use of specialised small scale creep testing techniques such as small punch or impression creep [14]. Either technique makes use of very small samples which can usually be removed from plant without a need for subsequent weld repair. Small punch testing uses a spherical indenter which is pushed into the test specimen in what is essentially a bend test. Impression creep uses a rectangular indenter which subjects the test specimen to compression. While the use of the data generated by either technique in quantitative creep life assessments remains a matter for debate, these methods are very useful in providing a comparative ranking of creep strength.

As an example a testing exercise, using both techniques, was carried out on samples taken from a number of grade 91 components selected on the basis of

low N:Al ratio and low hardness, along with samples from the Bar 257 material and the failed endplate. Both small punch and impression creep tests showed similar results. Those for the impression creep tests are shown in Fig. 8. It can be seen that the endplate shows a creep strain rate substantially higher than that of the other specimens tested under the same conditions. At the time this was used as evidence that the sampled components were significantly stronger in creep than the endplate and could remain in service without immediate remedial action. However the data also showed the sampled components to have a creep strength similar to the Bar 257 material. The subsequent demonstration, by full scale conventional testing, that the Bar 257 material was weaker than the expected lower bound for grade 91, raised doubts about these components in the longer term. This led to a decision to carry out early inspection.

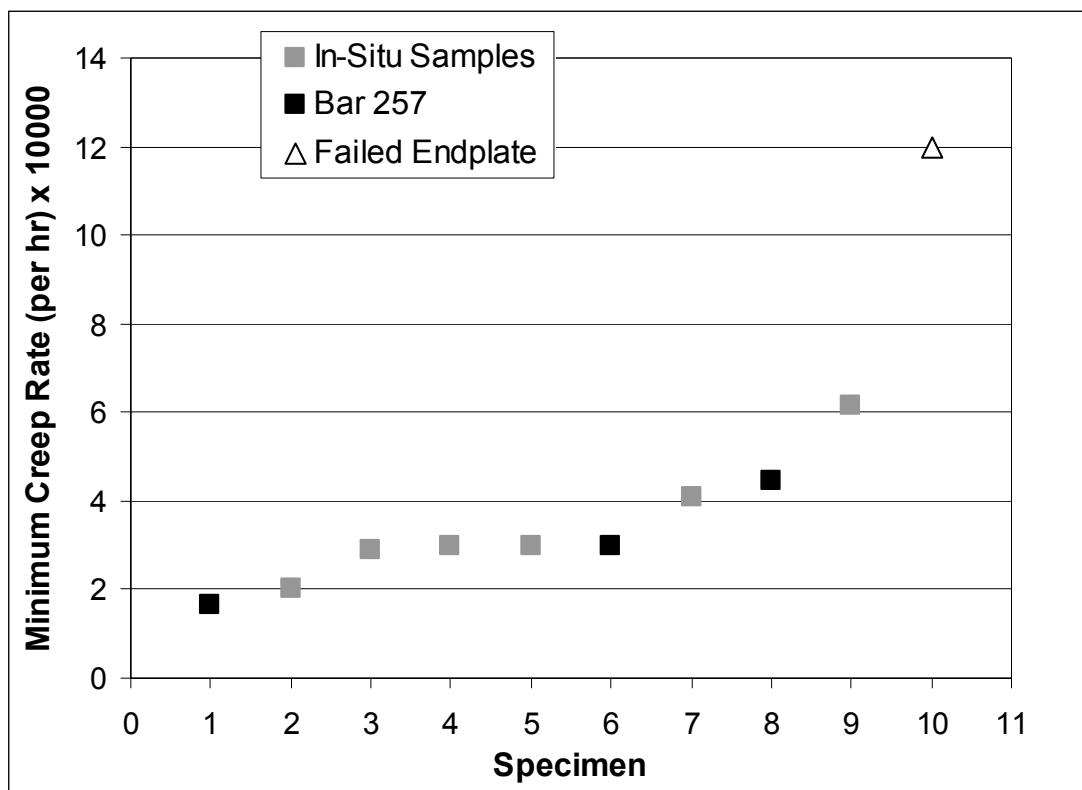


Figure 8. Impression creep results for in-situ sampled plant items, Bar 257, and endplate.

6. Summary

A number of problems with grade 91 steel have been encountered in service. These have ranged from problems related to incorrect processing at the manufacturing stage to problems related to compositional variation within the specified range. Various approaches are available to address these problems but

generating companies adopting them need to be aware of the limitations of individual techniques and the need to use them correctly.

Acknowledgements

The author would like to thank RWE npower for permission to publish this paper.

References

1. Cohn, M.J., Henry, J.F. and Nass, D. "Fabrication, Construction, and Operation Problems for Grade 91 Fossil Power Components," ASME/JSME-PVC Conference, La Jolla, July, 2004.
2. Brett, S.J. "In-Service Failures of Modified 9Cr (Grade 91) Components," IMechE Seminar – Forensic Investigation of Power Plant Failures, One Birdcage Walk, London, March 2, 2005.
3. Brett, S.J., Allen, D.J. and Pacey, J. "Failure of a Modified 9Cr Header Endplate," Conference: Case Histories on Integrity and Failures in Industry, Milan, 27th September – 1st October, 1999.
4. Brett, S.J., Oates, D.L. and Johnston, C. "In-Service Type IV Cracking on a Modified 9Cr (Grade 91) Header," ECCC Conference: Creep & Fracture in High Temperature Components – Design & Life Assessment Issues, IMechE, London, September 12–14, 2005.
5. Brett, S.J., Bates, J.S. and Thomson, R.C. "Aluminium Nitride Precipitation in Low Strength Grade 91 Power Plant Steels," EPRI 4th International Conference on Advances in Materials Technology for Fossil Power Plants, October 25–28, Hilton Head Island, South Carolina, 2004.
6. Brett, S.J. "Innogy's Approach to Identifying In-Service Modified 9Cr Forgings with Low Creep Strength," EPRI International Conference on Advances in Life Assessment and Optimization of Fossil Power Plants, Orlando, March 11–13, 2002.
7. Allen, D.J., Harvey, B. and Brett, S.J. "FOURCRACK – An Investigation of the Creep Performance of Advanced High Alloy Steel Welds," ECCC Conference: Creep & Fracture in High Temperature Components – Design & Life Assessment Issues, IMechE, London, September 12–14, 2005.

8. Brett, S.J., Allen, D.J. and Buchanan, L.W. “The Type IV Creep Strength of Grade 91 Materials,” 3rd International Conference on the Integrity of High Temperature Welds, London, April 24–26, 2007.
9. Sanchez-Hanton, J.J. “Precipitation of Carbide and Nitride Phases in High Chromium Steels,” BSc Project Dissertation, IPTME, University of Loughborough, April 2004.
10. Sanchez-Hanton, J. J. and Thomson, R.C. “The Effect of Initial Heat Treatment on Creep Behaviour of P91 Steels,” EPRI International Conference on Advances in Condition and Remaining Life Assessment for Fossil Power Plants, Louisville, October 16–18, 2006.
11. BS EN 10222-2:2000 Steel Forgings for Pressure Purposes – Part 2: Ferritic and martensitic steels with specified elevated temperature properties.
12. Rauch, M., Maile, K., Seliger, P. and Reuter, A. “Development of Creep Damage at Components made of X10CrMoVNb9-1 (P91),” VGB Powertech, September 2004, p. 71.
13. Brett, S.J. “The Creep Strength of Weak Thick Section Modified 9Cr Forgings,” Baltica V: Condition & Life Management for Power Plants, June 6–8, Porvoo, Finland, 2001.
14. Brett, S.J. and Merckling, G. “Comparative Applicability Evaluation of Specific Testing Techniques for Post Exposure Material Creep Behaviour Investigation,” Conference: Plant Life Extension, Cambridge University, April 14–16, 2004.

Life extension of hot steam piping after 200 000 h of service

Juhani Rantala, Jorma Salonen, Pertti Auerkari and Stefan Holmström
VTT Technical Research Centre of Finland, Espoo, Finland

Olli Lehtinen
Fortum Power and Heat, Naantali, Finland

Martti Pitkänen
Fortum Power and Heat, Espoo, Finland

Reino Nikkarila
Inspecta, Espoo, Finland

Abstract

The units 2 and 3 of Naantali power plant have been successfully operated for more than 200 000 h, and it is of interest to ensure the eligibility of the units for continued production. For this purpose and to assist in the related life assessments, the condition of the high temperature piping has been subjected to long term inspection and monitoring programs. Inspections have been concentrated on sites of earliest indications of creep damage or highest rates of damage accumulation as observed from monitoring and repeated measurements. Particular locations of interest are found at the welded branches of the high pressure steam mixing headers. With these example components, two traditional solutions of directly welded and wrought branch connections are compared in terms of observed creep damage and expected life.

1. Introduction

The Naantali power station on the south-western coast of Finland consists of three 135 MW coal-fired units, commissioned in the 1960's and early 1970's. The plant was initially covering peak loads, but since 1970's has been mainly used in base load mode for producing electricity for the grid, steam for nearby industrial process plants, and district heating for the Turku region. The oldest unit no. 1 is mainly used for back-up power (now at 95 000 hours), but the units 2 and 3 are important elements in the regional power infrastructure [1]. The plant has been maintained for good availability in base load service, using targeted and structured inspection and assessment programs [1, 2]. These programs have targeted e.g. boiler and hot steam line components to avoid unplanned shutdowns and unplanned corrective maintenance.

The units 2 and 3 have reached 200 000 hours of operation, and this has already required a partial design review because the original nominal design life of the high temperature sections was based on 100 000 h of service. However, there is interest in running the plant until 2020, or up to a total lifetime of 300 000 hours. Therefore in 2006 an exercise was carried out to evaluate the life potential of the boiler and piping components.

2. High pressure steam pipes

The main steam pipes are originally made of 1Cr-0.5Mo steel (13CrMo44 DIN 17175, corresponding to 13CrMo4-5 of EN 10216-2), and the design has followed the common practice and codes of 1960's. The live steam from each boiler is led through four parallel steam lines via bypass valves to the steam mixing header, where the steam is mixed and divided into two lines towards the turbine (Fig. 1).

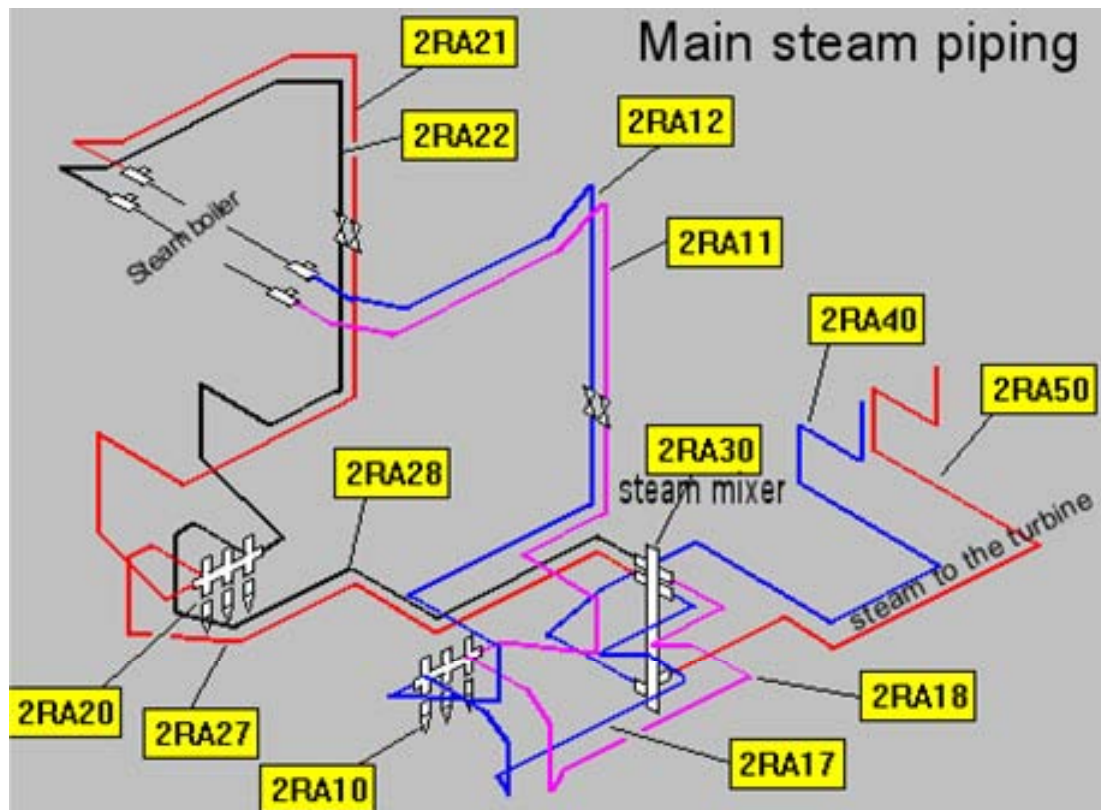


Figure 1. Layout of the steam piping of unit 2 with the mixing header 2RA30.

In unit 2 the mixing header was also originally made of the same steel, but after observing creep damage at about 100 000 h of service, the header was replaced in 1991 by using steel 2.25Cr-1Mo (10CrMo910 DIN 17175) using Rm/200 000 h as the criterion for design. The creep strength values for both 13CrMo44 and 10CrMo910 have been decreased in the European design codes and materials

standards after the plant was commissioned, but a review showed that the actual dimensions of the components compensated for the difference.

An outline of the steam mixing header of unit 2 is shown in Fig. 2. The four topmost branches are for steam inlet from the boiler to the mixing header, and the two bottom branches are for steam outlet to the turbine. In between there is a pair of horizontal support pipes to prevent the vertical movement of the header body. The codes for the branch welds are also shown in Fig. 2.

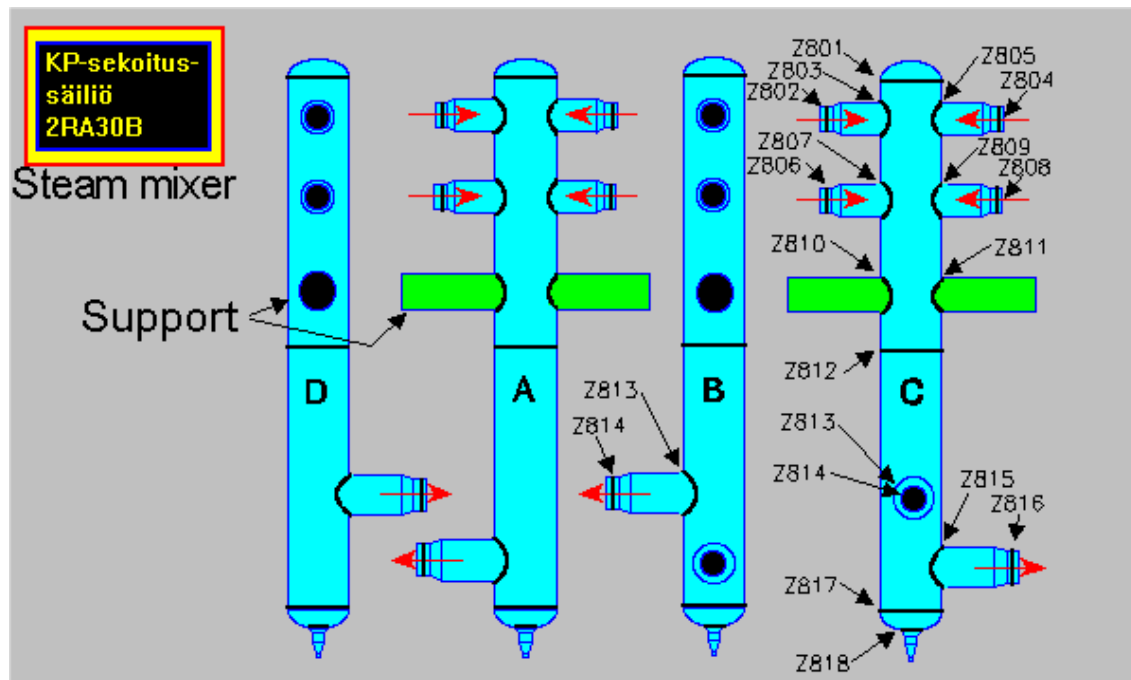


Figure 2. Steam mixing header of unit 2.

The corresponding mixing header of unit 3 has not shown similar damage or been replaced, in spite of exceeding 200 000 h of service under operating conditions that are thought to have been fairly similar to those in unit 2. The main reason for the longer life of the unit 3 mixing header is probably in the different manufacturing method, which is illustrated in Fig. 3. In the unit 3 the header body has been wrought to facilitate a normal circumferential girth weld as the branch joint. However, in the unit 2 the branches were joined to the main body directly by welding, and therefore the weld extends to the saddle point where it is heavily loaded across the HAZ. For both units, the steam values at the mixing header are nominally about 530°C / 185 bar. The actual steam temperature has been about 523°C during the recent years.

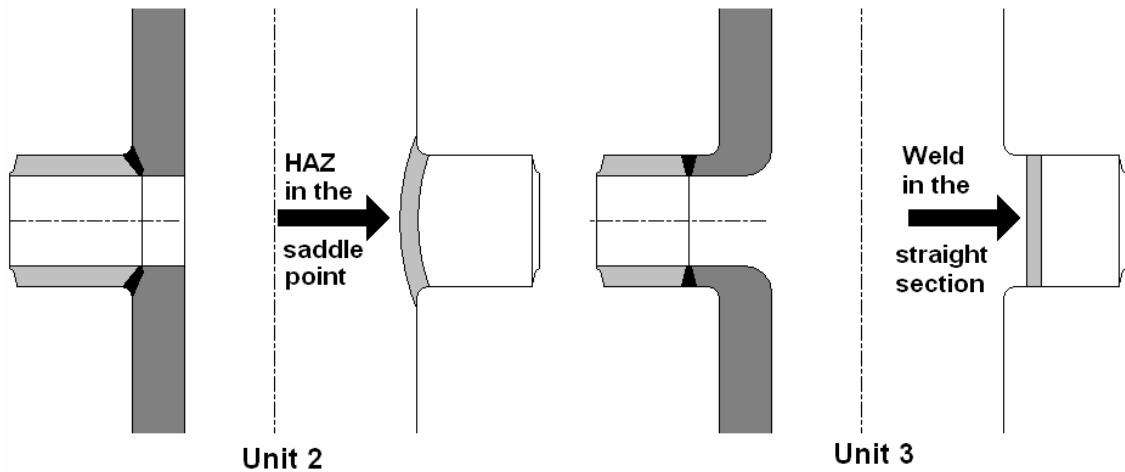


Figure 3. Differences in the mixing header geometry of the units 2 and 3.

Another difference to unit 2 is that in unit 3 the mixing header is already from the start made of the steel 10CrMo910. However, although this steel shows some advantage in creep strength at the nominal design temperature, at the actual operating temperature (520–525°C) the expected creep strength is similar to that of 13CrMo44 (Fig. 4).

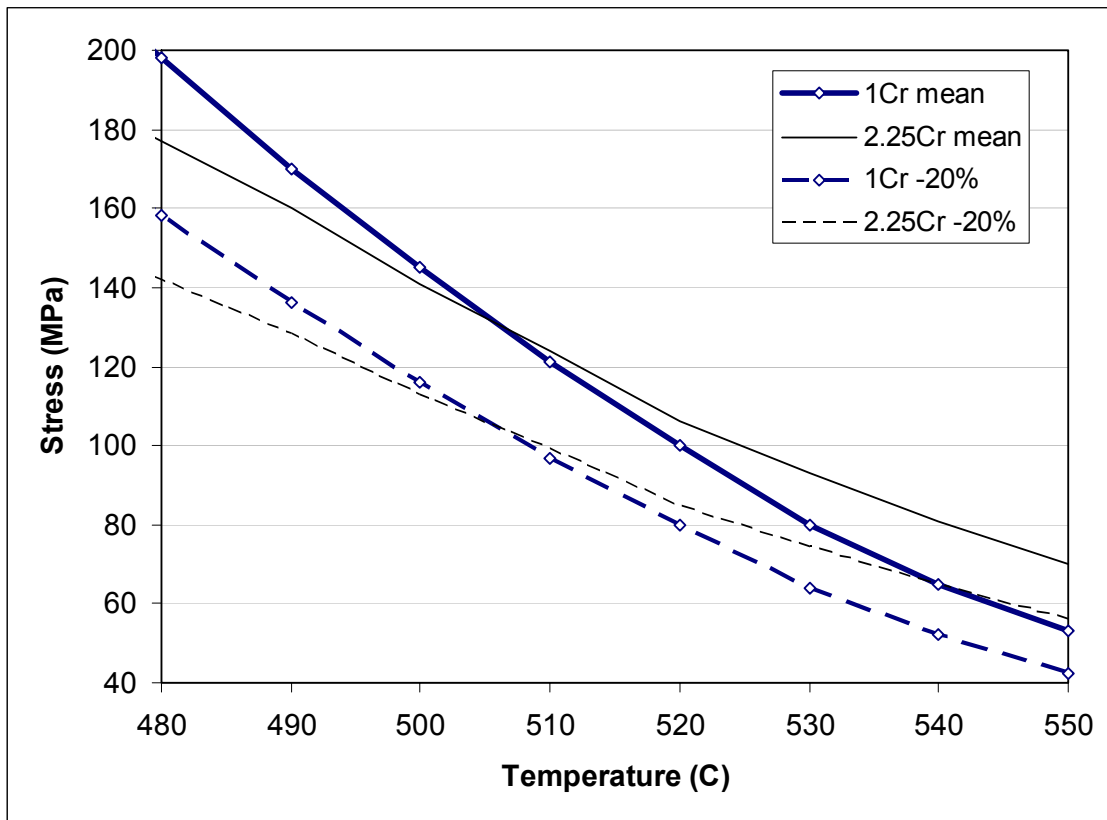


Figure 4. Comparison of 100 000 h creep strength (EN 10216-2) for 13CrMo4-5 (1Cr) and 10CrMo9-10 (2.25Cr), also showing the usual -20% scatter band.

Slight additional advantage for 10CrMo910 over 13CrMo44 may also exist in creep ductility, but probably not much after 100 000–200 000 h of service. After replacement of the unit 2 mixing header, even this small material difference would not have existed. As also the dimensional differences in terms wall thickness or diameters have been minimal, the principal difference between unit 2 and unit 3 mixing headers is thought to have been in the branch fabrication.

3. Inspection and maintenance history

Since early 1990's, inspection planning for the hot steam pipes has been based on piping stress analysis to pinpoint welds subjected to system stresses, and on the experience from inspections. The inspection results are stored in a data management system and applied for updated inspection and maintenance planning [2, 3]. The inspection programs have included replica inspections, dimensional measurements, ultrasonic and magnetic particle inspections in all units, and strain gauge measurements of the unit 3 mixing header. The capacitive strain gauges were installed in 1988 and most of them are still producing data. The locations and directions of the strain gauges are shown in Fig. 5. At the time of installation it was thought that there might be significant vertical bending loads, but this does not seem to be the case. Therefore in hindsight, the locations and directions of the gauges were apparently not entirely optimal.

The measured strains are shown in Fig. 6, indicating scatter after 180 000 hours of operation, or 85 000 hours of measurement. This scatter has been enveloped in Fig. 8, where also the negative strain indications of the gauge C7 have been converted into a positive signal to account for possible corresponding tensile strain (as a conservative assumption) elsewhere. For the predicted creep curve it has been assumed that the material is at the lower scatter bound (-20% of the mean strength of 10CrMo9-10), and the calculation was performed at two temperatures of 530 and 535°C, which should provide for a reasonable amount of conservatism. The measured data correspond fairly well with the predicted values, and after 300 000 hours of operation only 0.4% maximum strain is predicted (Fig. 8). The replica inspections of the main steam piping and the steam mixing header had shown only isolated (class 2) or orientated cavitation (class 3).

The results from the diametral measurements of the unit 3 mixing header are shown in Fig. 7. The indicated header body diameter has increased in the direction that is normal to the plane of the inlet steam lines (normal to the picture in Fig. 5). The readings with a negative trend have been observed in the plane of the inlet steam lines. The results suggest an initially stronger ("primary") straining and that 0.4% of strain has already been reached after 140 000 hours of service. However, very little strain accumulation has been indicated after some 50 000 h of operation.

The diametral measurements of the unit 3 mixing header have been discontinued after 1996.

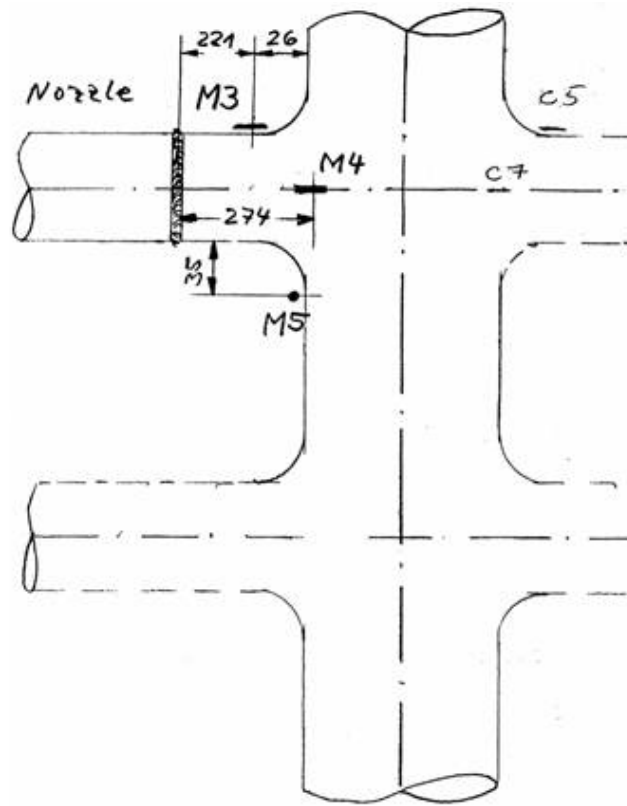


Figure 5. Locations of the capacitive strain gauges in the mixing header of unit 3.

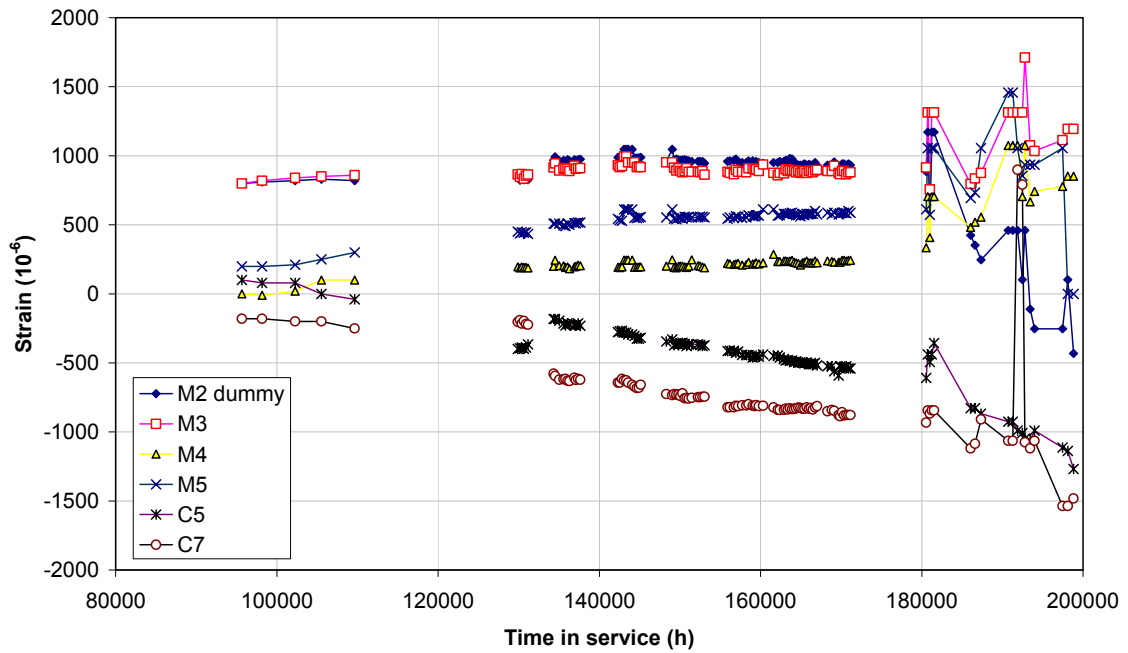


Figure 6. Strains indicated by the gauges of Fig. 5 on the unit 3 mixing header; note that $2000 \cdot 10^{-6}$ (or 2000 microstrains) corresponds to 0.2% strain.

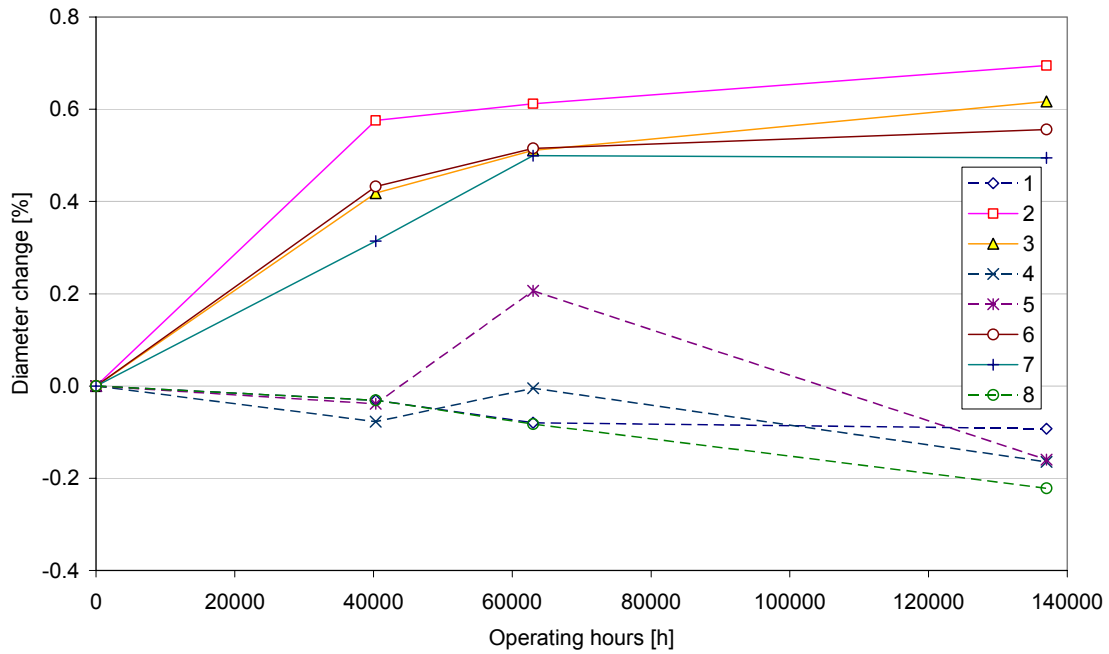


Figure 7. Measured change in the diameter of the unit 3 mixing header. The positive readings are in out of the branch plane direction, and the readings with a negative trend are in line with the inlet steam branches.

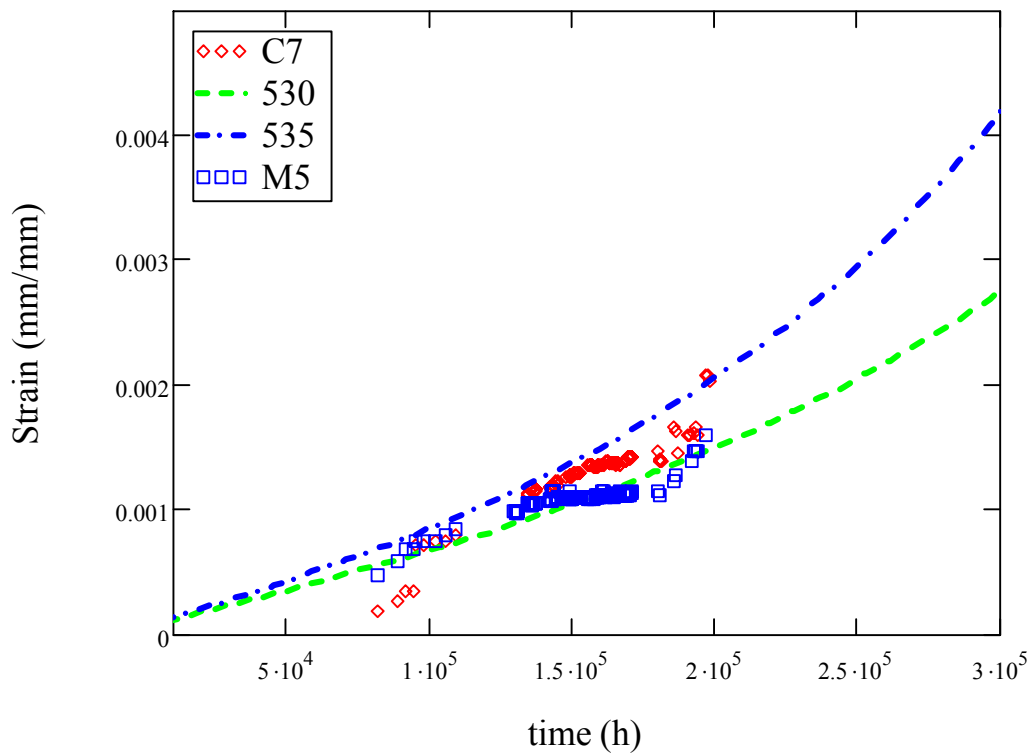


Figure 8. Predicted and measured strains of the mixing header at 530°C and 535°C. Strain 0.004 = 0.4%.

During the planned maintenance outage in 2006, macroscopic cracks were found at the saddle point position of all of the six nozzle welds, on the HAZ of the header body side of unit 2. The circumferential length of the cracks varied between 50 and 200 mm and the maximum depth was 4 mm. The longest cracks were found in the welds of the two lower (largest) branches leading to the turbine, and the cracks were surrounded by orientated creep cavitation. The damage was judged sufficiently extensive to require repairs.

As cracking of the unit 2 mixing header was found symmetrically on both saddle point sides of the branches, the damage is due to internal pressure and not bending (system loads). The maximum crack depth was in all cases in the HAZ of the header body near the saddle point. The larger diameter of the two lower branches had lead to more extensive cracking than in the upper smaller branches.

As the plant is aiming for life extension to 2020, particular care is needed to ensure the required viability of the unit 2 mixing header after the specified repair. Experience suggests that the life of a repair weld is typically only a quarter of the original weld without further modification or reduced steam values. Therefore, additional measures are probably needed to avoid repeated repair or replacement of this header body within the targeted life extension. In contrast, the corresponding mixing header of the unit 3 is likely to perform well to the required 300 000 h of service.

The differences in the expected life between the mixing headers of units 2 and 3 highlight the impact of original design of the branch connections. Although the weakness of saddle point welds is well known, such vintage solutions have recently replaced much of the forged T-joints and other wrought components in new plant. The above example suggests a lifetime difference at least by a factor of three, and therefore the lower cost manufacturing may require balancing in the expected life cycle cost.

4. Conclusions and summary

The case of Naantali power plant demonstrates the general potential of life extension, in this case to three times the original (nominal) design life. Long term service at high temperatures will exert some accumulating damage that in the end will limit the attainable life. However, this damage accumulation is very uneven in large systems, and is affected by local service conditions, state of the materials, quality and integrity at the time of fabrication, and structural details. Particular well known weak points in steam pipings can be expected in welds and branch connections.

The main steam mixing header at the unit 2 has been replaced already once, and after only 100 000 hours of operation macroscopic creep cracks have been found in the replaced component. No dimensional or material deviation, nor excessive system stresses were found have significantly influenced the observed damage. The header has been constructed with direct branch welding and was judged to require repair. In contrast, the corresponding mixing header of unit 3 with wrought header body and no saddle point welds shows no similar creep damage after 200 000 h of service under comparable service conditions. This header has been equipped with strain monitoring that shows relatively modest creep strain accumulation. The monitoring results together with strain modelling suggests that the header could well provide trouble-free service to 300 000 h of operation.

The benefits of the structural solution for unit 3 mixing header appear clear. It seems unfortunate that the directly welded branches with the unavoidable weakness in the saddle point position have again become popular in new plant.

References

1. Auerkari, P., Kauppinen, P., Lehtinen, O. and Nikkarila, R. Boilers and turbines – when to retire? *Voima & Käyttö* 102 (5–6) 2006, pp. 32–34. (In Finnish)
2. Salonen, J., Auerkari, P., Lehtinen, O. and Pihkakoski, M. Experience on in-service damage in power plant components. 2nd Int. Conf. on Engineering Failure Analysis (ICEFA-II), paper O8.1. Toronto, Canada, 12–15 Sept 2006.
3. Auerkari, P., Salonen, J., McNiven, U. and Jovanovic, A. Classification of damage and prediction of its development in high temperature components of the power industry. *Failures '96*. A. A. Balkema (1996). Pp. 269–280.

Predicting lifetimes of components in power station engineering plant

Andrew Morris¹, Amit Puri², Chris Maharaj², Miltiadis Kourmpetis²,
Mikael Sjö Dahl³ and John P. Dear²

¹ E.ON UK, Nottingham, UK

² Imperial College London, London, UK

³ Luleå University of Technology, Luleå, Sweden

Abstract

Today, there is increasing demand for power station plant to be operated cost effectively and to reliably maintain required electrical supply. This requires minimising the risk of having to shut-down the plant for emergency repairs. Of paramount importance, is plant operating integrity and well prepared and executed maintenance programmes. This paper reports on the recent developments to the Auto-Reference Creep Management & Control (ARCMAC) system used by E.ON UK. This includes achieving biaxial strain measurement with increased resolution and the employment of Digital Image Correlation (DIC).

Nomenclature

ARCMAC	– Auto-Reference Creep Management & Control
DIC	– Digital Image Correlation
ARAMIS	– DIC software
GOM	– Optical Measurement Company
ε_y	– strain in the y-direction (vertical)
ε_x	– strain in the x-direction (horizontal)
G_L	– installed gauge length (mm) between the weld pins
A	– manufactured reference distance (3 mm)
$B(t)$	– distance between two outer targets on the gauges.

1. Introduction

The life of steam pipes in power stations very much depends upon the material's steady state creep rate. Essential is that monitoring sensors are of a very rugged design well able to endure the demanding conditions related to environment of high-pressure steam pipes. This is to provide creep data for remnant life assessment of pipes when a power generating plant is closed down for periodic

maintenance. A combined approach using the ARCMAC gauge system developed by E.ON UK and Digital Image Correlation (DIC) to study the variations in creep strain on steam pipe networks will be presented. This is particularly useful, for example, when monitoring parent pipe material, welds and other localised features on the pipe network. Both circumferential and axial strain rates are monitored to provide for analysis to identify when pipes are approaching their reliable end-of-life point. This provides for planned replacement of pipes as part of cost effective management of power stations. The E.ON UK ARCMAC gauge system for measuring strain has been developed in the light of experience of its use to achieve high confidence ratings in the data obtained. This creep strain monitoring system provides data that can be used to underwrite life extension of power stations, many of which are now in operation in the UK beyond 225 000 hours.

2. ARCMAC System

This is a creep management system developed by E.ON UK Power Technology. The creep strain rate is calculated by comparing two captured images of a pair of gauges, the first of which is captured after installation and the subsequent one after two year's operation. Typically a secondary creep strain rate on main steam CMV pipes is ca. $2 \times 10^{-8} \text{ hour}^{-1}$ and the unit might operate for 12 000 hours over a 2 year period, for which there is an expected creep strain accumulation of 240 micro-strain.

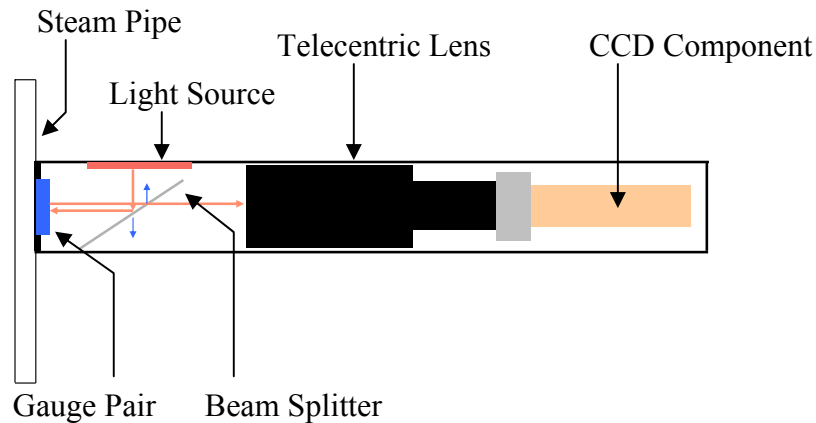


Figure 1. Schematic of ARCMAC camera unit.

The ARCMAC system has been designed to work with readily available equipment. For on-site measurement it requires a portable hand-held camera unit with image capture logger. This has been designed with a telecentric lens, beam splitter and diffuse light source. These are arranged so as to provide illumination along the axis of the camera, as shown in Fig. 1.

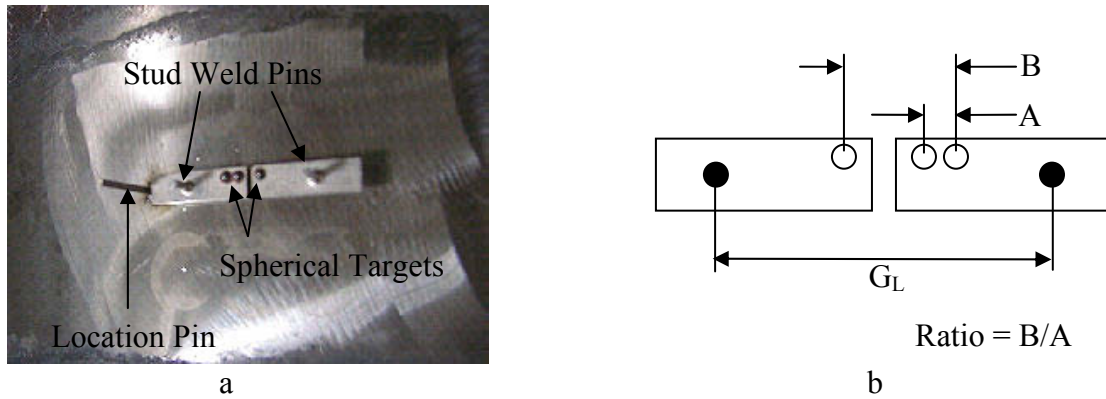


Figure 2. ARCMAC gauges: a) Located on stream pipe; b) Ratio calculation.

The gauges themselves are constructed from Inconel which allows welding onto the pipe surface. Mounted upon the gauges are SiNi target spheres, as shown in Fig. 2a above. It is important is that the SiNi target spheres are appropriately illuminated so as to provide for the needed measurement. The three target spheres provide images in the form of three circular points of light. Two of these points of light come from the two spheres on one Inconel gauge and these provide a reference dimension. Image analysis software calculates the distance between the centers of each light spot. This information is used then to calculate the ratio between the light spots, as shown in Fig. 2b, which is subsequently used to evaluate strain via Equation (1), where $Ratio_0$ is from the initial image, and $Ratio_t$ is from the subsequent one. Used in conjunction with the MPC project OMEGA methodology, [2], this will allow estimation of component remnant life.

$$e = \frac{Ratio_t - Ratio_0}{G_L/A} \quad (1)$$

2.1 Improved Resolution of ARCMAC System

Recently, the light source for the ARCMAC system has been upgraded from an electroluminescent strip to a high intensity Light Emitting Diode (LED) array. The increased illumination has produced an improvement in resolution and this is assessed using an Extensometer Calibration Rig (ECR) supplied by the National Physical Laboratory (NPL). The ECR has been calibrated in compliance with the BS EN 10002-4:1995 and ASTM E83-96 standards. The maximum error over a nominal extension of the ECR of 0–2.5 mm was 0.1 μm . Such a precise rig allowed the resolution of the ARCMAC camera to be obtained.

The ECR consists of a moving and fixed bar, upon which the two gauges were attached with a nominal gauge length of 31 mm, and the displacement between the two can thus be accurately altered. Three datum images are captured and then the gap between the two parts of the gauge is increased in steps of 1 or 5 μm . At the

end of each step, three images are captured. Once the maximum calibration extension has been reached the same process is repeated, this time decreasing the gap until the datum position is reached.

Site installation experience has shown that the camera unit will not always be positioned precisely normal to the target gauge. This is one of the reasons for the choice of a telecentric lens in the camera unit; it is tolerant of angular misalignments to a reasonable degree. However the downside is that the optimum distance between the lens and the target is at around 92 mm \pm 3 mm, so that the lens must be located inside the camera unit with reasonable precision. In addition, the working distance of the lens coupled with its physical length means that the camera unit is approximately 450 mm long. This means that some plant locations are inaccessible with this arrangement. Hence several calibration runs have been undertaken with the camera re-positioned to represent conditions on site.

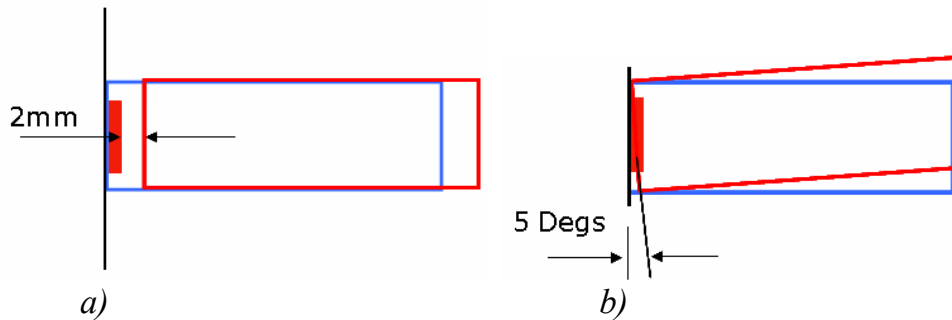


Figure 3. Example of types of camera offset: a) Axial; b) Angular.

To assess the accuracy of the system with the new light source, a comparison of percentage error obtained for the two different light sources for optimum working conditions and for situations when the camera is displaced from its optimum position is used. The purpose of these experiments was to demonstrate the tolerance of the strain measurement system. The two divisions of displacement considered are axial offset and angular offset, as highlighted in Fig. 3. For this image the blue box represents the camera at optimal position, and the red box represents the camera at the offset position. The details of the comparison are:

- Axial positioning: Camera unit normal to the gauge, with the axial position varied from nominal position to +4 mm, in steps of 1 mm (5 stages in total).
- Angular misalignment: Camera unit positioned at the nominal position, with angular misalignments up to $\pm 10^\circ$, in steps of 5° (5 stages in total).

Fig. 4 shows the comparison of the two light sources for the nominal operating position. The improvement at low values of strain and higher values is significant. A vertical red line is drawn at the 161 micro-strain limit (160 micro-strain corresponds to a displacement of 5 μ m). The error of the LED system is less than

10% for strain values as low as 64 micro-strain. The comparisons at the offset stages are shown for axial and angular offsets in Tables 1 and 2 respectively. These values were extracted at the 160 micro-strain point, and it can be seen that there is definite advantage gained by using the high intensity LED at the lower strains.

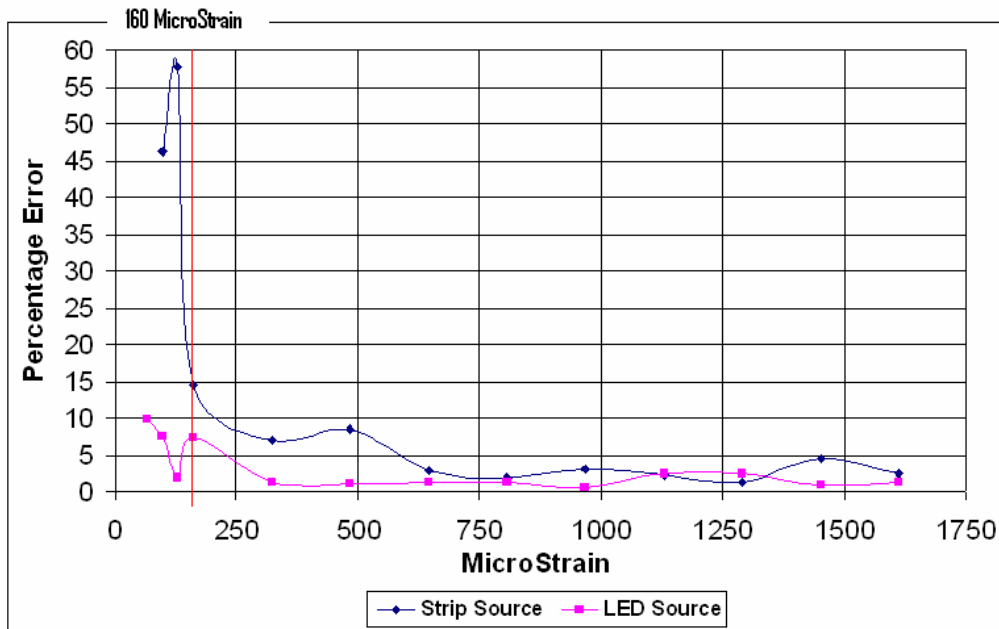


Figure 4. Comparison of LED source and Strip Light Source for nominal operating conditions.

Table 1. Percentage error for axial offset.

Offset	Percentage error obtained	
	Strip Source	LED source
Nominal (0 mm)	15	7
1 mm	12	2
2 mm	11	12
3 mm	37	2
4 mm	6	3

Table 2. Percentage error for angular offset.

Offset	Percentage error obtained	
	Strip Source	LED source
Nominal (0°)	15	7
5° left	21	4
10° left	39	6
5° right	22	3
10° right	8	2

In conclusion, angular misalignment, as well as axial displacement, has very little effect in reducing the accuracy of the ARCMAC camera when using the new LED source. In addition, the confidence strain value has been improved from 160 to 64 micro-strain. Fig. 5 shows three different creep rates with the resolution limits for the LED and strip sources as horizontal dotted lines. It is apparent with the new LED source, it is possible to measure with confidence the lowest creep rate of ca. $1 \times 10^{-8} \text{ hour}^{-1}$ after 2 years (12 000 hours of operation). It is to be noted that typical secondary creep strain rate on main steam CMV pipes are ca. $2 \times 10^{-8} \text{ hour}^{-1}$.

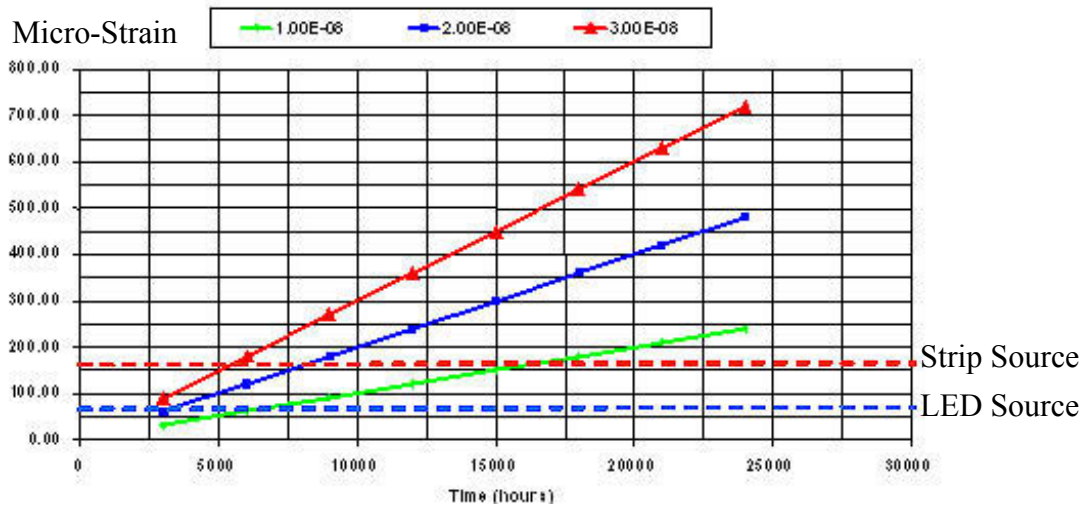


Figure 5. Improvement in creep measurement for LED source versus Strip light source.

3. Digital Image Correlation

DIC uses a series of digital images of a surface under various levels of load, upon which a high density random paint pattern has been applied [3]. The software divides the image into squares of pixels known as facets, from which the inter-facet displacements can be calculated between load levels, as shown in Fig. 6. For greater accuracy, the GOM ARAMIS software [4], uses an averaging method based on a group of facets. The evaluated displacement matrix can be differentiated to produce a full-field strain map of the surface. This allows for easy visualisation of the strain experienced by the component. In addition to this, the strain variation along a drawn line can be obtained, which allows precise numerical analysis of the observed strain.

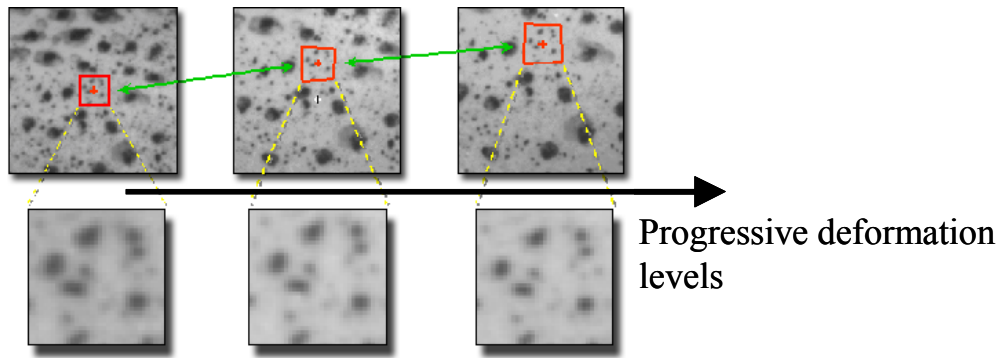


Figure 6. Example of DIC solution method [5].

The system requires the use of digital cameras. The ARAMIS system is able to capture strains as low as 500 micro-strain [6], which is more than twice the expected strain on a steam pipe after two years in service. Therefore, DIC will be used in conjunction with the ARCMAC gauges to evaluate any unusual strain distribution surrounding the gauge area, such as occurs with internal weld defects. The presence of such a defect is likely to cause higher strain levels in the pipe, and it is important to estimate the contribution of this towards the creep rate estimation.

3.1 Tensile Testing on Pipe Material

The typical pipe material used is CMV steel, whose major alloying elements consist of Chromium (0.5%), Molybdenum (0.5%) and Vanadium (0.25%). Upon hardening the material achieves a maximum tensile strength of 610 MPa [7]. The alloying elements serve to increase synergistically the high temperature creep rupture strength by reducing the coarsening mechanism of spheroidisation, which would occur in plain carbon steel at elevated temperatures [8]. Tests were conducted on 250 mm long tensile dog-bone specimens with a gauge length of 150 mm and thickness 6 mm. The width of the specimen was 37.5 mm along the gauge length. To simulate a weld imperfection, a small defect 3 mm deep, 15 mm long and 3.5 mm wide, was machined onto the back surface of the specimen, with the aim of performing DIC on the front side. This would allow simulation of non-destructive testing of an internal defect within a welded section of pipe, as might be encountered on-site.

The experiments were compared to a Finite Element (FE) model (ABAQUS version 6.6-1) using modulus of elasticity, yield strength, and Poisson's ratio values obtained from [7] and [9]. Work hardening values for the plastic range of the material were obtained by conducting a tensile test on a similar CMV sample without a defect. Elements used were of the second order, reduced integrated, 3D 20-node brick type. These elements were chosen as they were suitable for plastic deformation modelling and did not suffer from volumetric shear locking. Through end friction gripping, the specimen was constrained to move except in

the Y-direction. A surface traction load was applied up to the maximum test load of 60 kN at both gripping ends.

Fig. 7 shows a comparison of observed ϵ_x and ϵ_y obtained from both ABAQUS and ARAMIS at two different load levels. At both load levels the effects of the defect are clearly visible as a non-uniform strain pattern. The shape of the defect causes shear failure, which results in elevated strain levels at 45°. In addition, there is a region of high compressive strain in the region of reduced material cross-section for the ϵ_x plot, as would be expected.

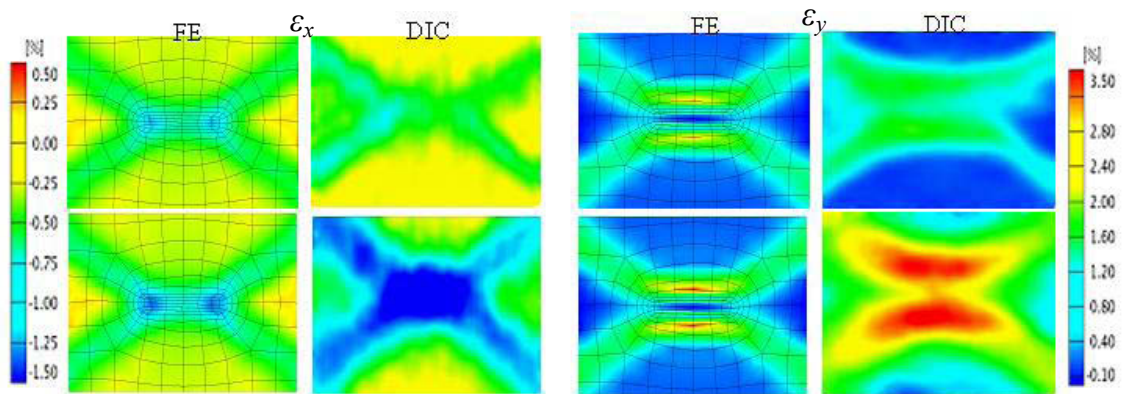


Figure 7. FE and DIC comparison: ϵ_x and ϵ_y plots for 88% (top row) and 100% (bottom row) of maximum load.

Table 3. Comparison of FE and DIC strain values for 100% load.

	ϵ_y		ϵ_x	
	FE	DIC	FE	DIC
Centre of defect	~ 0%	~ 2.8%	~ -1.0%	< -1.5%
Close to defect	> 3.5%	> 3.5%	~1.0%	~ 1.0%
Remote from defect	< 0.1%	< 0.1%	0%	0%

Table 3 summarises the correlation between FE and DIC. As can be seen there is good agreement between the two methods at points near and remote from the defect, substantiating the DIC method. There is a clear difference between the two methods, however, at the centre of the defect. To be noted is that, the DIC could be overestimating the absolute strain in both X and Y directions at this point.

There are three potential reasons for this, the first being that the DIC is more roughly averaging the image when formulating the displacement matrix. In other words, the DIC is unable to detect the step change in the observed strain over this small distance. The second possible explanation is that the FE mesh is modelled in such a way to promote this particular anomaly, and further refinements may result in closer agreement. The third possible explanation is that the thickness reduction in the centre is causing out-of-plane strain, a feature which would be

picked up by DIC as inaccurate in-plane strain, when using only one camera, but can be modelled exactly by FE. However, the use of a telecentric lens would minimise this effect. It is probable that the combined effects of these three processes will result in the differences shown in Table 3 and the fact that the majority of values do agree well can be considered as a positive result.

Another difference between the two sets of results is that the FE produces clearly defined crossed shaped regions of high strain, whereas the DIC is more diffuse. The principle reason for this is that the FE model does not incorporate inhomogeneities in the material. A further interesting difference between the two is that the formation of this distinctive pattern was observed at earlier strains in the FE model, specifically 36% and 54% for ϵ_y and ϵ_x respectively, as shown in Fig. 8. The most likely reason is that the resolution of the applied DIC pattern may be insufficient to pick up the slight difference in observed strain at the lower load levels.

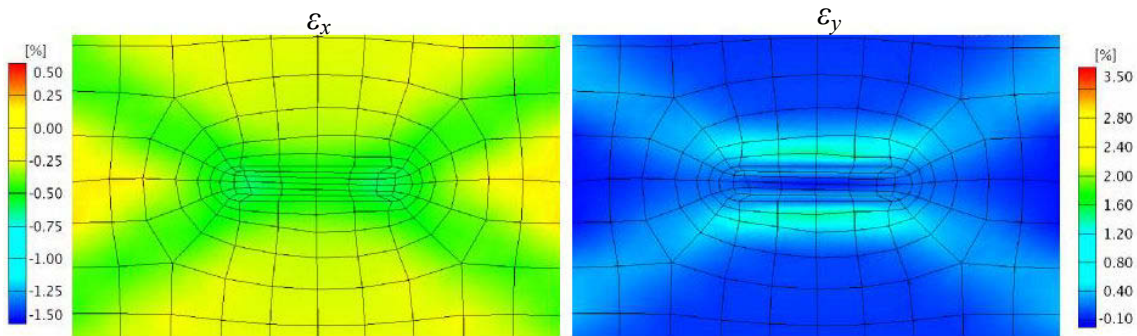


Figure 8. ϵ_x (left) and ϵ_y (right) strain maps for FE model at 36% and 54% respectively.

Further tests will incorporate using more refined FE models, in addition to comparison work with electronic strain gauges and ARCMAC gauges. However, the initial results show that the DIC system is able to detect effectively sub-surface defects within steam pipe material.

4. Combined ARCMAC and DIC

Following the calibration of the system using the LED light source, it was decided that specimens with ARCMAC gauges and DIC speckle coatings should be exposed to harsh real-life loading conditions, e.g. 568°C temperature and strain measurements should be provided by the ARCMAC camera. Hence, tensile dog-bone specimens were prepared from high pressure CMV steel pipe material. The specimens were designed with biaxial ARCMAC gauges on one side and a speckle pattern on the other side. This way the ARCMAC camera will produce strain measurements from both the ARCMAC gauges and the speckle pattern. High temperature paint was used as above to form a speckle pattern on

the surface of the CMV tensile specimens. The ARCMAC camera recorded a reference picture of the speckle pattern. The tensile specimens were then placed in an oven at 600°C for 1000 hours, which modestly exceeds typical operational temperatures of a high-pressure steam pipe. After exposure, the ARCMAC camera was used to record further images of biaxial ARCMAC gauges and high temperature paint speckle patterns.

The purpose of these experiments was to see if it was possible to obtain DIC strain data from a speckle patch that had been subjected to high temperature ageing conditions. Different finishes and coatings were applied on the specimens in order to investigate the environmental effect on the speckle pattern. Figs. 9a and 9b show images obtained with the ARCMAC camera of the speckle paint applied on a specimen with airbrush and aerosol respectively. The paint used here was FIRWOOD 75 [10], which has been rated as being able to withstand temperatures as high as 600°C. Fig. 9c shows an image of the ARCMAC gauges taken with the ARCMAC camera before the specimen was placed in the oven.

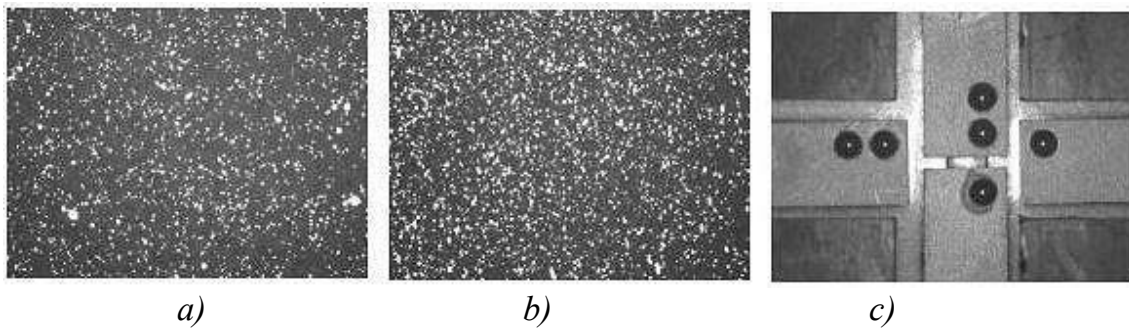


Figure 9. ARCMAC images: a) FIRWOOD 75 high temperature airbrushed paint, b) FIRWOOD 75 high temperature aerosol paint; c) Biaxial ARCMAC gauge.

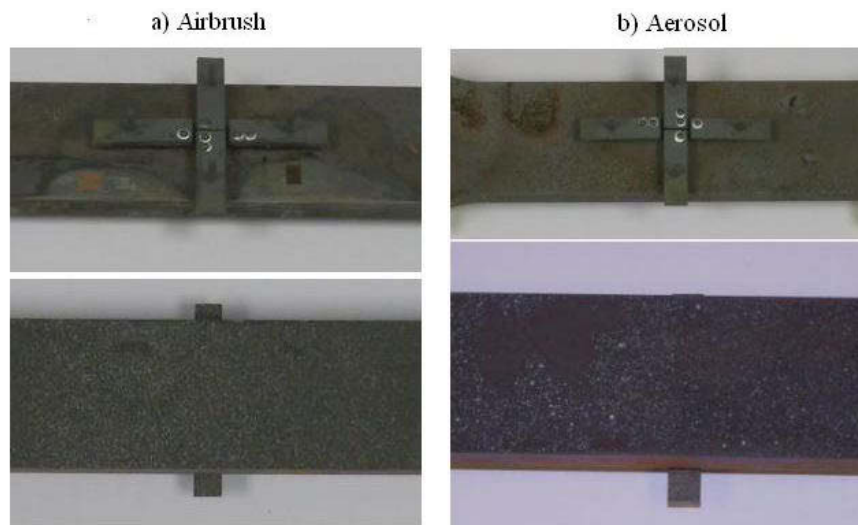


Figure 10. Biaxial ARCMAC gauges with speckle paint pattern after exposure in an oven at 600°C for 1000 hours: a) airbrush paint finish and b) aerosol paint finish.

Of the two speckle patterns, the airbrush applied speckle pattern survived better than the aerosol applied speckle paint finish. However, good DIC data was obtained from both finishes. Other paints and finishes are being investigated for DIC measurement studies.

The ARCMAC camera combined with DIC is being used to study specimens with different defects and other features. One example is a specimen with a central circular hole of 3 mm diameter. Images from the ARCMAC camera were imported into DIC software for strain analysis, in this case ARAMIS. The results are shown in Fig. 11 for two different load levels, and good DIC strain fields have been obtained using the ARCMAC camera.

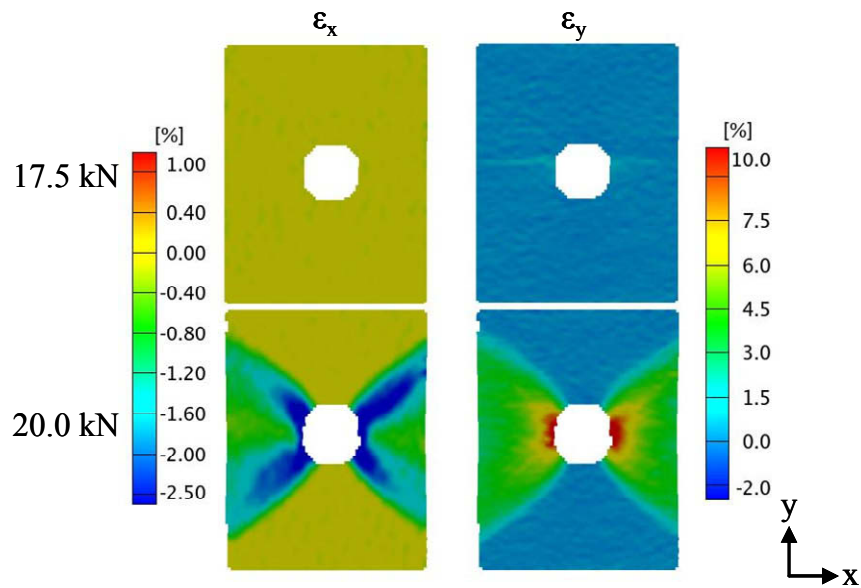


Figure 11. Comparison of ϵ_x and ϵ_y maps obtained with the ARCMAC camera for specimen loaded in tension (in the y direction) with a central circular hole.

5. Conclusion

The new LED source for the ARCMAC system has improved strain resolution limits. This has allowed low creep rates of ca. $1 \times 10^{-8} \text{ hour}^{-1}$ to be measured with confidence over 2 years (12 000 hours of operation). In addition, the DIC strain maps obtained from tensile dog-bone specimens with rear surface defects have been substantiated with FE analysis. Furthermore, speckle coatings using high temperature paints have been applied to CMV steel material and subjected to high temperature conditions. It has been found that the integrity of these speckle patches is maintained and speckle coating images recorded by the ARCMAC camera system can be analysed using DIC software to produce strain field maps. The ARCMAC camera is capable of capturing ARCMAC gauges and at the same time DIC strain patterns.

Acknowledgments

The authors acknowledge the support of E.ON UK and James Mithen [11] for his helpful contribution.

References

- [1] Morris, A. Dear, J. and Kourmpetis, M. “Life Assessment by Monitoring Biaxial Strain-Rates in High Temperature Steam Pipelines”, Proc. of ASME PVP 2006/ICPVT-11 Pressure Vessels and Piping Division Conference, July 23–27, 2006, Hyatt Regency Vancouver, BC, Canada, Paper Number: 93065.
- [2] Prager, M. Journal of Pressure Vessel technology, 1995, Vol. 117, (1995), p. 95.
- [3] Sjodahl, M. “Accuracy in Electronic Speckle Photography”, Applied Optics, Vol. 36, No. 13, pp. 2875–2885, 1997.
- [4] <http://www.gom.com> – Deformation measurement system developed by GOM mbH, Germany.
- [5] http://www.correlatedsolutions.com/index.php?option=com_content&task=view&id=23&Itemid=36 – Principle of Digital Image Correlation, Correlated Solution, West Columbia, USA.
- [6] GOM mbH, “ARAMIS User Manual: ARAMIS v5.4.1”, GOM mbH Germany, 2005.
- [7] BS3604-1:1990, Steel pipes and tubes for pressure purposes: ferritic alloy steel with specified elevated temperature properties. Specification for seamless and electric resistance welded tubes, British Standards Publishing Limited, London, 1990.
- [8] API RP 571, Damage Mechanisms Affecting Fixed Equipment in the Refining Industry, American Petroleum Institute, 2003.
- [9] BS806, Specification for the design and construction of ferrous piping installations for and in connection with land boilers. British Standards Publishing Limited, London, 1993.

- [10] <http://www.firwood.co.uk/webapp/wcs/stores/servlet/ProductDisplay?langId=-1&storeId=10001&catalogId=10001&productId=26255> – Firwood 75 High Temperature Resisting Paint information sheet, Firwood Paints LTD, UK.
- [11] Mithen, J. ARCMAC and DIC Applied to Power Station Engineering, Final Year MEng Project, Imperial College London, 2007.

Structural analysis and lifetime assessment of outlet headers

Kim Calonius, Otso Cronvall and Pasi Junninen

VTT Technical Research Centre of Finland, Espoo, Finland

Abstract

Main emphasis in this article is in the presentation of structural mechanics based lifetime analyses performed to an outlet header. The primary objective was to assess the effects of fatigue and creep on the lifetime of the header. The structural analyses were performed with the finite element analysis (FEA) code ABAQUS. The outlet header and the tubes connecting to it were analysed with both local and global FEA models. Fatigue and creep induced degradations were assessed by comparing the analysed stress distributions to fatigue and creep strength values given in applicable standards. The combined effect of fatigue and creep was assessed by using linear superposition (linear life fraction rule).

1. Introduction

Structural mechanics based lifetime analyses performed to an outlet header manufactured by Foster Wheeler Energy are presented in this article. For one load case also fluid mechanics based analyses were applied. The objective of this study was to assess the separate and combined effects of fatigue and creep induced degradation to the lifetime of the header. The analysed header is situated in Turow 3 power plant in Poland. The analyses included in addition to the header itself also to some length the numerous tubes that connect to it, and feed also the superheated steam to it.

The fluid mechanics analyses were performed with analysis code APROS, which has been developed at VTT. The structural analyses were performed with commercial FEA code ABAQUS. The results from APROS analyses include pressure and temperature distributions, which were used in some ABAQUS analyses to evaluate time dependent stress and displacement distributions. The results from ABAQUS analyses include stress and displacements distributions. The outlet header and the tubes connecting to it were analysed with both local and global FEA models. The performed analyses are presented in more detail in VTT analysis report [1].

The main locations of interest in the structural and degradation analyses were the joints connecting the tubes to the header. They are the most sensitive locations to degradation, due to e.g. the different shapes, wall thicknesses and materials of the header, the tubes, and the welds.

Due to lack of cracking data, fracture mechanics based degradation analysis was not applied. Instead, the fatigue and creep induced degradation was assessed by comparing the analysed stress distributions to respective fatigue and creep strengths found from appropriate standards. More specifically, concerning the assessment of the fatigue induced degradation, the so called *S-N* curves, that define the fatigue strength as a function of stress level and the number of load cycles, were used. The combined effect of fatigue and creep was assessed by using linear superposition.

2. Characteristics of the examined outlet header

The Geometry, material properties, loads as well as degradation issues of the header of Foster Wheeler Energy are described in this chapter.

2.1 Geometry

The relevant geometry data of the Turow 3 header and tubes connecting to it are described in the following. The data presented here are taken from the design drawings [2, 3, 4, 5].

The tubes connect actually to two headers, namely the inlet header and the outlet header. The former header is located 2926 mm above the latter header. The superheating zone is situated between the two headers. This zone is separated from the headers and other parts of the power plant with convection cage walls. Of the two headers it is the outlet header that is analysed here, and thus only geometry data concerning it and to some length the connecting tubes are presented here.

Below in Fig. 1 is an elevation of the outlet header, the tubes connecting to it, and the nearest convection cage walls, seen from front.

In the vertical direction the tubes connecting to the header run in five levels, as can be seen from Fig. 1. In the horizontal plane the nearly 20 m long header is joined longitudinally from its other to another pipe of the same section size, and the other end of the header is closed. In addition, in the horizontal plane the spacing of the tubes in the longitudinal direction of the header is 104 mm. All in all 870 tubes connect to the analysed header.

There are also six groups of tubes, each containing five tubes, the paths of which differ from the most of the tubes, which are regularly spaced and have identical geometries. In Fig. 1, one of these six tube groups is seen to connect to the header in two o'clock position.

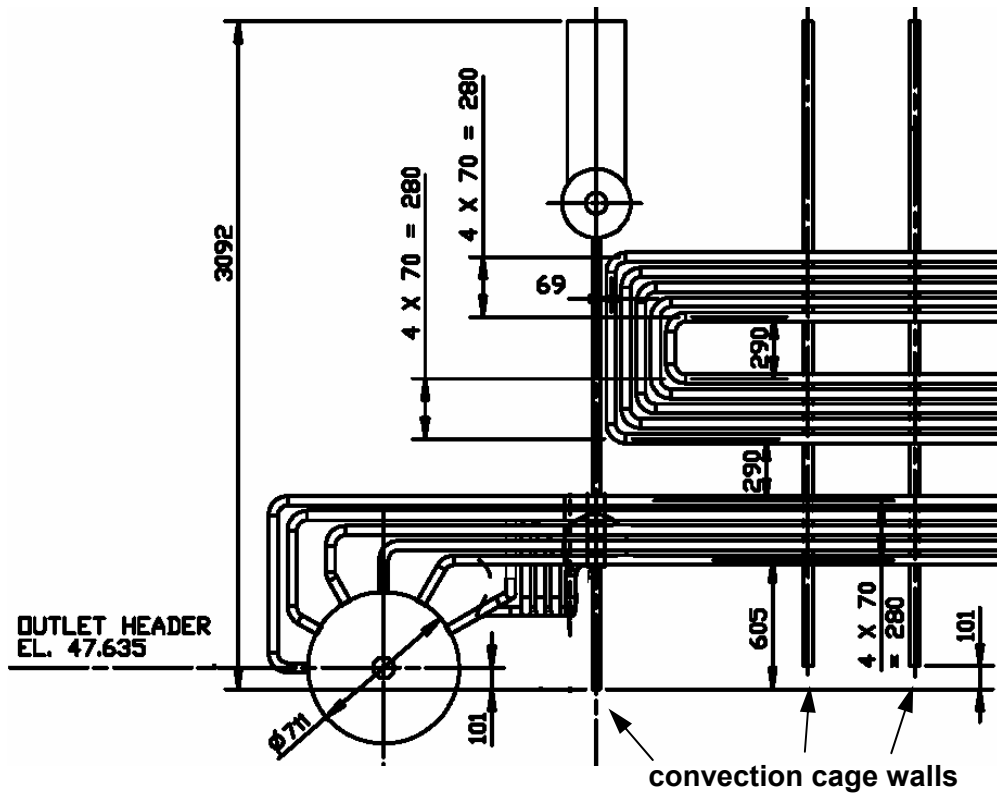


Figure 1. An elevation of the outlet header, the tubes connecting to it and the nearest convection cage walls, seen from front [2].

More specifically, in the horizontal plane the header and the connecting tubes are composed of fields the size of which is 2392 mm, and which are divided by field splits the size of all of which is 208 mm. The mentioned six differing tube groups run for most part in these field splits, one tube group per field split.

The main dimensions of the outlet header are the following:

- outer diameter: 711 mm
- wall thickness: 36 mm
- total length: 18 272 mm.

The main dimensions of the tubes connecting to the outlet header are the following:

- outer diameter: 44.5 mm
- wall thickness: 4.5 mm
- tube bend radius: 70 mm
- tube lengths: vary.

The tubes connecting to the outlet header also support it. The other pipe of the same section size as the header, and to which it joins longitudinally, provides also some minor additional support to the header. The tubes, in their turn, are supported by the convection cage wall nearest to the outlet header, to which wall they are joined by welding.

In the following Figs. 2 and 3 are shown some relevant dimensions and details of the outlet header and the tubes connecting to it. Fig. 2 shows the locations and orientations of the tubes in the vertical plane. Fig. 3 shows a detail of the joint between the outlet header and the tubes connecting to it.

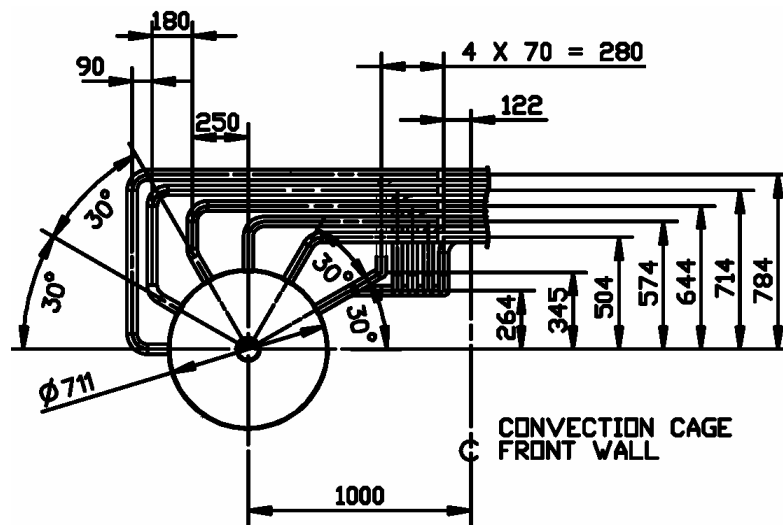


Figure 2. The locations and orientations of the tubes connecting to the outlet header, shown in the vertical plane [2].

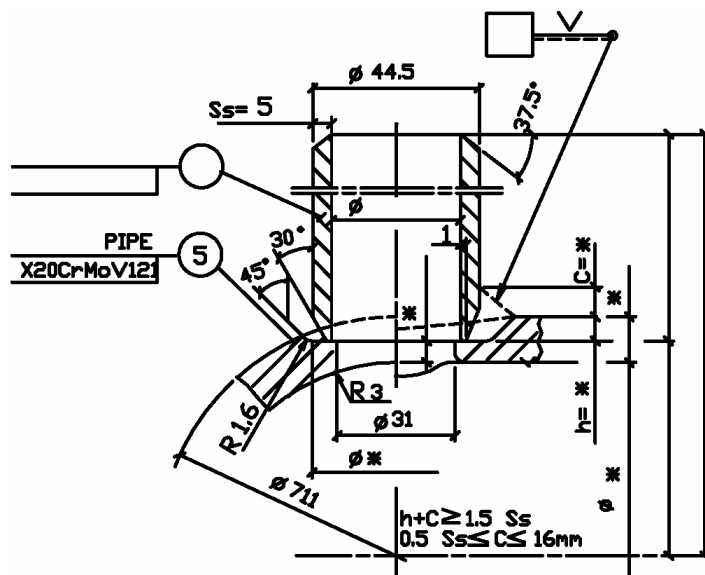


Figure 3. The detail of the joint between the outlet header and the tubes connecting to it [4].

2.2 Materials

The various materials of the outlet header and the tubes connecting to it, and their material properties are presented in this chapter.

In the following is a list of the materials of the outlet header, the tubes connecting to it, and the pipe joined to it longitudinally [2, 4]:

- header: X20CrMoV121
- tubes: 10CrMo910
- weld material in the joints between the header and the tubes: not available \Rightarrow the material properties of the weaker of the two considered base materials, i.e. 10CrMo910, were chosen for the weld material
- pipe: X20CrMoV121.

The relevant strength and mechanical properties of the materials X20CrMoV121 and 10CrMo910 are presented in Tables 1 and 2. These data are taken from Finnish standard SFS-EN 10216-2 + A1 [6], German standard DIN 17175 [7], ASM Metals Handbook, Vol. 1 [8] and The T23/T24 Book [9]. However, for the materials in question the strength properties were not available for all considered temperatures. In these cases interpolation or conservative extrapolation was applied.

Table 1. Strength and mechanical properties of steel X20CrMoV121 as a function of temperature.

Material property	Symbol	Unit	Temperature [°C]			
			0	200	400	500
Yield strength	σ_y	MPa	430	430	360	290
Rupture strength	σ_u	MPa	690	690	578	465
Young's modulus	E	GPa	200	184	167	159
Poisson's constant	ν	-	0.300	0.304	0.310	0.315
Density	ρ	kg/m ³	7900	7900	7900	7900
Coefficient of heat expansion	α_T	10 ⁻⁶ /°C	9.9	10.6	11.5	11.6
Thermal conductivity	λ	W/mK	24.9	25.9	27.8	28.7
Specific heat	c	J/kgK	460	460	460	460

Table 2. Strength and mechanical properties of steel 10CrMo910 as a function of temperature.

Material property	Symbol	Unit	Temperature [°C]			
			0	200	400	500
Yield strength	σ_y	MPa	249	234	207	180
Rupture strength	σ_u	MPa	480	451	399	347
Young's modulus	E	GPa	215	198	180	171
Poisson's constant	ν	-	0.288	0.292	0.297	0.302
Density	ρ	kg/m ³	7900	7900	7900	7900
Coefficient of heat expansion	α_T	$\cdot 10^{-6}/^{\circ}\text{C}$	11.5	12.7	13.7	14.1
Thermal conductivity	λ	W/mK	35.0	38.3	36.2	35.0
Specific heat	c	J/kgK	460	460	460	460

2.3 Loads and boundary conditions

The loads considered in the analyses are mechanical and thermal. The considered mechanical load is pressure, and the considered thermal load is temperature, both of which are caused by steam inside the outlet header and the tubes connecting to it. Five transient load cases and one quasi-stationary load case were considered. Besides load case start-up2 the presented data was provided by Foster Wheeler, see references [10, 11].

The considered load cases are:

- transient load cases;
 - start-up: T ; 20°C => 535°C, and p ; 0.1 MPa => 2.6 MPa, duration 2 h and 50 min, occurs 20 times per year
 - shut-down: T ; 535°C => 20°C, and p ; 2.6 MPa => 0.1 MPa, duration 2 h and 50 min, occurs 20 times per year
 - temperature variation during operation: T ; 540°C => 520°C => 540°C, and $p = 2.6$ MPa, duration 13 min, occurs 200 times per year
 - pressure variation during operation: $T = 535^{\circ}\text{C}$, and $p = 2.6$ MPa => 1.0 MPa => 2.6 MPa, duration 1 h and 4 min, occurs 300 times per year
 - modified start-up, denoted as start-up2: T ; 100°C => 535°C, and p ; 0.1 MPa => 2.6 MPa, duration 2 h and 25 min (taken from APROS analyses), occurs 20 times per year
- quasi-stationary load case:
 - operational conditions: $T = 535^{\circ}\text{C}$, and $p = 2.6$ MPa, T and p do not vary.

2.4 Degradation characteristics of the outlet header

Due to relatively high operational temperature, namely 535°C [10], of the outlet header and the tubes connecting to it, creep is a degradation mechanism that affects these components.

Also fatigue has been identified as an at least very potential degradation mechanism that could affect the welds connecting the tubes to the outlet header [12]. However, no cracking degradation data concerning these welds, or other parts of the considered components for that matter, was available.

3. Structural mechanics analyses

The structural behaviour of the outlet header is studied both with a global and a local finite element model. The local model is a more detailed model and it is used in evaluating the integrity of the joints between the header and the small tubes, which are the most critical locations. In this study, only load case start-up2 is analysed with the global model. Its purpose was now only to demonstrate the overall behaviour of the header when the temperature and pressure are raised to the operational conditions and to partly verify the local model results. The models were completely separate, but in the future they can be connected. The local model can be a sub-model to the global model. In this way, the global boundary conditions, loads and effects due to global geometry would be taken into account also in the local model.

3.1 Description of the local analysis model

The geometry of the local model of the outlet header and tubes connecting to it is composed in width of one tube spacing length, i.e. 104 mm, see Chapter 2 for geometry details. The geometry of the tubes connecting to the header is modelled up to the middle of the nearest convection cage wall, which is located in the horizontal direction 1000 mm from the centre of the header.

The boundary conditions of the local model of the header and the tubes are the following. As the local model is taken from the regular part of the considered components, and in such a way that the header is cut vertically from halfway of two adjacent tube spacings, the two header cut surfaces were limited to remain as straight vertical surfaces in the analyses. In addition, the displacements normal to the surface of the other one of these surfaces were limited to zero, and to the other surface was added a tension in magnitude directly proportional to the inner pressure. As for the tubes, the displacements of the cut surfaces normal to the surfaces and in the vertical direction were limited to zero. However, due to the scope of the local model it was not practically possible to take into account the

effects of the six groups of those tubes, which differ from the majority of the tubes, which are regularly spaced and have identical geometries, as well as the effect caused by the pipe, to which the header is longitudinally joined from its other end. On the other hand, these components are located relatively far from a regular header section located e.g. in the middle of a field nearer to the closed end of the header, and thus these effects would most likely be relatively small from the viewpoint of such a section. As for thermal boundary conditions, the outer surfaces in the local model of both the header and the tubes connecting to it were considered as adiabatic, since all these components are thermally insulated.

The element mesh of the local FEM model of the outlet header and the tubes connecting to it is shown in Figs. 4 and 5. The Fig. 4 shows the overall element mesh of the local model, and the Fig. 5 shows a detail and material areas of the joint between the header and the tube that connects vertically to it (the topmost tube). The element meshes of all joints between the header and the tubes are identical.

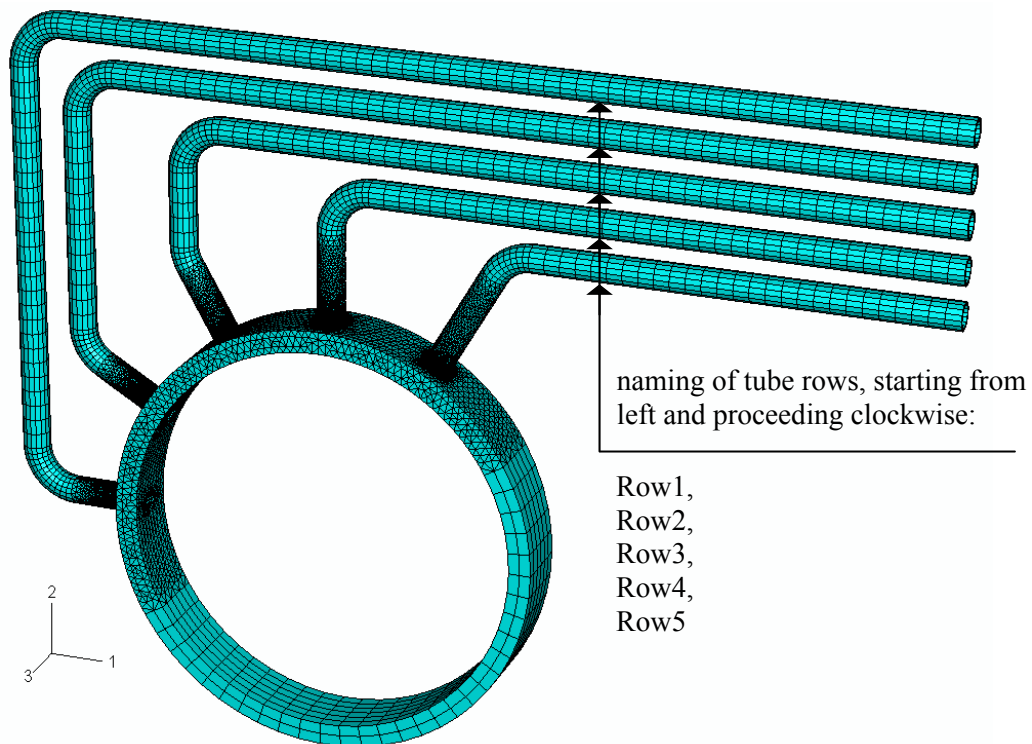


Figure 4. The overall element mesh of the local FEM model of the outlet header and tubes connecting to it, see Ref. [1].

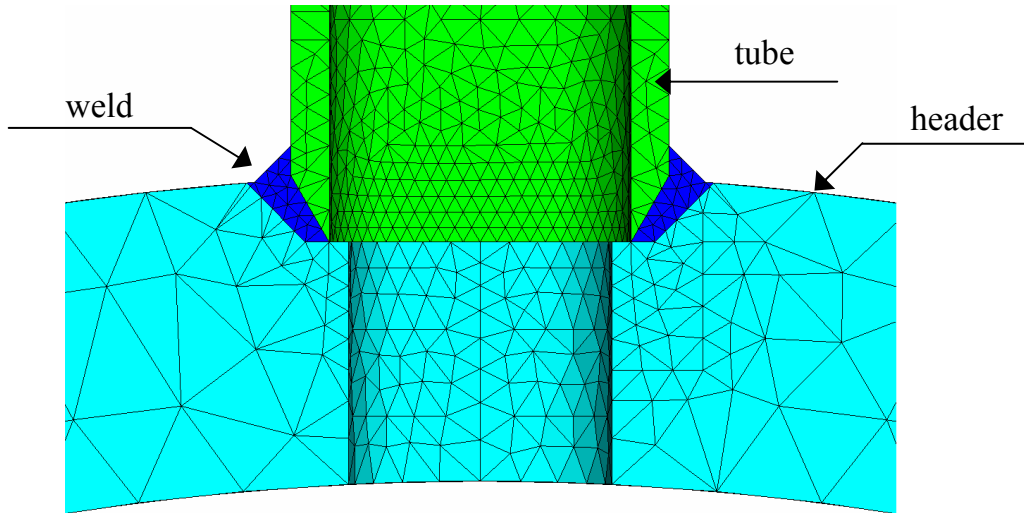


Figure 5. Detail and material areas of the element mesh of the local FEM model. Detail shows the midsection of the joint between the header and tube that connects vertically to it (the topmost tube), see Ref. [1].

The model was meshed with 3D general purpose continuum elements. As the chosen analysis type was sequentially coupled thermal-stress analysis, corresponding heat transfer and stress elements were chosen from the element library of ABAQUS. The types and numbers of used elements are presented in Table 3. More detailed descriptions of the element types in question are presented after that.

Table 3. The types and numbers of elements used in the heat transfer and stress analyses of the outlet header and tubes connecting to it, see Ref. [1].

Analysis type	Element type	No. of elements	Location
Heat transfer analysis	DC3D4	146667	Welds and zones near to them
	DC3D8	5848	Regular parts of header and tubes
	DC3D4, DC3D8	152515	Whole model
Stress analysis	C3D4	146667	Welds and zones near to them
	C3D8R	5848	Regular parts of header and tubes
	C3D4, C3D8R	152515	Whole model

The number of nodes in the FEM model of the header and the tubes connecting to it is 46052.

General descriptions of the used heat transfer analysis elements [13]:

- DC3D4: four node linear tetrahedron element, contains one integration point, not isoparametric, active degree of freedom is temperature, T
- DC3D8: eight node linear hexahedron “brick” element, contains four integration points, isoparametric, active degree of freedom is temperature, T

General descriptions of the used stress analysis elements [13]:

- C3D4: four node linear tetrahedron element, contains one integration point, not isoparametric, active degrees of freedom are axial displacements u_1 , u_2 and u_3
- C3D8R: eight node linear hexahedron “brick” element, reduced integration with hourglass control, contains one integration point, isoparametric, active degrees of freedom are axial displacements u_1 , u_2 and u_3

3.2 Description of the global analysis model

A narrow section of the whole outlet header, in which the joints were modelled very accurately, was considered in a detailed manner in the previous section. The overall global behaviour is studied in this section with a completely separate global finite element model. The joints are not examined but the effect of the small diameter superheater tubes on the large diameter header is studied in a moderately detailed overall manner.

The geometry of the global model of the outlet header and tubes connecting to it includes the whole length of the header. The geometry of the tubes connecting to the header is modelled up to the middle of the nearest convection cage wall, which is located in the horizontal direction 1000 mm from the centre of the header. The geometry of the global model together with the finite element mesh is presented in Figs. 6 and 7. Notice, that the header is modelled with shell elements, which represent only the centre surface of the wall thickness. The tubes are modelled with one-dimensional beam elements which are located to run through the centre lines of the pipe cross-sections.

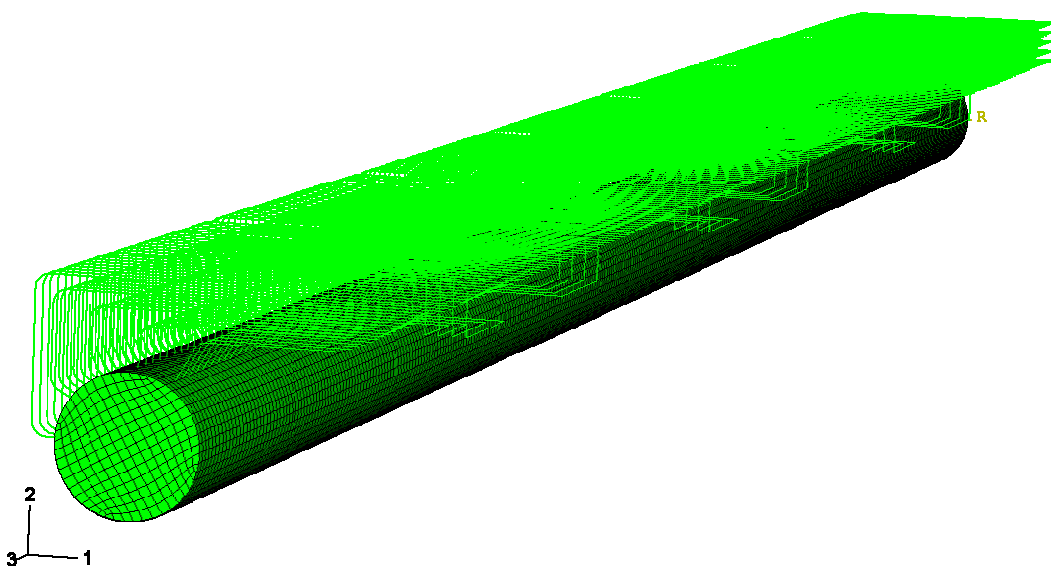


Figure 6. The overall element mesh of the global FE model of the outlet header, see Ref. [1].

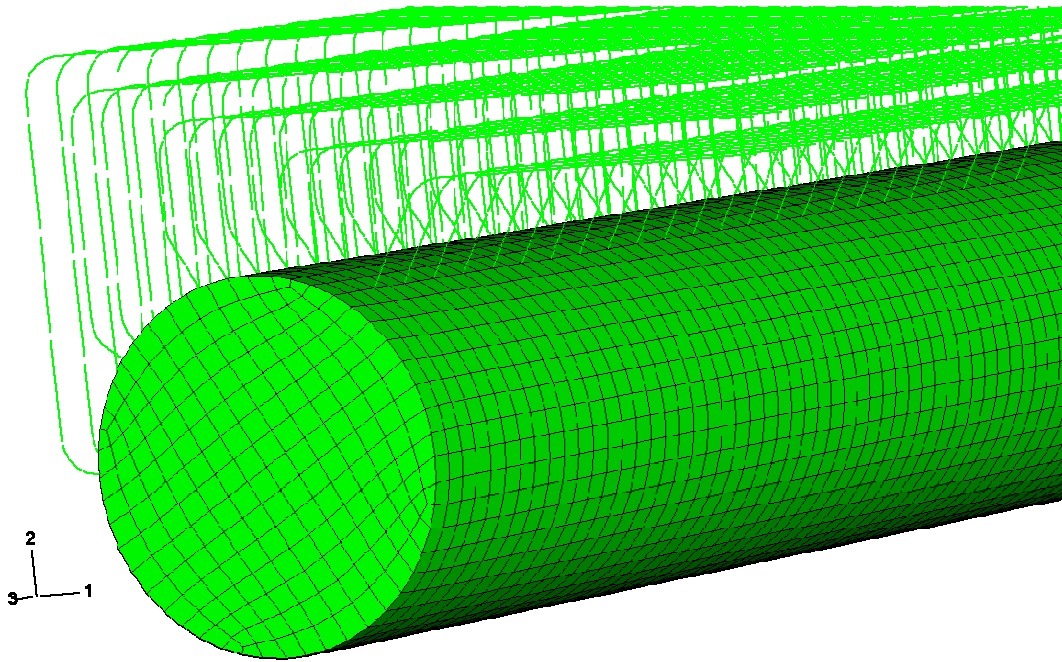


Figure 7. Closer look at the closed end of the global header model, see Ref. [1].

The boundary conditions and loads in the global model of the outlet header and the tubes are the following. The inner pressure is acting on the inner wall of the header. Gravitational force is acting upon the whole structure. The displacements normal to the open head of the header were limited to zero. The open head is not supported in any way in the model, but due to inner pressure a directly proportional tension is added on the cut surface of the open head wall in the axial direction. The other end, denoted as closed head, is not supported. The superheater tubes support the header and they are fixed from their other ends.

As for thermal boundary conditions, the outer surfaces in the global model of both the outlet header and the tubes connecting to it were considered as adiabatic, since all these components are thermally insulated. The inner wall surface was divided into 14 sections, each experiencing a slightly different temperature transient, as taken from the results of the fluid mechanics analyses.

The model was meshed with 4-node shell elements and 2-node beam or link elements. As the chosen analysis type was sequentially coupled thermal-stress analysis, corresponding heat transfer and stress elements were chosen from the element library of ABAQUS. The types and numbers of the used elements are presented in Table 4. More detailed descriptions of the element types in question are presented after that.

Table 4. The types and numbers of elements used in the heat transfer and stress analyses of the outlet header and tubes connecting to it, see Ref. [1].

Analysis type	Element type	No. of elements	Location
Heat transfer analysis	DS4	17615	outlet header
	DC1D2	70122	superheater tubes
	DS4, DC1D2	87737	whole model
Stress analysis	S4R	17615	outlet header
	B31	70122	superheater tubes
	S4R, B31	87737	whole model

The number of nodes in the FEM model of the header and the tubes connecting to it was 87763.

General descriptions of the used heat transfer analysis elements [13]:

- DS4: four-node quadrilateral heat transfer shell element in 3D space, active degree of freedom is temperature, T (number in element type is the same as the number of integration points)
- DC1D2: two-node heat transfer link element in 3D space, active degree of freedom is temperature, T (number in element type is the same as the number of integration points).

General descriptions of the used stress analysis elements [13]:

- S4R: four-node doubly curved general-purpose shell element in 3D space, contains 7 integration points through the thickness of the shell (in this particular analysis), reduced integration with hourglass control and finite membrane strains, active degrees of freedom are axial displacements u_1 , u_2 and u_3 , and rotations ur_1 , ur_2 and ur_3
- B31: 2-node linear beam element in 3D space, active degrees of freedom are axial displacements u_1 , u_2 and u_3 , and rotations ur_1 , ur_2 and ur_3 .

3.3 Results from ABAQUS analyses performed to local model

The heat transfer and stress/strain analyses were performed with ABAQUS as sequentially coupled thermal-stress analyses. Analyses of this type are carried out by performing first a heat transfer analysis, the temperature distribution results from which are saved to a separate file, from which they are read as a part of the input data to a stress analysis, which is performed next.

The considered load cases in the local model analyses were:

- start-up
- shutdown
- temperature variation during operation
- pressure variation during operation
- operational conditions
- modified start-up, denoted as start-up2.

An example of the stress analysis result distributions for the most stressed header/tube joint, namely that concerning Row5 tube, is presented in Fig. 6 below for load case start-up.

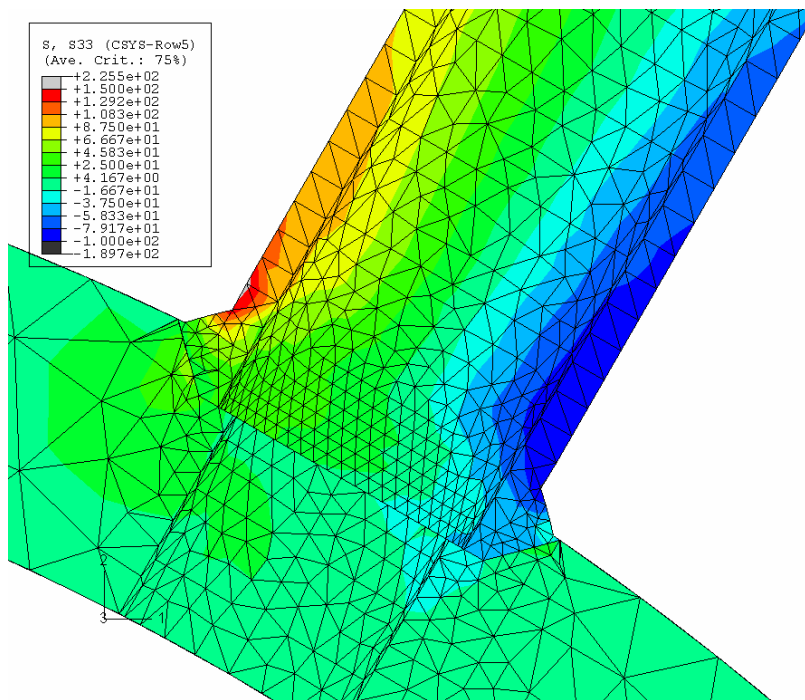


Figure 8. Distribution of axial stresses [MPa] in the Row 5 joint middle section of the local FEM model of the outlet header and the tubes in the middle of load case start-up, see Ref. [1].

Both the maximum stress ranges and absolute tensile stresses act on the welded joints or near them, and of them the highest stresses take place in the Row5 joint. In the following Tables 5 to 8 are presented the maximum stress ranges for the considered load cycles and the maximum tensile stresses, respectively. The stress data in the tables are taken from the results of the local model analyses of the outlet header and tubes connecting to it.

Table 5. For the considered load cycles, the maximum stress ranges in three welds connecting the header and the tubes. The presented stress results were calculated with the local model of the outlet header and tubes connecting to it. The stress results are taken from the integration points of the elements [1].

Load cycle	Joint	Axial stress range [MPa]	Circumf. stress range [MPa]
Start-up + shut-down	Row1	144	393
	Row3	239	381
	Row5	218	384
Pressure variation during operation	Row1	18	29
	Row3	49	50
	Row5	85	77

Table 6. For the load case operational conditions, the maximum quasi-stationary stresses in the header and in the three welds connecting the header and the tubes. The presented stress results were calculated with the local model of the outlet header and tubes connecting to it. The stress results are taken from the integration points of the elements [1].

Component	Location	Axial stress [MPa]	Circumferential stress [MPa]
Header	Near Row5 joint	90	100
Row1 joint	In the weld	6	-54
Row3 joint	In the weld	8	-48
Row5 joint	In the weld	9	-54

Table 7. For the considered load cycles, the maximum stress ranges in three tubes connecting to the header. The presented stress results were calculated with the local model of the outlet header and tubes connecting to it. The stress results are taken from the integration points of the elements. The load case pressure variation during operation was excluded here because the resulting stress ranges concerning it were insignificantly low [1].

Load cycle	Tube	Axial stress range [MPa]	Circumf. stress range [MPa]
Start-up + shut-down	Row1	117	298
	Row3	62	293
	Row5	209	185

Table 8. For the load case operational conditions, the maximum stresses in three tubes connecting to the header. The presented stress results were calculated with the local model of the outlet header and tubes connecting to it. The stress results are taken from the integration points of the elements [1].

Load cycle	Tube	Axial stress range [MPa]	Circumf. stress range [MPa]
Start-up + shut-down	Row1	23	25
	Row3	38	27
	Row5	45	38

3.4 Results from ABAQUS analyses performed to global model

The heat transfer and stress/strain analyses were performed with ABAQUS as sequentially coupled thermal-stress analyses.

Only one load case was considered in the global model:

- modified start-up, denoted as start-up2.

The primary interest in the global ABAQUS analyses was to get a general understanding of the stress state and behaviour of the outlet header and tubes connecting to it. The other interest was to show what kind of analyses can be done in the future.

An example of the stress analysis result distributions in the global model for the considered load case is shown in Fig. 9, in which are shown the axial stress distributions at the inner and outer wall when the steady state has been reached after start-up2.

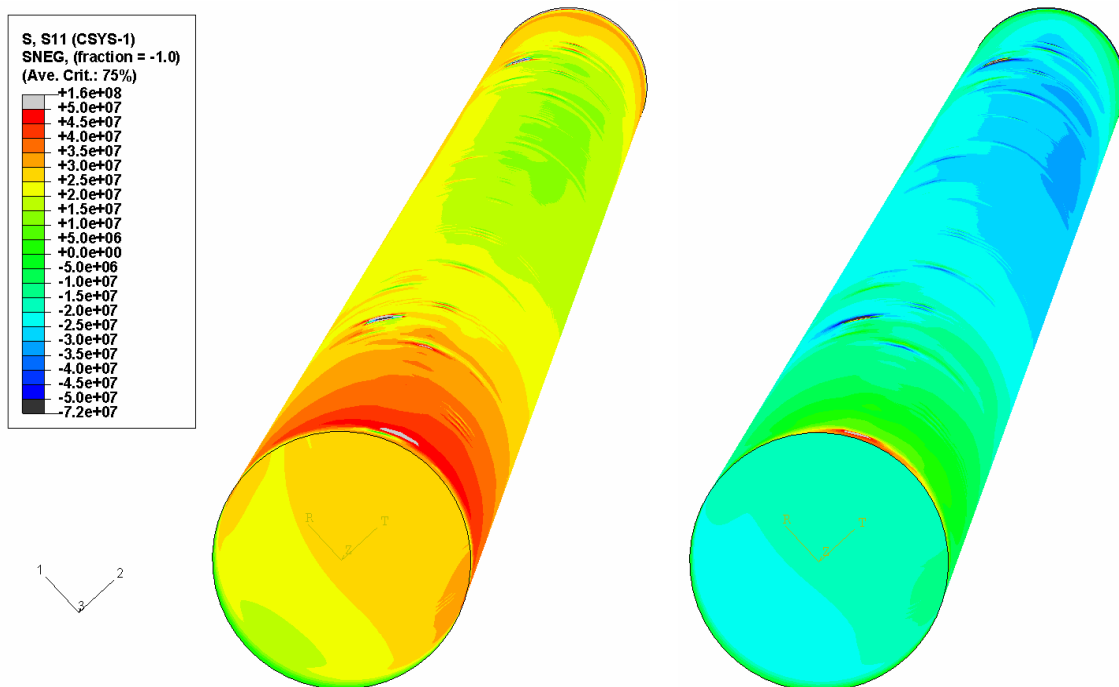


Figure 9. Axial stress distributions at the inner (on the left) and outer (on the right) wall when the steady state has been reached after start-up2. The scale goes from -50 MPa to +50 MPa. The closed end plate is excluded from these results, see Ref. [1].

The stress/strain analysis results taken from integration points showed, that both overall axial and hoop stresses remain relatively low through the duration of load case start-up2, their values varying as -70...+115 MPa for axial stress, and as -120...+180 MPa for circumferential stress, respectively. The temperature rises during start-up2 to some extent slower near the closed end of the header

than near the open end, and both the hoop and axial stresses are to some extent higher near the closed end than near the open end. Due to coarseness of the global model element mesh when considering smaller scale structural details, and especially the joints between the outlet header and tubes, the stress/strain analysis results concerning them are not accurate enough, and were thus omitted.

4. Structural lifetime analyses

This chapter deals with identification and straightforward analysis of the dominant degradation mechanisms of the Turow 3 outlet header and the tubes connecting to it. The degradation analyses concerned mainly the joints connecting the header and the tubes. The possible degradation mechanisms that are deemed to be the dominant ones are: fatigue and creep.

4.1 Description of the lifetime analyses

In order to be able to analyse the lifetime of the outlet header and tubes connecting to it, certain stress distribution data are needed. These were taken from the local model analysis results.

Namely, the fatigue lifetime assessment requires data concerning the maximum stress ranges experienced by the considered components during the considered load cycles. The definition of a load cycle is such that it must end to the same conditions from which it begins. Consequently, here one load cycle is composed of two load cases, whereas the other considered transient load cases form load cycles independently. Here the load case temperature variation during operation is omitted from the fatigue assessment, since the stress ranges caused by it are very low, reaching at maximum 10 MPa. Thus the two load cycles considered in the fatigue assessment here are:

- shut-down associated with start-up
- pressure variation during operation.

On the other hand, the creep lifetime assessment requires data concerning the maximum tensile stresses during those quasi-stationary conditions under which these components are for most of the time, i.e. operational conditions.

Both the maximum stress ranges and absolute tensile stresses act on the welded joints or near them. The highest stress ranges take place in the Row1 weld, and the highest quasi-static stresses near the Row5 weld, respectively. The maximum stress ranges for the considered load cycles and the maximum tensile stresses are presented in Tables 5 to 8.

4.2 Results from the lifetime analyses

In Table 9 below are presented the creep rupture strengths as a function of time in temperature 535°C, the operational temperature, for the analysed header material X20CrMoV121 and tube material 10CrMo910, see reference [6]. Due to lack of material data, the same material properties were assumed for the weld material as for the tube material. The values in the table are interpolated from the respective creep strength values defined in temperatures 530 and 540°C.

Table 9. The creep rupture strengths as a function of time in temperature 535 °C, the operational temperature, for the analysed header material X20CrMoV121 and tube material 10CrMo910 [6]. The values in the table are interpolated from the respective creep strength values defined in temperatures 530 and 540°C.

Material	Creep rupture strength values [MPa]			
	10 000 h	100 000 h	200 000 h	250 000 h
X20CrMoV121	215	157	139	-
10CrMo910	134	88	74	70

As for the welds connecting the header and tubes, since the stresses they experience during the quasi-stationary operational conditions are mainly compressive and the tensile stresses remain very low, it is not necessary to consider their creep induced degradation. The maximum stresses in the header during the quasi-stationary operational conditions are mainly tensile and remain mainly quite low, and creep may potentially to some extent degrade this component in some locations. As the stresses in the tubes during the quasi-stationary operational conditions are mainly compressive and the tensile stresses remain quite low, creep may not potentially degrade them severely.

The maximum tensile stress in the header during the operational conditions is 100 MPa of circumferential stress near the Row5 joint, see Table 6. The time for the header material creep strength to lower to 100 MPa was extrapolated from the respective creep strengths for 100 000 and 200 000 h. Consequently it takes 52 years for the header to reach the end of life due to creep induced degradation, assuming that the yearly time in operation of the header and the tubes is 8000 h.

During the operational conditions the maximum tensile stress in the tubes connecting to the header is 45 MPa of axial stress near the Row5 joint, see Table 8. The time for the header material creep strength to lower to 45 MPa was extrapolated from the respective creep strengths for 200 000 and 250 000 h. Consequently it takes 70 years for the tube in question to reach the end of life due to creep induced degradation, assuming that the yearly time in operation of the header and the tubes is 8000 h.

The applicable $S-N$ curves for the assessment of the fatigue induced degradation of the outlet header and tubes connecting to it are given in reference [14].

The maximum stress range in the header is 393 MPa of circumferential stress near the Row1 joint experienced during the load cycle composed of the combination of start-up and shut-down, according to the results from the local model analyses of the outlet header and tubes connecting to it, see Table 5. In the header the stress ranges caused by the other considered load cycle, pressure variation during operation, are so low that it is not necessary to take them into consideration in the fatigue life assessment. Thus, according to the $S-N$ curves in the reference [14] and keeping in mind that the considered temperature is 535°C, the number of load cycles it takes for the header to reach the end of fatigue life is assessed to be 18 000. As the yearly number of start-ups and shut-downs is 20 each, see Section 2.3, it takes 900 years for the header to reach the end of life due to fatigue induced degradation.

The maximum stress range in the tubes is 298 MPa of circumferential stress near the Row1 joint experienced during the load cycle composed of the combination of start-up and shut-down, according to the results from the local model analyses of the outlet header and tubes connecting to it, see Table 7. In the tubes the stress ranges caused by the other considered load cycle, pressure variation during operation, are so low that it is not necessary to take them into consideration in the fatigue life assessment. Thus, according to the $S-N$ curves in the reference [14] and keeping in mind that the considered temperature is 535°C, the number of load cycles it takes for the tubes to reach the end of fatigue life is assessed to be 100 000. As the yearly number of start-ups and shut-downs is 20 each, see Section 2.3, it takes 5000 years for the tubes to reach the end of life due to fatigue induced degradation.

As mentioned earlier, the combined effect of fatigue and creep was assessed by applying linear interpolation. In case of the header this necessitated the above mentioned extrapolation based assessment of the time when the creep strength has lowered to 100 MPa, the maximum quasi-stationary tensile stress during the operational conditions, which corresponds to reaching the end of life. Likewise, in case of the tubes this necessitated the above mentioned extrapolation based assessment of the time when the creep strength has lowered to 45 MPa, the maximum quasi-stationary tensile stress during the operational conditions, which corresponds to reaching the end of life. Also, it was again assumed that the yearly time in operation of the header and the tubes is 8000 h. The operational life of the outlet header and tubes connecting to it degraded by the combination of fatigue and creep are presented in Tables 10 and 11, as well as in Figs. 10 and 11 below. The time instant zero corresponds to the start of the operation of the power plant where the considered components are located.

According to the results from the assessment of combined effect of fatigue and creep, the minimum, i.e. limiting, lifetime of the outlet header and tubes connecting to it is approximately 49 years. However, due to lack of input data some conservative assumptions were made, and consequently in reality the expected lifetime of these components would be longer. If more input data were available, a more accurate and realistic lifetime analysis could be performed.

Table 10. The operational life of the outlet header degraded by the combination of fatigue and creep [1].

Time [year]	Remaining life [%]
0.00	100.0
9.85	80.0
19.69	60.0
29.54	40.0
39.39	20.0
49.23	0.0

Table 11. The operational life of the tubes connecting to the outlet header degraded by the combination of fatigue and creep [1].

Time [year]	Remaining life [%]
0.00	100.0
13.87	80.0
27.73	60.0
41.60	40.0
55.47	20.0
69.34	0.0

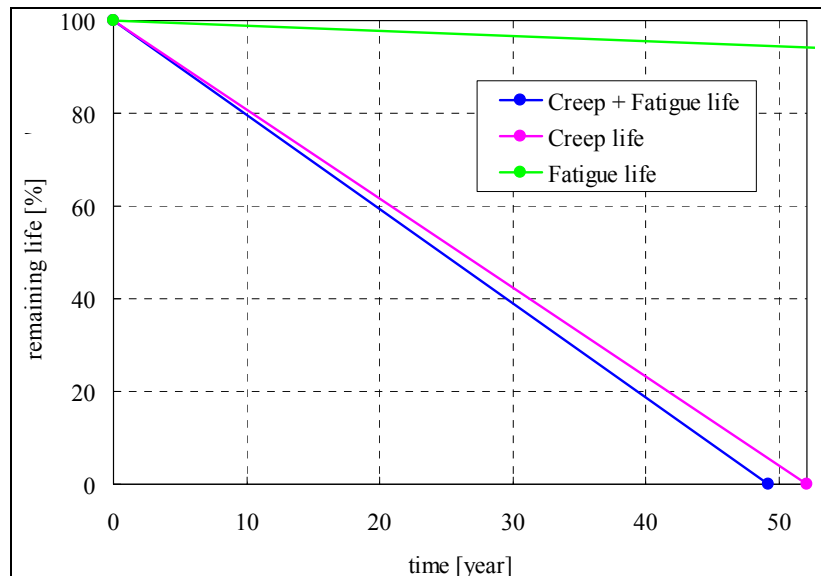


Figure 10. The operational life of the outlet header degraded separately and in combination by creep and fatigue [1].

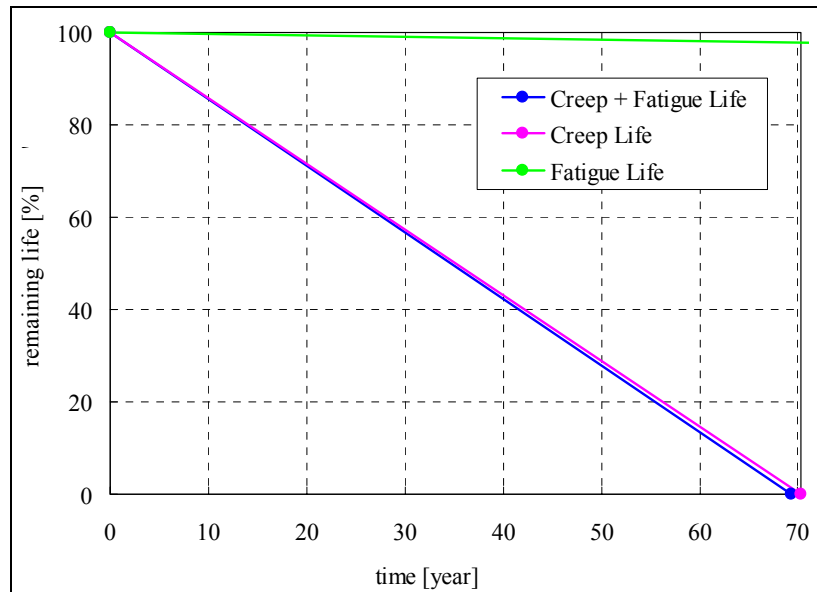


Figure 11. The operational life of the tubes connecting to the outlet header degraded separately and in combination by creep and fatigue [1].

5. Summary and conclusions

The objective of this study was to assess the separate and combined effects of fatigue and creep induced degradation to the lifetime of the header and tubes, situated in Turow 3 power plant in Poland.

Due to the relatively high operational temperature, namely 535°C , of the outlet header and tubes connecting to it, creep is a degradation mechanism that affects the analysed components. Also fatigue has been identified as an at least very potential degradation mechanism that could affect the joint welds connecting the tubes to the outlet header. However, no cracking degradation data concerning these joints, or other parts of the considered components for that matter, was available.

The fluid mechanics analyses were performed with analysis code APROS, which has been developed at VTT. The analysis results include the temperature distributions at the inner and outer surfaces of both the whole header and the tubes connecting to it. A part of these results were also used as input data in some of the structural mechanics analyses.

The stress/strain analyses were performed with FEM code ABAQUS. Two FEA models were prepared: the local model and the global model. Due to limited resources it was beyond the scope of this study to perform such transient FEM analyses that would have included several load cycles, i.e. load histories composed of all analysed load cases assembled in a realistic order. Thus it was

not analysed how the stress distributions lower/even out in the course of a longer time. Consequently the obtained stress distributions are to some extent conservative.

The fatigue and creep induced degradation was assessed by comparing the stress distributions from the ABAQUS analysis results to the respective strength values found from applicable standards and norms. In case of fatigue assessment these were the $S-N$ curves. The main locations of interest in the structural and degradation analyses were the joints connecting the tubes to the header. They are the locations most sensitive to degradation, due to e.g. the different shapes, wall thicknesses and materials of the header, tubes, and welds.

As the stresses in the welds during the quasi-stationary operational conditions are mainly compressive and the tensile stresses remain very low it was not necessary to consider their creep induced degradation. However, the stresses in the header and tubes are mostly tensile during the operational conditions, though they also mainly remain relatively low, and thus the creep induced degradation of these components was assessed. The assessed decrease rate of life due to creep induced degradation is 1.920% per year for the header, and 1.422% per year for the tubes, respectively. If creep data concerning the analysed components and their materials had been available, it would have been possible to perform an accurate creep analysis with ABAQUS, instead of the simple strength based assessment applied here.

For fatigue analyses, the maximum stress ranges were needed. These were taken from the results from the local model ABAQUS analyses of the outlet header and tubes connecting to it. According to the $S-N$ curves based assessment, the number of load cycles it takes to reach the end of fatigue life is 18 000 for the header, and 100 000 for the tubes, respectively. As the yearly number of start-ups and shut-downs is 20 each, it takes 900 years for the header and 5000 years for the tubes to reach the end of life due to fatigue induced degradation. Thus the assessed maximum decrease rate of life due to fatigue induced degradation is only 0.111% per year. Had fatigue induced cracking data concerning the analysed components been available, it would have been possible to perform an accurate fracture mechanics based degradation analysis, instead of the simple strength based assessment applied here. For instance with ABAQUS it is possible to perform three dimensional time dependent crack growth analyses.

The assessed decrease rate of life due to combined fatigue and creep induced degradation is 2.031% per year for the header, and 1.442% per year for the tubes, respectively.

The assessment of the combined effect of fatigue and creep is a quite complicated issue, involving open and unsolved characteristics. A commonly used straightforward linear interpolation was applied in this study. However, it is

not certain if this approach is even conservative in all conditions. So the combined effect of fatigue and creep, among other related degradation problems, should be researched further. In addition to scientific interests, this issue holds also considerable economical potential, as it is these time dependent degradation mechanisms that most severely limit the operational lifetime of headers and tubes connecting to them. However, due to lack of input data some conservative assumptions were made, and consequently the expected lifetime of these components would be longer. If more input data were available, a more accurate lifetime analysis could be performed.

Acknowledgements

This article is part of the VTT research project KOKOMO. The project was funded by VTT, which is gratefully acknowledged. The authors of the article are also grateful to Mr. Pentti Lankinen and Mr. Juha Hakkila from Foster Wheeler for the input data on the case study and for most pleasant co-operation.

References

1. Calonius, K., Cronvall, O., Junninen, P., Salonen, J., Tiihonen, O. Structural and fluid mechanics based life assessment of an outlet header. Technical Research Centre of Finland (VTT), Research Report VTT-R-02389-07. 126 p. + app. 31 p.
2. Design Drawing 57918103 - 003 - 0 - 1, Reheater II – Assembly Boiler 3 – Foster Wheeler Pyropower Inc., 1997.
3. Design Drawing 57918103 - 004 - 0 - 1, Reheater II – Assembly Boiler 3 – Plan View. Foster Wheeler Pyropower Inc., 1997.
4. Design Drawing 57918703 - 004 - 0 - 2, Reheater II – Outlet Header – Boiler 3. Foster Wheeler Pyropower Inc., 1997.
5. Design Drawing 57913403 - 001 - 0 - 2, Convection Cage Front Wall. Foster Wheeler Pyropower Inc., 1997.
6. Standardi (Standard) SFS-EN 10216-2 + A1, Saumattomat painelaite-teräsputket. Tekniset toimitusehdot. Osa 2: Kuumalujat seostamattomat ja seostetut teräsputket (Seamless steel tubes for pressure purposes. Technical delivery conditions. Part 2: Non-alloy and alloy steel tubes with specified elevated temperature properties). Suomen Standardisoimisliitto SFS (Finnish Standards Association), 16.8.2004. 1 + 78 p.

7. Standard DIN 17175, Nahtlose Rohre aus warmfesten Stählen; technische Lieferbedingungen (Seamless steel tubes for elevated temperatures; technical terms of delivery. 23 p.
8. Metals Handbook, Volume 1, Tenth Edition, Properties and Selection: Irons, Steels, and High-Performance Alloys. The Materials Information Society, ASM International. 1990. 1063 p.
9. The T23/T24 Book, New Grades for Waterwalls and Superheaters, 2nd Edition. Arndt, J. et al. Vallourec & Mannesmann Tubes. October 2000. 50 p.
10. Email from Foster Wheeler representative Pentti Lankinen, 3.10.2005.
11. Email from Foster Wheeler representative Pentti Lankinen, 27.10.2005.
12. Email from Foster Wheeler representative Pentti Lankinen, 26.5.2005.
13. ABAQUS/Standard User's manual, Version 6.4. ABAQUS Inc., 2002. Pawtucket, Rhode Island, U.S.A.
14. Technische Regeln für Dampfkessel, Taschenbuch-Ausgabe. Heymanns Beuth, 1997.

Remaining life assessment of steam turbine boilers

Václav Mentl and Václav Liska

SKODA Research Ltd., Pilsen, Czech republic

Abstract

Several steam turbine boilers were inspected according to the customer's demand to evaluate the remaining lifetime of the boilers that were operated more than 160 000 and 200 000 hours respectively. The evaluation was based on an extensive NDT inspection and the measurement of mechanical properties (including creep test data) of high temperature components. Making use of the Larson-Miller parameter in comparison with replica testing made it possible to evaluate quantitatively the lifetime exhaustion, make an assessment of the remaining lifetime and to offer recommendation as far as the future inspection intervals of the boilers are concerned.

1. Introduction

The paper summarizes the results of non-destructive (NDT) and destructive (mechanical) tests and the residual lifetime assessment of four Steam Turbine Boilers. On the basis of performed examination, the results provided customer the recommendations relating future safe and reliable operation of the boilers.

In comparison with the more sophisticated and much more expensive methods that use numbers of variables that enter the evaluation process of the lifetime exhaustion, or the metallographic non-destructive or even destructive methods that do not result often in a quantitative lifetime assessment, a relatively simple assessment method was used to evaluate the remaining lifetime of the high temperature components.

Four Power Plant Boiler Units were constructed in 1976–1980 and operated as base load units. Sections of 27 tube samples were removed from the superheater tube banks (made of SA-213 T11 and SA-213 T22 steels) for the purposes of mechanical testing and metallographic examination at Skoda and the subsequent integrity and reliability assessment. The operational hours of the respective boilers at the time of the inspection were as follows:

<u>Unit No.</u>	<u>Service hours</u>
1	171 231
2	171 886
3	166 686
4	160 547

According to the detailed scope of work, the following tests were requested by the customer and carried out at the Accredited Testing Labs of the Skoda Research Ltd., Pilsen, Czech republic in the case of the respective boilers:

A. Laboratory tests and metallographic analyses

- 1) Visual examination
- 2) Dimensional measurement
- 3) Magnetic particle inspection of the tube surface
- 4) Parent material hardness measurement and tensile test
- 5) Metallographic examination of tube materials
- 6) Chemical analyses of parent materials
- 7) Chemical analyses of scale deposits (Internal and external)
- 8) Thickness of scale deposits measurement
- 9) Density of scale deposit
- 10) Estimation of tube working temperature
- 11) To provide life assessment summary.

B. Creep tests

Short-term creep to rupture tests of selected tubes were carried out to make it possible to perform a quantitative assessment of the superheater tubes remaining lifetime.

2. Inspection

The following conclusions were summarised after acc. to the Part A:

- Neither significant reductions of the wall thickness nor discrepancies of the dimensions of the delivered tubes were found.
- No indications were found on the tube surfaces during the non-destructive magnetic particle test.
- Yield point values of many tested tubes were below the specification limit. Corresponding decrease of HB hardness were found.
- The ultimate strength values of the samples met the standard with the exception of one sample.
- The ductility of several tube samples was slightly below the limit.

- Several tubes revealed indications of larger microstructural changes. Their conditions could be assessed by a degree from III to V according to the “Classification of the microstructure condition”.
- The chemical composition met the specifications with one exception of the contents of silicon, manganese and a lower carbon content of one of the samples.
- The thickness of inner deposit scales were measured and used for the estimation of metal tube temperatures, as the first step in the assessment of the tube remaining life. The thickness of deposits varied from 0.03 mm to 0.4 mm (samples 2 and 3, Unit 1).

Accelerated creep tests were carried out for the creep samples machined of the respective tubes. The conditions of creep testing (stresses and temperature) were chosen in order that the resulting times to rupture were reached within the relatively short time to be able to evaluate the results in time according to the requirement of the customer.

The creep test results are included in the overall diagram in Fig. 1, the results separately for the individual boilers are shown in Fig. 2. The differences are well visible among the individual boilers and thus the creep results are given separately for the individual boilers in Figs. 3–6.

3. Remaining lifetime assessment

On the basis of creep data, the remaining lifetime hours, see Table 2, were calculated for three following „safety“ situations:

1. „ZERO SAFETY“ (neither recommended $k = 1,5$ safety coefficient for working stress nor $+70$ deg Celsius increase of working temperature were taken into consideration).
2. „STRESS SAFETY“ (1,5 safety coefficient for working stress and working temperature were taken into consideration).
3. „FULL SAFETY“ (1,5 safety coefficient for working stress and working temperature $+70$ deg Celsius were taken into consideration).

For the purposes of this evaluation, the regression lines were constructed through the experimental points, the resulting equations are given within the individual diagramms. These equations were then used to calculate the respective values of the Larson-Miller Parameters for the three abovementioned „safety“ situations what resulted in the remaining working hours given in the Table 2.

Table 1. Accelerated Creep Test Results.

Unit No.	Sample No.	Test temperature [°C]	Stress [MPa]	Time to rupture [hours]	Larson Miller Parameter
1	2	580	120	91	18731
	2a	580	90	486	19351
2	10	580	120	23,5	18229
	11	580	140	2,5	17399
	10a	580	90	246	19099
	11a	580	85	335	19213
3	18	580	120	76	18664
	19	580	140	6	17723
	18a	580	90	468	19337
	19a	580	80	2227	19915
4	23	580	120	27	18280
	23a	580	90	804	19538

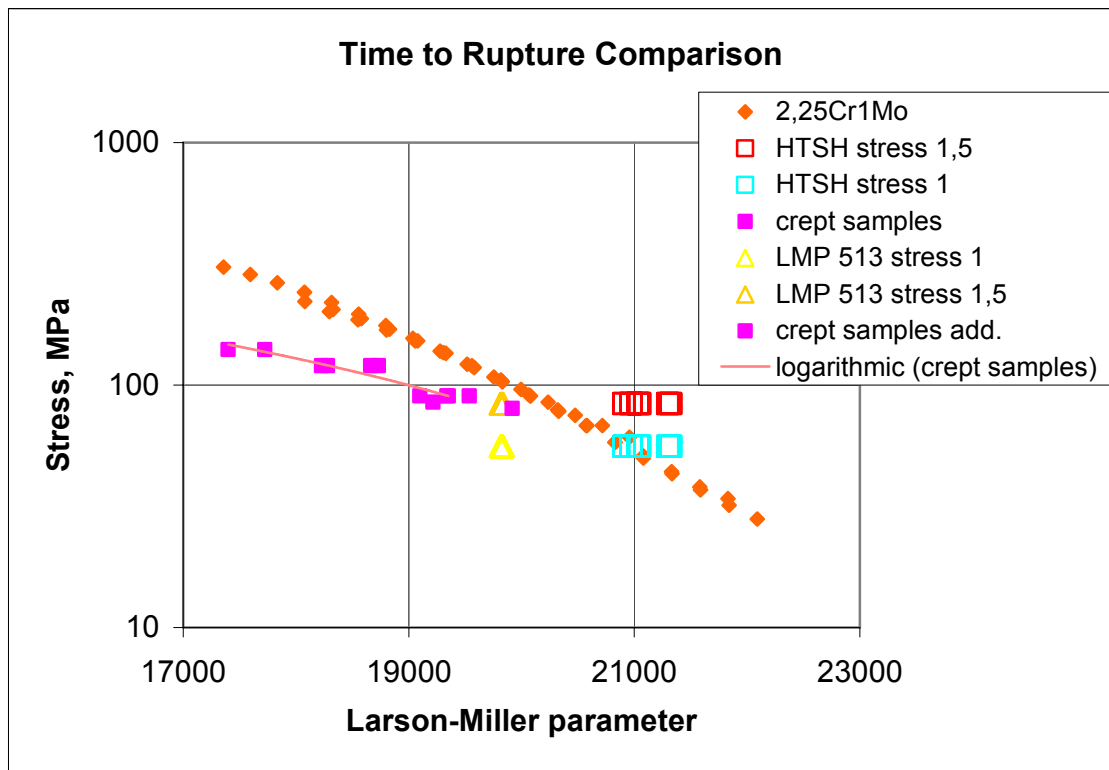


Figure 1. Detailed view of the T22 steel used in HTSHs. All additional creep results are included.

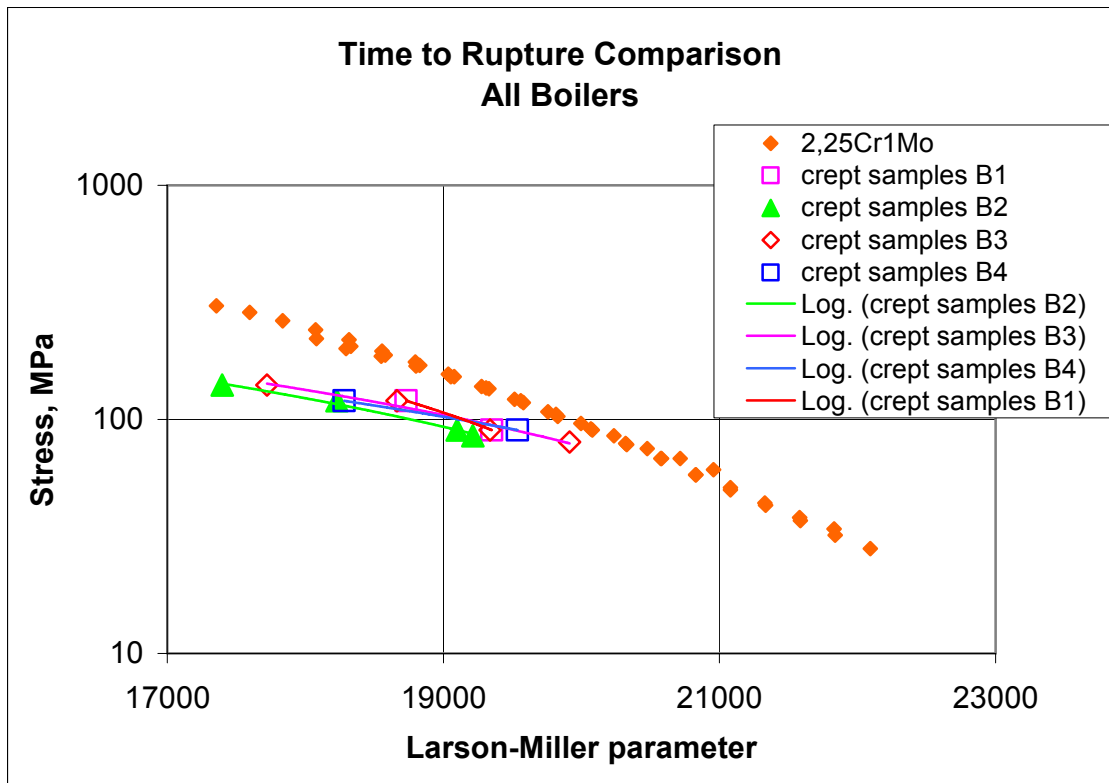


Figure 2. Summary of the creep results.

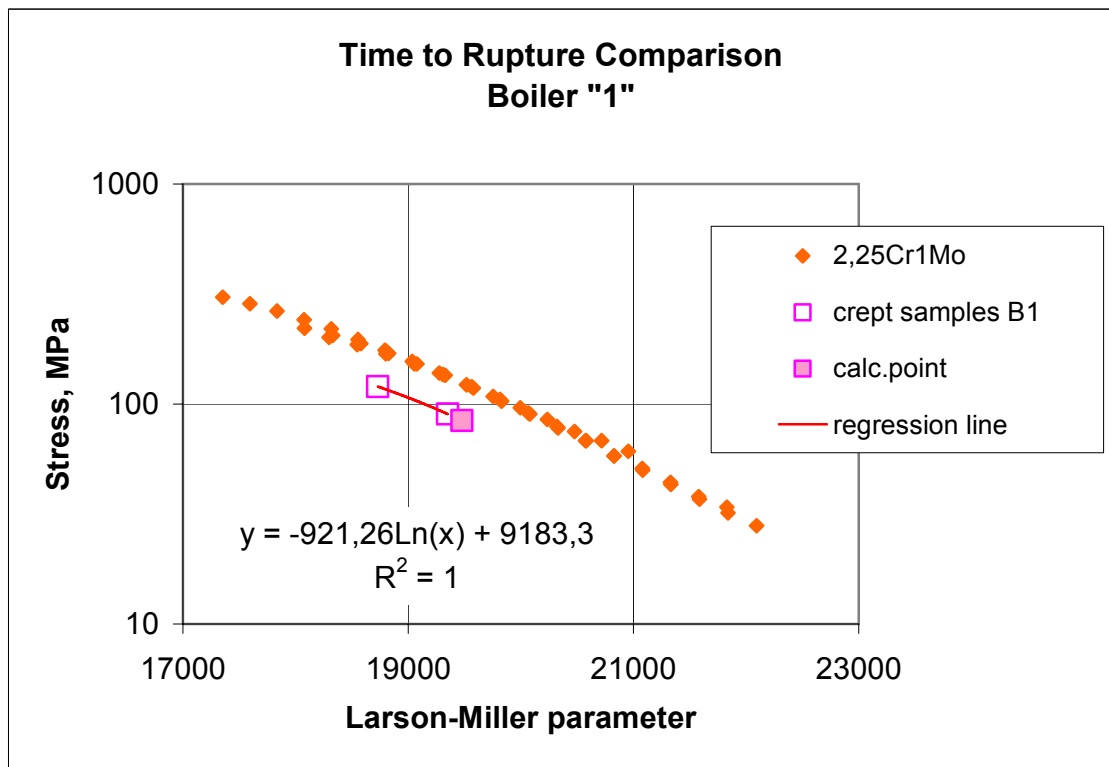


Figure 3. Creep data for the Boiler No. 1.

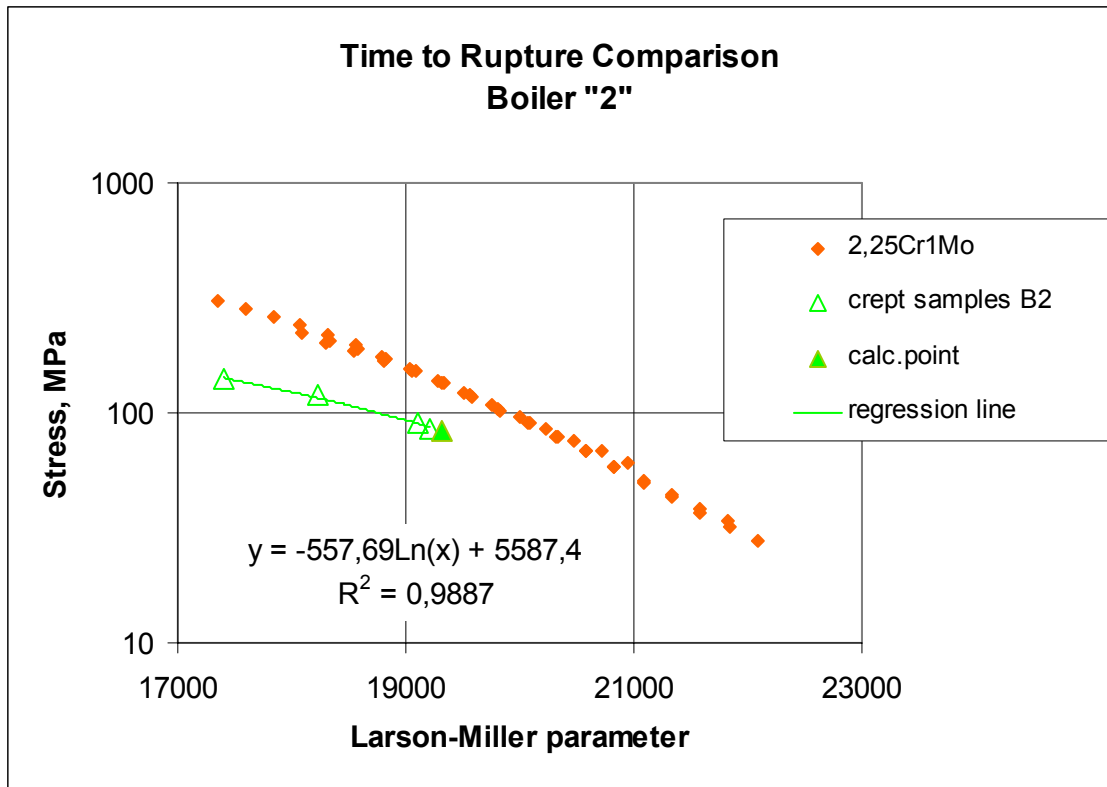


Figure 4. Creep data for the Boiler No. 2.

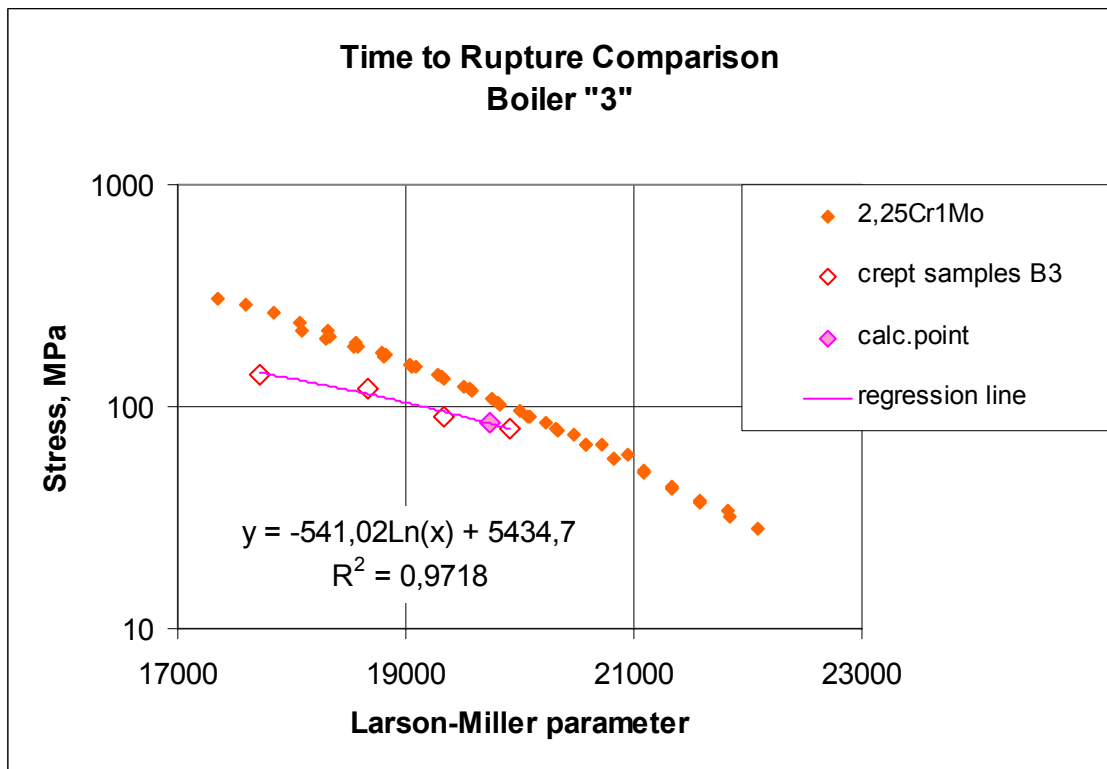


Figure 5. Creep data for the Boiler No. 3.

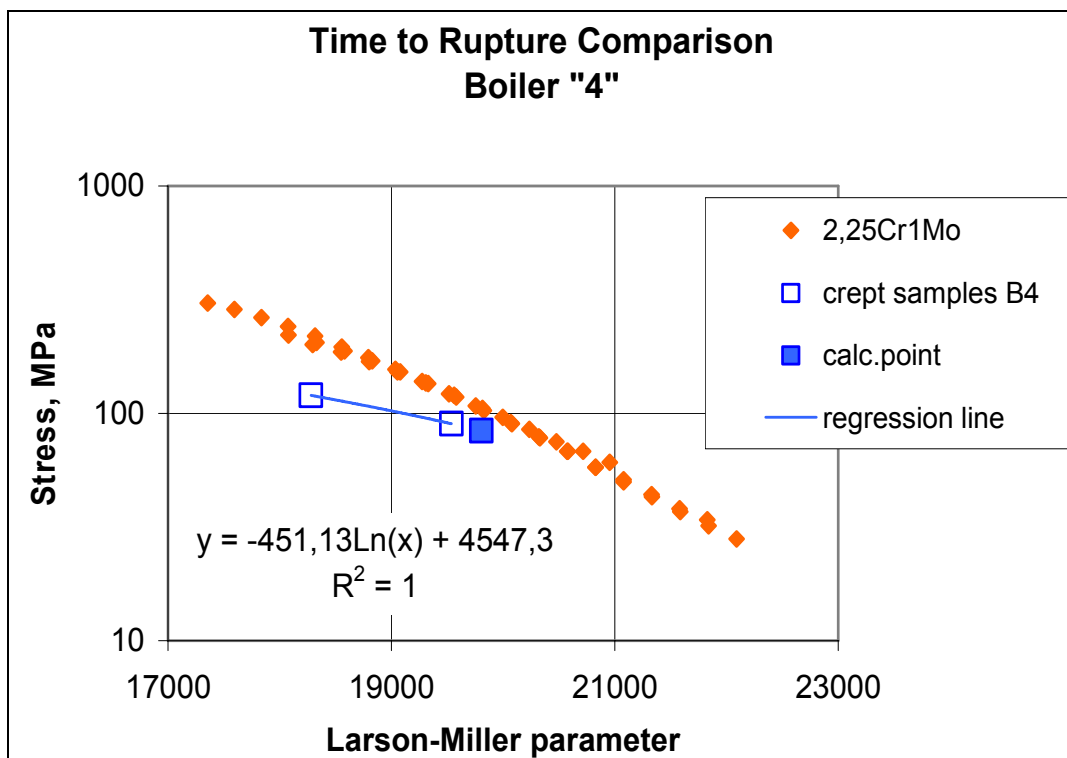


Figure 6. Creep data for the Boiler No. 4.

Table 2. Remaining lifetime determined on the basis of the accelerated creep-to-rupture data.

Boiler No.	Remaining lifetime (hours)		
	„ZERO SAFETY“	„STRESS SAFETY“	„FULL SAFETY“
1	5798	1129	19
2	11 399	757	13
3	83 342	4618	68
4	214 650	6415	91

4. Conclusions

Taking into consideration the full operational safety of the boilers, the abovementioned item No. 3 „Full safety“, the remaining lifetimes of the tubes tested, and the high temperature superheater components in question respectively, are unacceptably short and the components should be replaced immediately, or without delay as soon as possible.

The boilers thus can be further operated with reduced safety only. In such a case, if necessary, the urgent care should be taken as far as the working conditions (the steam pressure and working temperature) are concerned.

Typical failures of reheater coils

Ewa Zbroińska-Szczechura, Jerzy Dobosiewicz and Filip Klepacki

Pro Novum, Katowice, Poland

Abstract

The size of reheater steam coils especially their wall thickness are not determined on basis of pressure induced stresses. Their nominal wall thicknesses are as a rule at least twice as high as those sized on the basis of material effort only. Such a practice depends on numerous manufacturing and technological aspects and in particular on those connected with field welding of thin walled tubes (W.T. = 2 mm) and providing their rigidity. Despite of their excessive thickness the life of the coils is drastically limited by extremely hard service conditions whereby the wall thickness is reduced due to inner and outer corrosion, erosion, overheating, etc. This paper contains the photos, descriptions and causes of the occurrence of typical cases of damage to reheater coils operated in pulverized coal and fluidized bed boilers with biomass-coal co-combustion.

1. Introduction

Almost 90% reheater steam coils of boilers are damaged because of excessive corrosive wall tube thickness loss from outside and inside.

Design wall tube thickness of reheater steam doesn't exceed $g < 2,5$ mm because of low steam pressure, but in reality nominal wall thickness exceed $g > 4$ mm.

This situation is due to following features:

- technological:
 - ◆ difficult welding of thin-walled tubes
 - ◆ impossibility define technical state of welds by radiographic and ultrasonic examinations
- durable:
 - ◆ Low bending stress limit of thin-walled tubes (particularly horizontal sections) deriving from deadweight.

Though their excessive thickness, majority reheater coils damages are caused by wall tube thickness loss. Tube leakages are occurred when the thickness is lower than 1 mm ($g < 1$ mm). This situation is caused by temporary operating tube metal

in excessive temperatures which exceed design and allowable even values and flue gas aggressiveness.

Majority reheater leakages are caused by this kind of damages because stresses is increasing by significant wall tube thickness loss what leads to excess metal tensile strength without creep signs (diameter deformation, creep cavities). Damaged reheater coils on external and internal surfaces are very often covered by thick oxides layer. Excessive oxidation process occur when temperature of the coil exceed value defined for each alloy (Table 1) in this case the oxides layer are porous and cracked. Cracks and local losses of the oxides layer are caused by thermal stresses. This process occur as long as thin wall tube thickness can't resist increasing stresses and it burst.

Table 1.

Material	Temperature	
	Limit point	Allowable point
Carbon steel	400°C	<520°C
15Mo3	470°C	<530°C
13CrMo44	480°C	<560°C
10CrMo910	470°C	<590°C
14MoV63	500°C	<560°C
X20CrMoV121	480°C	<600°C

In case damages caused by flow limitation, diameter deformation and structural changes are found until creep cavities occurred.

The reheater reliability to a large extent depend from the reheater coil surface oxidation level because, how was mentioned before, excessive oxidation; firstly cause considerably wall tube thickness loss what due to stress increase, secondly oxide layer has tendency to segregation from metal surface causing choke bends of heating surface elements and excessive turbine lades wear. It must to be take into account that oxides isolating properties make worse heat exchange what causing increase wall tube thickness temperature. Above 560–600°C perlit steels are exposed on rapid oxidation.

Comparing intensity of oxidation process and structure changes are seen that oxidation had predominant influence on the reheater coils operating life.

The steam reheater are localized above furnace bridge and in second draught of boiler therefore heat exchange are occurred on convection way. This localization has essential influence on the tube metal operating conditions which depends very highly from boiler operation characteristic, furnace type and fuel burning. The reheater tubes of boilers with low NO_x emission furnace are mostly damaged.

1.1. Operation influence

Boilers with low NO_x emission furnace have tendency to decreasing heat exchange intensity in superheater and reheater area. In Boilers with reheaters, furnace modernization leads to decrease outlet reheated steam temperature and operating metal tube temperature under reducing atmosphere contains, to the tube metal, aggressive elements e.g. H₂S, CO and free C which accelerate formation corrosive losses on external surface. Furthermore external surfaces are covered thick slag layer under which intensive corrosion process are occurred. Although the metal tube temperature in boilers with low NO_x furnace are decreased real operating conditions favour corrosive devastation of the coils metal.

In Boilers which operate under low and changeable load, flow rate steam in superheater and reheater is very low what decrease heat exchange causing temporary increase tube metal temperature. It is due to by thermal inertia, flue gas temperature during some time are stayed high.

During low loads for hold NO_x emission in allowable limits boiler should operate only with the highest burners on but it cause flue gas temperature increase in the reheater area what is due to by raised core flame. Furthermore reburning unburned carbon elements and CO on the coils surface is occurred very often.

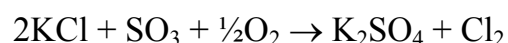
During Biomass combusting flue gas contains a lot of alkaline compounds in ash and chloride what cause reheater and superheater corrosion and aggressive deposits accumulation. Main elements of biomass combusting ashes are SiO₂, CaO and K₂O. Furthermore ashes from biomass combusting are characterized lower pour point (750–1000°C), therefore velocity of deposits accumulation on heated surfaces are increased. The ashes with low pour point have higher tendency to glue to metal surface what is due to by ash chemical composition. In Boilers with low NO_x furnace are occurred similar situation where in reducing atmosphere ash contains ferrite in oxide form FeO which pour point is lower than Fe₃O₄.

1.2. Reasons tube thickness loss

Form of devastating process is responded few corrosion types.

1.2.1. From flue gas side

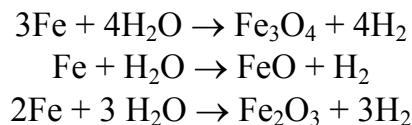
High-temperature corrosion occur in oxygen presence, it can increase under influence of free chlorine. Free chlorine arise from sodium or potassium chloride in oxidizing atmosphere and in ferrite oxides, sulfates, silicates presence which ash contain. Release of free chlorine from potassium chloride shows following reaction:



Reaction described above shows forming of low pour point mixture which can create eutectic with the ferrite oxides. Important is that during combustion Na and K chlorides sublimating and under vapour form are connecting with flue gas. Alloys in high temperature are stainless because of protective layer (magnetite) are covered. The magnetite is crystalline binding of two ferrite oxides FeO and Fe₂O₃ what creates stable compound Fe₃O₄ called magnetite. From chemical point of view it is spinel which in temperature above 560°C decomposes on two oxides (FeO and Fe₂O₃). If some part of Fe₂O₃ in magnetite are substituted by chromium oxides Cr₂O₃ then high-temperature resistance of the magnetite will increase, e.g. alloy contains about 10%Cr. The magnetite (spinel) is decomposing at 610°C decreasing heat resistant of alloy. Free chlorine presence in flue gas increase high-temperature corrosion process. In temperatures which exceeded allowable values the magnetite is decomposing, other oxides don't have heat resistance properties. Similar situation occur in reducing atmosphere.

1.2.2. From steam side

Typically example of chemical corrosion is steam decomposition. On this type of corrosion are exposed the superheater and reheater coils which operate in temperature above than 400°C. Among steam and ferrite occur following reactions:



The magnetite create up to 570°C. Above this temperature are created ferrite oxide. However oxide Fe₂O₃ in steam conditions is unstable.

Created oxides layer on internal surface is growing with time and temperature increase at the expense of wall tube thickness loss. Ferrite oxides are bad heat conductor what causing metal tube temperature increase.

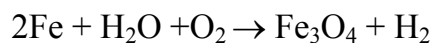
Operating life and chemical properties this layer are similar to layer on external surface.

Remark: *Either of corrosion type (from inside and outside) are chemical process and the wall tube thickness losses are regular which intensity is higher on half circumference directly expose on flue gas. Chlorides which are contained in flue gas very often condensing on the tube metal surface creating local deposits which react with oxides as result of eutectic created. Specific feature of eutectic is great ability to oxides dissolving. In this manner, in chloride segregation places are created significant irregular the wall tube metal losses in deep crater and gouge form.*

1.2.3. Oxygen corrosion

Pitting is caused by oxygen corrosion which occur during shut down of boiler. This type of corrosion mostly occur on not drained heat surfaces like reheater coils.

After boiler shut down the lowest parts of coils are filled condenser with removed from internal surface salts. In horizontal parts are condensing drops of water on top half circumference. The droplets are stayed with close contact with oxygen saturated air. If the droplet condenses on surface without protective oxides layer, metal dissolving will be occur according to following reaction:



Mostly of the protective layer leaks are occurring during boiler cooling. Cracks in the protective layer are creating anode spaces where bare metal is attacking by moisture contains oxygen. In this manner are creating deep and spherical shape local wall tube metal losses. This kind of the wall tube metal losses are difficult to detect what is caused by small dimension and local arrangement.

2. Failure character and appearance

Below are described failure examples of the reheater coils operating in various operating conditions (pulverized – coal fired boiler, pulverized – coal fired boiler with low NO_x burners, fluidized bed boilers).

Pulverized – coal boiler – low NO_x furnace

After 120 000 h operating time was occurred reheater coil failure what was caused by wall tube thickness loss in high-temperature corrosion process (Fig. 1). Wall tube thickness loss are occurred from both side – outside, inside (Fig. 2). Apart leaky tube, neighboring sheets had similar wall tube thickness losses from the gas flow side.

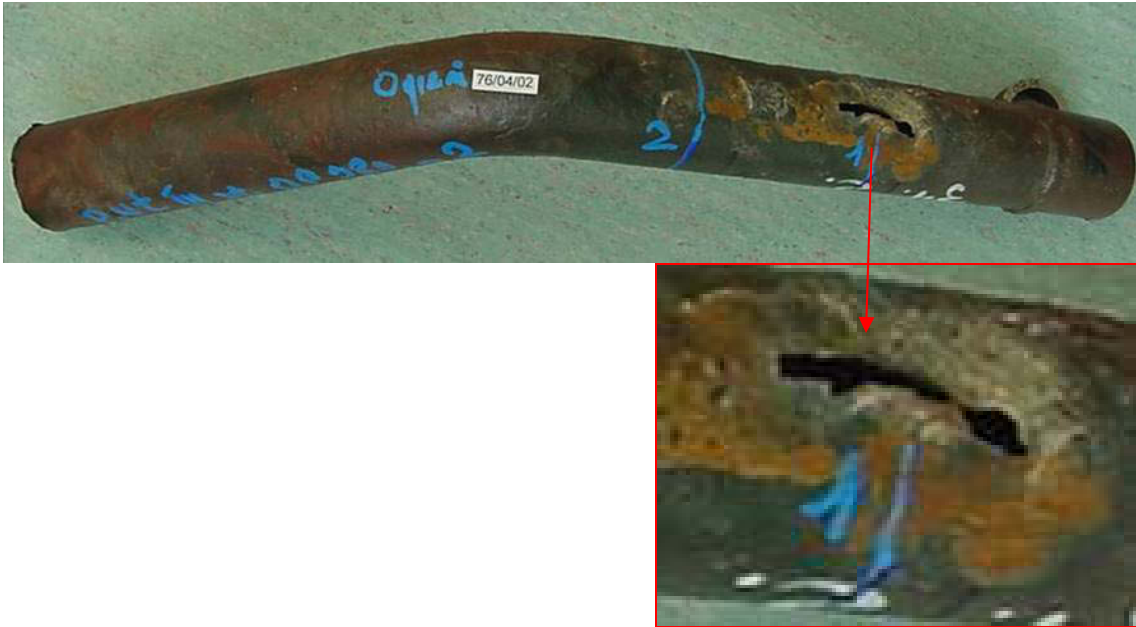


Figure 1. Leakages from the gas flow side.

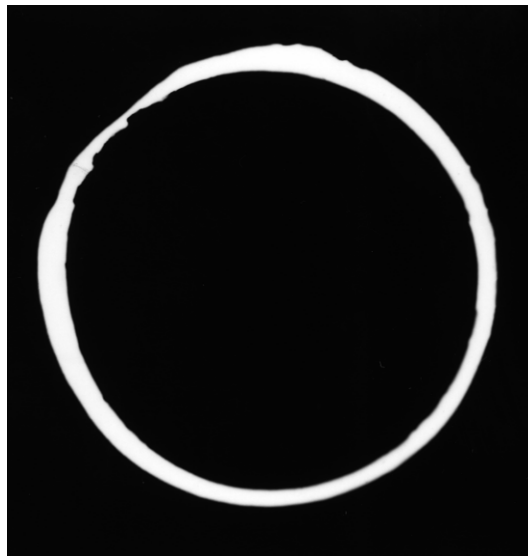


Figure 2. Ring ~ 150 mm from leakages.

The reheater coils design data:

- | | |
|-----------------------------------|-------------------------------|
| – dimensions | ϕ 51 x 4 mm |
| – material | 10CrMo910 |
| – design pressure | $p_o = 3,1$ MPa |
| – design temperature | $t_o = 575^\circ\text{C}$ |
| – allowable temperature | $t_{dop} = 580^\circ\text{C}$ |
| – operating wall tube temperature | $t_{sr} = 595^\circ\text{C}$ |

- diameter deformation near to failure $\varepsilon = 4\%$ at wall tube thickness
 $g \cong 0,8 \text{ mm}$
- stress at 51 x 4 mm dimensions $\sigma_r = 18,2 \text{ MPa}$
- allowable stresses for

100 000 h	$\sigma_{\text{dop}} = 36 \text{ MPa}$
200 000 h	$\sigma_{\text{dop}} = 29,6 \text{ MPa}$
- according to OCT should be fulfilled following condition $\sigma_{\text{dop}}/\sigma_r > 1,2$

$\frac{36}{18,2} = 1,99$	calculated at 100 000 h
$\frac{29,6}{18,2} = 1,6$	calculated at 200 000 h.

Design data are fulfilling requirements of reliability; but in reality they aren't fulfilled; the coil was failed because of allowable stresses are exceed by the wall tube thickness loss.

Pulverized – coal fired boiler – low NO_x furnace

After 85 000 h operation time was failed reheater coil from the gas flow side on outlet section of reheater. Failure was caused by wall tube thickness lost from both side – inside and outside (Fig. 3).



Figure 3. Double sided wall tube thickness losses are visible.



Figure 4. Longitudinal crack, thick layer of deposits on the tube surface.

The coil was covered thick cracked slag layer (Fig. 4), apart this, thick layer of oxides was presented on either of surfaces (inside and outside). In deposits covering external surface are found following compounds: up to 3,7% sulfur (sulfide), sodium and potassium. Sulfur content is significant greater in close to metal layer than to middle layer. This is evidence that the coil was operated in reducing atmosphere what increasing external protective oxide layer damage intensity. Near to crack significant diameter deformation external was found.

The reheater coil design data:

– dimensions	$\phi 51 \times 4 \text{ mm}$
– material	10CrMo910
– design pressure	$p_o = 3,1 \text{ MPa}$
– design temperature	$t_o = 580^\circ\text{C}$
– allowable temperature	$t_{\text{dop}} = 580^\circ\text{C}$
– operating wall tube temperature	$t_{\text{sr}} = 595^\circ\text{C}$
– diameter deformation near to failure	$\varepsilon = 7,3\%$
– wall tube thickness near to failure	$g_r = 0,85 \text{ mm}$
– design wall tube thickness	$g_o = 2,63 \text{ mm}$
– nominal wall tube thickness	$g_n = 4 \text{ mm}$.

If operating wall tube temperature had been correct (up to 580°C) reheater should have been reliable operate more than 150 000 h but operating time was shorter about 50%. It was caused by increase stresses – corrosive wall tube thickness loss.

Pulverized – coal fired boiler – low NO_x furnace

After 80 000 h operating time were failed few reheater coils caused by wall tube thickness losses from flue gas flow side (Fig. 5). Deposits on external surface from the flue gas flow side were contained significant carbon quantities (~14–19%). This is evidence that the reheater had operated in reducing atmosphere and combustion process had occurred on the coils surfaces what has significant influence on the tube metal temperature increase. Sulfur compounds can accelerate corrosive wall tube thickness losses.



Figure 5. The wall tube thickness loss from the flue gas flow side.

The reheater coils design data:

– dimensions	$\phi 44 \times 4 \text{ mm}$
– material	10CrMo910
– design pressure	$p_o = 2,95 \text{ MPa}$
– design temperature	$t_o = 575^\circ\text{C}$
– allowable temperature	$t_{dop} = 580^\circ\text{C}$
– operating wall tube temperature	$t_{sr} = 585\div 590^\circ\text{C}$
– diameter deformation near to failure	$\varepsilon = 3\%$
– wall tube thickness near to failure	$g_r = 0,2 \text{ mm}$
– allowable stress:	
at 200 000 h:	$\sigma_{dop} = 0,8 \times R_{z/2 \times 10^5 / 575} = 31 \text{ MPa}$
– design wall tube thickness	$g_o = 2,2 \text{ mm}$
– nominal wall tube thickness	$g_n = 4 \text{ mm}$
– design operating life	
at $t = 575^\circ\text{C}$ and $g_n = 4 \text{ mm}$:	$\tau \cong 180 \text{ 000 h.}$

In this case indirect reason of failure (excessive high-temperature corrosion) was boiler operating conditions not appropriate with design assumption e.g. low load operating less than 60% rate and/or rapid shutdowns, what significant shortened coil operating life.

Fluidized bed boiler

Fluidized bed boiler with biomass-coal co-combustion. Overhangs on reheater sections are shown in Fig. 6. Major compound in deposit chemical composition is calcium sulfate which is combusting process product with calcium and aluminum silicate, silica and hematite addition.

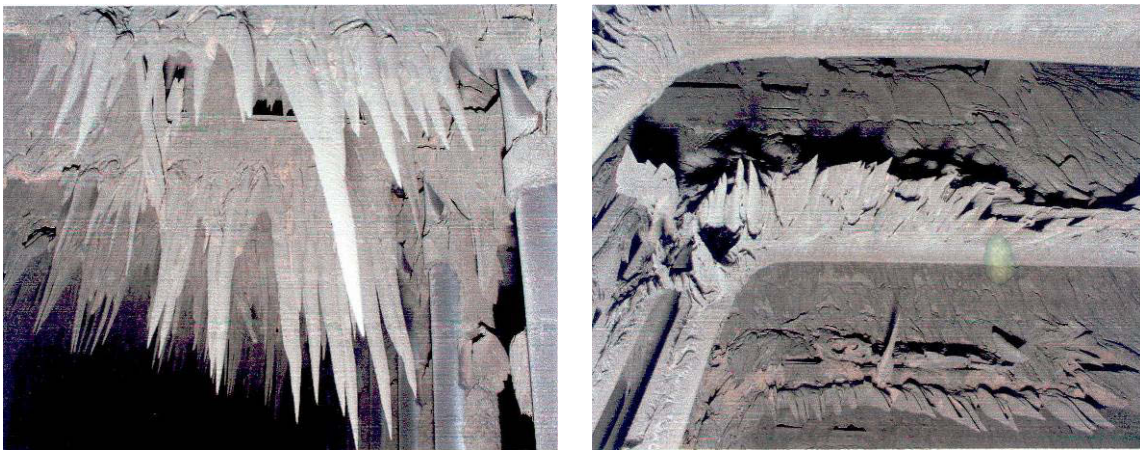


Figure 6. Overhangs on the reheater coils fluidized bed boiler.

Pulverized – coal fired boiler

After 60 000 h operating time of reheater occurred failures which had caused by wall tube thickness loss during high-temperature corrosion process (Fig. 7). The wall tube thickness loss was occurred on either of side (outside, inside) from flue gas flow side (Fig. 8). Either of surfaces (internal, external) were covered cracked oxides layer (Fig. 9).



Figure 7. Place of failure.

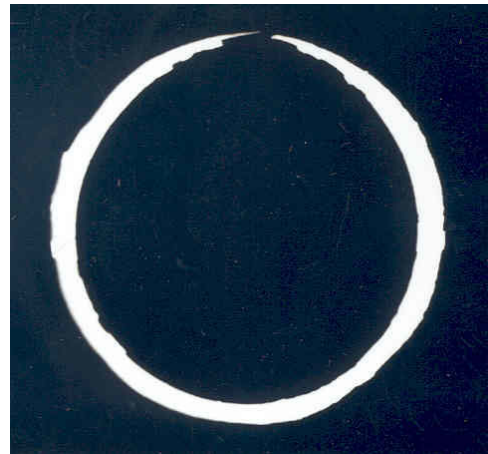


Figure 8. Two sided wall tube thickness loss.

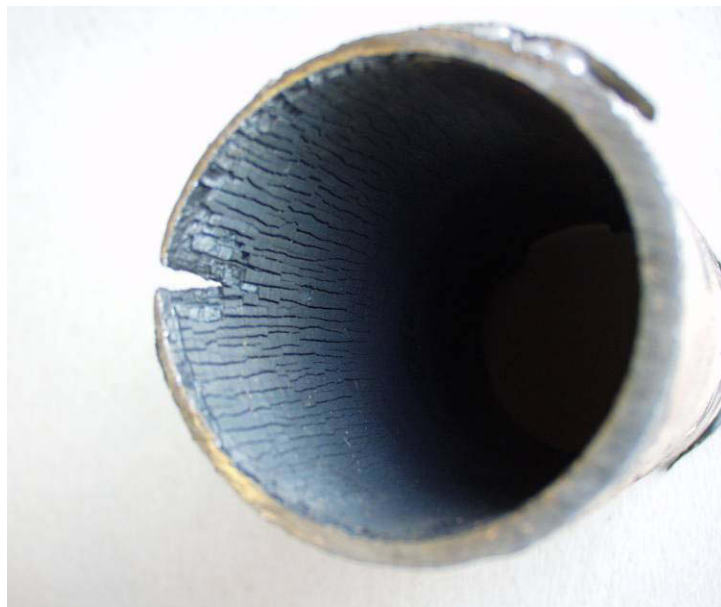


Figure 9. Cracked oxides layer increasing metal temperature.

The reheater coils design data:

- dimensions ϕ 51 x 4 mm
- material 13CrMo44

- design pressure $p_o = 2,94 \text{ MPa}$
- design temperature $t_o = 560^\circ\text{C}$
- allowable temperature $t_{dop} = 560^\circ\text{C}$
- operating wall tube temperature $t_{sr} = 575^\circ\text{C}$
- diameter deformation near to failure $\varepsilon = 2\%$
- wall tube thickness near to failure $g_r = 0,85 \text{ mm}$
- allowable stress:
 - at 200 000 h: $\sigma_{dop} = 0,8 \times R_{z/2 \times 10^5 / 560} = 37,6 \text{ MPa}$
- design wall tube thickness (at 560°C)
 - at 100 000 h $g_o = 1,1 \text{ mm}$
 - at 200 000 h $g_o = 1,25 \text{ mm}$
- nominal wall tube thickness $g_n = 4 \text{ mm}$.

Design operating life according to BSEN 12952-4/2000 at 575°C and 585°C temperature for variable wall tube thickness is shown in table 2.

Table 2.

Temperature	Wall tube thickness [mm]	
	$g_{obl} = 2,2$	$g_n = 4,0$
575°C	150 000 h	170 000 h
585°C	130 000 h	150 000 h

Pulverized – coal fired boiler

After 148 000 h operating time of reheater was occurred failure of horizontal section coil. Single corrosive pits were presented on internal surface (Fig. 10) which deep has reached up to 80% wall tube thickness (Fig. 11). Pitting had caused by oxygen corrosion which can occur during stop of operation without preservation of boiler internal surfaces. This process doesn't occur during boiler operation.



Figure 10. Corrosive pit on upper half of the coil tube.



Figure 11. Visible significant wall tube thickness loss.

The reheater coil design data:

- dimensions ϕ 51 x 4 mm
- material 10CrMo910
- design pressure $p_o = 3,1$ MPa
- steam temperature $t_c = 480^\circ\text{C}$
- design wall tube temperature $t_o = 575^\circ\text{C}$
- operating wall tube temperature $t_r = 510^\circ\text{C}$
- allowable stresses for 250 000 h:
 - at 575°C $\sigma_{dop} = 0,8 \times R_{z/2,5 \times 10^5 / 575} = 29,6$ MPa
 - at 510°C : $\sigma_{dop} = 0,8 \times R_{z/2,5 \times 10^5 / 510} = 82,4$ MPa
- stress in wall tube at 51 x 4 mm dimensions $\sigma_r = 19,2$ MPa
- according to OCT should be fulfilled following condition $\frac{\sigma_{dop}}{\sigma_r} > 1,2$

$$\frac{29,6}{19,2} = 1,49 \text{ calculated for 250 000 h at } t_o = 575^\circ\text{C}$$

$$\frac{82,4}{19,75} = 4,1 \text{ calculated for 250 000 h at } t_o = 510^\circ\text{C}.$$

For either of temperatures without include wall tube thickness losses caused high-temperature corrosion, operating life is exceed 250 000 h. Pitting occur in temperatures which enable steam condensing especially during shot downs and stop of operation.

Pulverized – coal fired boiler

After 75 000 h operating time reheater coils ware failed (Fig. 12). It had caused by excessive wall tube thickness loss from flue gas flow side because of corrosion process presented on internal surface (Fig. 13).



Figure 12. Failures with great deformation.



Figure 13. Corrosive wall tube thickness loss on internal surface.

The reheater coils design data:

– dimensions	ϕ 51 x 5 mm
– material	10CrMo910
– design pressure	$p_o = 2,95$ MPa
– design temperature	$t_o = 575^\circ\text{C}$
– operating wall tube temperature	$t_r = 590^\circ\text{C}$
– diameter deformation near to failure	$\varepsilon = 4\%$
– wall tube thickness near to failure	$g_r = 1,7$ mm
– allowable temperature	$t_{dop} = 580^\circ\text{C}$
– allowable stress	$\sigma_{dop} = 0,8 \times R_{z/2,5 \times 10^5 / 575} = 29,6$ MPa
– design wall tube thickness	$g_o = 2,2$ mm
– nominal wall tube thickness	$g_n = 5$ mm.

The operating life of the reheater for design conditions should be about 181 000 h. The reheater coil have operated only 75 000 h.

Pulverized – coal fired boiler

After 140 000 h operating time reheater coil was failed. The tube covered thick rough deposits layer contain sulfur (1,5%) and potassium (0,5%).



Figure 14. Thick deposits layer near to failure.



Figure 15. Visible corrosion from external surface.



Figure 16. Deposits on external surface of the reheater.

The failure was caused by chemical corrosion in eutectic place (eutectic is created by potassium sulfate K_2SO_4 or $K_2S_2O_7$). Near to failure wall tube thickness loss had almost 90% nominal wall tube thickness. 100 mm from failure wall tube thickness losses were regular and didn't exceed 10% at nominal wall tube thickness. Boiler firing coal and 15% biomass.

3. Conclusions

- Majority reheater failures are caused by wall tube thickness loss.
- From technological reasons in design calculations, wall coils thickness of reheater is assumed with great excess, sometimes 100% even but operating time in some cases didn't obtain 100 000 h.

- Direct reason of the wall tube thickness loss is high-temperature corrosion, intensify by aggressive operating condition (flue gas), it concern especially pulverized coal fired boilers with low NO_x furnace and boilers firing biomass.
- Generally bends of reheater coils which are directly expose on flue gas flow are failed.
- Most of coils failures occur in pulverized coal fired boiler with low NO_x furnace.

4. Summary

- Indirect reasons of excessive corrosion which untimely (before design operating life) wear reheater coils are boiler operating conditions not appropriate with design assumptions.
- Carrying out measurements of wall tube thickness and oxides thickness on internal surface preventing unsuspected and rapid failures. These measurements are helpful to estimate operating temperature and stresses in operating wall tube. These examinations should be carry out with high frequency but not less than 40 000 ÷ 50 000 h operating time.
- In case pitting caused by oxygen corrosion is only one solution – remove all bends and horizontal section of reheater coils.
- If results from wall tube thickness measurement are available, possible is remove the coils with the greatest level of wear. Operating life can be extend by use more high-temperature corrosion resistant materials e.g. T91 or T92.

References

- [1] Pronobis, M. “Evaluation of the influence of biomass co-combustion on boiler furnace slagging by means of fusibility correlations” *Biomass & Bioenergy* 2005, Vol. 28, Issue 4, (April), pp. 375–383.
- [2] Ścieżko, M., Zuwała, J. and Pronobis, M. ”Zalety i wady współpalania biomasy w kotłach energetycznych na tle doświadczeń eksploatacyjnych pierwszego roku współpalania biomasy na skalę przemysłową” *Energetyka* 2006/3 (marzec), pp. 207–220.

Reheat cracking susceptibility of new generation 2%CrMo(W)V P23 steel multipass welds made using matching and mis-matching filler metals

Pekka Nevasmaa, Jorma Salonen and Stefan Holmström

VTT Technical Research Centre of Finland, Espoo, Finland

Abstract

In comparison with conventional creep resisting grade T/P22, the modified 2%Cr steels T/P23 and T/P24 show nearly twice the creep strength at typical service temperatures of about 520–570°C. The possibility of welding thin-wall boiler tubes without preheating or PWHT has promoted the use of T23 and T24 in practical boiler service. For thick-wall applications and multipass welds, welding consumables still require further development to improve creep strength and ductility. Susceptibility to reheat cracking and hydrogen cracking increase with the wall-thickness and structural rigidity of the component. Consequently, thick-wall sections generally require the use of PWHT and sometimes preheating as well. This paper is concerned with weldability of P23 pipe steel, with particular emphasis on reheat cracking sensitivity of simulated HAZ microstructures and thick-section multipass welds made using closely matching and mis-matching filler metals. The results demonstrate that the weld metal is far more critical than the parent steel HAZ, both in terms of reheat cracking sensitivity and ductility & toughness. In the as-welded condition, the weld metal exhibited excessive hardness of ≈ 380 HV and only diminutive Charpy toughness at room temperature. Adoption of the PWHT (760°C/2h) enhanced the weldment toughness; however, it also inevitably raises risk to reheat cracking in the weld metal that showed values of reduction of area (RA) no more than 2–3% in the BWI cracking test. The results imply that thick-section multipass welds made using filler metal with the chemical composition closer to P24 grade material are much less susceptible to reheat cracking than ‘matching’ P23 grade welds.

1. Introduction

Weldability of low alloy creep-resisting steels is mainly governed by their hydrogen cold cracking and reheat (stress-relief) cracking tendency, as well as ductility of the heat-affected zone (HAZ) and the weld metal. Owing to the relatively high contents of Cr, Mo and V, rapid weld cooling cycles easily lead to hard bainitic-martensitic microstructures in the welded joint. Welding procedures

must therefore contain the necessary safeguards against cracking, which calls for appropriate preheating and the use of optimised filler metals [1].

Current environmental policy sets greater demands for higher efficiencies and the increase of operating pressure and temperature in thermal power stations, with the aim at making use of the fossil fuels more efficiently. The high maximum temperatures of gas and steam turbine power plants require the development of advanced steels with better creep rupture strength at elevated steam temperatures and pressures. As a result, new grades have been developed especially for the tubes in water-walls of the modern boilers. These new grades provide enhanced creep properties at 550°C, as well as low hardness in the as-welded condition and hence lesser risk to HAZ cracking. In comparison with conventional creep resisting grade T/P22 (10CrMo9-10), the modified 2%Cr steel T/P23 (HCM2S 2%CrMo(W)V, 7CrWVMoNb9-6) and T/P24 (7CrMoVTiB10-10) show approx. twice the creep strength at typical service temperatures of about 520–570°C. Since the oxidation properties of T23 and T24 seem comparable to those of T22, the modified steels are attractive for super-heaters and waterwalls. Using grade T/P23, thin-wall components can be welded without preheating or post-weld heat treatment (PWHT), yet ensuring sufficient mechanical properties. The economy of both new investments and later maintenance are supported by the possibility of welding thin-wall boiler tubes without preheating or PWHT; consequently, T23 and T24 have been introduced to practical boiler service [2].

Further application of these steels in thick-wall components, such as waterwalls, super-heater headers and steam pipes, appears accordingly attractive, in principle. However, weldability of thick-wall sections is usually limited by tendency to hydrogen cold cracking and reheat cracking in the HAZ and/or the weld metal. Low impact toughness can also occur, especially in thick multipass weld metals [1, 2]. Susceptibility to reheat cracking also increases with the wall-thickness and structural rigidity of the component. Thus, the balance of adequate weld metal toughness, suppressed cracking sensitivity and sufficient creep strength cannot be considered fully solved particularly for thick-wall components, which curtails practical application of the P23 (and P24) materials. Also, as the toughness of the as-welded joints appears to be adversely affected by the strengthening mechanisms to improve creep resistance in base materials, the toughness requirements should be addressed specifically according to the application [1, 2].

Consequently, thick-wall sections generally require the use of PWHT and sometimes preheating as well. For thick-wall applications and multipass welds, welding consumables still require further development to improve creep strength and ductility of weld metal [1]. With improvements for welding procedures and tailoring of filler metal chemistries, P23 (and P24) steel grades can be economical materials for waterwalls and super-heater headers, as well as hot steam lines operating under temperature range within power plants [2].

This paper is concerned with weldability of the P23 grade (ASTM A335 P23: 219.1 × 31.75 mm) pipe steel, with particular emphasis on reheat cracking sensitivity of simulated HAZ microstructures and thick-section multipass welds made using ‘closely matching’ and ‘mis-matching’ filler metals.

2. Materials and experiments

The P23 grade pipe steel was produced as seamless pipe at Dalmine mill. The austenisation temperature range was 1040–1070°C. Tempering is usually carried out between 750–780°C to ensure adequate creep strength and good toughness properties. Here, the applied tempering temperature was 780°C, with the aim at improving the impact toughness properties [3]. The mechanical properties of a set of large OD pipes are given in Table 1. The present P23 steel studied here was delivered in the quenched & tempered condition; consequently, the parent steel microstructure comprised tempered bainite and martensite [3].

Table 1. Mechanical properties of large OD pipes of P23 grade steel – the steel studied here denoted as ‘bold’ [3].

Pipe size ODxWT	Heat	YS (MPa)	UTS (MPa)	A (%)
P23 219.1 x 31.75 mm	274 284	581	675	26
P23 457 x 17.5 mm	274 284	602	687	39
P23 219.1 x 31.75 mm	945 203	525	635	29
P23 355 x 35 mm	274 284	519	627	29

Property	ODxWT 219 x 31.75 mm, 945 203	
Temperature (°C)	CVN energy (J)	Shear Area (%)
-40	38	10
-20	62	17
±0	377	100
+20	399	100

The investigated P23 linepipe weldment was made at ISQ using Metrolde B323(experimental) filler metal with closely matching chemical composition. For comparison, another multipass weldment made using a consumable intended for P24 grade steel was also subjected to reheat cracking tests. The chemical compositions of the two weld metals are given in Tables 4 and 5, respectively.

The Gleeble 1500 simulator was applied to thermally simulate different HAZ microstructures using single-cycle and multi-cycle (double- and triple-cycle) simulations with different peak temperatures (T_p) and weld $t_{8/5}$ cooling times. Regarding the actual P23 weld metal, Gleeble simulation was applied to produce a set of thermally re-heated multipass weld metal microstructures. To ensure compatibility between thermal cycles experienced in real pipe welding and

thermal simulation, authentic welding parameters were analysed from a typical *WPQT* certificate [3, 4] for a thick-wall P23 pipe and applied further to derive the corresponding thermal cycles for thermal simulations.

Reheat cracking tests for the Gleeble-simulated HAZ and thermally re-heated multipass weld metal microstructures were carried out using the isothermal slow strain rate tensile test denoted as ‘Belgian Welding Institute (BWI) type RC test’. In the test, cylindrical round-bar specimens ($L = 110$ mm, $L_m = 10$ mm, $\phi = 7$ mm) are firstly exposed to the thermal cycle with the peak temperature T_p resulting in the desired HAZ (or re-heated weld metal) microstructure, then let to cool down following the chosen weld $t_{8/5}$ and subsequently re-heated ($100^\circ\text{C}/\text{sec}$) to the temperature of 760°C (that corresponds to the actual PWHT temperature for the P23 steel). Immediately after reaching this temperature, the specimen is strained to fracture at a low tensile velocity of 0.5 mm/min. This means, a ‘break in tension’ type of RC test is used instead of a ‘constant loading until rupture’ type of test. Specimen’s reduction of area (RA-%) is then measured from the fractured specimen and the thereby obtained ‘relative’ value is used to assess susceptibility of a given microstructure to reheat cracking [3, 6].

Microstructural investigation of the simulated HAZs and re-heated weld metals was performed by preparing metallographic longitudinal sections from the selected Charpy-V specimens; these sections were then investigated with an optical microscope [3, 4]. Hardness testing as Vickers hardness numbers was performed on the metallographic sections using the load of 49.1 N (1 kp).

3. Results

Results of the reheat cracking tests for thermally simulated HAZs and thermally re-heated weld metals are presented, with metallographic investigation of microstructures and fractographic studies on specimen’s fracture surfaces. The complete results of the weldability studies are reported in full elsewhere [3, 4].

3.1 Thermally simulated HAZ zones

Results of the reheat cracking tests using the BWI tensile test are given in Table 2. The results are presented in terms of the attained value of the reduction of area (RA-%) in a specimen. It can be seen that there is a substantial difference in reheat cracking susceptibility between the two examined HAZ microstructures. Whereas the single-cycle CGHAZ exhibits comparatively low RA values in the range of 15–19%, introduction of the second re-heating thermal cycle leads into remarkable elevation of the RA values for the FG(R)-CGHAZ for which the measured RA values range from 57 to 73%. The $t_{8/5}$ cooling time had no measurable influence on the recorded RA values.

Table 2. Reheat cracking test results for the simulated HAZ of the P23 steel.

Specimen / Case	Initial ϕ [mm]	Final ϕ [mm]	RA [%]
CGHAZ_10	7	6.45	15.1
CGHAZ_10	7	6.4	16.4
CGHAZ_15	7	6.3	19.0
CGHAZ_15	7	6.4	16.4
CGHAZ_25	7	6.4	16.4
CGHAZ_25	7	6.4	16.4
FG(R)-CGHAZ_10	7	4.5	58.7
FG(R)-CGHAZ_10	7	4.5	58.7
FG(R)-CGHAZ_25	7	3.6	73.5
FG(R)-CGHAZ_25	7	4.6	56.8
FG(R)-CGHAZ_25	7	3.85	69.7

Note: CGHAZ_10, CGHAZ_15 and CGHAZ_25: single-cycled CGHAZ ($T_p = 1340^\circ\text{C}$); weld $t_{8/5} = 10, 15$ and 25 sec., respectively.

Note: FG(R)-CGHAZ_10 and FG(R)-CGHAZ_25: double-cycled FG(R)-HAZ ($T_{p1} = 1340^\circ\text{C}$; $T_{p2} = 1020^\circ\text{C}$); weld $t_{8/5} = 10$ and 25 sec., respectively. FG = fine grained; CG = coarse grained

3.2 Thermally re-heated multipass weld metals

The macrograph of the original P23 multipass weldment is shown in Fig. 1. Results of Vickers hardness measurements (HV5) on the weldment are given in Table 3. Comparatively high hardness in the range of 378–384 HV was recorded from the actual (as-welded) weld metal in the re-heated weld metal areas.

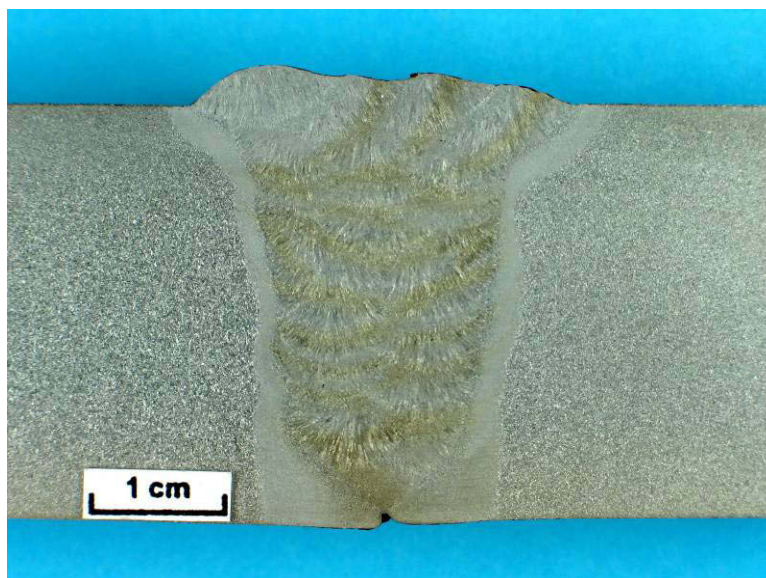


Figure 1. Macrograph of the P23 weldment – filler metal: B323(experimental).

Table 3. Hardness of original P23 weldment and simulated P23 steel HAZs.

Weld/simulated microstructure	Condition	Hardness (HV5)
weld metal	as-welded/as-cast (final bead)	313; 328
weld metal	as-welded	315–353
weld metal	re-heated (softened) ^(*)	288–312
weld metal	reheated (coarse-grained) ^(*)	353–384
CGHAZ	close to fusion boundary	341–368
FGHAZ	approx. 1.5 mm from the fusion boundary	324
ICHAZ	approx. 2.0 mm from the fusion boundary	285
Gleeble CGHAZ	as-simulated	356
Gleeble CGHAZ	PWHT	216
Gleeble FGHAZ	as-simulated	311
Gleeble FGHAZ	PWHT	190
Gleeble IC(R)-CGHAZ	as-simulated	291
parent steel	as-delivered	194–203

(* Note: reheated by repetitive thermal cycles caused by subsequent weld bead layers.

Results of the chemical analysis of the P23 weldment made using *Metrode B323(experimental)* filler metal are given in Table 4. It can be seen that the chemical compositions of the filling layer (surface bead) and the weldment mid-thickness areas (centre bead) appear nearly identical. Thus, dilution from parent steel is practically negligible. The weld Nb content was found quite high, i.e., 0.09%. Otherwise, the weld chemical composition is considered typical to a weld deposit made using P23 consumable of closely matching chemistry.

Table 4. Chemical composition of multipass P23 weld – filler metal: Metrode B323(experimental).

Sample	Chemical composition (w-%)							
	C	Si	Mn	S	P	Cr	Ni	Mo
Surface bead	0.06	0.35	0.57	0.007	0.011	2.15	0.06	0.11
Centre bead	0.07	0.35	0.57	0.007	0.010	2.13	0.06	0.11
Parent steel	0.07	0.24	0.46	0.0015	0.012	2.08	0.09	0.108

Sample	Chemical composition (w-%)							
	Cu	Nb	Al	W	V	Ti	Co	B
Surface bead	0.04	0.09	0.007	1.54	0.27	0.02	0.02	0.0050
Centre bead	0.05	0.09	0.006	1.60	0.26	0.02	0.01	0.0050
Parent steel	0.11	0.05	0.022	1.51	0.22	0.033	n.a.	0.0016

Table 5 shows the chemical composition of another multipass weld made using consumable intended for P24 grade steel (denoted as ‘P24’ weld). In comparison to the P23 weld, the ‘P24’ weld metal is seen to contain slightly higher C, Cr, Ni and Mo, as well as Nb instead of Ti, whereas W is obviously non-existent. The other alloying elements are more or less similar to the P23 weld.

Table 5. Chemical composition of multipass weld made using ‘P24 filler metal’.

Sample	Chemical composition (w-%)							
	C	Si	Mn	S	P	Cr	Ni	Mo
Weld surface	0.09	0.22	0.56	0.003	0.011	2.54	0.16	0.89
Weld root	0.10	0.24	0.56	0.003	0.011	2.54	0.18	0.89
Parent steel	0.05	0.24	0.43	0.001	0.013	2.30	0.13	0.90

Sample	Chemical composition (w-%)							
	Cu	Nb	Al	W	V	Ti	Co	B
Weld surface	0.02	0.05	<0.003	<0.01	0.26	0.003	<0.003	n.a
Weld root	0.05	0.05	<0.003	<0.01	0.22	0.064	0.004	n.a
Parent steel	0.08	0.01	0.012	<0.01	0.24	0.004	0.003	n.a

Table 6 summarises the results of the reheat cracking tests for both the P23 and ‘P24’ grade multipass weld metals. The applied test temperatures for the P23 and P24 weld metals were 760°C and 740°C, respectively. Specimens were extracted both in transverse and longitudinal directions in relation to weld. In the former case, the weld was an authentic circumferential pipe weld, whereas the latter case employed multiple-pass welded pads (deposited onto the plate). The results are presented in terms of the attained value of the RA-% in a specimen.

Table 6 shows a remarkable difference in reheat cracking susceptibility between the two re-heated P23 weld metal microstructures. Whereas the CG(R)-WM exhibits extremely low RA values of no more than 1.5–3%, introduction of the second re-heating thermal cycle leads into modest elevation of the RA values for

the FG(R)-CG(R)-WM; consequently the measured RA values range from 15 to 17%. The orientation of a specimen had no influence on the results. Overall, the RA values for the re-heated P23 weld metal are found significantly lower than in the case of the simulated HAZs of the P23 parent steel, although the applied Gleeble thermal cycles were identical, see Table 6.

Table 6. Reheat cracking test results for the thermally re-heated microstructures of P23 (B323 experimental) and ‘P24’ grade multipass weld metals.

Weld metal specimen / Case	Weld configuration	Specimen orientation	Reduction of area RA (%)
AloAS P23 weldment; filler metal Metrode B323(experimental)			
CG(R)-WM_10	circumferential pipe butt-weld	transverse	3.0
		transverse	3.0
	welded pad	longitudinal	1.7
		longitudinal	1.4
FG(R)-CG(R)-WM_10	circumferential pipe butt-weld	transverse	15
		transverse	15
	welded pad	longitudinal	16
		longitudinal	17
‘P24’ weldment; Nb-alloyed filler metal intended for P24 grade steel			
CG(R)-WM_10	circumferential pipe butt-weld	transverse	18
		transverse	15
	welded pad	longitudinal	19
		longitudinal	19
FG(R)-CG(R)-WM_10	circumferential pipe butt-weld	transverse	28
		transverse	28
	welded pad	longitudinal	33
		longitudinal	32
IC(R)-CG(R)-WM_10	welded pad	longitudinal	43
		longitudinal	42
SC(R)-CG(R)-WM_10	welded pad	longitudinal	19
		longitudinal	16

Note: CG(R)-WM: Tp1 = 1340°C ; FG(R)-CG(R)-WM: Tp1 = 1340°C & Tp2 = 1020°C ; IC(R)-CG(R)-WM: Tp1 = 1340°C & Tp2 = 900°C ; SC(R)-CG(R)-WM: Tp1 = 1340°C & Tp2 = 675°C ; t8/5 = 10 sec.; PWHT = 760°C (P23 weldment) and 740°C (‘P24’ weldment).

According to Table 6, there appears a significant difference in reheat cracking susceptibility between the P23 and ‘P24’ grade weld metals. When exposed to equivalent reheating thermal cycles, the ‘P24’ weld displays the RA values in the range of 15 to 40%, that is, about 2 to 5 times greater than those for the P23 weld. The difference in favour of the ‘P24’ weld is particularly evident in the case of the CG(R)-WM, i.e., the region that generally tends to have the highest sensitivity to reheat cracking. Irrespective of specimen orientation, the CG(R)-WM of the ‘P24’ weld made using consumable intended for P24 grade steel exhibits RA-% values 5 to 6 times greater than those for the CG(R)-WM of the P23 weld made using closely matching *B323(experimental)* filler metal.

3.3 Microstructural investigation and fractography

With respect to the 'AloAS' P23 weldment, microscopy revealed that the reheating thermal cycles of subsequent weld layers had resulted in formation of new grains into the originally as-welded (as-cast) weld metal microstructure. In the case of the as-welded weld metal reheated into high peak temperature region corresponding to the grain coarsening zone, the inherent solidification grain size had coarsened substantially and newly formed, "prior-austenite" grain boundaries were clearly visible. There existed only minor, if hardly any, traces of the original weld solidification structure. This applied more or less also to weld microstructures that had become re-heated into the lower peak temperatures, albeit the effects of reheating appeared less pronounced. In comparison to the FGHAZ and the ICHAZ microstructures, the corresponding weld metal microstructures looked more complex and 'disorderly' in nature. The original columnar grain solidification structure was still visible in the FG(R)-WM and, particularly, in the IC(R)-WM and co-existed with newly formed small-grained martensitic-bainitic structure at the prior-austenite grain boundaries.

Comparison of microstructures between simulated HAZs and the thermally reheated weld metals proves that the overall microstructural features of the CG(R)-WM ($T_p = 1340^\circ\text{C}$) are practically identical to that of the accordingly simulated P23 steel CGHAZ. In both cases, the microstructure consists essentially of martensite and bainite. In accordance with the CGHAZ, the prior-austenite grain boundaries in the CG(R)-WM microstructure are clearly discernible.

Fractography of the reheat-cracking test specimens showed clear evidence of pronounced localisation of damage at the "prior-austenite" grain boundaries in early stages of micro-crack formation, see Fig. 2. This was the case for both the CG(R)-WM and FG(R)-CG(R)-WM, even though the localisation was more accentuated in the former, because of coarser grain size. It was found that propagation of reheat cracking did not follow any original weld solidification cell boundaries, but the "prior-austenite" grain boundaries that, in this case, had formed as a result of subsequent re-heating of the actual multipass weld metal into the coarse-grained temperature region ($T_p = 1340^\circ\text{C}$).

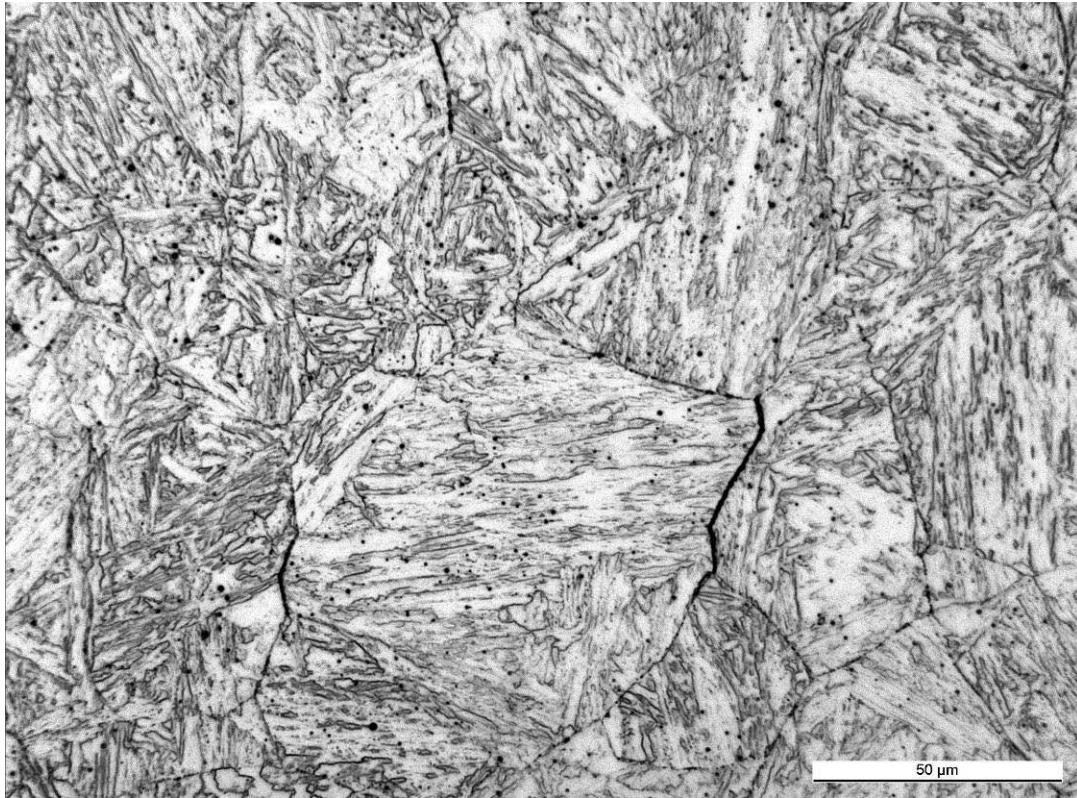


Figure 2. Reheat cracking in P23 weld metal subsequently reheated into the coarse-grained-temperature region ($T_p = 1340^\circ\text{C}$): CG(R)-WM.

4. Discussion

According to previous research works [5–7], the applied criteria to assess the degree of reheat cracking susceptibility are given in terms of measured value of the reduction of area (RA-%) associated with a given microstructure, as:

- $RA < 5\%$ \rightarrow extremely susceptible
- $RA \approx 5\text{--}10\%$ \rightarrow highly susceptible
- $RA \approx 10\text{--}20\%$ \rightarrow slightly/to some extent susceptible
- $RA \gg 20\%$ \rightarrow not susceptible.

Consequently, the single-cycle CGHAZ and the double-cycle FG(R)-CGHAZ microstructures of the P23 steel studied here can be characterised as “slightly / to some extent susceptible” and “not susceptible” to reheat cracking, respectively. The results c.f. Table 2 indicate that reheat cracking susceptibility of the FG(R)-CGHAZ remains significantly lower than for the initial CGHAZ. The remarkable elevation of the measured RA values associated with the FG(R)-CGHAZ (exposed to T_{p2} of 1020°C) is in line with previous work [5] that attributed the elimination of stress-relief cracking in the multi-cycle FG(R)-CGHAZ to

formation of a uniformly softened HAZ microstructure that did not contain strength gradients associated with a hard grain interior and soft denuded zone. Consistent with this, Table 3 shows evidence of substantial HAZ hardness reduction of approximately 60 HV units associated with the multi-cycle simulated IC(R)-CGHAZ, compared with the single-cycle CGHAZ.

A startling observation was that the thermally (Gleeble) re-heated P23 weld metal, i.e., the CG(R)-WM ($T_{p1} = 1340^{\circ}\text{C}$) exhibited extremely low, nearly non-existent RA values of no more than 1.5–3%, see Table 6. In this respect, the CG(R)-WM appeared far more critical than the corresponding CGHAZ of the P23 parent steel that, after all, displayed RA values around 15%, see Table 2. It is therefore evident that reheat cracking susceptibility of the present P23 multipass weldment made using *B323(experimental)* filler metal with closely matching chemical composition to P23 steel, is classified as “extremely susceptible”. It is considered somewhat surprising that, overall, the recorded RA values for the re-heated weld metal were significantly lower than those for the simulated HAZ microstructures of the P23 steel, although the applied Gleeble thermal cycles were identical, compare Tables 2 and 6.

Fractography of reheat cracking test specimens revealed clear evidence of pronounced localisation of damage characteristic to the thermally re-heated P23 weld metal microstructures, see Fig. 2. This localisation had occurred at the ‘prior-austenite’ grain boundaries of the thermally re-heated weld metal at an early stage of micro-crack formation. This was the case for both the CG(R)-WM and the FG(R)-CG(R)-WM, even though localisation was more accentuated in the former case, obviously because of the coarser grain size. An essential finding was that once initiated, extension and propagation of cracking did not follow any original weld solidification boundaries (that might have retained), but the new ‘prior-austenite’ grain boundaries that, in the present case, had been formed as a result of thermal Gleeble re-heating of the weld metal into the coarse-grained temperature region, i.e., $T_{p1} = 1340^{\circ}\text{C}$. This proves that the occurrence of reheat cracking had been controlled by the re-heated weld metal microstructure and not the original, retained as-cast weld solidification structure. Thus, the underlying causes of deficient RA-% values and, hence, extremely high susceptibility to reheat cracking associated with the P23 weld metal cannot be attributed to the original weld solidification (macro)structure, but to the chemical composition and sub-structure of the weld metal. This is interesting if one considers that the original weld metal had a chemical composition closely matching to that of the P23 parent steel, not to mention that the re-heating thermal cycles for the weld metal and the parent steel HAZ were identical. As far as optical microscopy is concerned, the overall microstructural features appear more or less similar between the thermally re-heated weld metals and the simulated HAZs associated with identical thermal cycles. This leaves one with the conclusion that differences in reheat cracking sensitivity between the weld metal and the HAZ

microstructures in the present case must originate from sub-structural features, such as carbide precipitation structure and/or martensite lath morphology, which would be discernible only using transmission electron microscopy.

Apart from the aforementioned reheat cracking tests, E.ON/Powergen has simultaneously reported [8] indications of occasional, very low creep strength associated with transverse (i.e., cross-weld) creep tests made using the same *B323(experimental)* filler metal. In the longitudinal weld metal creep tests, however, no such low values were recorded. Consequently, the P23 weld metal behaved in a very different manner depending whether the creep tests were conducted using transverse or longitudinal specimens. These orientation dependencies were traced back to the appearance of macroscopic inhomogeneity that manifested itself as pronounced orientation and non-uniformity of the original weld solidification structure. Consequently, poor creep behaviour of the P23 weld metal associated with the cross-weld creep tests was attributed [8] to un-isotropic properties of the weld macrostructure. Metallographic investigation revealed [8] the occurrence of micro-cracking along the as-cast columnar weld metal grain boundaries, rather than the re-heated weld metal zones. This implies that non-uniformity of oriented weld macrostructure can provoke and accentuate localisation of stress and strain and, hence, the mis-match effect, which thereby deteriorates the creep performance of the weld metal. The creep tests carried out at E.ON [8] seem to bear out the trend that welds made using low ductility filler metals are the ones that do worst in the transverse pad tests or in cross-weld tests. This, in turn, suggests that creep tests on more ductile weld metals might exhibit rather less orientation-dependent performance [8].

As a result, it is evident that in the case of the present P23 multipass weldment made using the *B323(experimental)* filler metal, two different modes of ‘low ductility’ behaviour can be defined, namely:

- (i) Low ductility associated with *equiaxed coarse-grained microstructure* where all traces of the original weld solidification structure, such as columnar grain orientation, columnar and refined zones, had become eliminated by the subsequent re-heating thermal cycles. This pertains to the thermally re-heated weld metal and thermally simulated HAZ microstructures subjected to reheat cracking tests, with the following characteristics:
 - no overall difference between the CG(R)-WM and the CGHAZ microstructures (produced using equivalent thermal re-heating cycles)
 - very low RA values in the weld metal reheat cracking tests, both with longitudinal and transverse specimens, no orientation effect recognised
 - behaviour attributes to chemical composition and microstructure/sub-structure related features

- (ii) Low ductility associated with *oriented, non-uniform weld deposit macro-structure* that reveals features of original weld solidification structure, e.g., columnar grain orientation and weld bead structure with clearly discernible columnar and refined weld metal zones. This pertains to multipass welds and pads subjected to cross-weld creep tests, with the following characteristics:
- very poor weld creep life performance in cross-weld creep tests, presumably due to pronounced localisation of stress and strain mis-match due to macro-structural orientation
 - inferior creep behaviour is generally in connection with weld metal with low ductility.

Table 6 shows significant differences in reheat cracking susceptibility between the P23 and the ‘P24’ grade weld metals. When exposed to equivalent re-heating thermal cycles, the ‘P24’ weld displayed RA values about 2 to 5 times greater than those for the P23 weld. The underlying mechanisms for the discovered differences are not fully understood. It is noteworthy that the P23 weld metal studied here contained a considerable amount of Nb, i.e., 0.09%. From reheat cracking standpoint, Nb content for P23 grade weld metal is recommended [2] usually not to exceed 0.05%. On the other hand, it has been shown [6] that too low Nb contents of less than 0.02% can impair weld metal’s creep strength, hence promoting creep rupture in the weld metal. According to the present knowledge [5–7], the P24 grade parent steel generally appears less susceptible to HAZ reheat cracking than the P23 grade steel. Thus, higher reheat cracking sensitivity of the P23 weld metal might be explained by its high Nb (and W) and hence pronounced strengthening of grain interiors because of W in solution and/or precipitates and precipitation of fine, coherent Nb-rich carbides/carbonitrides. As a result, steep hardness (and strength) gradient would exist between the grain interiors and the grain boundary areas. Whether the role of Nb and W in strengthening the grain interiors is crucial for high reheat cracking sensitivity of the investigated P23 weld metal cannot, however, be either confirmed or ruled out, since no electron microscopy (TEM) was performed in the present work.

Similarly to the simulated HAZ, introduction of the second re-heating thermal cycle, i.e., $T_{p2} \approx 900\text{--}1020^\circ\text{C}$ was found to result in modest elevation of the weld metal RA values from those recorded for the single-cycle CG(R)-WM, see Table 6. This suggests that the P23 steel will benefit from multipass welding techniques that maximise the microstructural refining (i.e., normalising) effect introduced by repetitive thermal cycles of successive weld bead layers.

The present results clearly demonstrate that in the case of P23 material, the multipass weld metal is far more critical than the parent steel HAZ, both in terms of reheat cracking sensitivity and ductility. In the as-welded condition, the weld metal exhibited excessive hardness of 378–384 HV and only diminutive Charpy

toughness of ≈ 7 J at room temperature. It is noteworthy that the highest and the lowest hardness both were associated with re-heated microstructures close to bead boundaries between successive weld layers. Formation of local, hardened and softened microstructures within re-heated multipass weld metal c.f. Table 3 is presumably a result of complex precipitation reactions causing re-precipitation, over-ageing and tempering. The excessive hardness of the weld metal is thought to accrue from its slightly higher alloying content compared to the HAZ, as well as from the absence of the PWHT in the present case. Naturally, a PWHT would normally be carried out for any P23 linepipe weldment with 31 mm wall thickness. Adoption of PWHT, however, inevitably raises risk to reheat cracking in the P23 grade weld, which manifested itself as attained RA values of no more than 2–3% in the reheat cracking tests c.f. Table 6. The results show that thick-section multipass welds made using consumable with the chemical composition intended for P24 grade steel are much less susceptible to reheat cracking than ‘matching’ P23 welds. It is therefore obvious that with improvements for welding procedures and tailoring of filler metal chemistries, P23 (and P24) grades can be economical materials for waterwalls and super-heater headers, as well as hot steam lines operating under temperature range within power plants.

5. Summary and conclusions

With respect to weldability and reheat cracking susceptibility of ‘ALoAS’ P23 linepipe steel and thick-section welds, the following conclusions can be drawn:

- Single-cycle coarse-grained HAZ has a risk to reheat cracking. For the CGHAZ, the RA values ranged from 15 to 20%.
- Introduction of the second thermal cycle ($T_{p2} = 1020^{\circ}\text{C}$) producing grain refining effect resulted in remarkable elevation of the attained RA values, thereby reducing CGHAZ cracking risk significantly. For the FG(R)-CGHAZ, the RA values exceeded 55%.
- Multipass P23 weld metal made using closely matching *B323(experimental)* filler metal was found “extremely susceptible” to reheat cracking as regards the CG(R)-WM exhibiting RA values less than 3%, and “susceptible” to reheat cracking as it comes to the FG(R)-CG(R)-WM that showed RA values in the 15–17% range.
- Reheat cracking in weld metal did not coincide with any original weld solidification boundaries, but the new ‘prior-austenite’ grain boundaries formed as a result of thermal re-heating of the original weld metal.
- Multipass welding techniques that maximise the normalising (and tempering) effect of successive weld passes will have a beneficial effect in lowering reheat cracking susceptibility.

- Weld made using consumable intended for P24 material was less susceptible to reheat cracking than the P23 weld made using closely matching filler metal.
- PWHT seems mandatory in order to guarantee weld metal hardness not exceeding 350 HV and to ensure adequate toughness in thick-section multipass weld metal made using ‘matching’ P23 filler metal.

Acknowledgements

The present work belongs to ‘ALoAS’ WP2. Technical contributions by E.ON, U.K., and TenarisDalmine, Italy, are highly appreciated. Financial support by the European Commission and VTT is gratefully acknowledged.

References

- [1] Bauné, E., Leduey, B., Bonnet, C. and Bertoni, A. ‘Development of welding consumables dedicated to the welding of new generation 21/4Cr-1Mo pipe materials P23 and P24 for power generation and hydrogen service’. Proc. Conf. “*European Symposium on Pressure Equipment (ESOPE 2004)*”. Palais des Congrès, Paris, 28–30 September 2004. France: Association Francaise des Ingenieurs en Appareils a Pression (A.F.I.A.P.).
- [2] Auerkari, P., Salonen, J. and Nevasmaa, P. *VTT Research Report No TUO74-055258*. Technical Research Centre of Finland, Espoo 2005.
- [3] Nevasmaa, P., Holmström, S., Salonen, J. and Caminada S. *VTT Research Report No VTT-R-03109-06*. VTT, Espoo 2006.
- [4] Nevasmaa, P., Salonen, J., Holmström, S. and Caminada, S. *IIW-Doc. IX-L-1003-07 / VTT Research Report No VTT-R-02973-07*. VTT, Espoo 2007.
- [5] Nawrocki, J. G., DuPont, J. N., Robino, C. V. and Marder, A. R. *Welding Journal* 80(2001), Welding Research Supplement, pp. 18-s–24-s.
- [6] Dhooge, A. & Vekeman, J. *Welding in the World* 49(2005)9/10, pp. 75–93.
- [7] Brózda, J. B. *Welding International* 18(2004)10, pp. 761–770.
- [8] Private information: David Allen / E.ON/Powergen, March–August, 2006. United Kingdom 2006.

Long-term creep testing and microstructure evaluation of P91 steel weld joints

Dagmar Jandová, Josef Kasl and Václav Kanta

ŠKODA VÝZKUM s.r.o., Plzeň, Czech Republic

Abstract

Trial weld joints were made from wrought and cast modified 9Cr-1Mo-V steel using GTAW & SMAW methods. Creep testing was carried out at temperature range from 525°C to 625°C and stresses from 50 to 240 MPa. Time to rupture of welds made from tube segments and cast plates reached almost 30 000 hours and 20 000 hours respectively. Creep strength was evaluated according the Larson-Miller parametric equation and microstructure was investigated using both light and electron microscopy. Creep rupture strength of both weld joints tested at temperatures below 600°C falls into the $\pm 20\%$ scatter band of the creep rupture strength of the parent material. At 600°C and 625°C the creep strength dropped by 27% and 30% for the plate weld and the tube weld respectively. All ruptures occurred in fine grain and intercritically reheated heat affected zones either in the parent material or in the weld metal. Observation of thin foils prepared from selected regions of the weld joints revealed differences in precipitation processes and the structure recovery causing decrease of dislocation density in some regions. Fine ferritic grains with low density of fine carbonitride precipitate occurred in critical localities. Soft grains were deformed and cavities at grain boundaries initiated the crack propagation.

1. Introduction

The steel grade P91 is the main representative of modified 9%Cr steels. It is used for production of boiler and turbine components in fossil fuel power plants due to their excellent combination of mechanical and oxidation-resistant properties [1, 2]. Some large casting components as well as parts of tubes or pipe lines are jointed together by welding. The knowledge of the behaviour of welds during long time service is therefore of great importance because welds are commonly susceptible to fracture. Fracture is usually initiated in a specific microscopic region as a result of structural heterogeneity of the weld joint [3, 4]. Therefore a study of microstructural changes taking place in different regions of welds during creep exposures can clarify a drop of the creep rupture strength in the weld joints. In this paper the microstructural evolution of two trial weld joints under different temperature and stress conditions and their relations to creep behaviour are investigated.

2. Experiments

Weld joints were fabricated from wrought and cast 9Cr-1Mo steel (ASME-P91) using GTAW & SMAW method. The first circumferential weld was made of segments of tubes made of X10CrMoVNb 9 1 steel with an external diameter of 325 mm, a length of 400 mm and a wall thickness of 25 mm, which were joined in PC position (a longitudinal axis of tubes was vertical). The second weld of the cast plates with dimensions of 500 x 150 x 25 mm made of GX12CrMoVNbN 91 steel were joined in PA position (a horizontal position of plates). Welding was carried out using internal protection of the weld root by inert gas. Inductive heating with thermal insulation ensured a preheating temperature in the range of 200–250°C. The interpass temperature was kept below 300°C. Root pass was formed with Thermanit MTS3 and Chromo 9V was used as an electrode. The chemical composition of the base material and the consumables used is given in Table 1. The parent material was used after austenitization at 1050°C for 1.5 hrs, oil quenching and tempering at 750°C for 3.5 hrs. The post-weld heat treatment (PWHT) 760°C/2.5 hrs was carried out for the tube weld and 740–750°C/2.5 hrs for the plate weld. Integrity and mechanical properties of weld joints have been evaluated to the welding standards EN 288-2,3. Required mechanical properties as well as non-destructive testing in accordance with quoted standards were satisfied. Smooth cross-weld specimens with a length of 92 mm and a diameter of 8 mm underwent the creep testing. Fractographic analysis of ruptured samples was also undertaken.

Table 1. Chemical composition of weld joints examined (wt. %).

	C	Mn	Si	Cr	Mo	V	Ni	Nb	N	P	S
P91	0.12	0.50	0.29	8.5	0.93	0.20	0.27	0.050	0.02	0.010	0.004
Thermanit MTS3	0.13	0.61	0.24	8.93	0.99	0.18	0.67	0.069	0.058	0.007	0.002
Chromo 9V	0.10	0.62	0.24	9.05	1.05	0.20	0.73	0.05	0.40	0.009	0.006

Creep rupture samples were cut along their longitudinal axis. Macrostructure was revealed using Vogel's reagent and location of fracture in different regions of weld joints was specified. The hardness profile across the weld joint was measured and microstructure was observed in metallographic samples etched with Vilella's reagent. Extended metallography was carried out using light (LM), scanning (SEM) and transmission electron microscopy (TEM). Thin foils and extraction carbon replicas were prepared from selected regions of weld joints. The foils were thinned to by jet electropolishing in a 6% solution of perchloric acid in methanol at the temperature of -40°C.

3. Results

3.1 Creep testing

The creep testing was carried out at temperatures in the range from 525°C to 625°C and stresses from 40 MPa up to 240 MPa. The creep testing of the tube weld has been finished while creep tests on the plate weld are still running. Up to now 11 specimens from a total number of 16 pieces have ruptured. Time to the rupture of the tube weld and the plate weld ranged from 200 hrs to about 30 000 hrs and from 1000 hrs to about 20 000 hrs respectively. Creep rupture strength was evaluated using the Larson-Miller parametric equation

$$P = T \cdot [C + \log \tau],$$

where T represents temperature given in degree Kelvin, C is a specific constant for a given material (C = 25 for 9Cr-1Mo steel) and τ means time to fracture in hours. The creep rupture strength of cross-weld specimens was compared with the creep rupture strength of the base materials and is graphically represented in Figs. 1 and 2. Vertical dashed line corresponds to a temperature of 600°C and a time to rupture of 100.000 hrs.

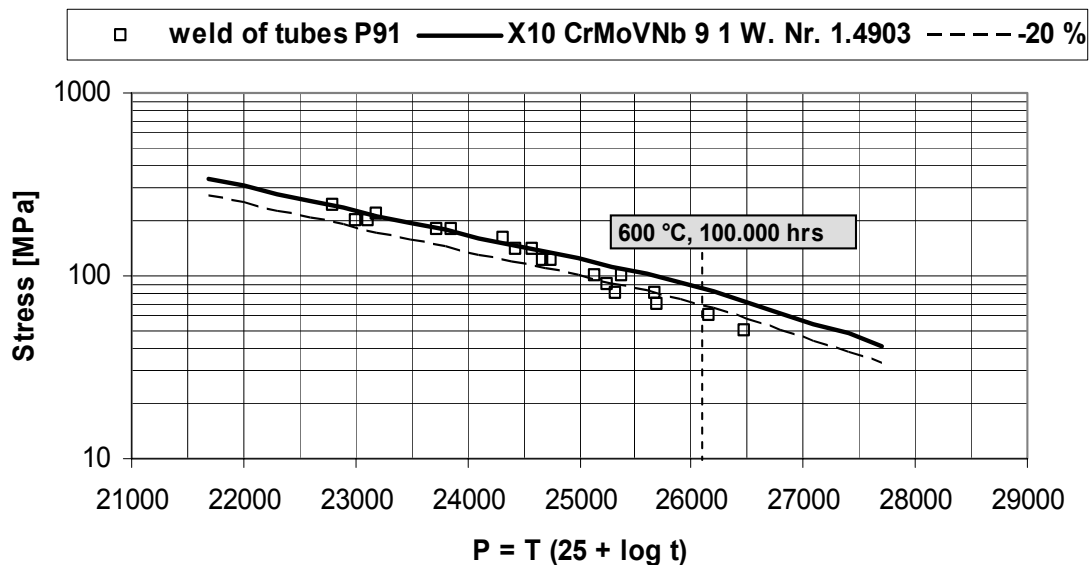


Figure 1. Creep rupture strength of the tube weld in comparison with creep rupture strength of the parent material X10CrMoVNb 9 1 steel.

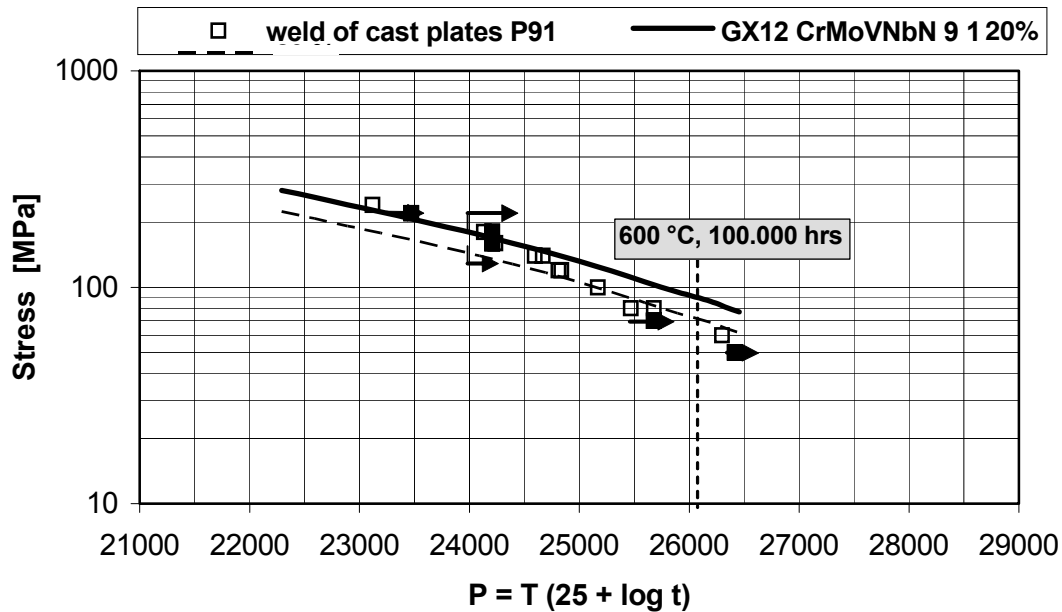


Figure 2. Creep rupture strength of the plate weld in comparison with creep rupture strength of the parent material GX12CrMoVNbN 9 1 steel.

The creep rupture strength of the tube weld is similar to the creep rupture strength of the parent material at applied stresses above 140 MPa. At lower stresses the creep rupture strength of the weld decreased below the bottom margin of $\pm 20\%$ scatter band of the creep rupture strength of GX12CrMoVNbN 9 1 steel. A drop in the creep strength of the weld increased with increasing creep test temperature. The maximum drop was 27%.

The creep rupture strength of the plate weld is comparable with the parent material of X10CrMoVNb 9 1 steel at stresses above 100 MPa. At lower stresses the creep rupture of the weld decreased and fell even by 30% in comparison to the parent material. If we compare both weld joints it can be concluded, that the plate weld is stronger than the tube one, however at high temperatures and stresses below 120 MPa the creep strength of both welds is almost the same.

3.2 Macrostructure and hardness measurement

Both the welds were of the W-type, with heat affected zones (HAZ) ranging in width from 3 to 4 mm. The HAZ consisted of a coarse grain structure close to the fusion boundary, followed by a fine grain and an intercritical structure merging with un-affected parent material. Macrograph and the hardness profile across the tube weld after post-weld heat treatment is shown in Fig. 3. Hardness across the weld joint varied from about 180 to 232 HV10. Hardness of unaffected parent material was 200 HV10, hardness of the weld metal (207–224) HV10. Maximum value of hardness corresponded to the coarse prior austenite grain HAZ. Creep exposures at temperatures ranging from 525 to 575°C did not significantly

influence the hardness, while exposure at 600°C resulted in an increase by about 20 HV10. After exposure 625°C / 50 MPa / 29 962 hrs hardness of the weld metal decreased in comparison to hardness of weld after post-weld heat treatment (Fig. 4).

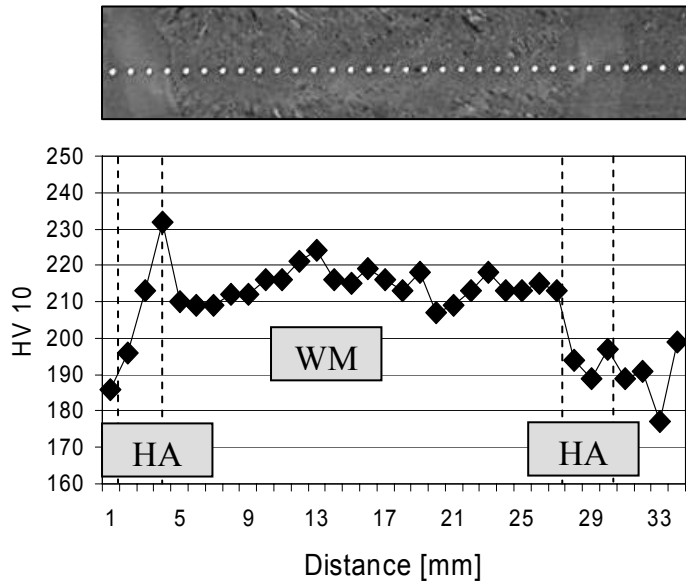


Figure 3. Macrograph and cross-weld hardness profile of the tube weld after post-weld heat treatment.

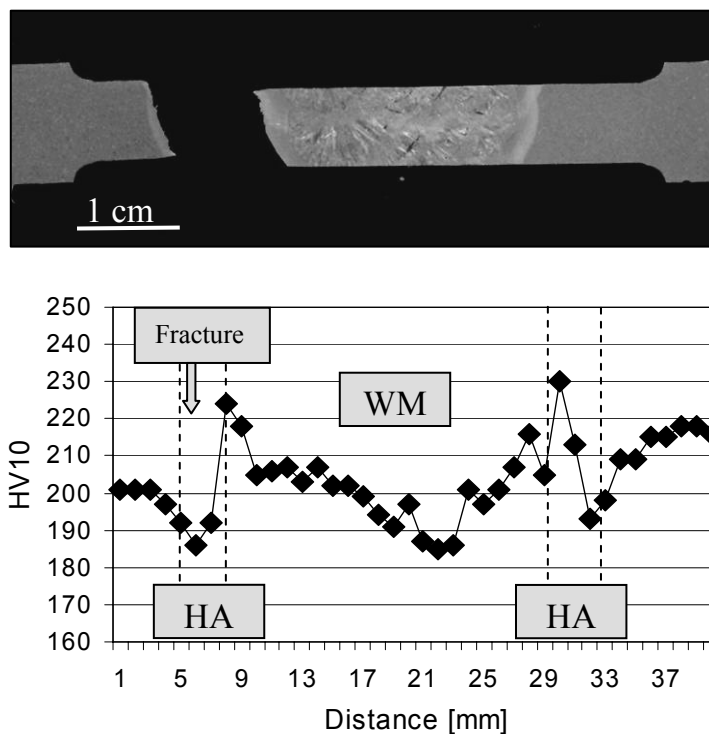


Figure 4. Macrograph and cross-weld hardness profile of the tube weld after the creep test 625°C / 50 MPa / 29 996 hrs.

The macrostructure and the hardness distribution across the plate weld are shown in Fig. 5. Hardness of the weld metal and unaffected parent material was 225 HV and 210 HV respectively. Hardness peaks were detected in the region close the fusion boundary and hardness troughs were found at the parent metal – HAZ boundary.

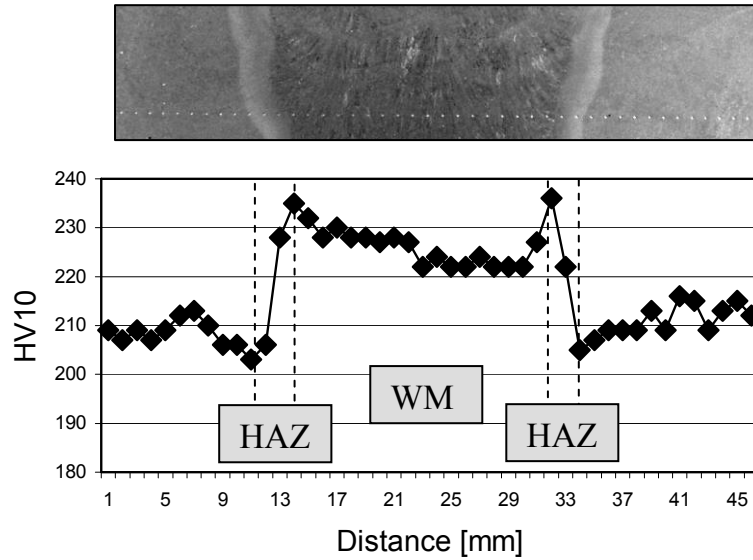


Figure 5. Macrograph and cross-weld hardness profile of the plate weld after post-weld heat treatment.

Creep exposures did not influence the hardness profile markedly. Vickers hardness values of specimens exposed at temperatures up to 575°C were comparable to those before the creep test. A slight increase in hardness of the parent material and a significant decrease in hardness of the weld metal were found out after the creep tests at 600°C and 625°C (Fig. 6).

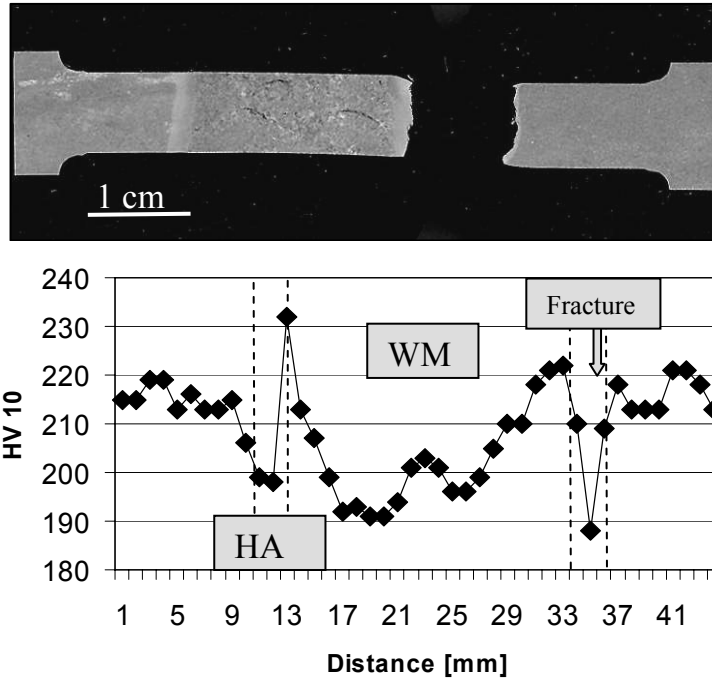


Figure 6. Macrograph and cross-weld hardness profile of the plate weld after the creep test 600°C / 60 MPa / 19 210 hrs.

3.3 Fractography

Fractures of the tube weld were located in various regions of the weld depending on the creep test conditions. Fracture occurred in the weld metal after creep exposures at lower temperatures and higher stresses and in the fine grain heat-affected zone of the parent material after creep tests at higher temperatures and lower stresses.

Fracture surfaces of the tube weld crept at 525°C and 550°C revealed a dimpling morphology, which is typical for ductile transcrystalline fracture (Fig. 7a). After creep exposures at higher temperatures surfaces were covered with thick oxide layers, which made it impossible to specify the rupture mechanism. Fracture surfaces gave some evidence for a dimpling morphology (Fig. 7b).

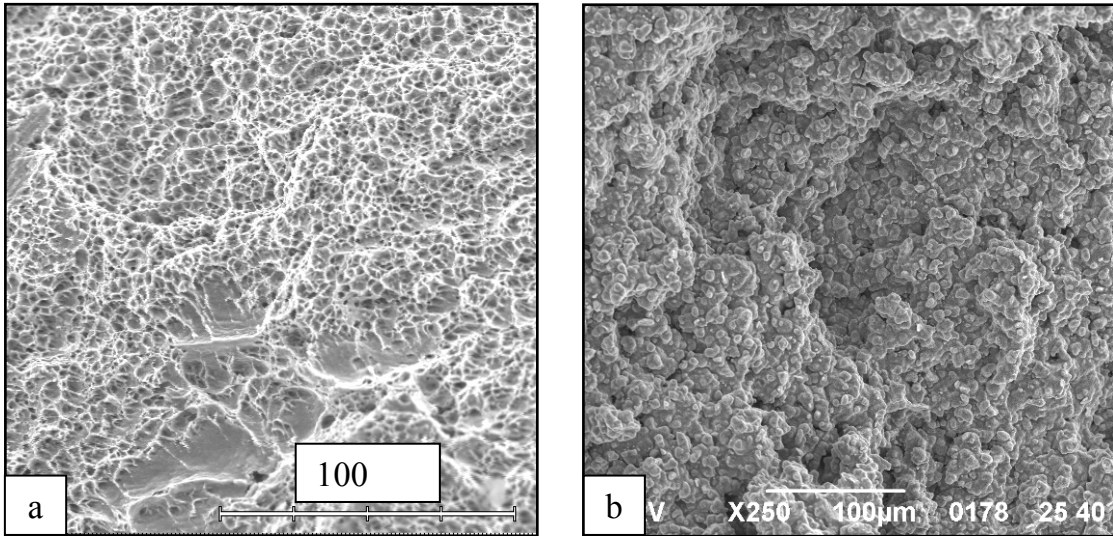


Figure 7. SEM micrographs of the fracture surfaces of the tube weld after the creep exposure: a) 525°C / 220 MPa / 11 546 hrs, b) 625°C / 50 MPa / 29 962 hrs.

All of crept test-pieces of the plate weld ruptured in the HAZ of the parent material. Fracture surfaces were again covered with oxide layers; therefore it was difficult to distinguish the fracture mechanism. Nevertheless fracture indicated transcrystalline creep failure and at some of specimens exposed at a temperature of 575°C intercrystalline facets were also detected (Fig. 8).

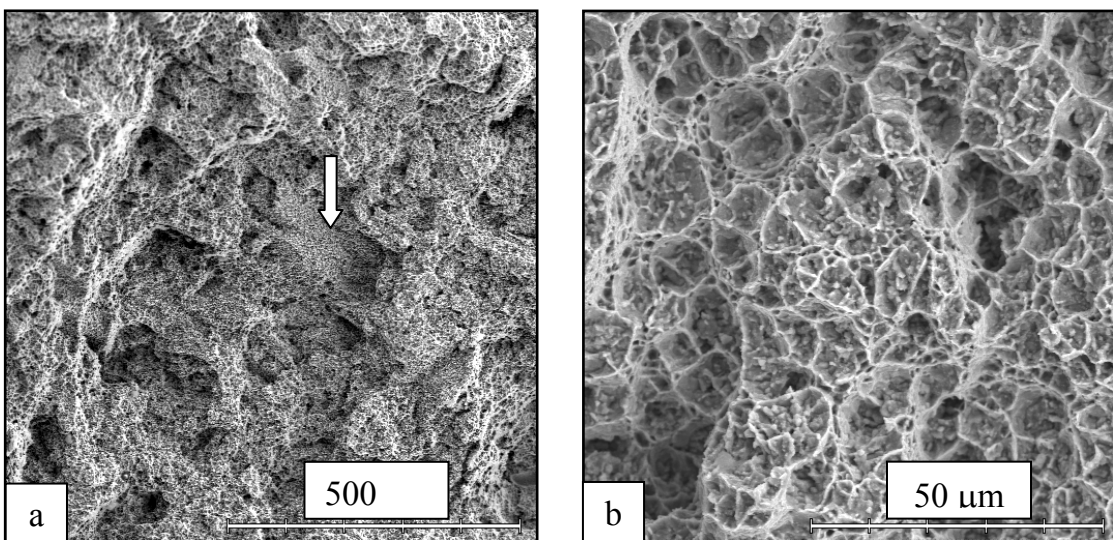


Figure 8. SEM micrographs of the fracture surfaces of the plate weld after the creep exposure 575°C / 180 MPa / 2853 hrs: a) a general view with an intercrystalline facet, b) a detail.

3.4 Microstructure

Microstructural study was concentrated on critical zones of weld joints after long-term creep exposures at high temperatures. Microstructures before and after the creep testing were compared.

All regions of weld joints were formed by severely tempered martensitic structures. All structures observed in different regions of weld joints corresponded to tempered martensite. Segregation and some casting defects were evident in the parent material of the plate weld. Fracture of both the welds at creep exposures at temperatures above 575°C occurred predominantly in the HAZ, at a distance of about 1.5 mm from the fusion line. Microstructure in this critical zone consisted of fine grained martensite. Cavities were observed near fracture surfaces. Their size and density increased with increasing temperature and duration of creep tests. A lot of cavities occurred in the HAZ on the opposite side of the cross-weld creep test specimens (Fig. 9). Cavities were concentrated in fine prior austenite grain heat affected zones. In the tube weld after the longest creep exposures (600°C / 70 MPa / 27 471 hrs and 625°C / 50 MPa / 29 962 hrs) some isolated cavities occurred also in other parts of weld joint – in the weld metal and unaffected parent material.

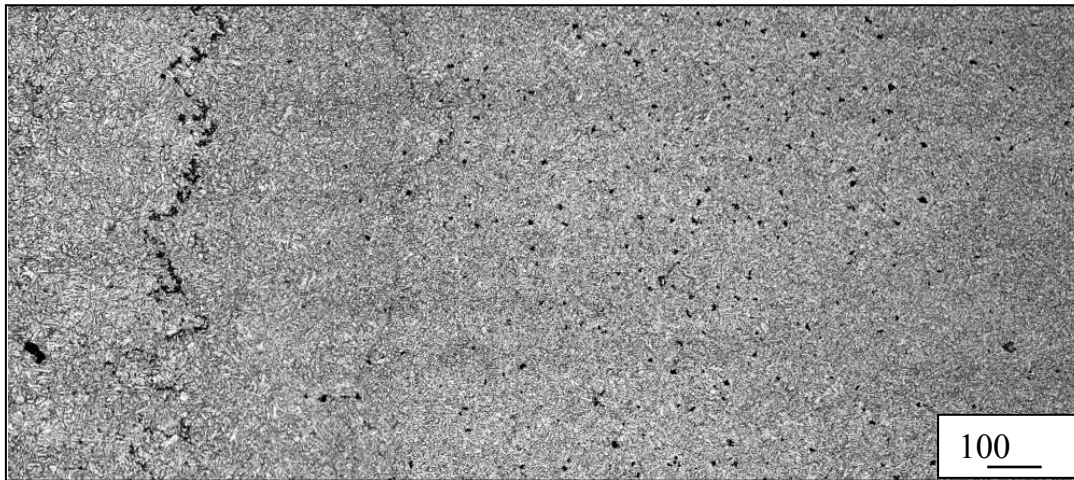


Figure 9. LM micrograph of the fine grain HAZ on the opposite side of fracture surface of the tube weld after the creep exposure 625°C / 60 MPa / 13 673 hrs.

Dislocation substructure and particles of secondary phases were observed in foils and extraction replicas using TEM and EDX microanalysis (Fig. 10, 11). The parent material and also the weld metal had a lath-like microstructure with a large number of coarse $M_{23}C_6$ carbide particles on grain and subgrain boundaries (Fig. 10a, 11a, b). After the post-weld heat treatment fine precipitates of M_2C and $V(C,N)$ were found in some of the laths. After the creep exposures at 600°C and 625°C which exceeded 10 000 hrs to the rupture M_2C carbides were dissolved while coarse particles on grain and subgrain boundaries built up. A slight

increase in particle size was proved by quantitative evaluation of particles with a diameter above 10 nm. Vanadium carbonitride particles were detected. Particles were identified using selected area electron diffraction and EDX microanalysis. Predominant content of chromium was detected in $M_{23}C_6$ carbides. Vanadium and niobium were the main elements in fine MX carbides and carbonitrides. Several coarse particles with a high concentration of molybdenum were found in the tube weld after the creep test under conditions 625°C / 60 MPa / 13 673 hrs. They could correspond to the Laves phase [5].

Densities of individual secondary phases were different in various regions of the weld joint. The parent material contained more precipitates than the weld metal. In the coarse prior austenite grain heat affected zones the lath-like microstructure with high dislocation density, a dispersion of fine precipitate and a low density of coarse particles were observed. On the contrary the fine prior austenitic grain HAZ consisted of small ferritic grains and subgrains with a low dislocation density and plenty of carbide particles at the grain and/or subgrain boundaries. Sporadic occurrence of intragranular fine precipitate was observed in this region. Microstructure in the marginal regions of the HAZ contained ferritic laths with relatively high dislocation density and dispersion of a fine precipitate [6].

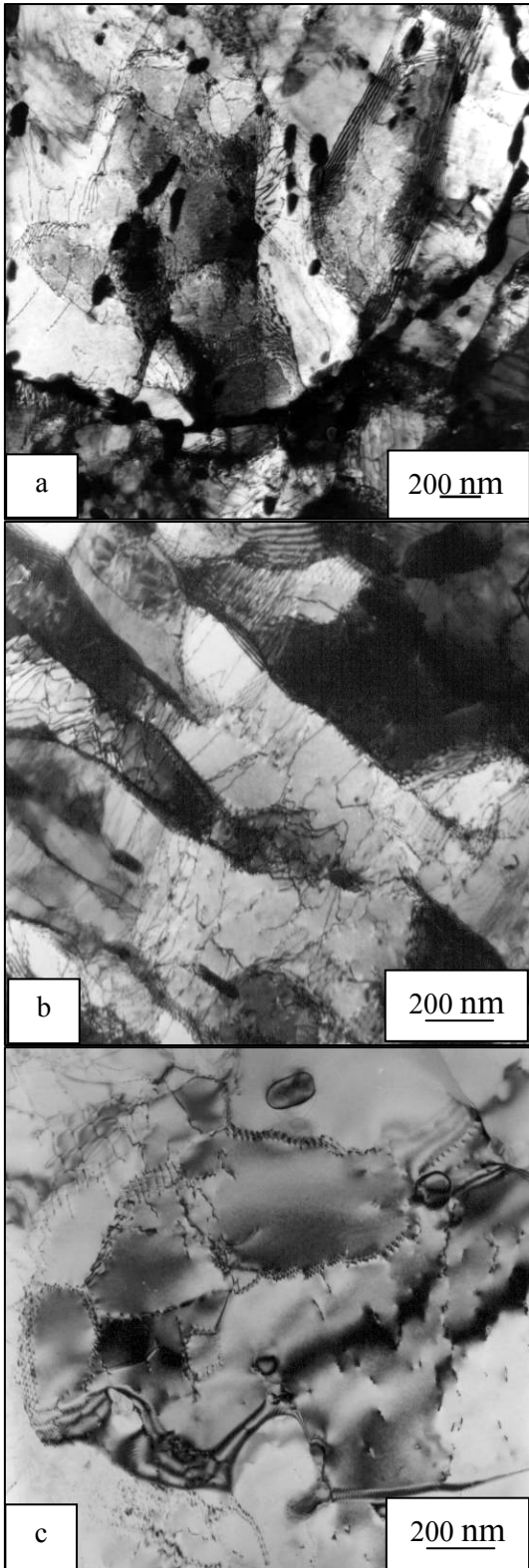


Figure 10. TEM micrographs of the tube weld: a) the parent material after PWHT, b) the coarse grained HAZ and c) the fine grain HAZ after creep test 625°C / 60 MPa / 13673 hrs.

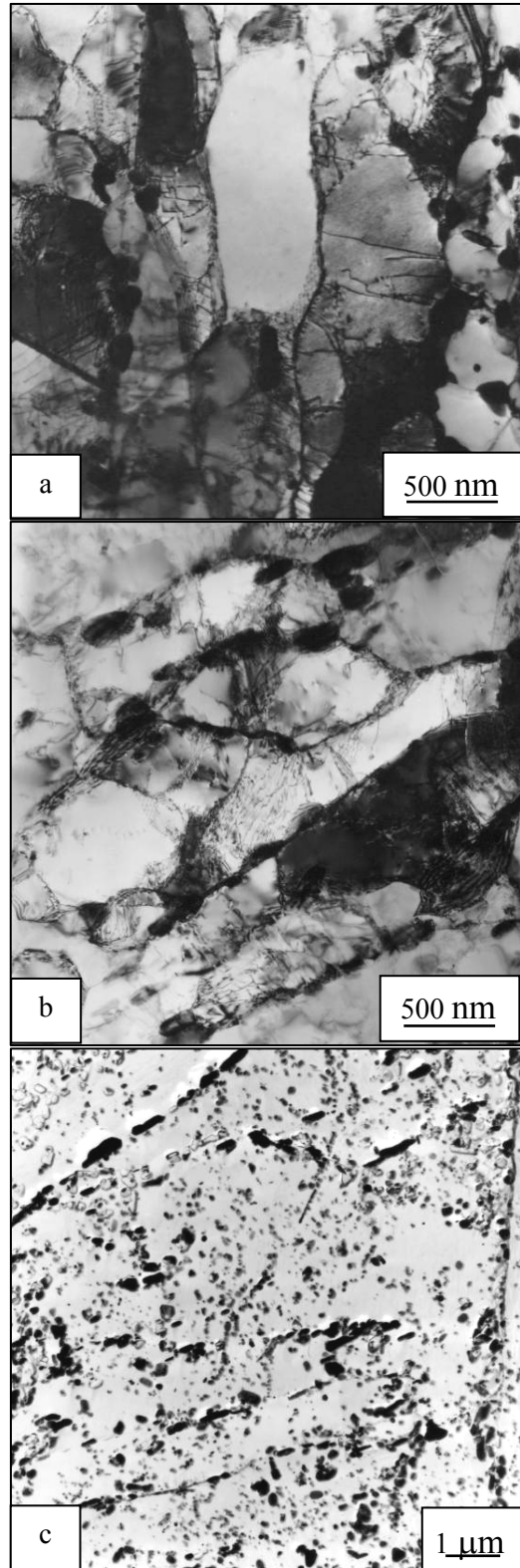


Figure 11. TEM micrographs of the plate weld after PWHT: a) the parent material, b) the weld metal and c) particles in the parent material.

4. Discussion

Weld joints which were exposed under high stresses and at temperatures below 575°C ruptured by transcrystalline creep ductile mechanism similar to the fracture at room temperature. Rupture of the tube weld occurred in the weld metal, because this region of the weld joint has a lower strength in comparison with surrounding wrought material. Fracture of the plate (up to now only one crept piece has ruptured) was located partly in intercritically reheated HAZ and partly in unaffected parent material. In this case creep strength of the weld metal and creep strength of the cast parent material were comparable and “soft zones” were spread in marginal regions of heat affected zones. During creep exposures strain was concentrated in these soft regions and fracture occurred.

If weld joints underwent the creep testing at lower stresses and at temperatures ranged from 575°C to 625°C the creep failure was concentrated in the fine grained HAZ. This critical region consisted of fine ferrite grains and/or subgrains, which were almost free of fine precipitate and with a low dislocation density. At grain and subgrain boundaries coarse secondary phase particles occurred. These small grains /subgrains were intensively strained as a result of dislocation creep and steps were formed at grain boundaries. These steps together with coarse particles in grain/subgrain boundaries served as nucleation centres for cavities. Due to high grain/subgrain diffusion at high temperatures cavities grew, coalescenced and crack propagated in fine grained regions of heat affected zones.

After creep exposures at 600°C and 625°C for about 30 000 hrs cavities were observed not only in the critical HAZ but also in other parts of the creep test specimens. Isolated cavities occurred on prior austenitic grain boundaries in the weld metal and unaffected parent material.

5. Conclusions

The critical zone from a point of view of the creep failure in weld joints of both variant the steel grade P91 – wrought X10CrMoVNb 9 1 steel and cast GX12CrMoVNbN 9 1 steel is the fine grain heat affected zone. Large area of the grain and subgrain boundaries promotes diffusion growth of cavities and the crack propagation. Improvement of the creep strength of weld joints could be achieved by two ways: (i) to reduce a width of HAZ using appropriate welding conditions and (ii) to balance the chemical composition of the parent and filler materials in order to obtain stable fine dispersion of precipitates in all regions of the welded joint, it means also in fine grain heat affected zones.

Acknowledgements

This work was supported by Grant projects number MSM 4771868401 and 1P05OC024 COST 536 from the Ministry of Education, Youth and Sports of the Czech Republic.

References

- [1] Abe, F., Horiuchi, T., Taneike, M. and Sawada, K. *Materials Science and Engineering*, Vol. A 378 (2004), pp. 299–303.
- [2] Bhadeshia, H.K.D.H., *ISIJ International*, Vol. 41, No. 6 (2001), pp. 626–640.
- [3] Moskal, G., Herna, A. and Pasternak, J. In: *Proc. of the 8th Liege Conference Materials for Advanced Power Engineering 2006*. J. Lecomte-Beckers, M. Carton, F. Schubert, P.J. Ennis Eds., Forschungszentrum Jülich GmbH, Liege, 2006. Pp. 1357–1367.
- [4] Jandová, D., Kasl J. and Kanta V. *Materials at High Temperatures*, Vol. 23, No. 3–4, (2006), pp. 165–170.
- [5] Jandová, D., Kasl, J., Folková, E. and Kanta, V. In: *Proc. of the 8th Liege Conference Materials for Advanced Power Engineering 2006*. J. Lecomte-Beckers, M. Carton, F. Schubert, P.J. Ennis Eds., Forschungszentrum Jülich GmbH, Liege, 2006. Pp. 1401–1416.
- [6] Jandová, D., Kasl, J., Kanta, V. and Folková, E. In: *Proc. of the 5th International Conference on Mechanics and Materials in Design*. J.F. Silva Gomes, S.A. Meguid Eds., INEGI-Instituto de Engenharia Mecânica e Gestão Industrial, Leca do Balio, Portugal, 2006. P. 179 [CD- A0409.0408].

A hardness-based creep rupture model for new and service aged P91 steel

David J. Allen and Simon T. Fenton
E.ON UK plc
Power Technology, Nottingham, UK

Abstract

The use of creep rupture data in remanent life assessment is complicated by performance differences between different casts and between new and service degraded materials. Direct tests on suspect components are not always feasible. This paper describes a novel approach which enables the component – specific remanent life to be estimated, and requires only a measurement of hardness at room temperature to characterise the component material.

The basic principles are to normalise the creep test stress by reference to the material flow stress at the test temperature, and to use cast-specific hardness data to estimate the cast-specific flow stress. Statistical analysis shows that rupture data on a range of new P91 materials of varying hardness >200 HV then fall naturally into two regimes. The data at a high ratio of test stress to flow stress can be fitted to a “high n ” line (high Norton exponent), while data at a lower stress ratio fit a “low n ” line. This analysis shows substantially reduced scatter compared with conventional methods. An empirical refinement, allowing the hardness exponent to vary from unity, further reduces scatter and eliminates bias.

The model derived for new P91 materials is then applied to ex-service materials of hardnesses from above 200 HV down to 154 HV. In general, the fit is almost as good as that to the original new material data set. The model thus provides a reasonably accurate and far less onerous alternative to direct component testing in remanent life assessment.

1. Introduction

Creep rupture represents one of the major threats to the integrity of high temperature plant. Despite extensive testing and data assessment, the long term creep performance of high alloy steels such as P91 is still subject to large uncertainties. ECCC (European Creep Collaborative Committee) assessments based on procedures such as PD6605 [1] have generally obtained over-optimistic results. Extrapolated long term creep strength values have consequently had to be revised downwards when actual long term data have become available.

Part of the problem is that short and longer term test data exhibit very different stress-temperature-life relationships. Hence, it may be that any attempt to fit a single mathematical equation within both regimes is simply doomed to failure. It has been shown that censoring out short term data enables a much more realistic assessment of the long term data trend [2, 3].

1.1 Correlation of creep and high temperature tensile strength

Conventional models also treat cast-to-cast material strength variations purely as a cause of scatter. Hence, the basic PD6605 procedure does not identify whether casts of higher tensile strength might reliably be predicted to have higher creep strength. Further, as there is no means of taking into account the effects of in-service degradation and weakening, the procedure cannot aim to predict the remanent creep life of service-aged material.

Creep properties often show some correlation with ambient temperature strength and hardness. Hence, hardness compensation may reduce the level of scatter in creep data assessment [4]. However, it is reasonable to suppose that creep data should correlate most closely with tensile data at the test temperature itself.

When weak ex-service material is creep tested, its performance at high stress is often very poor, while data at lower stresses may be much closer to that on as-manufactured material [5]. A plausible explanation is that in a high stress test, the weakened ex-service material is above or close to its flow stress and suffers rapid plastic deformation and failure, whereas the stronger as-manufactured material remains below its flow stress and hence has a much longer creep life. Thus, high temperature strength and deformation behaviour are of key importance in the high stress regime, whereas other factors may play a more important role at lower stresses.

A simple hardness compensation model, therefore, can only provide a partial explanation of the correlation between creep and tensile properties. What is needed is a model which takes full account of the temperature dependence of high temperature tensile properties, and is able to differentiate between the different regimes, close to and well below the (material dependent) flow stress.

1.2 An ideal creep rupture model

On these arguments, an ideal methodology for creep rupture modelling can be outlined quite simply. A suitable recommendation for consideration by ECCC is that all future creep test programmes should include high temperature tensile testing – on all tested materials, at all creep test temperatures. Since the additional cost will be comparatively minor, it is argued that this should become a standard requirement. It will then become possible to express each individual creep test

data point in terms of the ratio of creep test stress to tensile strength at the test temperature. This will assist the development of models which explore correlations between creep performance and high temperature tensile properties, such as that recently proposed by Wilshire and Scharning [6].

A normalised stress model of creep behaviour should also be able to explore the influence of tensile property variations which arise from quite different causes: the variations between different material casts, and the changes in tensile properties which take place when materials are heat treated, thermally aged, or exposed in long term service. Naturally, it is possible that when the range of potential variations in cast composition, microstructure, and service exposure are all considered, the factors governing creep performance do not all affect high temperature tensile properties in the same way, or indeed at all. Hence, normalised stress modelling may be considered as an experimental development, a key aim being to determine to what extent any simple universal correlation between creep and tensile properties can be justified.

1.3 A practical model for plant application

Unfortunately, this ideal approach cannot yet be widely applied. Extensive creep data sets have been compiled at great expense on key high temperature materials. Generally, however, only a few of these data points are supported by high temperature tensile data. Rather more, though not all, may be supported by ambient temperature mechanical properties data. All too commonly, test material stocks and certificates of manufacture no longer exist, and the manufacturer's original tensile data have been lost.

For operational plant components, a similar lack of proper records is unfortunately not uncommon. However, the material still exists, albeit after service exposure. Physical sampling and testing may be possible, though this is often less readily accomplished with high alloy steels, where the need to carry out heat treatment after weld repair can be a severe disincentive. What is generally feasible, simple and relatively rapid – though requiring care and expertise – is to measure the material hardness in situ. As hardness is correlated with tensile strength, this does indicate a possible option for the development of a normalised stress model.

2. Data

For this project, creep data on as-manufactured P91 materials, for which start-of-life hardness values were available, were compiled from several sources. Six P91 material casts were tested in the UK power industry "ERA 2021" programme, while two further casts were tested in COST 501, and data on high aluminium

Grade 91 material provided by RWE npower [7] was included in later work. Hardness values varied from 203–254 HV. The assessed as-manufactured data set contained a total of 112 failed tests within the temperature range 500–700°C, of which 25 extended beyond 10 000 hours, the maximum being 92 070 hours.

A separate data set on ex-service materials was also compiled. This covered four materials, including two high aluminium components, one low aluminium cast with a non-martensitic microstructure ascribed to faulty post-weld heat treatment on installation, and one low-aluminium cast from a component removed for design modifications. Hardness values after service ranged from 206 HV down to 154 HV. The 17 failed tests generally extended to around 1000 hours.

A third set of data was compiled on materials which had been subjected to additional furnace heat treatment. This included extended tempering and preageing heat treatments which caused softening. It also included a renormalising and light tempering procedure applied to a high aluminium cast of Grade 91 to minimise its thermal exposure and produce a harder product [7, 8].

3. Model

3.1 A cast-specific normalised stress parameter

In the Power Technology model, the applied stress is first normalised by reference to high temperature tensile data on the relevant material grade to produce a dimensionless parameter S , where $S = \text{applied stress} / \text{flow stress}$. In principle, only a single representative cast of material need be tested for this purpose, although averaged data from six casts were used for P91. The normalising tensile strength value is taken as the average of the 0.2% proof stress and the ultimate tensile stress. This provides a simple approximate measure of the material flow stress during testing.

In the original version of this model, the normalising parameter is then effectively made cast-specific by dividing S by the ambient temperature Vickers hardness H_v of the actual material involved. Since hardness is closely correlated with the ambient temperature ultimate tensile strength, for cast-to-cast variations within a specified material grade, hardness should also be quite well correlated to high temperature tensile properties [9]. Hence, the parameter (S/H_v) provides an approximate means of characterising the test stress in relation to the high temperature flow stress properties of a specific P91 material cast, without the need for direct high temperature testing on that cast.

3.2 Hardness data requirements

Laboratory hardness data are obviously preferable when available. However, portable hardness test data on installed components are admissible, with due regard to their potential inaccuracy. At Power Technology, the Krautkramer Microdur Mic10 is the currently preferred portable hardness test instrument. When this equipment is in good working order, is used correctly by a trained operator, is calibrated correctly against matching grade material, is applied to a properly prepared surface, and is subject to suitable data averaging procedures, then the accuracy of the final data can be to within +/- 5 HV or better. It will be recognised that these standards are not always easily achievable, but when high accuracy is called for, it is often achieved with perseverance. One further caveat to be applied when testing P91 is that a thin soft surface layer, generally associated with decarburisation during steelmaking heat treatment, can produce highly misleading results. Surface reparation, if necessary repeated with deliberate material removal, can often be necessary to establish with reasonable confidence that a hardness value which can be taken as representative of the bulk material has finally been obtained.

3.3 Original model

The basis of the model is very simple. The creep rupture equation is based on Norton's law with a constant activation energy:

$$t_r = A \sigma^{-n} \exp (+Q / RT) \quad (1)$$

where t_r is rupture life, A is a constant, σ stress, n the Norton's law constant, Q the activation energy, R the gas constant, and T absolute temperature. However, the normalised stress parameter is substituted in place of σ giving:

$$t_r = B (S / Hv)^{-n} \exp (+Q / RT) \quad (2)$$

where B is a constant.

Curve fitting by multiple regression analysis of the as-manufactured data set is then carried out, with equation (2) in the form:

$$\ln [t_r] - [Q / RT] = \ln (B) - n \ln (S / Hv) \quad (3)$$

The data naturally fall into two regimes, Fig. 1. In each regime, a simple linear Norton's law relationship is found to fit the data well. However, the value of the constant n alters between a "low n " regime at low stress, and a "high n " regime above a critical value of the normalised stress parameter (S / Hv), which is identified empirically from the data plot. A simple physical explanation for this

behaviour, as observed elsewhere [2, 3], may be based on the onset of plastic flow on transition to the high n regime. This then leads to a sharper rise in the deformation rate, and hence a steeper fall in rupture life, with further increases in stress.

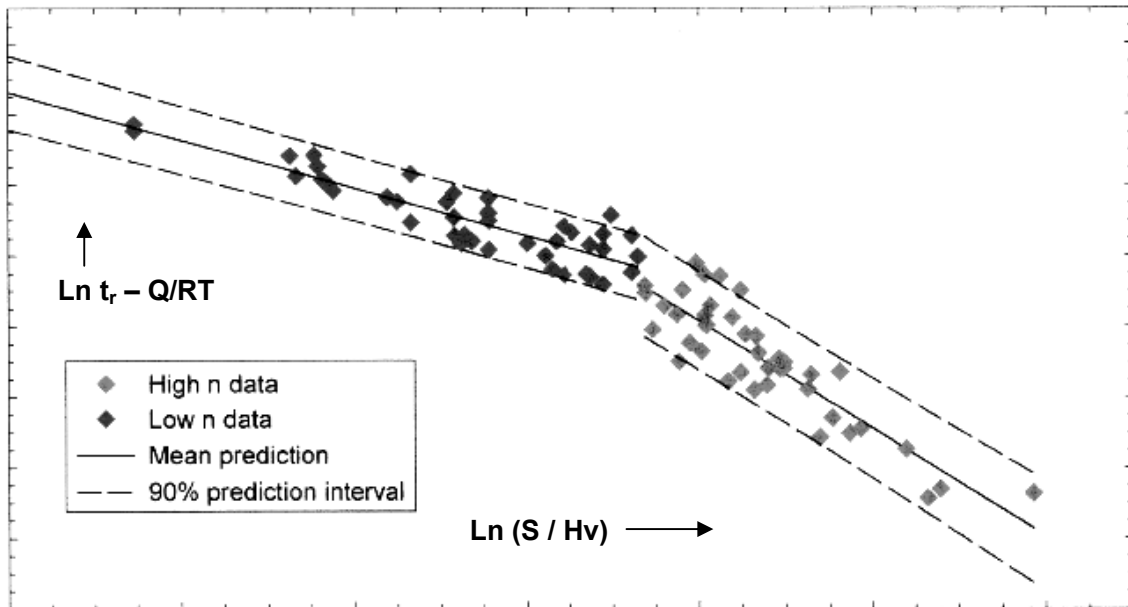


Figure 1. Data fit with original model.

The activation energy obtained from the data fit was 285 KJ/mol, fairly close to the activation energy for self-diffusion. Conventional creep models tend to obtain higher values. In this model, the flow stress is temperature-dependent. The two axes in Fig. 1 thus incorporate two quite separate factors which both act to determine the temperature dependence of creep phenomena – the diffusional activation energy (y axis), and temperature-dependent tensile properties (x axis). Since the new model obtains a physically realistic diffusional activation energy value, it appears to be soundly based. The predicted form of temperature dependence is rather different from that obtained when a simple effective activation energy term is used in data fitting. Potentially, therefore, the new model may provide a better data fit over a varying temperature range.

The effectiveness of this model may be compared with the PD6525 formula of Orr and Burton [10]. The PD6525 formula over-predicts life for softer materials and under-predicts life for harder materials, Fig. 2 (a). The original hardness model substantially reduces scatter, Fig. 2 (b). However, the bias towards life underprediction for harder materials is not wholly eliminated.

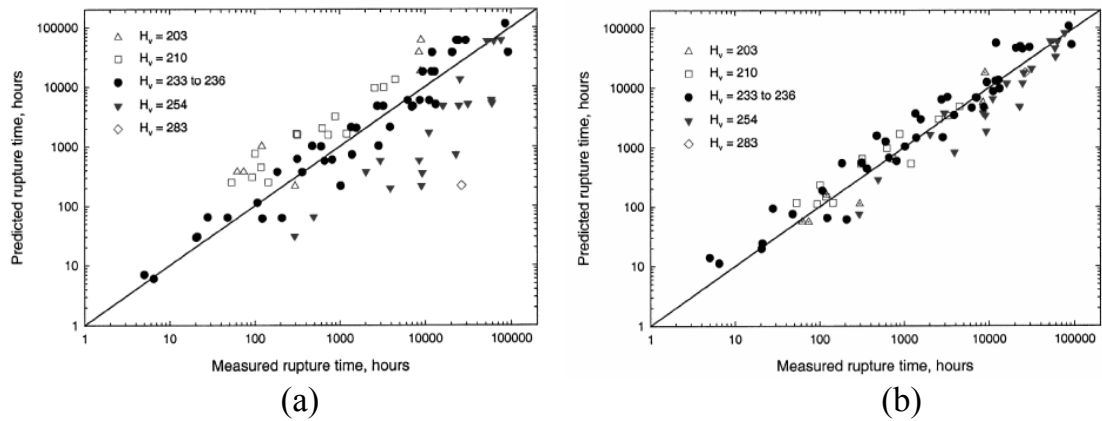


Figure 2. Predicted versus measured life: (a) PD6525 (b) original hardness model.

3.4 Improved model

The supposition that high temperature flow stress should be proportional to ambient temperature hardness is physically reasonable, but may not be exactly correct. The above results suggest that a simple empirical modification, replacing H_v with H_v^p such that $p > 1$, could be preferable. Then:

$$\ln [t_r] - [Q / RT] = \ln (B) - n \ln (S) + pn \ln (H_v) \quad (4)$$

For this model, multiple regression data fits were carried out on the assumptions that the value of the activation energy is the same in the low n and high n regimes, but the values of the exponent p may differ. For the as-manufactured data set, the resulting p values in the low n and high n regimes both fall within a range from 1.4 to 1.5. The activation energy Q is further reduced to 260 kJ/mol, and the values of n are also slightly reduced, Fig. 3.

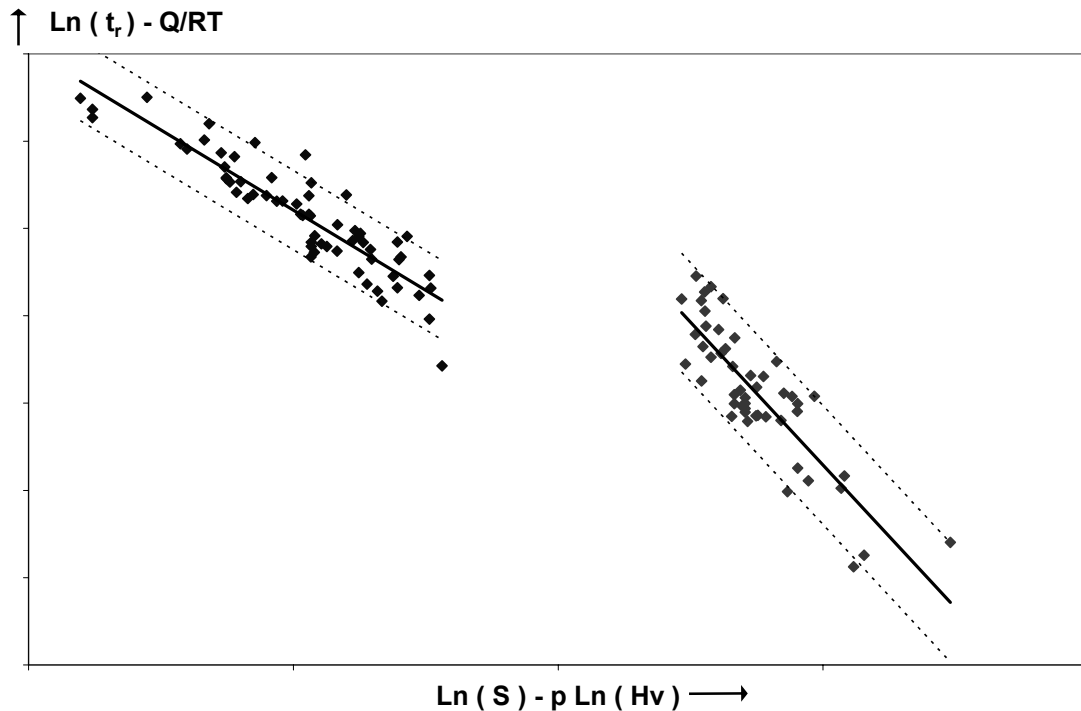


Figure 3. Data fit with the improved model.

The derived p values for the two regimes are quite similar. They may well differ only because of random data variability. It seems plausible that $p \neq 1$ because high temperature tensile properties are not quite linearly proportional to ambient temperature tensile and hardness properties. Alternatively, it may be that the correlation between creep strength and high temperature tensile strength is not precisely linear.

The improved model further reduces data scatter. It also predicts a somewhat reduced dependence of creep life on both stress and temperature. It may be noted that creep data sets usually show a strong inverse correlation between stress and temperature, with low temperature tests predominantly at high stress and vice versa. Hence, there is a risk that an imperfect data analysis will tend to confuse the two factors. For example, an excessive activation energy value will tend to result in the overprediction of creep life in low temperature tests: but an excessive value for the stress exponent n will (broadly) tend to compensate for that error by reducing predicted creep life in high stress tests. Conventional creep rupture models frequently do predict high temperature dependence, e.g. with an activation energy greater than that for self-diffusion, or equivalently, with a Larson-Miller constant much greater than $C=20$. It is tempting to conclude that such models may be inherently liable to overpredict both Q and n . A physics-based model, which incorporates the temperature dependence of flow stress in its formulation, may thus be necessary to minimise such errors.

4. Application

4.1 Validation

The proposed model was validated by expressing each data point as a residual error value, $\log(\text{measured life} / \text{predicted life})$, and then plotting these residual values against stress, temperature, hardness, and stress-temperature interaction parameters. The graphs for the as-manufactured data set showed some inevitable scatter, but no significant trends. Hence, the model fitted the data well. The plot against hardness shows that whilst certain casts show some tendency toward systematic under- or over- prediction, most are predicted quite well, with mean residual errors close to zero, Fig. 4.

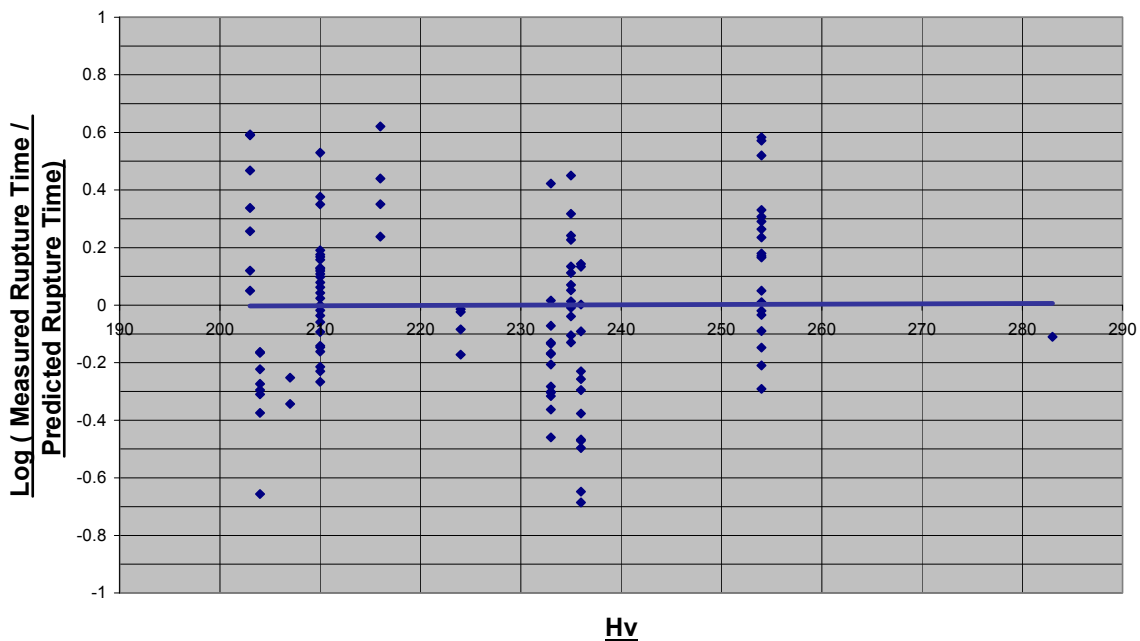


Figure 4. *Log measured / predicted life versus hardness – as-manufactured data.*

4.2 Remanent life prediction for ex-service materials

The predictive equation obtained from the as-manufactured data set was then applied to the whole data set, including softer ex-service materials for which it had not been derived, Fig. 5. Inevitably, the fit is then poorer, but the slope of the trendline is surprisingly slight.

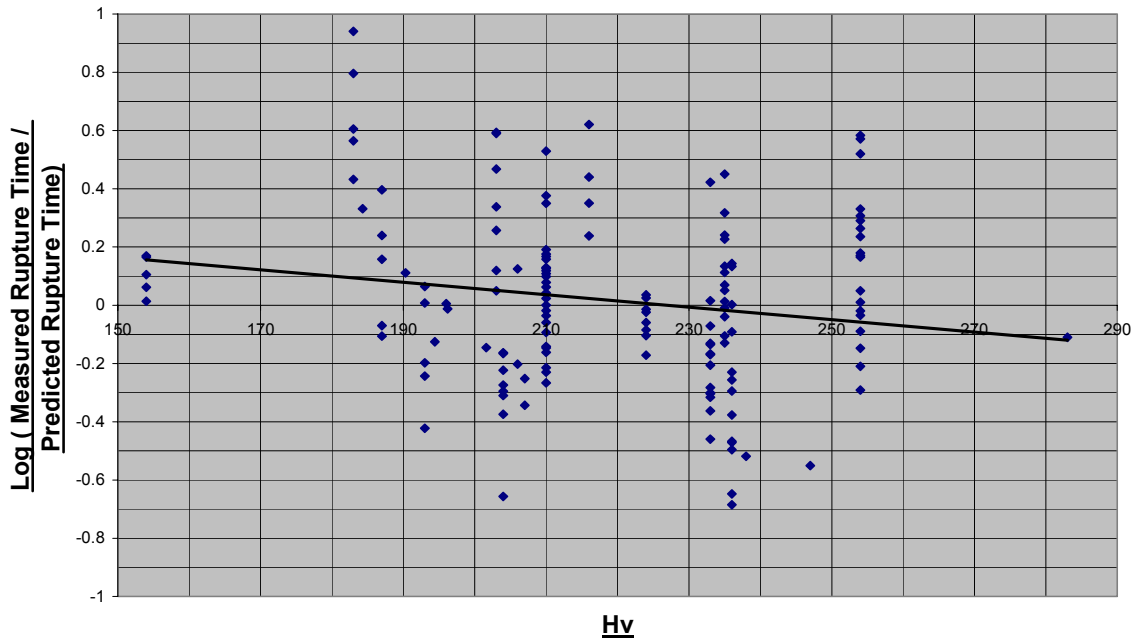


Figure 5. Log measured / predicted life versus hardness- all data.

Fig. 6 (a) shows the results of applying the improved ($p \neq 1$) model equation derived from the as-manufactured data to the ex-service materials alone, while Fig. 6 (b) shows the corresponding results with the original ($p = 1$) model. Whereas the original model substantially over-predicts the creep lives of these soft ex-service materials, the improved model appears to predict their behaviour quite accurately, both for non-martensitic (154 HV) and high aluminium (187 HV, 193 HV) materials.

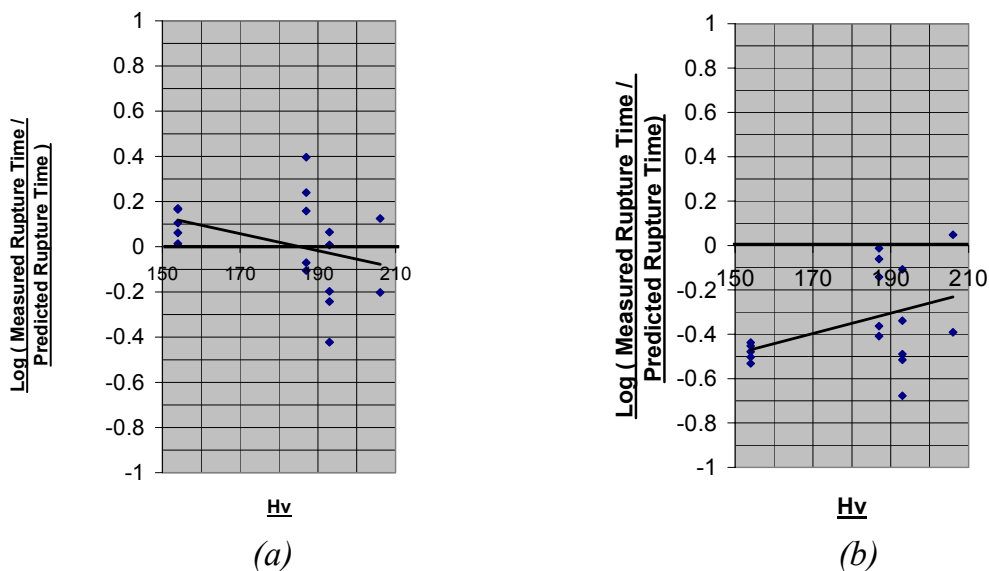


Figure 6. Log measured / predicted life versus hardness for ex-service data only: (a) with the improved model ($p \neq 1$), (b) with the original model ($p = 1$).

The indications are, therefore, that the improved model can be used to estimate the remanent lives of soft ex-service P91 components with reasonable accuracy. At present, this conclusion is tentative, and so a conservative allowance must be made when the model is used to predict remanent life. Further creep data will be required to clarify the applicability of the model to ex-service materials and, if appropriate, reduce the conservative allowance required.

Somewhat surprisingly, these results seem to bear out the simplistic supposition that for P91, creep and tensile properties may be inextricably linked, such that any factor which alters tensile properties will have a corresponding effect on creep properties, whether that factor be composition, microstructure, or even service degradation. Concluding this paper, two further factors are analysed. One again accords with this supposition, but the other does not. The results thus provide further evidence on both the strengths and limitations of the model.

4.3 Influence of aluminium content

Aluminium is known to have a marked detrimental influence on the creep properties of P91 (11). It ties up nitrogen in large aluminium nitride precipitates, thereby impairing formation of the fine dispersion of vanadium carbonitride precipitates required for creep strengthening. Its addition also appears to promote softening on tempering. However, while there is some tendency toward lower hardness for higher aluminium contents, the correlation seems rather weak and subject to scatter. It would not be unreasonable, therefore, to suppose that the creep life prediction equation (4) might be improved by including a separate aluminium term, as well as the hardness term.

Fig. 7 however shows that when residual error is plotted against aluminium content, there is no trend at all. It must be concluded that the detrimental effect of aluminium on creep rupture of parent P91 is, in fact, fully accounted for in terms of its effect on hardness. This might be because its effect on precipitation strengthening affects dislocation behaviour equally in tensile and creep processes.

Two points of clarification should be added here. First, it should not be inferred that hardness control should replace restrictions on aluminium content. On the contrary, Fig. 7 is fully consistent with the finding [11] that aluminium promotes both softening and loss of creep strength. Secondly, a caveat must be entered with regard to weld HAZ cracking, which is the actual damage mechanism now encountered quite widely on plant. This may not necessarily be equally simply correlated with parent material hardness alone, irrespective of aluminium content. Weld HAZ performance does not always simply mirror that of the parent material [7]. The relationships between creep performance, parent (or HAZ) hardness, and aluminium content may therefore be rather different for the case of weld HAZ cracking.

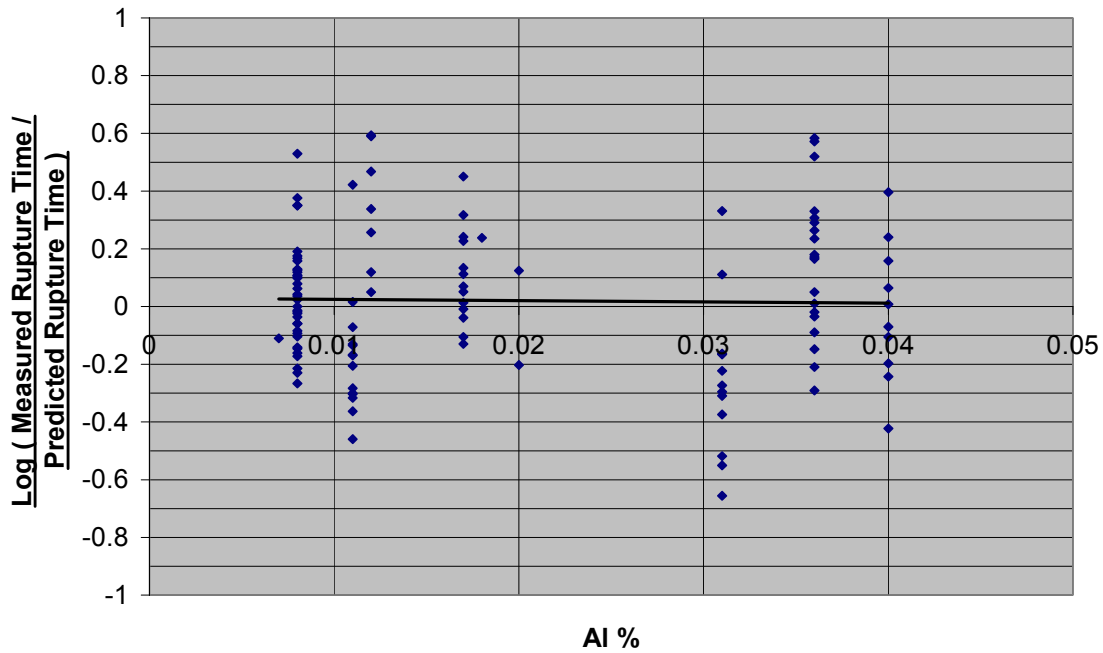


Figure 7. Log measured / predicted life versus aluminium content – all data.

4.4. Influence of abnormal tempering conditions

By contrast, the residual error data for the abnormally furnace heat treated materials show a clear trend, and the hardness model predictions for these data points are less accurate, Fig. 8. Overtempering causes substantial loss of hardness but a lesser reduction in creep strength, and so the model under-predicts creep life. Conversely, renormalising and undertempering causes a significant increase in hardness but a relatively slight improvement in creep strength, and so the hardness model over-predicts creep life.

Materials which have been subjected to an abnormal level of tempering thus fail to obey the same correlation between creep rupture strength and tensile strength as that which applies to normally tempered materials. However, a plausible explanation is that this is due to the effects of metallurgical degradation during the creep test itself. Thus, an undertempered material is metallurgically unstable, and degrades substantially during the creep test. Creep life is influenced by this degradation, but as-supplied tensile properties are not. Conversely, overtempered material exhibits an abnormally low level of metallurgical instability during the creep test. Its creep performance is consequently rather better than would have been predicted from its poor tensile properties prior to creep testing.

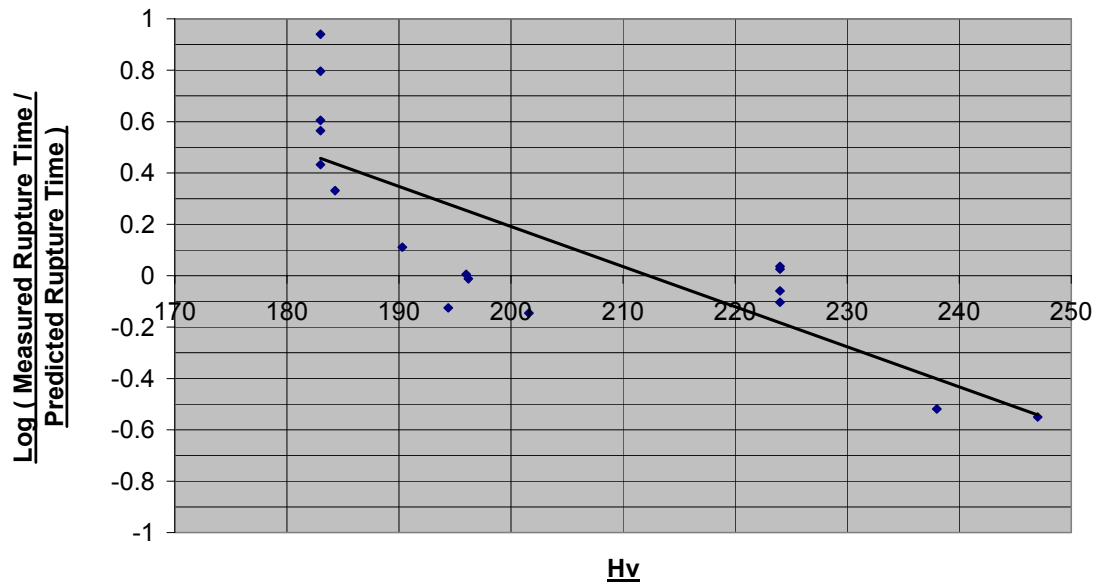


Figure 8. Log measured / predicted life versus hardness – abnormally tempered materials.

On these arguments, the data of Fig. 8 do not reveal any fundamental flaw in the model. There is merely a difficulty in that creep properties should ideally be compared with tensile properties as they vary throughout the creep life, rather than simply measuring tensile properties at start of life. Variations in initial tempering conditions do, therefore, introduce a slight element of uncertainty into the model. However, it may be possible to develop correction procedures as required to estimate the remanent life of P91 components with a suitable level of confidence.

5. Conclusions

1. A normalised stress creep model, in which creep test stress is normalised by reference to the material-specific high temperature tensile strength, provides a sound physical basis for the analysis of creep data.
2. The model identifies that two separate temperature-dependent factors are involved in creep phenomena: thermally activated creep deformation, and temperature-dependent tensile properties. When the latter factor is included in modelling, a more realistic activation energy for creep deformation, close to that for self-diffusion, is obtained.
3. A practical hardness-based normalised stress model, in which cast-specific tensile strength information is incorporated via a simple measurement of room temperature hardness, has been developed. One advantage of this model is that direct high temperature testing on the cast of material to be assessed is

not required. A second advantage is that creep strength need not be assumed linearly proportional to hardness. Instead, a hardness exponent $p \neq 1$ can be optimised in the course of data analysis, improving data fitting and flexibility.

4. The modelling equation, derived from creep test data obtained on a range of as-manufactured P91 materials, then also appears to provide a reasonably accurate fit to creep data on softer ex-service materials. Hence, with a suitable conservative allowance to cover uncertainties, the model can be used to make a cast-specific estimate of the remanent life of an in-service P91 component, provided only that its hardness is known.
5. The simple hypothesis that creep rupture strength may be uniquely correlated with variations in tensile properties, irrespective of whether these are due to differences in composition, microstructure, or service exposure, thus seems to apply remarkably well to P91 parent material. It may not, of course, apply universally to all materials. Indeed, the hypothesis might be expected to fail with materials where high temperature tensile behaviour is ductile, but long term creep behaviour is affected by an embrittlement mechanism.
6. An analysis of the influence of aluminium also confirms the model. Aluminium is known to degrade creep properties and to promote softening. Examination of the data shows that the hardness model takes full account of these parallel factors. Hence, when hardness is taken into account, no separate allowance for the effect of aluminium on creep performance is required.
7. The one factor identified which does not conform with the standard modelling equation, but instead alters the form of the correlation between creep and tensile properties, is abnormal variation in the extent of initial tempering. Variations in tempering conditions have disproportionately large effects on tensile properties when compared to creep properties. This result may be understood by considering the effects of metallurgical instability during the creep test. This complication introduces some uncertainty into the model, but it may prove possible to develop correction procedures.

Acknowledgements

Thanks are due to Steve Brett of RWE npower for provision of creep data on abnormally tempered Grade 91 material, and to James Mithen for data analysis. This paper is published by permission of E.ON UK plc.

References

- [1] PD 6605-1:1998, “Guidance on methodology for assessment of stress-rupture data – Part 1: Procedure for derivation of strength values”, British Standards Institute.
- [2] Allen, D.J. and Servetto, C. “An Assessment of Creep Rupture Data on Steel E911”, 7th Liege Conference on Materials for Advanced Power Engineering, 2002. Pp. 1487–1496.
- [3] Kushima, H., Kimura, K. and Abe, F. (2002), “Long Term Creep Strength Prediction of High Cr Ferritic Creep Resistant Steels”, 7th Liege Conference on Materials for Advanced Power Engineering, 2002. Pp. 1581–1590.
- [4] Townsend, R.D., Timmins, R., Finch, D.M. and Brear, J.M. “Microstructural Stability of Creep Resistant Alloys for High Temperature Applications” No. 2, The Institute of Materials, London, (1998). P. 145.
- [5] Ennis, P.J., Schuster, H., and Bendick, W., (1995), “A Comparison of the Creep Rupture Behaviour of New and Service Exposed Low Alloy Steels”, *Matls at High Temps.*, 13, pp. 87–92.
- [6] Wilshire, B., and Scharning, P.J. (2007), Design Data Prediction For Grade 92 Steel, PVP-2007-26754, submitted to CREEP8: Eighth International Conference on Creep and Fatigue at Elevated Temperatures, July 22–26, 2007, San Antonio, USA.
- [7] Allen, D.J., Harvey, B., and Brett, S.J. (2005) ”FOURCRACK – An Investigation of the Creep Performance of Advanced High Alloy Steel Welds”, Proc. ECCC Creep Conf., London, UK, Sept 2005. Pp. 772–781.
- [8] Brett, S.J. RWE npower, private communication.
- [9] Metals Handbook, Desk Edition, ASM, 1987. Pp. 1–60.
- [10] Orr, J. and Burton, D. Experience in Data Collection and Assessment for Material Standards. ECSC Information Day: The Manufacture and Properties of Steel 91 for the Power Plant and Process Industries, VDEh, Dusseldorf, November 5, 1992.
- [11] Brett, S.J. “Identification of Weak Thick Section Modified 9Cr Forgings in Service”, Proc. 3rd Conf. on Advances in Materials Technology for Fossil Power Plant, Swansea, 2001. Pp. 343–351.

Impurity effects on heat-to-heat variation in creep life for some heat resistant steels

F. Abe, H. Tanaka and M. Murata

National Institute for Materials Science, Tsukuba, Japan

Abstract

Heat-to-heat variation in creep life has been investigated for ferritic-pearlitic 2.25Cr-1Mo, tempered martensitic 12Cr-1Mo-1W-0.3V, austenitic 18Cr-8Ni, 18Cr-12Ni-Mo, 18Cr-10Ni-Ti and 18Cr-12Ni-Nb steels, using long-term creep data in NIMS Creep Data Sheets. The variation of available nitrogen concentration, defined as the concentration of nitrogen free from AlN and TiN, is a main factor for the heat-to-heat variation in creep life of 12Cr-1Mo-1W-0.3V, 18Cr-8Ni and 18Cr-12Ni-Mo steels, where certain amount of dissolved nitrogen remains after heat treatment. The heat-to-heat variation in creep life of 18Cr-10Ni-Ti and 18Cr-12Ni-Nb steels is explained by the variation of boron content and of grain size, respectively.

1. Introduction

In the NIMS Creep Data Sheet Project, long-term creep and creep rupture tests have been carried out using about ten heats in each material, where the heat means different ingots and different products [1]. The materials have been sampled from commercial stocks, which were produced in Japan. The creep rupture data sometimes exhibit large scattering as shown by about one order of magnitude difference between the strongest and weakest heats [2–7]. The large scattering of creep rupture data makes it difficult to assess satisfactorily long-term creep strength. Because the NIMS Creep Data Sheets contain a full set of data, such as creep rupture data, minimum creep rates, time to tertiary creep, short-time tensile data and optical micrographs, together with the details of materials production procedures and chemical compositions, we can analyze the origins of the difference in creep strength among different heats based on the NIMS Creep Data Sheets.

The purpose of the present research is to investigate metallurgical factors causing the heat-to-heat variation in creep life for some principal ferritic and austenitic steels, using creep data in the NIMS Creep Data Sheets.

2. Heat-to-heat variation in time to rupture

2.1 12Cr-1Mo-1W-0.3V steel

Fig. 1 shows the creep rupture data for 12Cr-1Mo-1W-0.3V steel at 550 and 600°C by different symbols for the nine heats [1]. The heat-to-heat variation in time to rupture is very large as shown by about one order of magnitude difference between the strongest and weakest heats at long times, while each heat exhibits the distinct stress dependence of time to rupture. The chemical compositions of 12Cr-1Mo-1W-0.3V steel examined are given in Table 1, together with the requirement of chemical compositions for this steel. The variation of alloying elements C, Si, Mn, P, S, Ni, Cr, Mo, W and V, which are specified by JIS, is not large among the nine heats. Grain size and hardness of as-received materials, namely, after heat treatment were not different so much among the nine heats. Therefore, these parameters are excluded as the main explanation of the observed heat-to-heat variation in time to rupture. The contents of impurity Al and nitrogen, which are not specified by JIS, are rather low but they are different so much among the nine heats; about 8 times and 2 times difference for Al and nitrogen, respectively, between the highest and lowest values. It has been well known that nitrogen has a beneficial effect on long-term creep strength of heat resistant steels but that Al and Ni cause deteriorative effects [8–11].

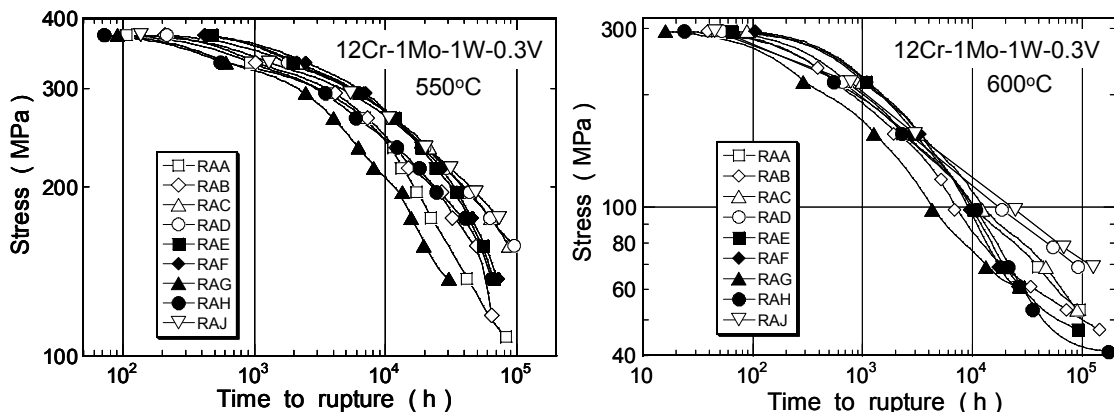


Figure 1. Creep rupture data for 12Cr-1Mo-1W-0.3V steel at 550 and 600°C.

Table 1. Chemical compositions of 12Cr-1Mo-1W-0.3V steel, JIS SUH616 [1].

	(mass%)															
	C	Si	Mn	P	S	Ni	Cr	Mo	Cu	W	V	Co	Ti	Al	N	N _{AV} (at%)
requirement by JIS	0.20 - 0.25	≤0.25	0.50 - 1.00	≤0.040	≤0.030	0.50 - 1.00	11.00 - 13.00	0.75 - 1.25		0.75 - 1.25	0.20 - 0.30					
RAA	0.20	0.50	0.59	0.021	0.007	0.78	11.0	1.10	0.09	1.07	0.21	0.04	0.0003	0.030	0.015	-0.0026
RAB	0.23	0.37	0.55	0.023	0.008	0.64	11.3	1.20	0.11	0.96	0.22	0.04	0.0003	0.039	0.019	-0.0053
RAC	0.23	0.30	0.59	0.028	0.008	0.67	12.1	1.22	0.12	1.09	0.24	0.04	0.0007	0.020	0.021	0.0412
RAD	0.19	0.33	0.87	0.029	0.011	0.90	11.4	0.91	0.11	1.07	0.24	0.12	0.0003	0.007	0.020	0.0644
RAE	0.21	0.53	0.80	0.029	0.009	0.68	12.3	0.94	0.14	1.10	0.23	0.04	0.0001	0.040	0.020	-0.0031
RAF	0.21	0.41	0.60	0.026	0.009	0.67	12.9	0.93	0.13	0.93	0.21	0.15	0.0001	0.023	0.021	0.0356
RAG	0.23	0.40	0.73	0.009	0.008	0.68	11.7	0.92	0.15	0.90	0.27	0.04	0.0006	0.037	0.032	0.0495
RAH	0.25	0.35	0.70	0.016	0.008	0.75	11.9	0.99	0.03	0.95	0.28	0.05	0.0011	0.027	0.021	0.0263
RAJ	0.23	0.32	0.69	0.016	0.009	0.68	11.2	1.00	0.03	1.13	0.30	0.04	0.0001	0.005	0.029	0.1042

Fig. 2 shows the time to rupture of 12Cr-1Mo-1W-0.3V steel at 550°C, as functions of Al, nitrogen and Ni contents. There is no distinct relationship between the time to rupture and the Al, nitrogen and Ni contents, suggesting these parameters are excluded as the main explanation of the observed heat-to-heat variation in time to rupture. Taking into account that dissolved nitrogen or fine vanadium nitrides are beneficial for creep strength and that the amount of dissolved nitrogen and fine vanadium nitrides are reduced by the formation of AlN and TiN, Fig. 3 shows the time to rupture of 12Cr-1Mo-1W-0.3V steel at 550°C, as a function of available nitrogen concentration. The available nitrogen concentration is defined as the concentration of dissolved nitrogen free from AlN and TiN. Al and Ti are strong nitride forming elements than vanadium. Assuming the formation of stoichiometric compounds of AlN and TiN, the available nitrogen concentration N_{AV} is described as

$$N_{AV} = N - Al - Ti \text{ (at\%)} \quad (1)$$

where N , Al and Ti are the concentrations of total nitrogen, Al and Ti, respectively, in at%. The evaluated N_{AV} is also given in Table 1. In Fig. 3, the time to rupture simply increases with increasing available nitrogen concentration, which becomes more significant at low stress and long time conditions. This suggests that the formation of AlN and TiN takes place for up to long times over 10^5 h during creep.

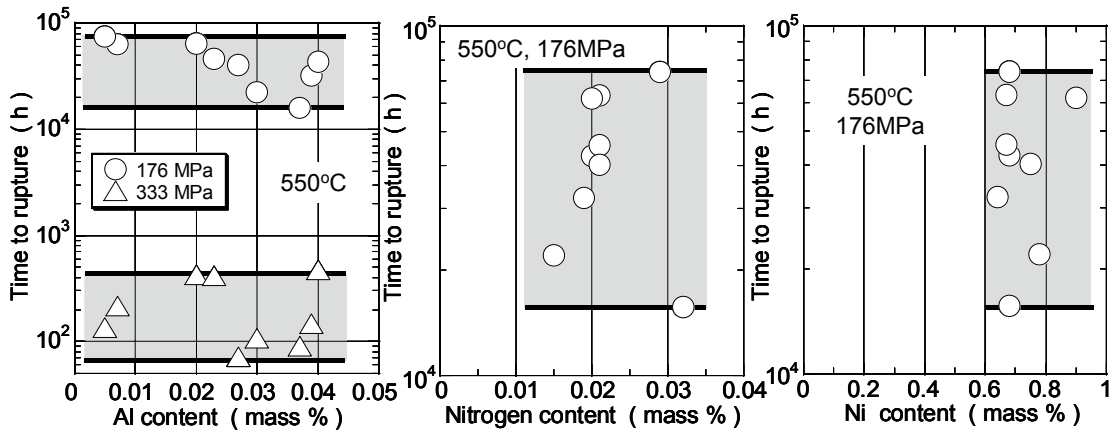


Figure 2. Time to rupture of 12Cr-1Mo-1W-0.3V steel at 550°C, as functions of Al, nitrogen and Ni contents.

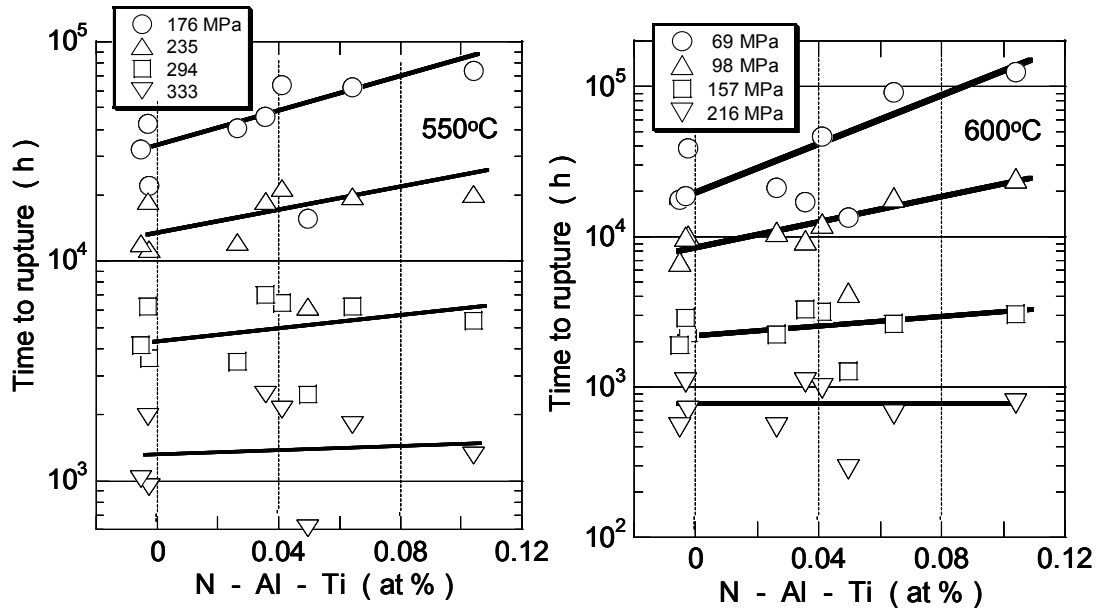


Figure 3. Time to rupture of 12Cr-1Mo-1W-0.3V steel at 550 and 600°C, as a function of available nitrogen concentration given by Eq. (1).

The heat-to-heat variation in creep deformation behavior was examined for the heats RAA, RAG and RAJ, which contained 0.030, 0.037 and 0.005 mass% Al, respectively. This is shown in Fig. 4 in the form of creep rate versus time curves and creep rate versus strain curves at 650°C and 69 MPa. The available nitrogen concentration was -0.0026, 0.0497 and 0.1042 at% for heats RAA, RAG and RAJ, respectively. The creep and creep rate curves consist of the primary or transient creep region, where the creep rate decreases with time, and of the tertiary or acceleration creep region, where the creep rate increases with time after reaching a minimum creep rate. There is substantially no steady-state region, where the creep rate is constant. The present author has revealed for martensitic 9Cr steels that the transient creep is basically a consequence of the movement and annihilation of a high density of dislocations produced by martensitic transformation during cooling after normalizing and that the acceleration creep is a consequence of gradual loss of creep strength due to the microstructure evolution [12–13]. In Fig. 4, the creep rates in the transient region decreases with increasing available nitrogen concentration. The onset of acceleration creep is retarded to longer times with increasing available nitrogen concentration. Higher available nitrogen concentration causes larger amount of vanadium nitride precipitation during tempering, which decreases the creep rates due to precipitation strengthening and also stabilizes martensitic microstructure. The stabilization of martensitic microstructure retards the onset of acceleration creep. Once the acceleration creep begins, the acceleration of creep rate $d \ln \dot{\epsilon} / d \epsilon$ is substantially the same among the three heats.

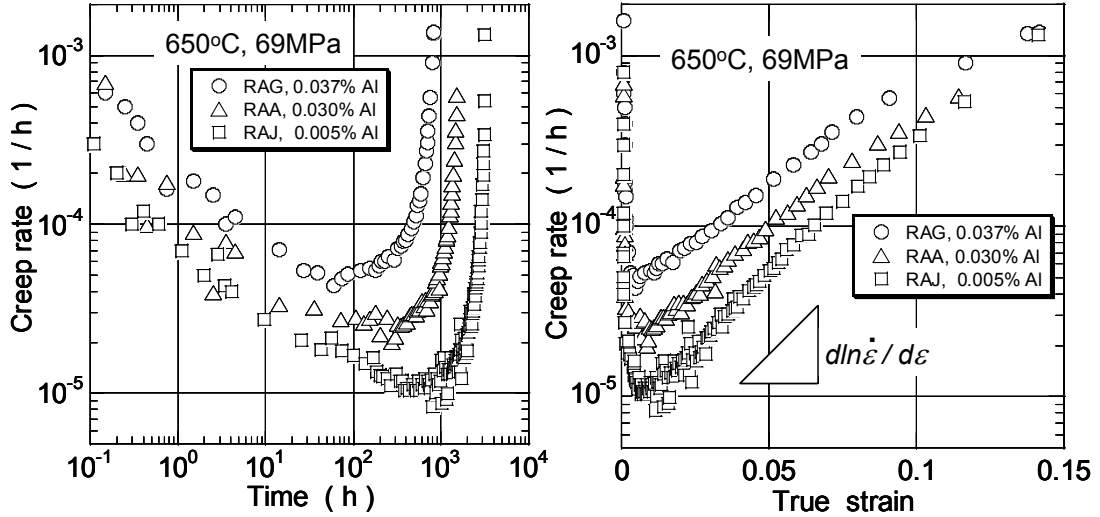


Figure 4. Creep rate versus time curves and creep rate versus strain curves of heats RAA, RAG and RAJ of 12Cr-1Mo-1W-0.3V steel at 650°C and 69 MPa.

Fig. 5 shows the relationship between the time to rupture and minimum creep rate (Monkman-Grant plot) and that between the time to tertiary creep and minimum creep rate for the 12Cr-1Mo-1W-0.3V steel at 500 to 650°C. The time to tertiary creep corresponds to the duration of transient creep. The relationship can be described for all the heats by unique lines for both the time to rupture and the time to tertiary creep. For all the heats, the relationship between the time to rupture t_r and minimum creep rate $\dot{\epsilon}_{min}$ is described by

$$t_r = c / (\dot{\epsilon}_{min})^m \quad (2)$$

where c and m are constants of $c = 11.78$ and $m = 0.76$. On the other hand, the relationship between the time to tertiary creep and minimum creep rate $\dot{\epsilon}_{min}$ is also described for all the heats by

$$(time\ to\ tertiary) = c' / (\dot{\epsilon}_{min})^{m'} \quad (3)$$

$$(\dot{\epsilon}_{min}) = [c' / (time\ to\ tertiary)]^{1/m'} \quad (4)$$

where $c' = 6.78$ and $m' = 0.76$. The minimum creep rate dependence of the time to rupture, $m = 0.76$, is the same as that of the time to tertiary creep, $m' = 0.76$.

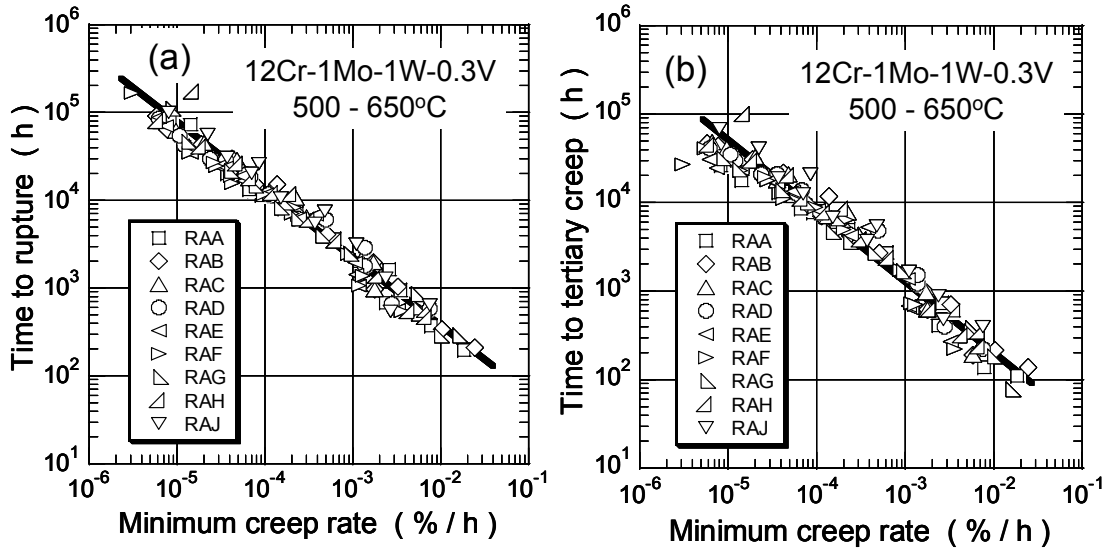


Figure 5. Relationship (a) between time to rupture and minimum creep rate and (b) between time to tertiary creep and minimum creep rate for 12Cr-1Mo-1W-0.3V steel at 500 to 650°C.

The minimum creep rate is inversely correlated with the time to tertiary creep, namely, the duration of transient creep, and is given by a unique equation of Eq. (4) for all the heats. Fig. 6 shows the time to tertiary creep data at 550°C, showing a large heat-to-heat variation similar as the time to rupture shown in Fig. 2. The present results indicate that the observed large heat-to-heat variation in time to rupture results from the heat-to-heat variation in minimum creep rate as can be seen from the Monkman-Grant relationship of Eq. (2), which results from the heat-to-heat variation in time to tertiary creep given by Eq. (4).

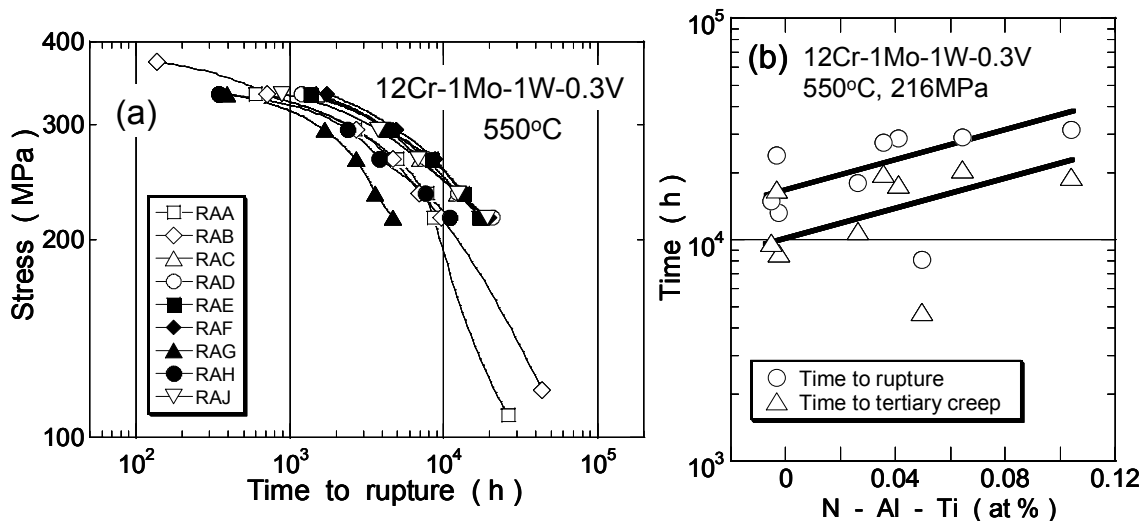


Figure 6. (a) Time to tertiary creep for 12Cr-1Mo-1W-0.3V steel at 550°C and (b) time to rupture and time to tertiary creep at 550°C and 216 MPa as a function of available nitrogen concentration.

Yokoi and co-workers [14] observed that aluminum nitrides AlN formed in the heats RAB and RAG containing high aluminum content during thermal aging at 600°C. Their results indicated that the nitrogen concentration in solution was decreased by the precipitation of AlN in the heats containing high aluminum content during aging. The TEM observations showed that a recovered zone of martensitic microstructure, where fine precipitates and high density of dislocations were disappeared, started to form along prior austenite grain boundaries [15–16]. The local softening due to the development of recovered zone along prior austenite grain boundaries is mainly responsible for the development of acceleration creep.

It is concluded that the preferential recovery of martensitic microstructure is promoted in the vicinity of prior austenite grain boundaries of the heats containing high aluminum content during creep, because of reduced amount of dissolved nitrogen and fine vanadium nitrides due to the formation of aluminum nitrides AlN. The preferential recovery of martensitic microstructure promotes the onset of acceleration creep, which results in higher minimum creep rate and shorter time to rupture in the heats containing high aluminum content. This is a main reason causing the observed heat-to-heat variation in time to rupture.

2.2 2.25Cr-1Mo steel and 9Cr-1Mo steel

The ferritic-pearlitic 2.25Cr-1Mo steel [1] exhibits the small variation in time to rupture at long times above 10^4 h as shown in Fig. 7, while that of ferritic 9Cr-1Mo steel [1] becomes increased with test duration but it is much less than that of 12Cr-1Mo-1W-0.3V steel.

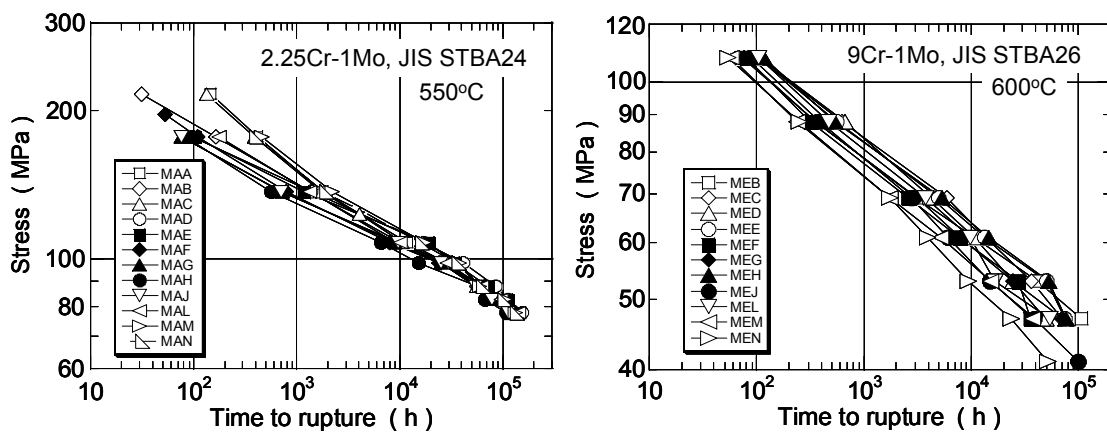


Figure 7. Creep rupture data for 2.25Cr-1Mo steel specified as JIS STBA24 at 550°C and those for 9Cr-1Mo steel specified as JIS STBA26 at 600°C.

Fig. 8 shows the concentration of nitrogen and Al in the respective heats of 2.25Cr-1Mo, 9Cr-1Mo, 12Cr-1M-1W-0.3V and austenitic 18Cr-8Ni steels examined in the NIMS Creep Data Sheet Project. The variation of nitrogen and

Al contents increases with increasing Cr content. The narrow range of nitrogen and Al contents in the 2.25Cr-1Mo and 9Cr-1Mo steels than in the 12Cr-1Mo-1W-0.3V steel causes the smaller variation in time to rupture in the 2.25Cr-1Mo and 9Cr-1Mo steels than in the 12Cr-1Mo-1W-0.3V steel.

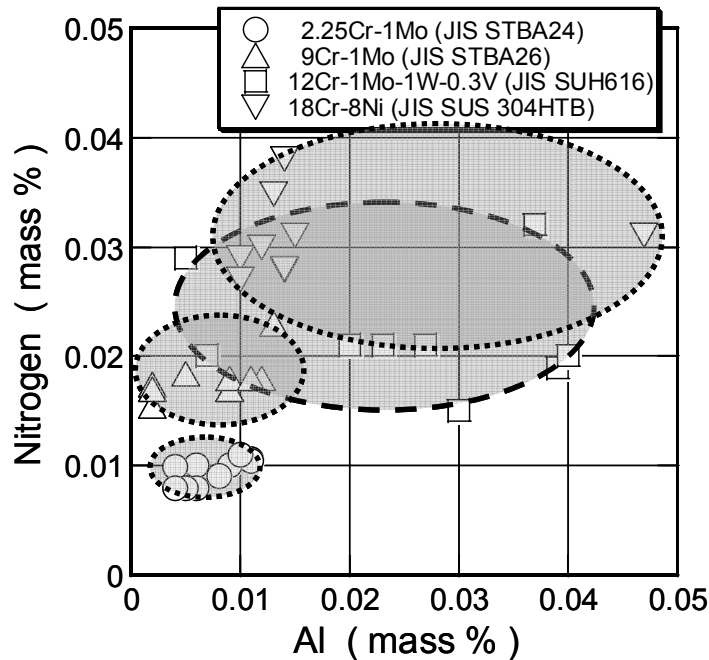


Figure 8. Contents of nitrogen and Al in respective heats in the steels.

2.3 18Cr-8Ni, 18Cr-12Ni-Mo, 18Cr-10Ni-Ti and 18Cr-12Ni-Nb steels

Fig. 9 shows the creep rupture data for austenitic 18Cr-8Ni (JIS SUS 304HTB), 18Cr-12Ni-Mo (JIS SUS 316HTB), 18Cr-10Ni-Ti (JIS SUS 321HTB) and 18Cr-12Ni-Nb (JIS SUS 347HTB) steels at 700°C, appeared in NIMS Creep Data Sheets. The heat-to-heat variation in time to rupture of the 304HTB and 316HTB steels is quite different from that of the 321HTB and 347HTB steels. The heat-to-heat variation in time to rupture of the 304HTB and 316HTB steels is not large at short times but it becomes more significant with increasing test duration at long times above 10^4 h. On the other hand, the heat-to-heat variation in time to rupture of the 321HTB and 347HTB steels is very large even at short times and this continues for up to long times over 10^5 h.

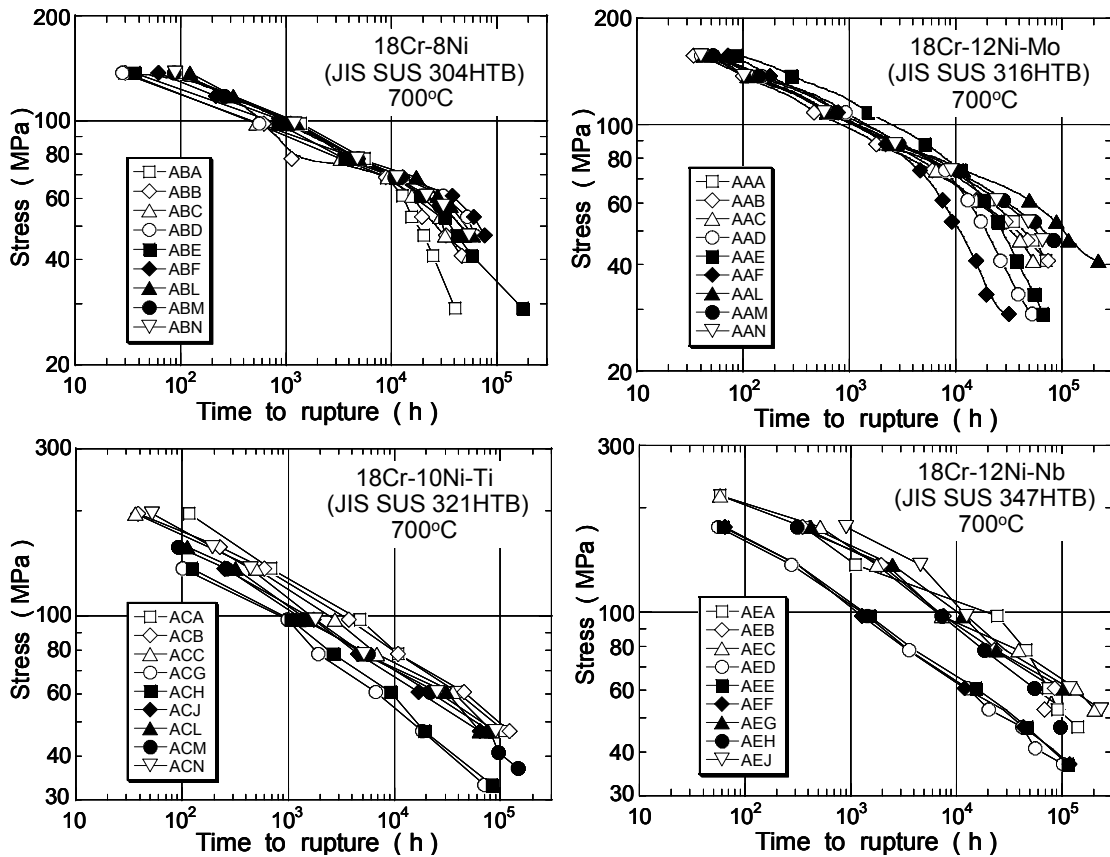


Figure 9. Creep rupture data for the austenitic steels at 700°C.

Fig. 10 shows the contents of Ti and Nb and that of nitrogen in the four steels. In the 304HTB and 316HTB steels, the contents of Ti and Nb are much less than that of nitrogen and hence even if impurities Ti and Nb form inclusions of nitrides at high temperature, certain amount of dissolved nitrogen remains after heat treatment and hence the concept of available nitrogen concentration can be applied to these steels. In the 321HTB and 347HTB steels, on the other hand, the content of Ti and Nb is much higher than that of nitrogen, because these steels are alloyed with 0.39 to 0.55 mass% Ti and 0.72 to 0.88 mass% Nb, respectively. We observed a large number of inclusions of Ti- and Nb-carbonitrides in the 321HTB and 347HTB steels, respectively, after heat treatment, indicating substantially no dissolved nitrogen. Therefore, the concept of available nitrogen concentration cannot be applied to these steels and other factors cause the observed heat-to-heat variation in time to rupture.

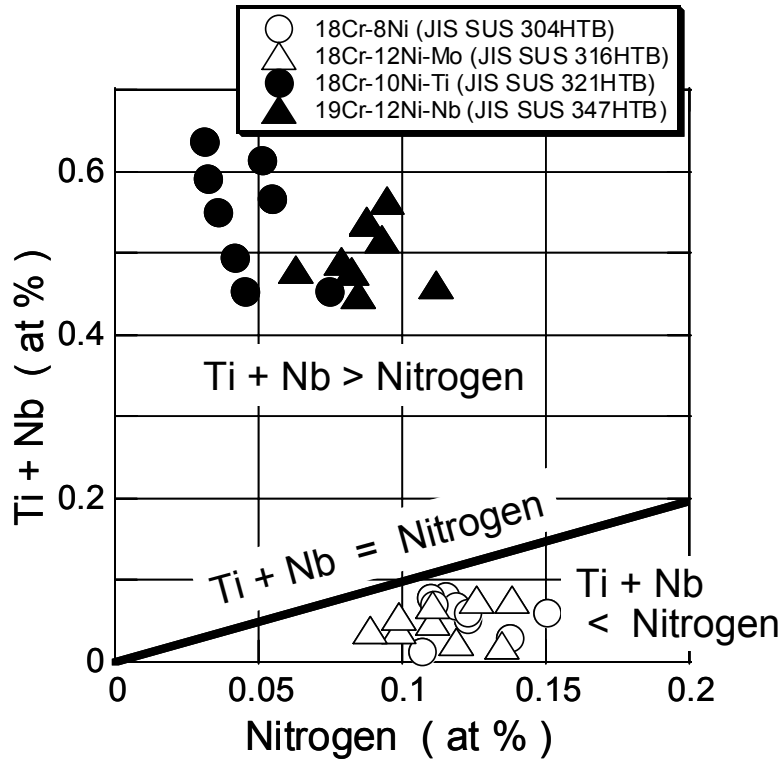


Figure 10. Contents of Ti plus Nb and that of nitrogen in at% in the steels.

2.3.1 18Cr-8Ni and 18Cr-12Ni-Mo steels

Fig. 11 shows the time to rupture of the 304HTB steel at 650 and 700°C, as a function of available nitrogen concentration [5]. The chemical compositions of the 304HTB steel are given in Table 2, where the available nitrogen concentration was evaluated by (total nitrogen – soluble Al – Ti) in at.%. At a high temperature of 700°C and long times, the time to rupture simply increases with increasing available nitrogen concentration. At short times less than about 10^3 h, the dependence of available nitrogen concentration is split into the two lines having approximately the same slope. The line with longer time to rupture represents the data for the heats ABA, ABL, ABM and ABN, which contained higher content of Nb(Ta) than the other heats. It is well known that 304HTB steel is strengthened by $M_{23}C_6$ carbides alone at short time conditions. Recently, however, we observed that the precipitation of fine Nb carbides having a size of 10 to 20 nm took place in the matrix of high-Nb steel at relatively short times less than 10 000 h at 650°C. The coarsening of fine NbC took place at long times above 10 000 h and most of the fine NbC disappear at long times. The present results suggest that the difference in precipitation strengthening due to fine NbC causes the large heat-to-heat variation in time to rupture at relatively short times. However, the precipitation strengthening due to Nb(Ta)-carbides disappears at long times because of their coarsening during creep and the heat-to-heat variation in time to rupture is mainly explained by the concept of available nitrogen concentration at

long time conditions. The concept of available nitrogen concentration is also successfully applied to the 316HTB steel as the main explanation of heat-to-heat variation in time to rupture.

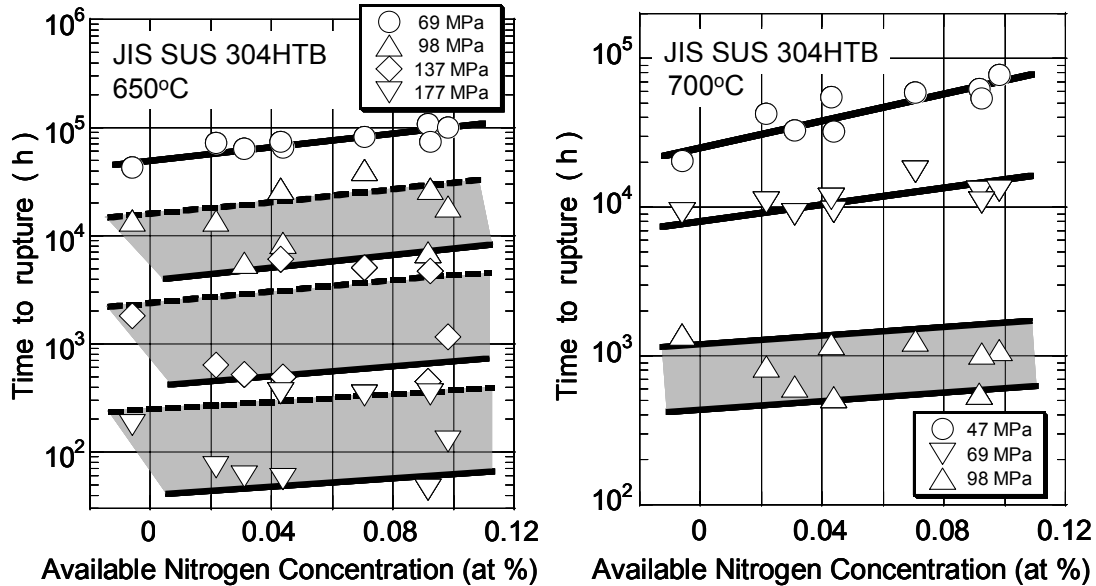


Figure 11. Time to rupture of 304HTB steel at 650 and 700°C, as a function of available nitrogen concentration given by Eq. (1).

Table 2. Chemical compositions of 18Cr-8Ni steel, JIS SUS 304HTB.

heat	(mass%)														
	C	Si	Mn	P	S	Ni	Cr	Mo	Ti	Al		B	N	Nb + Ta	N-Al-Ti (at%)
										sol.	insol.				
ABA	0.062	0.62	1.56	0.025	0.013	10.69	18.70	0.47	0.040	0.040	0.007	0.0007	0.0310	0.01	-0.006
ABB	0.054	0.41	1.52	0.031	0.020	10.15	18.34	0.36	0.064	0.005	0.005	0.0010	0.0290	0.01	0.031
ABC	0.056	0.40	1.52	0.030	0.016	10.10	18.50	0.36	0.054	0.006	0.006	0.0011	0.0300	0.01	0.044
ABD	0.070	0.52	1.49	0.023	0.006	9.68	18.70	0.06	0.006	0.004	0.006	0.0013	0.0270	0.01	0.092
ABE	0.070	0.55	1.46	0.023	0.006	9.57	18.95	0.04	0.062	0.008	0.006	0.0018	0.0278	0.01	0.022
ABF	0.080	0.62	1.34	0.021	0.006	9.80	18.25	0.06	0.020	0.008	0.005	0.0017	0.0348	0.01	0.098
ABL	0.070	0.58	1.47	0.022	0.013	9.80	18.16	0.05	0.031	0.008	0.007	0.0003	0.0310	0.04	0.070
ABM	0.090	0.61	1.56	0.022	0.014	10.27	18.24	0.32	0.036	0.008	0.006	0.0001	0.0380	0.03	0.092
ABN	0.070	0.60	1.58	0.022	0.012	10.26	18.18	0.31	0.040	0.008	0.006	0.0008	0.0280	0.04	0.043

2.3.2 18Cr-10Ni-Ti and 18Cr-12Ni-Nb steels

We observed that the precipitation of $M_{23}C_6$ carbides and fine TiC or NbC carbides took place mainly along grain boundaries and in the matrix, respectively, in these steels in the initial stage of creep [17–18]. The precipitated $M_{23}C_6$ carbides became dissolved in favor of further precipitation of thermodynamically more stable TiC or NbC. The dissolution of grain boundary $M_{23}C_6$ carbides accelerates grain boundary sliding and grain boundary cracking [19]. This suggests that the creep rupture strength of 321HTB and 347HTB steels is closely correlated with the stability and number density of grain boundary $M_{23}C_6$ carbides.

In the 347HTB steel, the number density of $M_{23}C_6$ carbides along grain boundaries increased with increasing boron content ranging from 0.0004 to 0.0040 mass% in this steel, while the size of the $M_{23}C_6$ carbides decreased [20]. This effectively suppresses grain boundary sliding. The time to rupture increases with increasing boron content and then saturates at high concentration of boron of about 0.002 mass% (20 ppm), as shown in Fig. 12(a).

In the 321HTB steel alloyed with Ti, the boron content was very low from 0.0001 to 0.0010 mass%, which was much lower than that of the 347HTB steel. Therefore, there is no correlation between the time to rupture and boron content. The dissolution of precipitated $M_{23}C_6$ carbides along grain boundaries took place by 200 to 300h at 700°C in the 321HTB steel, which was much shorter than in the 347HTB steel. One possibility for the main reason causing heat-to-heat variation in time to rupture of the 321HTB steel is the variation of grain size. Smaller grain size promotes grain boundary sliding and hence decreases the time to rupture, as shown in Fig. 12(b).

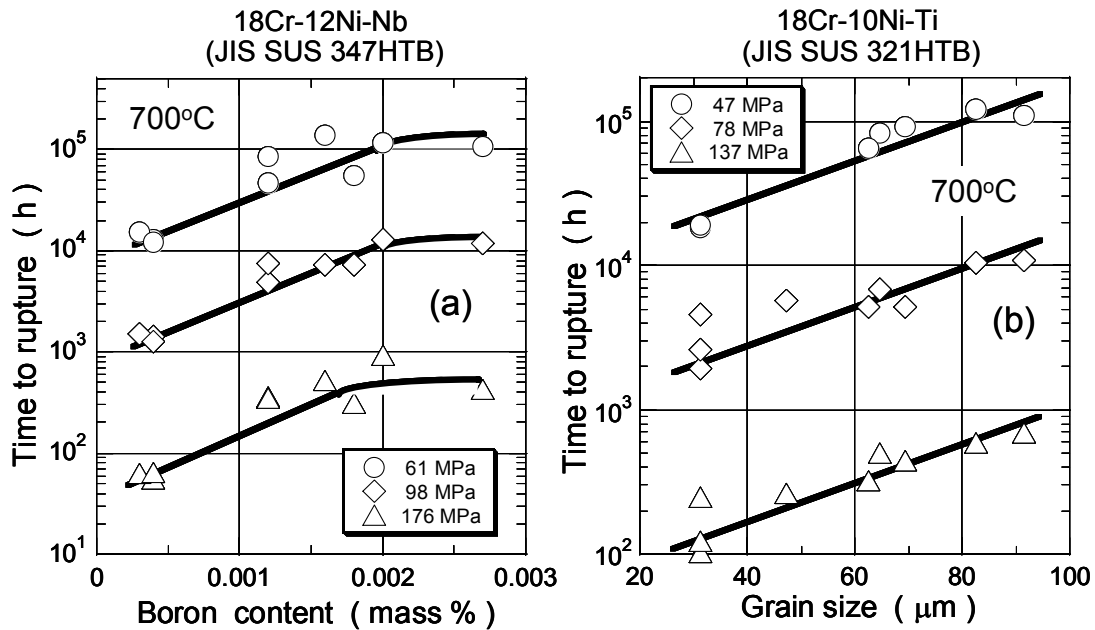


Figure 12. Time to rupture of (a) 347 HTB and (b) 321 HTB steels at 700°C, as functions of boron content and grain size, respectively.

3. Conclusions

1. Empereed martensitic 12Cr-1Mo-1W-0.3V, austenitic 304HTB, 316HTB, 321HTB and 347HTB steels exhibit large heat-to-heat variation in time to rupture, while ferritic-pearlitic 2.25Cr-1Mo and ferritic 9Cr-1Mo steels exhibit small heat-to-heat variation in time to rupture.

2. The variation of available nitrogen concentration, defined as the concentration of nitrogen free from AlN and TiN, is a main factor for the heat-to-heat variation in time to rupture of the 12Cr-1Mo-1W-03V, 304HTB and 316HTB steels at long times.
3. The heat-to-heat variation in time to rupture of the 347HTB steel is mainly explained by the variation of boron content among the different heats. In the 321HTB steel, one possibility for the main reason causing heat-to-heat variation in time to rupture is the variation of grain size.
4. Taking the mechanisms responsible for heat-to-heat variation in creep life into account, reliability of remaining life estimation can be further improved.

References

1. Series of NIMS (formerly NRIM) Creep Data Sheets No. 1–52. Tokyo, Tsukuba, National Institute for Materials Science, 2006.
2. Abe, F. Proc. International Conference on Advances in Condition and Remaining Life Assessment for Fossil Power Plants, USA (2006) CD-ROM.
3. Abe, F. Proc. NRIM-MPA Workshop 2001, Tsukuba, Japan (2001). Pp. 1–10.
4. Abe, F., Tanaka, H., Murata, M., Irie, H. and Yagi, K. Proc. 4th Japan-China Bilateral Symposium on High Temperature Strength of Materials, Tsukuba, Japan (2001) pp. 83–88.
5. Miyazaki, H., Tanaka, H., Murata, M. and Abe, F. J. Japan Inst. Metals, 66 (2002), pp. 1278–1286.
6. Abe, F. In: ‘Creep Properties of Heat Resistant Steels and Superalloys’, Landolt-Borstein Group VIII Advanced Materials and Technologies Vol. 2, Eds. by K. Yagi, G. Merckling, T.-U. Kern, H. Irie and H. Warlimont, Springer-Verlag, Berlin, Heidelberg, New York (2004). Pp. 161–169.
7. Tanaka, H., Murata, M. and Abe, F. Proc. 2nd International Workshop on Risk-based Engineering, Nagoya, Japan (2005), p. 48.
8. Yukitoshi, T. and Nishida, K. Trans. ISIJ, 12 (1972), pp. 429–434.
9. Shinya, N., Kyono, J., Tanaka, H., Murata, M. and Yokoi, S. Tetsu-To-Hagane, 69 (1983), pp. 1668–1675.
10. Schirra, M. and Anderko, K. Steel Research, 61 (1990), pp. 242–250.

11. Naoi, H., Ohgami, M., Liu, X. and Fujita, T. *Metall. Trans.*, 28A (1997), pp. 1195–1203.
12. Abe, F., Nakazawa, S., Araki, H. and Noda, T. *Metall. Trans.*, 23A (1992), pp. 469–477.
13. Abe, F. *Materials Science and Engineering*, A319–321 (2001), pp. 770–773.
14. Yokoi, S., Shinya, N. and Kori, M. *J. Soc. Mater. Sci. Japan*, 26 (1977), pp. 241–247.
15. Waranabe, T., Monma, Y., Matsuo, T. and Kikuchi, M. Report of the 123rd Committee on Heat-Resisting Metals and Alloys, Japan Society for the Promotion of Science, 32 (1991), pp. 137–148.
16. Matsuo, T., Kikuchi, M., Watanabe, T. and Monma, Y. Proc. Fifth International Conference on Creep of Materials, Florida, USA (1992). Pp. 271–279.
17. *Metallographic Atlas of Long-term Crept Materials No. M-3*. Tokyo, Tsukuba, National Institute for Materials Science, (2004).
18. *Metallographic Atlas of Long-term Crept Materials No. M-5*. Tokyo, Tsukuba, National Institute for Materials Science, (2006).
19. Tanaka, H., Murata, M., Abe, F. and Yagi, K. *Materials Science and Engineering* A234–236 (1997), pp. 1049–1052.
20. Tanaka, H., Murata, M., Abe, F. and Yagi, K. *Tetsu-to-Hagane*, 83 (1997), pp. 72–77.

Predicting creep strain response from rupture data and a robust creep curve model

Stefan Holmström and Pertti Auerkari
VTT Technical Research Centre of Finland, Espoo, Finland

Stuart Holdsworth
EMPA, Dübendorf, Switzerland

Abstract

Creep strain evolution plays a critical role in design and in life assessment of components subjected to service at high temperatures. For instance in turbines, boilers and steam pipes the recommended limits are 1% or 2% of strain. Unfortunately, straightforward engineering methodologies for predicting long term creep strain are not readily available. Robust methods for creep rupture extrapolation have been developed for example in the recommended procedures of the European Creep Collaborative Committee (ECCC) and PD6605 of BSI. The recently developed logistic creep strain prediction (LCSP) model transfers robustness into creep strain modelling. The LCSP model is directly linked to the rupture model and applies a small set of creep curve shape parameters to adjust primary, secondary and tertiary creep properties. The stress and temperature dependence of these shape parameters is optimised by fitting the available strain data. In this work the LCSP model was acquired for P22 steel from a small data set (max 3000 h) together with standard data for time to 1% strain. The model was then used to predict time to strain (0.5 to 5%) for two other P22 data sets using only true time to rupture. The model was also inversely applied to predict time to rupture from values of time to given strain for one of the data sets. The approach appears to be very competitive in spite of its simplicity, and is thought to hold considerable promise for e.g. creep modelling of new materials and welds, and when using FEA in creep analysis.

1. Introduction: data and method of assessment

Three P22 (10CrMo9-10) data sets have been assessed for predicting time to specified strain. The first data set is a small data set consisting of 30 creep curves previously assessed for several creep strain models in the ECCC intercomparison actions [1]. This data set has a maximum rupture time of 3000 h with five isotherms between 510 and 600°C and a stress range of 120–280 MPa. The data was extended with standard strength values for rupture from the EN 10216 standard [2] together with corresponding strength values for 1% strain from the

DIN 17243 standard [3] to optimise the shape of the creep curve. The creep curve shape equations extracted from this exercise were then without any further fitting or modifications used for predicting time to specified creep strain in the two other data sets that were considerably larger and with longer rupture times.

The second data set was NIMS data [4] for the same steel type, heat MAF, consisting of 29 data points ranging in temperature between 450 and 650°C and in stress between 22 and 333 MPa. This data set has previously been assessed by Evans [5] using a generalised Monkman-Grant relationship with the 4 Θ -methodology.

A comparison was also done with selected rupture data (see Table 1), same as in [5], for comparison of time to strain, minimum strain rate and time to rupture. In this case time to rupture was predicted from the measured time at 0.5%, 1%, 2%, and 5% of strain.

Table 1. Creep data set (P22, heat MAF [4]) used in assessments.

Temperature °C	Stress MPa	Time to 0.5%, h	Time to 1%, h	Time to 2%, h	Time to 5%, h	Time to rupture, h
450	216	2800	15 200	-	-	97 010
475	196	1300	2970	4700	8380	16 671
475	177	2340	4680	7700	15 200	37 039
500	216	42	84	246	485	926.5
500	177	248	535	880	1670	4027
500	157	714	1180	1940	3900	9446
500	137	942	2420	4500	11 800	29 438
500	127	1530	4110	8400	27 500	63 537
525	177	24.5	65.2	122	248	613
525	157	74.5	134	238	531	1567
525	137	204	340	588	1450	4158
550	108	160	400	1020	3530	8014
550	98	305	1100	3250	12 300	24 224
550	88	434	3150	14 100	55 800	67 392
550	83	1500	8040	32 200	80 600	85 906

The third assessed data set is a multi-heat data set provided by ECCC WG1, consisting of 178 creep rupture data points where the creep strain data was withheld. The strain data was then assessed after the time to strain predictions were delivered. The temperature range of the data set was between 450°C and 600°C and in stress between 31 and 465 MPa. For this data set the time to 0.5%, 1%, 2% and 5% were predicted.

The accuracy of a model is described by a scatter factor Z calculated from the root mean square (RMS) error and predicted time to strain or rupture. RMS and Z are defined as

$$RMS = \sqrt{\frac{\sum (\log(t_{\varepsilon-actual}) - \log(t_{\varepsilon-predicted}))^2}{n}} \quad (1)$$

where n is the number of data points. The fitting efficiency is the better the smaller the scatter factor Z , defined as

$$Z = 10^{2.5 \cdot RMS} \quad (2)$$

2. Creep strain model

In this work the new logistic creep strain prediction model (LCSP) [6] is used for predicting the creep strain response of P22 steel. The model is the result of time temperature parameter based creep strain model development ongoing over a number of years [7–9].

In LCSP time t_ε to strain ε is defined as

$$\log(t_\varepsilon) = \frac{(\log(t_r \cdot \alpha) + \beta)}{1 + \left(\frac{\log(\varepsilon)}{x_0}\right)^p} - \beta \quad (3)$$

where t_r is the true time to rupture or a predicted one acquired from a creep rupture model, and x_0 , p and β are fitting constants for each creep curve defining the curve shape. Factor α corrects the strain at rupture to the creep ductility ε_R . By adjusting these constants and their temperature and stress dependence the sought creep response can be found and extrapolated.

By differentiating Eq. 1 with respect to time, the strain rate can be written as

$$\dot{\varepsilon} = -\varepsilon \cdot k1 \cdot k2 \cdot x_0 \quad (4)$$

$$k1 = \frac{(LTF - 1)^{\frac{1}{p}}}{p} \quad \text{where } LTF = \frac{\log(\alpha \cdot t_r) + \beta}{\log(t_\varepsilon) + \beta} \quad (5)$$

$$k2 = \frac{\log(\alpha \cdot t_r) + \beta}{(\log(t_\varepsilon) + \beta)^2 \cdot t_\varepsilon \cdot (LTF - 1)} \quad (6)$$

The normalised strain (ϵ/ϵ_R) as a function of the normalised life (t/t_R) modelled with the LCSP at 550°C and 70 MPa is shown in Fig. 1.

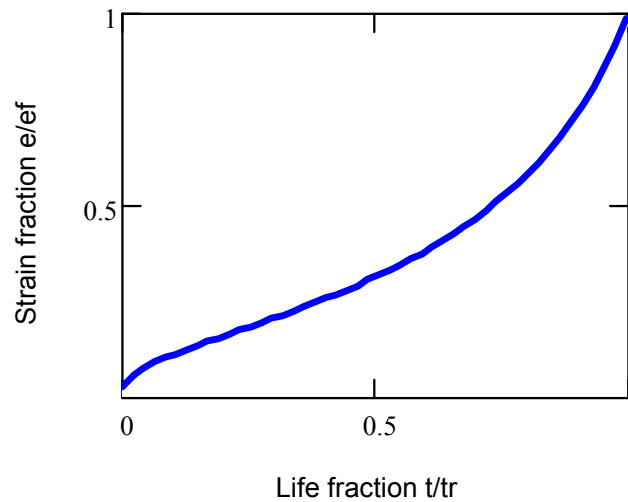


Figure 1. Life fraction (t/t_R) versus strain fraction (ϵ/ϵ_R) for P22 at 550°C / 70 MPa (100 000 h).

3. Predicting creep strain and strain rate from rupture data

The predicted minimum creep strain rates were calculated from Eq.4 (at time to minimum strain rate) using the rupture times of Table 1 and shape parameters x_0 and p presented in Table 2. The shape parameters were acquired from the ECCC short term data together with 1% strains from DIN 17243. The predicted minimum creep strain rates plotted against the measured ones are presented Fig. 2. It can be seen that the LCSP model provides predictions with good accuracy, i.e. within a factor of 3 ($Z = 2.7$) in strain rate.

Table 2. Shape factors for parent P22 (10CrMo9-10) steel.

$x_0(\sigma, T)$	$p(\sigma, T)$	β
$-0.391+0.696 \cdot \log(\sigma)-3392.5/(T+273)$	$4.363-2.271 \cdot \log(\sigma)+3874.9/(T+273)$	3.49

The NIMS rupture data was also used for predicting time to specified strain (0.5, 1%, 2% and 5%). The LCSP model predicts these within a factor of 3.4 to 6 in time (Fig. 3) which corresponds to the scatter expected for rupture data in a multi-heat data set. The predicted times are in most cases longer than the measured ones for strains above 0.5%. As an example the normalised creep curve for P22 predicted by Eq. 1 ($x_0 = -3.178$ and $p = 4.713$) from the NIMS data at 550°C / 83 MPa is shown in Fig. 4.

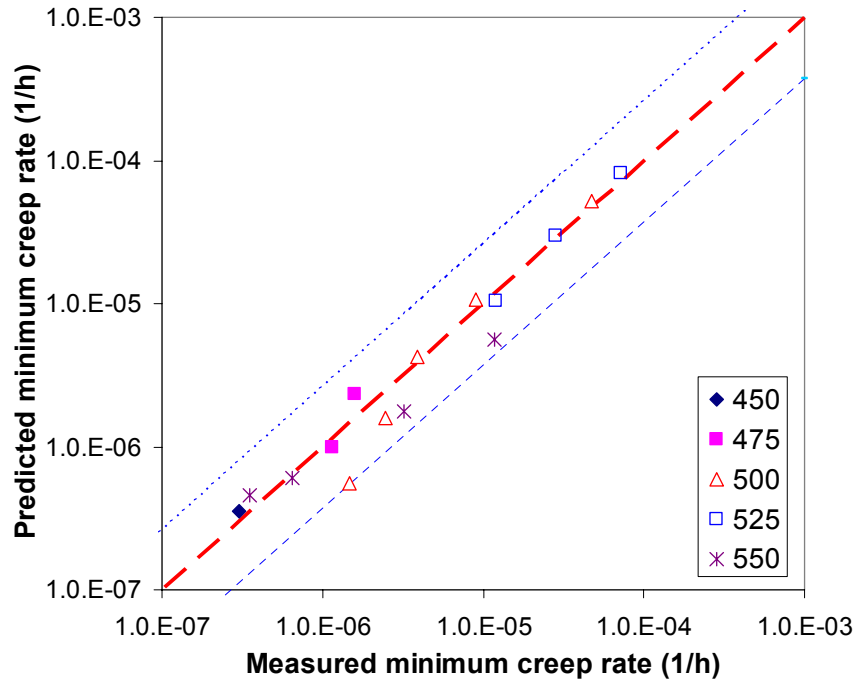


Figure 2. Measured vs. predicted minimum strain rate (LCSP-NRIM data). $Z_{rate} = 2.7$.

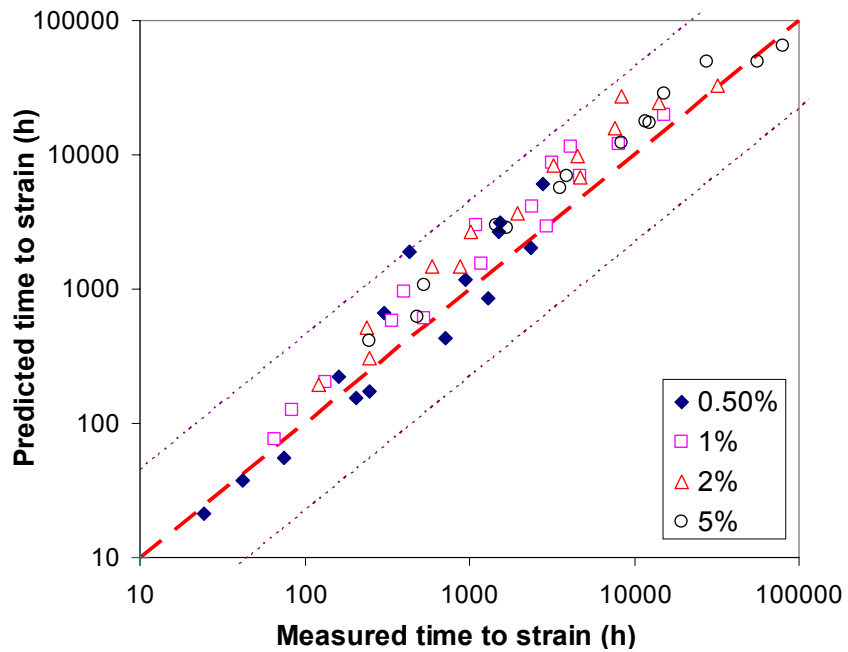


Figure 3. Measured vs. predicted time to specified strain (LCSP-NIMS data), $Z_{0.5\%} = 4.4$, $Z_{1\%} = 4.4$, $Z_{2\%} = 6.0$, $Z_{5\%} = 3.4$, $Z_{all} = 4.5$.

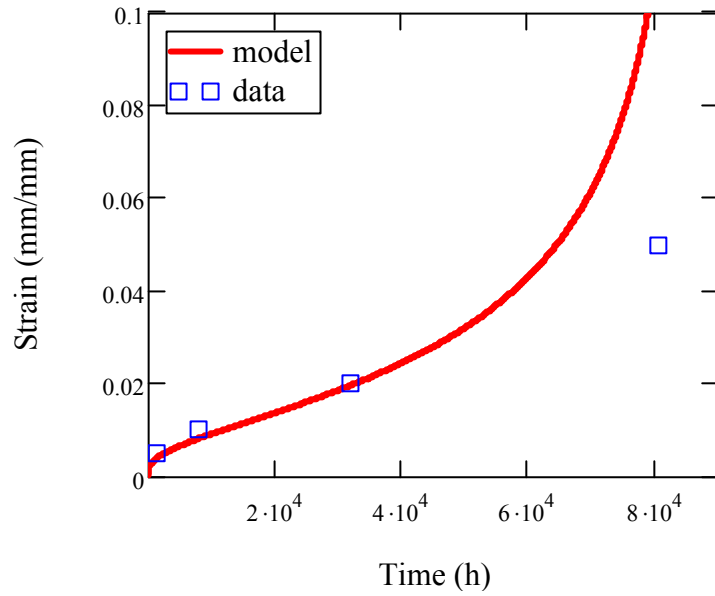


Figure 4. Measured vs. predicted time to specified strain for P22 at 550°C/83 MPa (NIMS data, heat MAF).

For the third larger data set (ECCC) the predicted and measured times to specified strain (0.5–5%) are presented in Figs. 5–6.

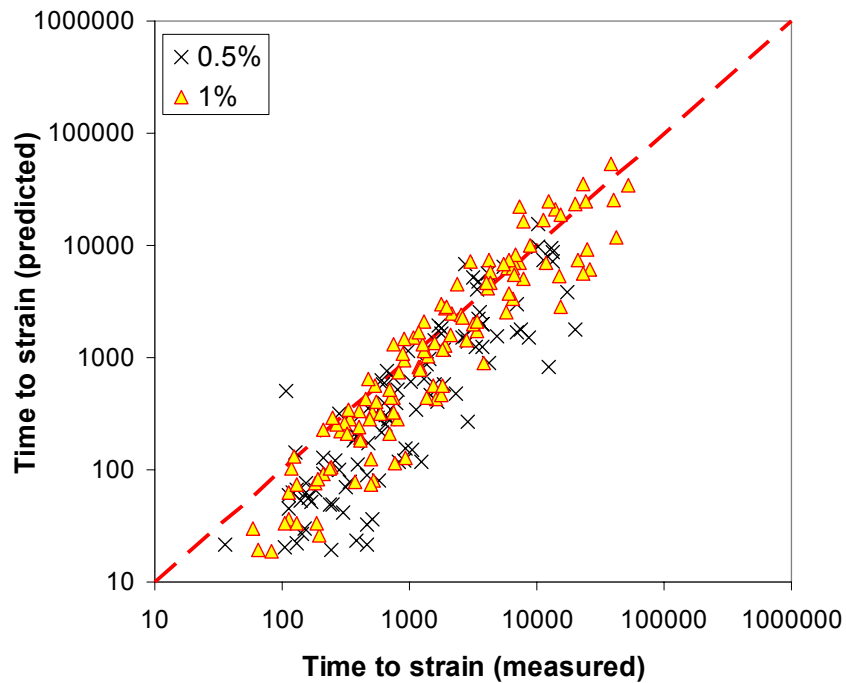


Figure 5. Measured vs. predicted time to specified strain; $Z_{0.5\%} = 25.4$, $Z_{1\%} = 7.4$.

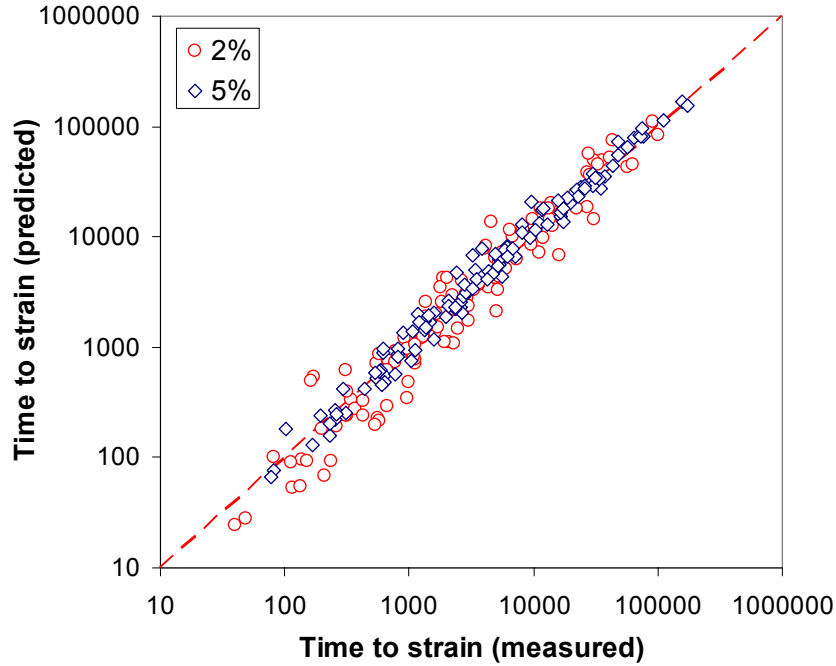


Figure 6. Measured vs. predicted time to specified strain; $Z_{2\%} = 5.9$, $Z_{5\%} = 1.9$.

The results show a clear under prediction of time to 0.5% strain but also indicate a rapidly improving accuracy for larger strains. The impact of the data set being from interrupted tests on the 0.5% predictions has not been analysed as yet. Also the effect of the different heats in the data will deserve further study.

4. Predicting time to rupture from time to specified strain

The predictive powers of the LCSP model was also investigated by inverting Eq.3 to predict time to rupture from measured time to strain values. This gives the time to rupture t_r at time to strain t_ε and strain ε as

$$\log(t_r \cdot \alpha) = (\log(t_\varepsilon) + \beta) \left(1 + \left(\frac{\log(\varepsilon)}{x_0}\right)^p\right) - \beta \quad (7)$$

where α , x_0 , p and β again define the shape of the creep curve.

Predicted time to rupture is produced by inserting the NIMS time to strain data into Eq. 7. The resulting scatter factors and predicted vs. measured rupture times are shown in Figure 7. As can be seen the LCSP method produces conservative values for time to rupture in nearly all cases except for the smallest strain (0.5%).

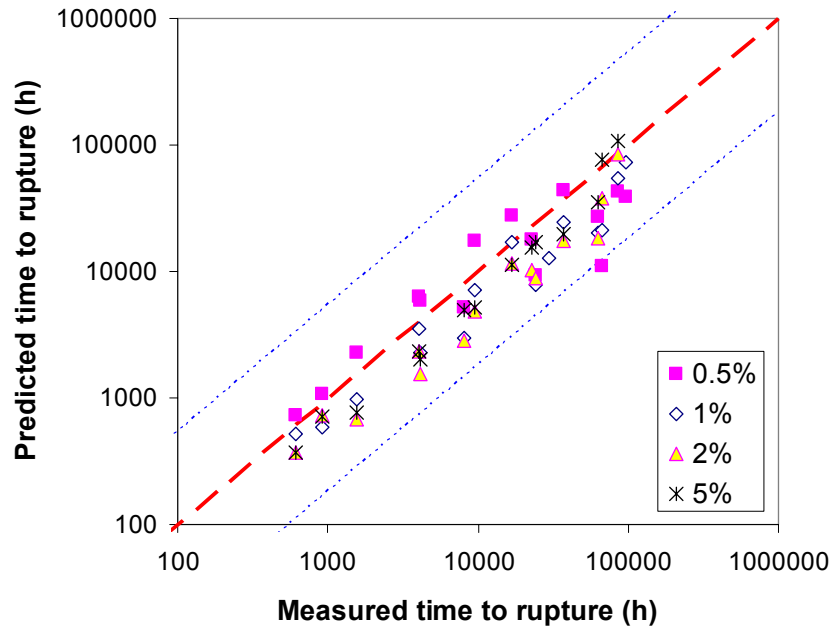


Figure 7. Measured vs. predicted time to rupture using time to specified strain; $Z_{0.5\%} = 6.0$, $Z_{1\%} = 5.5$, $Z_{2\%} = 6.7$, $Z_{5\%} = 3.5$, $Z_{all} = 5.4$.

These results can be compared with the 4Θ -predictions of Evans [5].

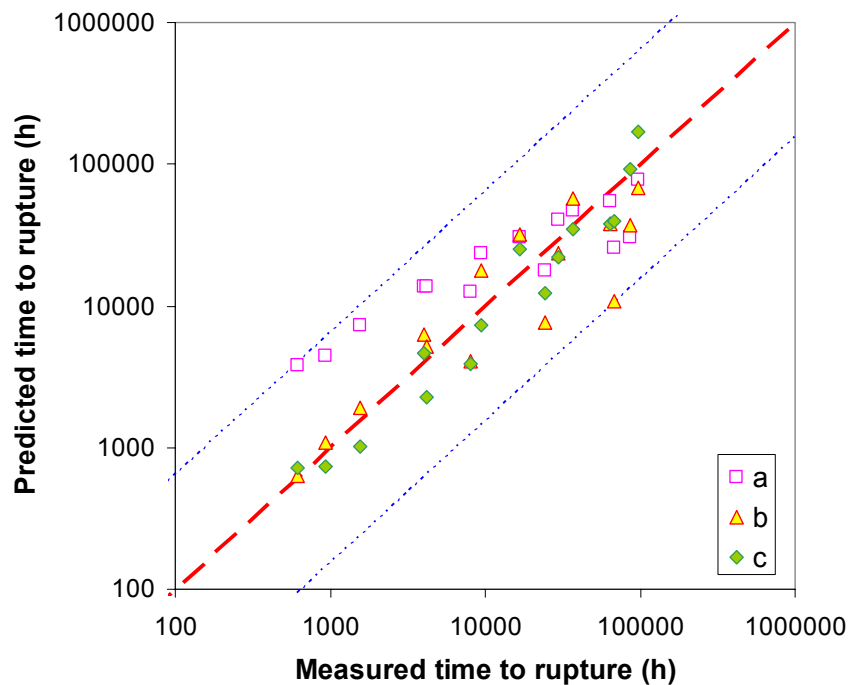


Figure 8. Measured vs. predicted time to rupture for P22 steel (data from [5]); a = traditional 4Θ -predictions, b = simplified 4Θ -predictions using strain rate at 0.5% strain, c = as in b but at 1% strain; $Z_a = 11.9$, $Z_b = 5.9$, $Z_c = 2.9$, $Z_{all} = 6.5$.

The simplified 4Θ -predictions (or modified Monkman-Grant) were considered by Evans to give the best results. Indeed, at the 1% strain level this approach appears to perform well. Of these models, only LCSP will directly predict time to any strain or strain at arbitrary time, and can therefore be implemented as a creep model in FEA.

The benefit of using a defined strain criterion is that it avoids the uncertainty over whether minimum strain rate has been reached or not. Considerable flexibility is provided by using strain rate at or time to specified strain as a base for predicting time to rupture. An additional benefit of using time to specified strain is that errors due to different calculation approaches and/or different data acquisition rates are minimised.

5. Discussion and concluding remarks

The predicted and measured times to given creep strain were found to be very consistent with the LCSP model for P22 steel, even when the model was established with a small set of short term creep data unrelated to the measured data used in the comparison. Apart from apparently good predictive accuracy, the LCSP model is simple and robust with small number of fitting factors (in total 8), because it is bound by the corresponding creep rupture model for the same material type. The small number of fitting factors minimises the extent of experimental data needed to establish the model. Mathematical simplicity also helps in using the model e.g. to predict minimum strain rate, strain at given time or time to rupture, and in implementation of the model to finite element (FE) codes. Flexibility, robustness and accuracy appear to promise good potential for the LCSP model in supporting life prediction from early stages of creep curves (relatively short term data), and in detailed analysis of the creep behaviour of complex welded structures. Further improvement in the model accuracy is expected when the model is optimised using larger and more representative creep data sets.

The competitive performance of the LCSP model was also confirmed by comparison to results (predicting rupture) obtained with the full and simplified 4Θ models [5] for the same data set of P22 steel. However, in comparison to the full 4Θ model the LCSP model required much less fitting factors and yet performed better in terms of errors in the predicted time to rupture. The simplified 4Θ (or modified Monkman-Grant) requires less fitting factors than full 4Θ , with good predictive capability using strain rate at 1% strain as base, but does not provide the flexibility of LCSP.

The LCSP model has been implemented in FE code using Comsol software for creep strain modelling of more complex structures.

Acknowledgements

The support of the Academy of Finland, decision nr. 117700 (Prof. Kim Wallin), the VTT internally funded project “Extreme”, the RFCS project “Aloas” and the Tekes funded project “LC-Power” are gratefully acknowledged. The authors also wish to acknowledge the permission by WG1 of ECCC to use the two P22 datasets.

References

- [1] Holdsworth, S.R., Askins, M., Baker, A., Gariboldi, E., Holmström, S., Klenk, A., Merckling, G., Sandström, R., Schwienheer, M. and Spigarelli, S. (WG1/ ECCC) Factors Influencing Creep Model Equation Selection. Proc. ECCC Conf. on Creep & Fracture in High Temperature Components, Design & life assessment issues, 12–14/9/2005, London, UK.
- [2] EN 10162, 2002. Seamless steel tubes for pressure purposes. Technical delivery conditions. Part 2: Non-alloy and alloy steel tubes with specified elevated temperature properties. CEN, Brussels. 59 p. + app.
- [3] DIN 17243, 1987. Weldable heat resisting steel forgings and rolled or forged steel bars; Technical delivery conditions. Deutsche Institut für Normung E.V.
- [4] NRIM creep data sheet, No 3B, National Research Institute for Metals, Tokyo, Japan, 1986.
- [5] Evans M. Combining predictions in a simplified 4 Θ methodology for creep life assessment: an application to 2Cr-1Mo steel. Materials Science and Technology. Vol. 22, No. 2, Feb. 2006, pp. 173–185.
- [6] Holmström, S. and Auerkari P. Robust prediction of full creep curves from minimal data and time to rupture. Energy Materials: Materials Science and Engineering for Energy Systems. To be published, accepted on 11/01/2007.
- [7] Holmström, S., Auerkari, P. and Holdsworth, S. An effective parametric strain model for creep. Materials for Advanced Power Engineering 2006. Proceedings of the 8th Liege Conference, Part III. Forschungszentrum Jülich GmbH (2006). Pp. 1309–1318.
- [8] Holmström, S., Auerkari, P. and Rantala, J. Engineering approach to creep strain modelling for multicast 9Cr steel. ASME PVP 2006/ICPVT11 Conference. 11th Conference on Pressure Vessel Technology, Vancouver, BC, Canada 2527. July 2006, American Society of Mechanical Engineers, ASME (2006).

- [9] Holmström, S. and Auerkari, P. Prediction of creep strain and creep strength of ferritic steels for power plant applications. Proc. Baltica Conf. on Life Management and Maintenance for Power Plants, VTT Symposium 234, 8–10/6/2004, Espoo, Finland.

A new methodology for long term creep data generation for power plant components

B. Wilshire^a, P.J. Scharning^a and R. Hurst^b

^a) Materials Research Centre, School of Engineering, University of Wales, Swansea, SA2 8PP, UK

^b) European Commission Joint Research Centre, Institute for Energy, P.O. Box 2, Petten, The Netherlands

Abstract

Using stress rupture results openly available for Grade 91 steel, three features of a new methodology for creep data analysis are summarized. Firstly, in contrast to traditional power law and parametric methods, 100 000 h creep strengths of power plant steels are predicted accurately by extended extrapolation of creep lives from tests lasting a maximum of 5000 h. Secondly, related approaches rationalize creep ductility measurements in a manner which provides information relevant to creep damage evolution in operational plant. Finally, reference is made to a set of new relationships developed to offer a physically-meaningful foundation not only for rationalization and extrapolation but also for interpretation of the creep and creep fracture properties of metals and alloys.

Key words: Creep life prediction; Creep ductility rationalization; Grade 91 steel.

1. Introduction

For large-scale power plant components, Grade 91 steel is currently being selected for component replacement in ageing plant and increasingly for new construction. For thick-section components such as mains steam pipe and headers [1], Gr. 91 can serve at temperatures up to 853 K (580°C), but determination of the tensile stresses which can be sustained at the operating temperatures without creep failure occurring in 100 000 h has proved to be an expensive and protracted task. To obtain design stress estimates, in Europe, ISO 6303 requires data from stress rupture tests lasting up to 30 000 h for five melts of each steel grade. However, as more results of longer duration have been obtained, the 100 000 h strength estimates have been reduced progressively [2–4]. This observation appears to justify the completion of long-term multi-batch test programmes. Alternatively, the fact that analysis of even 30 000 h stress rupture measurements can lead to substantial overestimation of 100 000 h performance emphasizes the unreliability of the data extrapolation procedures adopted over the last half century.

For these reasons, the limitations of the approaches widely used to quantify stress rupture behaviour are now documented, before summarizing new methodologies for data rationalization and extrapolation [5–11] by reference to property sets available [12] for Gr. 91 steel (9Cr-1Mo-V-Nb).

2. Results and Discussion

Despite the distinctive shape of the normal creep strain/time curves recorded for most metals and alloys, creep and creep fracture properties are usually described by monitoring just the minimum creep rate ($\dot{\epsilon}_m$) and the time to failure (t_f) for each curve. Even so, with large numbers of tests performed to estimate the 100 000 h strengths of power plant steels, the experimental programmes generally focus on stress rupture rather than more costly creep tests. Hence, in addition to t_f , only the corresponding total creep strains to failure (ϵ_f) and the associated reductions in specimen cross-sectional area at fracture (RoA) are then obtained.

In the present overview of the ‘Wilshire equations’ [5–11], to ensure that the procedures adopted and the results obtained are open to independent scrutiny, all analyses are based on the internationally-respected measurements reported [12] by the National Institute for Materials Science (NIMS), Japan. For Gr. 91 tube steel, NIMS Creep Data Sheet, No. 43, includes

- (a) the t_f , ϵ_f and RoA values at various stresses applied at 773 to 973 K and
- (b) the values of the 0.2% proof stress (σ_Y) and the ultimate tensile stress (σ_{TS}) determined from high-strain-rate ($\sim 10^{-3} \text{ s}^{-1}$) tests at the creep temperatures for each batch of steel investigated.

2.1 Power Law Data Representation

Since the early 1950s, most theoretical and practical studies have discussed the creep and creep fracture properties of metals and alloys through the dependences of $\dot{\epsilon}_m$ and t_f on stress (σ) and temperature (T) using power law equations of the form

$$M / t_f = \dot{\epsilon}_m = A \sigma^n \exp(-Q_c / RT) \quad (1)$$

where $M = \dot{\epsilon}_m \cdot t_f$ and $R = 8.314 \text{ kJmol}^{-1}$. Although the product, $\dot{\epsilon}_m \cdot t_f$, is not always a constant, the fact that t_f increases as $\dot{\epsilon}_m$ decreases with decreasing stress and temperature signifies that creep damage development and eventual failure are strain controlled. Moreover, the parameter (A), the stress exponent (n) and the activation energy for creep (Q_c) are also functions of stress and temperature.

As evident from the stress rupture plots in Fig. 1, a decrease from $n \cong 16$ to $n \cong 5$ is observed on increasing the test temperature from 773 to 973 K, with Q_c ranging from 600 to 700 kJmol⁻¹. These anomalously large and variable values of n and Q_c are typical of the results obtained for many engineering steels and other particle-hardened alloys. Then, because n and Q_c vary in an unpredictable manner, long-term strengths cannot be estimated satisfactorily using power law equations to extrapolate short-term measurements. Instead, reliance continues to be placed on various parametric methods, many of which were also devised in the early 1950s [13–15].

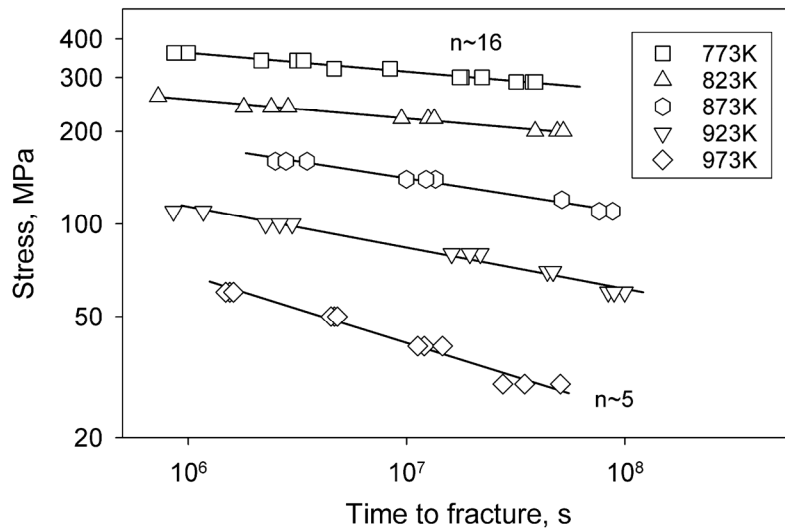


Figure 1. The stress dependences of the creep life at 773 to 973 K for tube samples of Gr. 91 steel [12].

2.2 Parametric Approaches to Data Analysis

Parametric relationships define ‘correlation parameters’, incorporating creep life and temperature, which can be plotted as functions of stress to superimpose multi-batch results onto a ‘master curve’ for a given steel. Yet, the limitations of parametric methods are easily revealed by considering the Larson-Miller relationship [13], the most widely adopted of these empirical approaches. The Larson-Miller parameter (P_{LM}) is written as

$$P_{LM} = T (\log t_f + C_{LM}) \quad (2)$$

where the ‘constant’ (C_{LM}) contains the Q_c term from Eq. 1 [16]. Hence, the variable Q_c value ensures that Larson-Miller plots are non-linear, so that extrapolation of short-term results overestimates long-term strengths. In addition, different values can be chosen for C_{LM} , with the estimated 100 000 h creep rupture strengths for Gr. 91 steel differing considerably when taking $C_{LM} = 20$ and $C_{LM} = 36$, (see Ref. 2 in Table 1).

While recognizing that adjusting the analysis procedures predicts different long-term strengths, it has been suggested that the critical factor is not the analysis method but the maximum test duration [17]. Certainly, for Gr. 91 steel, the 100 000 h creep rupture strengths have decreased progressively as continuing test programmes have increased the numbers of results available and the maximum creep lives recorded [2–4]. In fact, it has also been proposed that short-term data should be excluded from the analysis exercises [3, 18], giving lower predicted strengths (see Ref. 3 in Table 1). However, no quality-assured method was defined to decide on the results to be discarded.

2.3 Rationalization of Stress Rupture Data

Without recourse to empirical parametric relationships, the t_f values recorded over broad stress ranges at different temperatures are superimposed [5–11] simply by normalizing the applied stress (σ) through the measured values of σ_{TS} for each batch of steel investigated. Hence, Eq. 1 becomes

$$M/t_f = \dot{\epsilon}_m = A^* (\sigma/\sigma_{TS})^n \exp(-Q_c^*/RT) \quad (3)$$

but compared with Eq. 1, $A^* \neq A$ and $Q_c^* \neq Q_c$. In this case, Q_c^* is determined from the temperature dependence of t_f at constant (σ/σ_{TS}) in Eq. 3, whereas Q_c is calculated at constant σ with Eq. 1. Using Eq. 3, together with NIMS σ_{TS} values [12], the creep life results presented for Gr. 91 steel in Fig. 1 are superimposed [10, 11] in Fig. 2. Furthermore, as found for several different steels, $Q_c^* \cong 300 \text{ kJmol}^{-1}$, a value close to that for lattice diffusion in the alloy steel matrices. Similarly, for a series of commercial aluminium alloys, $Q_c^* = 145 \text{ kJmol}^{-1}$, again a value equal to that for matrix diffusion [6, 19].

The ‘master curve’ in Fig. 2 is at least as impressive as those obtained using standard parametric methods, but the empirical terms in the parametric relationships are replaced by physically-meaningful properties in Eq. 3, namely, a sensible activation energy and the appropriate values of σ_{TS} . Inspection of the results in Fig. 2 then shows [10, 11] that Eq. 3 avoids the large and variable Q_c values observed when the creep rupture properties of Gr. 91 steel are described using Eq. 1, but does not eliminate the decrease from $n \cong 16$ to $n \cong 5$ in Fig. 1. Indeed, this trend is generally expected to continue towards $n \cong 1$ or less as (σ/σ_{TS}) decreases. Because of this unpredictable fall in n value as the test duration and temperature increase, even Eq. 3 does not permit reliable extrapolation of short-term creep life measurements. For this reason, new methodologies have been developed [5–11] for cost-effective and accurate prediction of long-term design strengths.

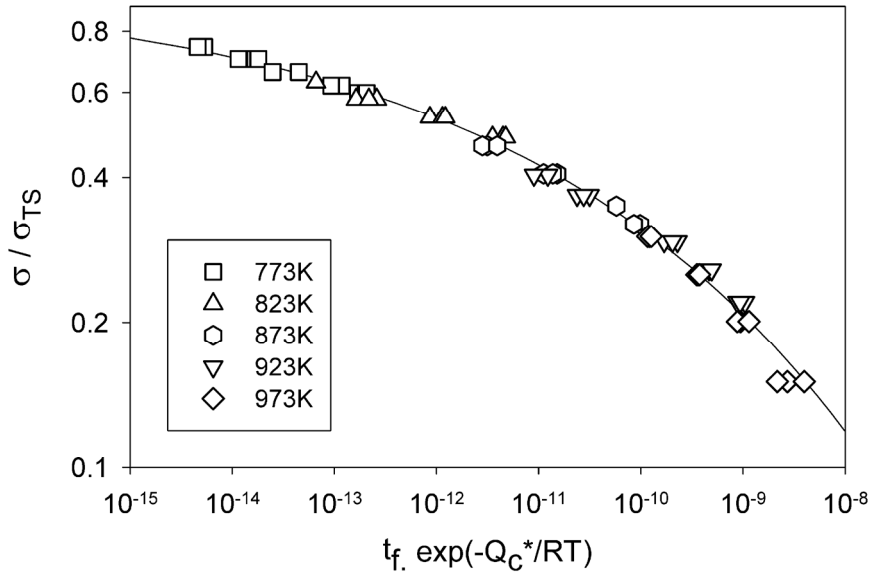


Figure 2. The dependence of the temperature-compensated creep life on (σ/σ_{TS}) , using Eq. 3 with $Q_c^* = 300 \text{ kJmol}^{-1}$ for Gr. 91 tube steels [10, 11].

2.4 Prediction of Long-Term Stress Rupture Data

Standard stress rupture plots based on Eq. 1 (Fig. 1) can be rationalized effectively by normalizing σ through σ_{TS} in Eq. 3 (Fig. 2) or through σ_Y [5–11]. However, advantages are gained by using σ_{TS} rather than σ_Y . Specifically, σ_{TS} represents the maximum stress which can be applied at the creep temperature, so data sets can be described over the entire stress range from $(\sigma/\sigma_{TS}) = 0$. In this way, when $(\sigma/\sigma_{TS}) \rightarrow 1$, the creep life approaches zero. Conversely, when $(\sigma/\sigma_{TS}) \rightarrow 0$, creep failure will not occur, so the creep life becomes infinite. These essential criteria are met by modifying Eq. 3 to quantify the stress and temperature dependences of t_f measurements as [5–11]

$$(\sigma/\sigma_{TS}) = \exp\{-k_1[t_f \cdot \exp(-Q_c^*/RT)]^u\} \quad (4)$$

where k_1 and u are evaluated from plots of $\ln [t_f \cdot \exp(-Q_c^*/RT)]$ against $\ln [-\ln (\sigma/\sigma_{TS})]$, with $Q_c^* = 300 \text{ kJmol}^{-1}$, as demonstrated for Gr. 91 steel in Fig. 3 [10, 11]. In this case, the k_1 and u values were determined for results acquired only under test conditions such that the times to failure were less than 5000 hours, but virtually identical values would be derived by including all available t_f measurements [10, 11].

By incorporating the derived k_1 and u values, Eq. 4 allows the stress rupture data for Gr. 91 steel to be rationalized onto the sigmoidal ‘master curve’ presented in Fig. 4 [10, 11]. From this curve, t_f values can be computed over extended stress

ranges at various creep temperatures. These predictions are included in Fig. 5 [10, 11], showing a good fit with recent multi-batch t_f data produced through NIMS for test conditions giving creep lives up to almost 100 000 hours for Gr. 91 type steel plates, pipes, forgings and tubes [3]. Moreover, noting that the present predictions in Fig. 5 were obtained using only short-term properties [10, 11], the extrapolated values (Ref. 8 in Table 1) agree impressively with the latest 100 000 hour rupture strength estimates determined from long-term test programmes (Refs. 3 and 4 in Table 1).

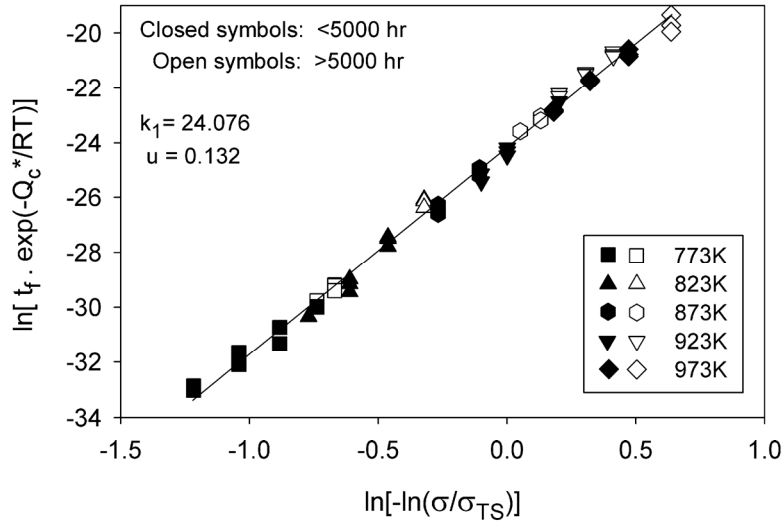


Figure 3. The dependence of $\ln [t_f \exp (-Q_c^*/RT)]$ on $\ln [-\ln (\sigma/\sigma_{TS})]$ for Gr. 91 tube steel, with $Q_c^* = 300 \text{ kJmol}^{-1}$. Test conditions such that $t_f < 5000$ hours are shown as closed symbols, while results for $t_f > 5000$ hours are included as open symbols [10, 11].

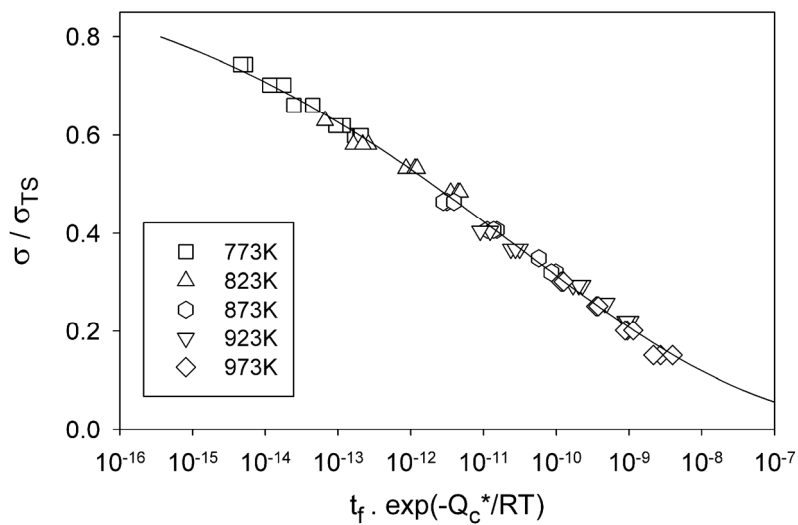


Figure 4. The dependence of $\log [t_f \exp (-Q_c^*/RT)]$ on (σ/σ_{TS}) for Gr. 91 tube steel, using Eq. 4 with $Q_c^* = 300 \text{ kJmol}^{-1}$ [10, 11].

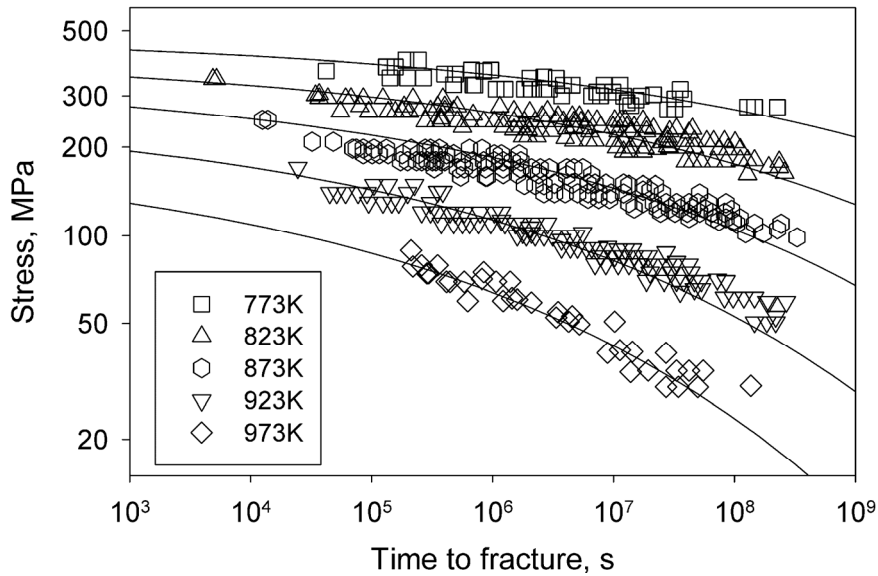


Figure 5. The stress/creep life behaviour predicted [10, 11] from Eq. 4 for Gr. 91 tube steel (solid lines) compared with long-term multi-batch stress rupture data for plate, pipe, forgings and tube samples at 773 to 973 K [3].

Table 1. 100 000 h creep rupture estimates (MPa) for Gr. 91 steel.

Temperature	Present Estimates (Note 1)	Ref. 2 (Note 2)		Ref. 3 (Note 3)	Ref. 4 (Note 4)
		A	B		
823 K (550°C)	154	132	159	150	153
873 K (600°C)	87	83	100	98	86
923 K (650°C)	43	48	56	42	46

Note 1. (Ref. 8). Estimates derived using Eq. 4, analysing creep life data only from tests lasting less than 5000 h for Gr. 91 tube steel [12].

Note 2. (Ref. 2). Estimates obtained for Gr. 91 plate using the Larson-Miller relationship with $C_{LM} = 20$ (Set A) and $C_{LM} = 36$ (Set B).

Note 3. (Ref. 3). Estimates obtained using the Larson-Miller relationship to analyse data for Gr. 91 pipe, tube, forgings and plate at stresses less than 180, 130 and 90 MPa at 823, 873 and 923 K respectively whereas, by describing the full data sets from tests lasting up to almost 100 000 hours, significantly larger estimates were derived.

Note 4. (Ref. 4). Estimates obtained for Gr. 91 tube and pipe, with the longest test having a creep life exceeding 110 000 h under a stress of 150 MPa at 823 K.

2.5 Rationalization of Creep Ductility Data

In addition to cost-effective prediction of accurate allowable design stresses, safe plant operation requires information on creep damage development for monitoring component life consumption during service. With components produced from low alloy steels, a measure of life exhaustion can be provided by inspection schedules which estimate the gradual increase in the incidence of cavities and cracks, but cavitation occurs late in the creep life with Gr. 91 steel. Even so, to assist with ‘run, repair or replace’ decisions, one option is to consider creep ductility trends [9, 11], even though multi-batch ϵ_f and RoA values are usually characterized by a high degree of scatter [20].

With superimposition of t_f data achieved in Fig. 4 by considering the stress dependence of $t_{f.exp}$ ($-300\,000/RT$), efforts have been made to identify a suitable ‘time-temperature term’ which rationalizes ductility measurements [9, 11]. Of course, under the same applied stress, relatively small changes in temperature can alter t_f by several orders of magnitude, whereas creep ductility values normally vary only over more limited ranges. Hence, to relate ϵ_f and RoA to creep life, temperature compensation of t_f must involve an activation energy lower than 300 kJmol^{-1} . In fact, Fig. 6 shows that the creep ductilities are well described [9, 11] as functions of $t_{f.exp}$ ($-150\,000/RT$), providing an indication of the failure characteristics of Gr. 91 components in relation to service exposure times and temperatures.

Fig. 6 illustrates the trends not only in ϵ_f and RoA but also in the (RoA/ϵ_f) ratio, because failure is preceded by neck formation when $(RoA/\epsilon_f) > 1$, whereas fracture occurs without prior necking when $(RoA/\epsilon_f) \rightarrow 1$. With Gr. 91 steel, ϵ_f and RoA, as well as (RoA/ϵ_f) , begin to decrease when $t_{f.exp}$ ($-150\,000/RT$) > 0.1 , i.e. exposure times exceeding 50 000 h at the maximum recommended temperature of 853 K. Indeed, $\epsilon_f > 0.1$ and $RoA > 0.3$, with $(RoA/\epsilon_f) > 2$, indicating that failure occurs in a relatively ductile manner even after times approaching 100 000 h at 853 K [9, 11].

Although the data sets in Fig. 6 suggest that premature cracking should not occur within the planned service lives of Gr. 91 components operating up to 853 K, the 100 000 h creep rupture strengths listed in Table 1 will not be attained in the heat-affected regions of components adjacent to welds. Hence, with power plant components and structures produced from Gr. 91 steel, the principal on-going source of concern must be Type IV weldment cracking [21, 22]. Moreover, the substantial batch-to-batch scatter in creep ductility measurements will also be reflected in component-to-component and particularly weldment-to-weldment variations in damage development.

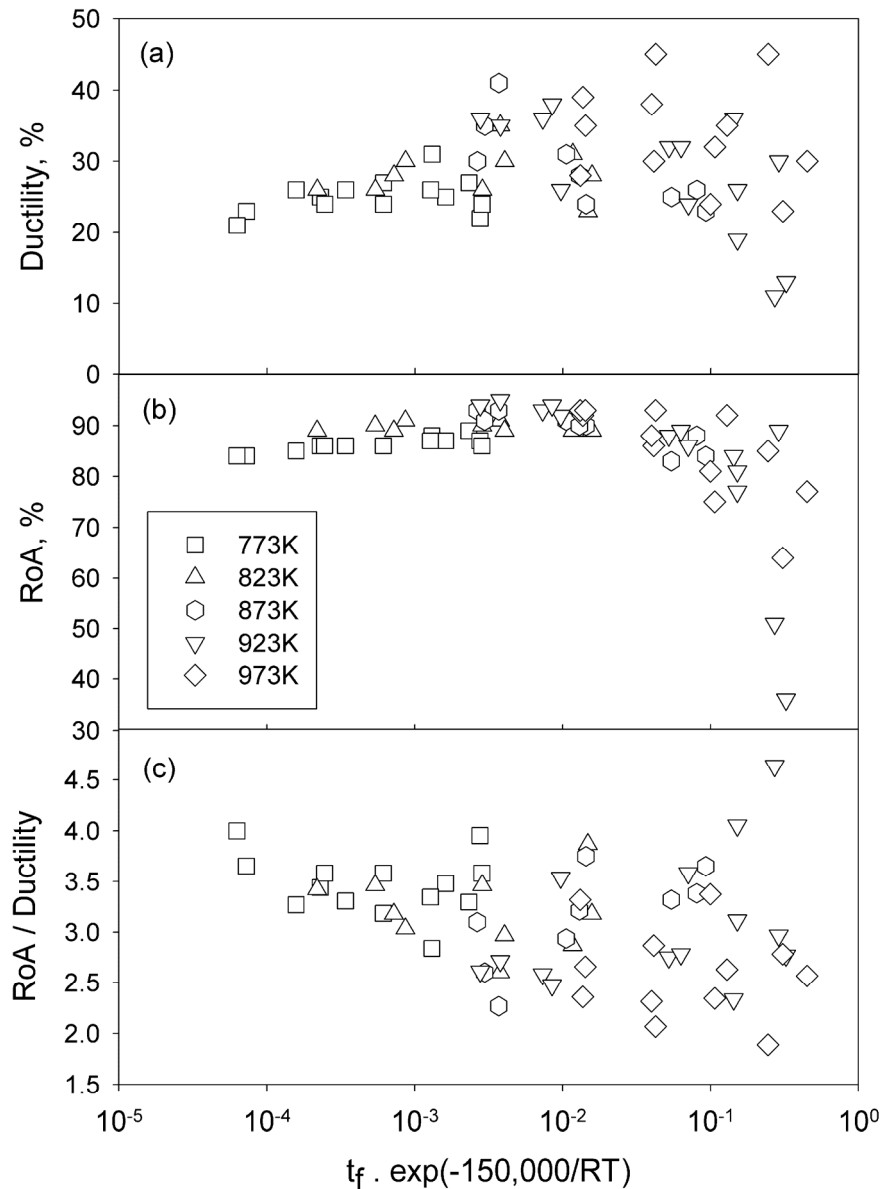


Figure 6. The variations in (a) the creep ductility, ϵ_f , (b) the reduction in area, RoA , and (c) the (RoA/ϵ_f) ratio as functions of $t_f \cdot \exp(-150\,000/RT)$ for Gr. 91 steel [9, 11].

3. Concluding Comments

The present overview summarizes the progress recently made [5–11] towards accurate prediction of 100 000 h rupture strengths by extended extrapolation of t_f values from tests lasting a maximum of 5000 h, as illustrated for Gr. 91 steel in Table 1. These long-term predictions were derived through Eq. 4, which superimposes multi-batch stress rupture measurements onto sigmoidal ‘master curves’. These curves are at least as impressive as those obtained with parametric

methods, but with the empirical terms in parametric expressions replaced by physically-meaningful properties, namely, the activation energy for matrix diffusion (300 kJmol^{-1}) and the relevant σ_{TS} values. In addition, new procedures allow rationalization of creep ductility trends relevant to damage evolution during power plant service [9, 11]. Even so, the predicted long-term strengths will not be achieved in the heat-affected regions of welds, so that Type IV cracking must be expected with Gr. 91 components and structures operating at temperatures approaching 850 K.

Relationships equivalent to Eq. 4 also quantify other creep properties. Thus, the stress and temperature dependences of $\dot{\epsilon}_m$ are well represented [5–11] as

$$(\sigma / \sigma_{\text{TS}}) = \exp\{-k_2[\dot{\epsilon}_m \cdot \exp(Q_c^* / RT)]^v\} \quad (5)$$

where the coefficients (k_2 and v) are again evaluated by plotting the temperature-compensated $\dot{\epsilon}_m$ values as a function of $(\sigma / \sigma_{\text{TS}})$. Similarly, when full creep curves are available, the times to reach pre-defined creep strains (t_ϵ) can be quantified [10, 11] as

$$(\sigma / \sigma_{\text{TS}}) = \exp\{-k_3[t_\epsilon \cdot \exp(-Q_c^* / RT)]^w\} \quad (6)$$

with sets of k_3 and w values defining the behaviour patterns in a manner which provides stress-strain-time-temperature descriptions for incorporation into modern finite element codes for high-temperature engineering design. Moreover, the ‘Wilshire equations’ allow not only data rationalization and extrapolation but also straightforward interpretation of all features of the behaviour patterns displayed by pure copper [5] and commercial aluminium alloys [6], as well as a range of power plant steels [7–11].

The comprehensive NIMS Creep Data Sheets provide the information required for independent assessment of the new relationships for many alloy steels. In addition, programmes are already underway at Swansea with partners in the UK power, aeroengine and automotive industries to evaluate the predictive capabilities of Eqs. 4, 5 and 6 for steels and nickel-base superalloys, as well as commercial aluminium and titanium alloys. Validation of these predictive methodologies would then minimize the durations and costs of acquiring long-term design data, simultaneously reducing the delay times between development and application of new creep-resistant alloys.

References

1. Blum, R. In: 'Materials for advanced power engineering', (ed. D. Coutsouradis), 15–30, 1994, Liege, Kluwer Academic Publ.
2. Masuyama, F. In: 'Creep and fracture in high temperature components – design and life assessment issues', (I.A. Shibli, S.R. Holdsworth and G. Merckling Eds.), 983–996, 2005, London, DEStech Publ.
3. Kimura, K. *ibid*, pp. 1009–1022.
4. Cipolla, L. and Gabrel, J. 'Super-high strength steels', 2005, Rome, Associazione Italia di Metallurgia (CD Rom).
5. Wilshire, B. and Battenbough, A.J. *Mater. Sci. Eng. A.*, 2007, 443A, pp. 156–166.
6. Wilshire, B., Burt, H. and Lavery, N. *Mater. Sci. Forum*, 2006, 519–521, pp. 1041–1046.
7. Wilshire, B. and Burt, H. *Mater. Sci. Forum*, 2007, 539–543, pp. 254–261.
8. Wilshire, B. and Scharning, P.J. *Scripta Mater.*, 2007, 56, pp. 701–704.
9. Wilshire, B. and Scharning, P.J. *Scripta Mater.*, 2007, In press.
10. Wilshire, B. and Burt, H. In: 'Creep resistant steels', (F. Abe, T.-U. Kern and R. Viswanathan Eds.), 2007, Woodhead Publishing, Cambridge, In press.
11. Wilshire, B. and Scharning, P.J. *International Materials Reviews*. 2007, In press.
12. NIMS Creep Data Sheet No: 43, 1996.
13. Larson, F.R. and Miller, J. *Trans ASME*, 1952, 74, pp. 765–775.
14. Manson, S.S. and Haferd, A.M. NASA TN2890, 1953.
15. Orr, R.L., Sherby, O.D. and Dorn, J.E. *Trans ASM*, 1954, 46, pp. 113–128.
16. Evans, R.W. and Wilshire, B. 'Creep of metals and alloys', 1985, London, The Institute of Metals.

17. Foldyna, V., Gakobova, A. and Kupka, V. Fifth Inter. Conf. on 'Creep and creep fracture of engineering materials and structures', (eds. B. Wilshire and R.W. Evans), 1993, London, The Institute of Materials. Pp. 573–582
18. Kimura, K. In: 'Creep deformation and fracture, design and life extension', (R.S. Mishra, J.C. Earthman, S.V. Raj and R. Viswanathan Eds.), 2005, Pittsburg, MS&T. Pp. 97–106.
19. Wilshire, B. and Burt, H. In: 'Creep Deformation and Fracture, Design and Life Extension', (R.S. Mishra, J.C. Earthman, S.V. Raj and R. Viswanathan eds.), 3–12, 2005, Pittsburgh, MS&T.
20. Hald, J. *Materials at High Temperatures*, 2004, 21, pp. 41–46.
21. Allen, D.J., Harvey, B. and Brett, S.J. In 'Creep and fracture in high temperature components – design and life assessment issues', (I.A. Shibli, S.R. Holdsworth and G. Merckling eds.), 2005, London, DEStech Publ. Pp. 772–781.
22. Auerkari, P., Holmstrom, S., Veivo J. and Salonen, J. *ibid*, pp. 783–791.

VTT technology strategy in novel base load concepts

Pertti Aaltonen, Liisa Heikinheimo, Timo Vanttola and Jouni Hämäläinen

VTT Technical Research Centre of Finland, Espoo, Finland

Abstract

One third of the power generation capacity in Europe is older than 30 years. The new replacement capacity has been estimated to be 550 GW by 2030. Modernization of current power generation capacity can make it more environmentally friendly by reducing emissions, while simultaneously improving efficiency.

Development of both the coal fired power plants as well as the high efficiency advanced nuclear power plants is needed to replace the ageing existing base load capacity. The media for heat transfer to be used in new power plant concepts is either super-critical water, e.g., fluid or very high temperature inert gas. The development of new power generation concepts has brought the coal fired concepts closer to the nuclear reactor concepts, producing similar challenges, excluding irradiation effects.

The idea of the Key Technology Action (KTA) initiated by VTT is to focus the research efforts at VTT on the future power generation concepts, development and maintenance of testing facilities needed as well as training of personnel. At the moment the KTA of energy production novel base load concepts covers:

- Process development for novel base load concepts
- Material design, life time management and ageing / degradation mechanisms
- Zero emission concepts.

VTT has accumulated experience in the fields of reactor and boiler material research, oxygen combustion concepts, and in the modelling of nuclear reactor operation and safety. The KTA intends to join these activities for developing novel base-load concepts.

The KTA activity can lean on the existing knowledge from coal fired and nuclear plants. However, totally new challenges are new temperature range defined for Super Critical Light Water Reactors (SCLWR), and the behaviour of SC fluid as a coolant. Particularly challenging will be material selection for these operational conditions, taking into account mechanical and corrosion resistance under irradiated conditions.

1. Coal fired combustion

The increase in atmospheric CO₂ has been proposed as a cause of global warming. About 30% of man-made CO₂ emissions originates from power generation by fossil fuels. Oxygen combustion (nitrogen free combustion) is one of the promising technologies to reduce the CO₂ emissions of power production.

1.1 Oxygen combustion

One of the promising technologies to reduce the CO₂ emissions of power production is oxygen combustion. The main approaches in oxygen combustion for CO₂ emission reduction in energy production are as follows:

- Increase of efficiency provides emission cuts proportional to the rise in efficiency
- Co-firing of fossil fuels with CO₂-neutral fuels provides a technically and economically feasible solution for CO₂ reduction up to certain degree
- When bigger emission cuts are required, CCS (Carbon Capture and Storage) offers potential for near zero emission power production from fossil fuels, though at the expense of efficiency and costs.

1.2 Materials for oxygen combustion conditions

Material service conditions in oxygen combustion of coal will differ from any present day coal combustion environment because of the higher temperature, the higher concentration of O₂, H₂O and CO₂ in flue gases, as well as changes in the activities of corrosive species such as SO₃ and Cl in the deposits. Current high temperature steel grades have not been developed nor tested for such aggressive conditions. It has been recently found that the current high temperature steel grades can suffer vast corrosion in atmospheres containing high contents of H₂O. It is obvious that also other structural alloys, Ni- or Co-based, or novel PM-alloys may be required for the components operating under highest temperatures and O₂-gas contents.

By combining oxygen combustion process modelling and material tests, the worst process conditions can be estimated. Based on laboratory scale corrosion tests conducted in these conditions, materials degradation mechanisms can be defined and modelled for the targeted process conditions, Fig. 1.

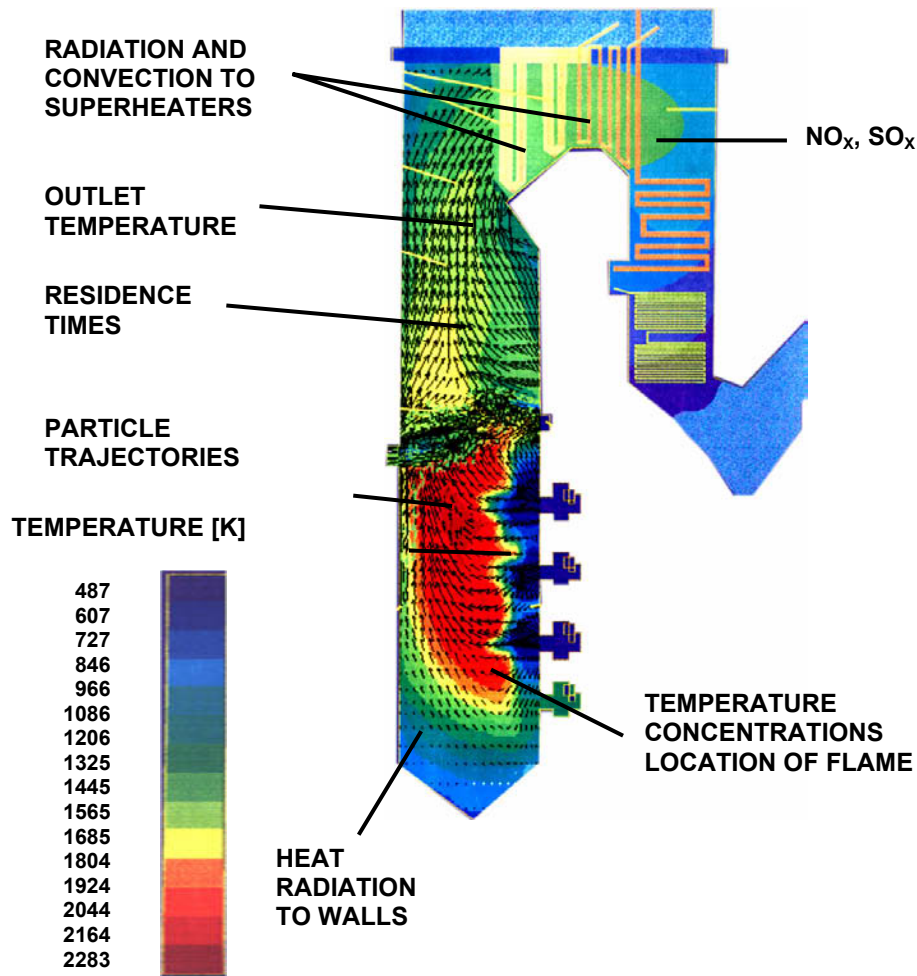


Figure 1. Modelling combustion process conditions.

2. Gen IV NPP's in Finland

During the lifetime of the Gen III+(OL3), completely new types of nuclear reactors will emerge. Safe operation of NPPs and timely, beneficial decision-making for new installations requires national expertise and international co-operation. Finland shall be capable of deploying Gen IV NPPs.

KTA is actively involved in the international research concerning Gen IV reactor concepts. Six different concepts have been proposed:

- Very high temperature reactor (VHTR)
- Supercritical-water-cooled reactor (SCWR)
- Gas-cooled fast reactor (GFR)
- Lead-cooled fast reactor (LFR)
- Sodium-cooled fast reactor (SFR) and
- Molten salt reactor (MSR).

VTT aims to increase the knowledge in the field of nuclear power safety and material technologies, and to maintain or improve the ability to support power plants and authorities in the nuclear sector and to establish knowledge on new concepts for future needs. The education of new experts in the field is realized through R&D projects, research exchanges with European and overseas partners, and contract research to customers. Innovative laboratory and on-line monitoring devices need to be developed for materials performance testing for increased service requirements (higher pressure, temperature), enabling unique experimental work and to support advanced modelling work. These efforts make it feasible to participate in European/global collaboration through focused topics that support VTT's strategy for energy research, further customer needs, and enable participation in challenging technology projects that provide opportunities to learn conceptual design and the manufacturing of components, Fig. 2.

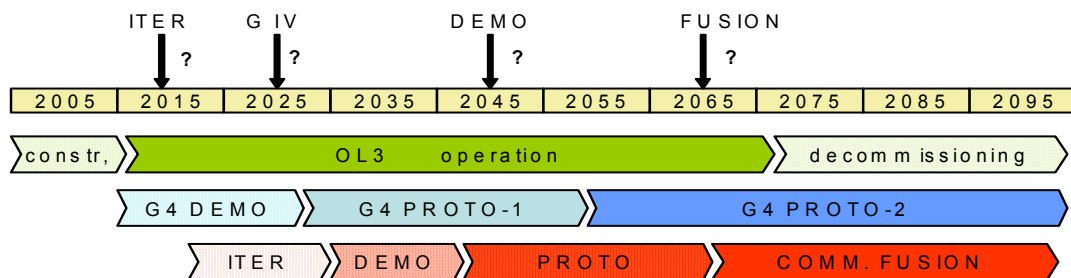


Figure 2. Long term plans and commitments for nuclear energy production.

2.1 Thermo-hydraulic and safety modelling for SC processes

Based on the existing data and information of steam properties, models can be refined for dealing with super-to-sub-critical transition. Calculation of reactivity transients in the super-critical regime, and calculation of transients with pressure drop are near future goals for process modelling within the Gen IV concept. In the future modelling concerning moderation of neutrons in SC conditions also needs to be done.

2.2 Gen IV related material research

The research concerning material performance in SC conditions of Gen IV NPP concepts, has been initiated already. Tests have been carried out for ferritic and martensitic 9–12% Cr steels, austenitic stainless steels, Ni based superalloys, some Ti alloys and ODS materials. Test temperatures vary from 400 to 650°C. The final completed test matrix should cover dimensional and microstructural stability, oxidation kinetics, mechanical properties, susceptibility to any forms of environmentally assisted cracking phenomena and radiation damage. Additionally, the materials' compatibility with coolant requires understanding of SC fluid chemistry, oxide structures metallurgy and related mechanical properties. The ultimate goal is obtained by multi-scale modelling of materials performance in SC fluid.

Generation IV material issues

Liisa Heikinheimo, Pertti Aaltonen and Aki Toivonen

VTT Technical Research Centre of Finland
Espoo, Finland

Abstract

Generation IV nuclear power concepts have become an active research topic all over the world during the last 5–10 years. There are six concepts accepted for the GenIV international forum (GIF) with the common aims to promote both efficiency and safety of the technology. Moreover, the issues of uranium sources and the use of closed fuel cycles are included in the discussions and concepts. Thus the new concepts will offer attractive features but at the same time they also bring new and demanding challenges for the materials technology due to increased operating temperatures and irradiation doses as well as more aggressive coolants and or longer life time expectations than operated today. In this paper an overview of the material issues is given with special emphasis on one of the concepts, super critical light water reactor concept.

1. Introduction

To meet the increasing global energy demand and the requests for cutting the green house emissions the nuclear power is now accepted as a very potential source of energy. Today there is a growing number of activities aiming to upgrade old nuclear power plants or extend the plant life or to start new projects. New projects have been started especially in China (more than 30 GW by 2020), India (more than 20 GW by 2020) and Korea (+9 GW by 2015) but today also in USA and Europe. Thus the future of nuclear power is after a long period positive and this has also opened the discussion for the next generation concepts, so called Generation IV (Gen-IV) concepts.

There are today six commonly accepted Generation IV nuclear power concepts that are listed in international GIF forum:

- Very high temperature reactor (VHTR)
- Supercritical-water-cooled reactor (SCWR)
- Gas-cooled fast reactor (GFR)
- Lead-cooled fast reactor (LFR)
- Sodium-cooled fast reactor (SFR) and
- Molten salt reactor (MSR).

Research on all the concepts has started in main participating countries and partners: USA, Japan, Korea, Kanada and Euratom, with contributions from China, South Africa, India and individual European countries like France. Euratom started research programmes in the 6th frame work programme on all six concepts and the topics are included in the new R&D programme as well.

Today the R&D activities are concentrating on basic technologies and concept development, the design phase is started next and the demonstration is expected to take place first in France for the SFR type reactor concept by 2020.

2. Cross cutting materials issues

The material technology and plant life assessment for these concepts will be developed timewise and technologically between the present nuclear power concepts (mainly Gen-III) and the development of Fusion technology.

The operating parameters of these new concepts are summarised on a general level in Table 1 and Fig. 1. The data is based on current knowledge and discussions in the GIF forums, according to the presentation of Murty in 2007 [1]. The presented SCWR dose range in Fig. 1 applies to a thermal core design. With a fast core design the expected dose would be 100–150 dpa.

Table 1. Features of Gen-IV Nuclear Reactor Systems.

Reactor system	Coolant	Neutron spectrum	Core outlet temperature (°C)
GFR	Gas (e.g. He)	Fast	~ 850
LFR	Liquid metal (e.g. Pb-Bi)	Fast	550–800
MSR	Molten salts (fluorides)	Thermal	700–800
SFR	Liquid Metal (Na)	Fast	~ 550
VHTR	Gas (e.g. He)	Thermal	> 900
SCWR	Water (supercritical fluid)	Thermal / Fast	500–620

The materials selection is to be made based on the specific service conditions and the material coolant interaction issues of each concept. However, there will remain many cross cutting materials aspects to be studied at this stage of development before the design of the plants can be started.

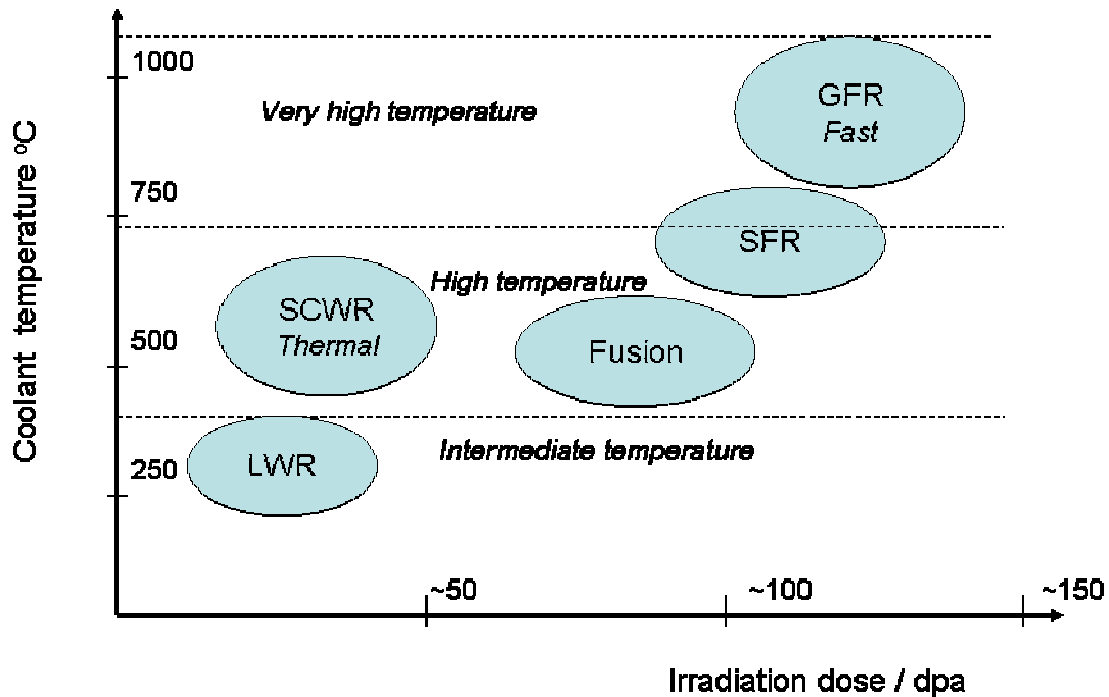


Figure 1. General features of GenIV concepts compared to present LWRs and proposed characteristics of Fusion technology. Coolant temperatures and irradiation doses are selected as most severe operating parameters.

The cross cutting aspects of the desirable characteristics of Gen-IV materials (materials properties as a function of temperature and dose) are:

- Excellent dimensional stability (creep, void swelling)
- Good mechanical properties (strength, ductility, creep rupture, fatigue, creep-fatigue etc.)
- Resistance to irradiation damage (irr. hardening and embrittlement) under high neutron doses (10–150 dpa), He embrittlement etc.
- High degree of chemical compatibility between coolant, structural materials and fuel (e.g., potential to stress corrosion cracking (SCC or IASCC) and many other issues depending on the coolant type lead to concept specific aspects).

To realise components and to assess the life time of under operation also monitoring and manufacturing issues need to be included, mainly:

- Development of on line monitoring and NDE technologies for new designs and materials
- Development of welding methods for the new high temperature materials (ODS, alloys and composites)
- Development of test facilities (corrosion loops and other test reactor facilities).

The main material groups of interest for pressure vessel, reactor internal and cladding uses today are:

- Ferritic/martensitic (F/M) steels up to 500–650°C (depending on the environment)
- Stainless steels operating up to 650–700°C
- Ni-based alloys operating < 950°C
- ODS alloys < 1050°C.

Main application for F/M-steels will be the reactor pressure vessel (RVP) and ex-core components, eg. pipings. The austenitic and high-Cr alloys are studied for the internals, cladding materials and heat exchangers. Both Ni-based alloys and ODS-materials may be alternatives to replace austenitic steels at high operating temperatures or severe corrosion environments.

In the frame of novel fuel material development also refractories (Nb, Mo, Ta etc.), graphite, composites (SiC/SiC) and ceramics are studied for very high temperature components (> 1000°C). A specific area will be the selection of heat exchanger materials due to the fact that these will be operating at very high temperatures and under vast gas/coolant flows (especially in the case of VHTR concept). In many of the concepts an alternative for a secondary coolant is supercritical fluid.

3. Concept specific issues in SCWR and VHTR

The SCWR and VHTR concepts are very attractive due to the fact that they offer a high efficiency and the basic concepts are close to the present LWRs. Moreover, VHTR offers a possibility for hydrogen production as well. In addition to these concepts also SFR is expected to be feasible for demonstration in an intermediate time range.

3.1 Challenges in VHTR concept

The operating temperature, coolant and the size of the pressure vessel of the VHTR concept are all above the figures of the nuclear plants today. The size of the reactor pressure vessel may be twice that of the present vessels and the outlet temperature of the coolant, He-gas, will exceed 900°C.

The expected material degradation will be related to the high operating temperature and high irradiation dose resulting from the long operating life. A special challenge will be the control of the impurities of the coolant (mainly H₂, H₂O, CO, CH₄, N₂ etc. in the circulating He-gas), the expected range of impurities is assumed to be in total 40–70 ppm. This will mean a risk for oxidation,

carburization or nitridation of the materials. The heat exchanger will be designed for temperatures of 850–950°C and pressures of 50–70 bar for 100 000 h life time. The wall thickness is planned to be only a few mm for high heat transfer, which results in very high demands on the HT mechanical properties and chemical compatibility with the flowing gas.

The most potential RPV material will be T/P91 type F/M steel with a good creep resistance. The control rods will be made of 800 H or SiC/SiC composites. Other internals could be made of In690 type alloy, based on present research results by Cebel et al. [2].

3.2 Challenges and research for SCWR concept

In the SCWR concept the main challenges are related to the supercritical fluid coolant (SC fluid) and high operating temperature, Fig. 2. The RPV material will be either the same type as used today in LWRs or a steel with a higher alloying content for higher creep resistance (T/P91). The biggest challenge will be the fuel cladding material because Zr-alloys used in present day LWRs oxidise too quickly at the SCWR temperatures. The choices will be mainly a stainless steel or a novel ODS alloy. ODS-alloys with a Cr-content of 9–19% are widely studied in Japan. Irradiation tests are included today as well [3]. A summary of the damage types relevant to the SCWR candidate materials in question is shown in Table 2.

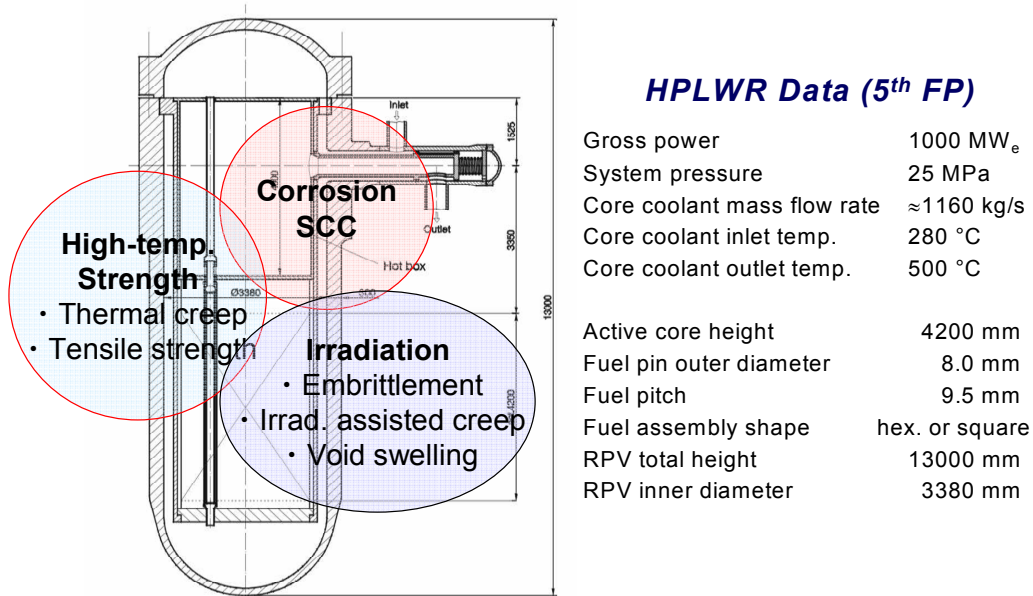


Figure 2. The operation parameters of SCWR concept based on Euratom project HPLWR [4].

Table 2. The damage mechanisms and applicability of various structural material types in SCWR concept by Kaneda 2005 [5].

Alloy type	Corrosion resistance		Radiation damage resistance		HT mechanical integrity	Economics
	General corrosion	SCC	Swelling	Embrittlement		
Austenitic steel	High	Medium	Low	High	Medium	High
Ferritic steel	Medium	High	High	High	Low	High
Ni-base alloy	High	Medium	Low	Medium	High	Medium
Ti-base alloy	Medium – High	Limited data			Medium – High	Low

The fluid characteristics can be seen from Fig. 3. The critical point is at 374°C and 22.1 MPa. At this critical point there is a dramatic change in most of the physical properties of water, e.g., density, specific heat, viscosity etc. Therefore, water chemistry (including radiolysis) will be a challenging research topic for the SCWR concept.

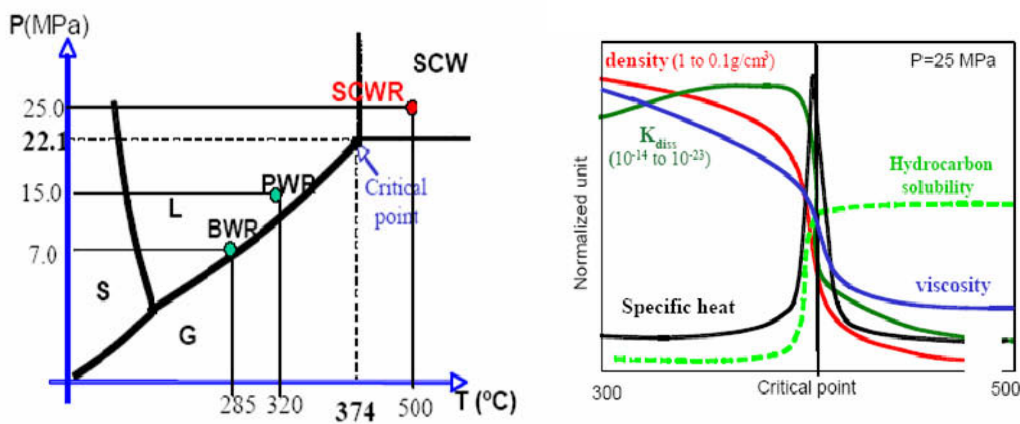


Figure 3. The stability diagram of H₂O as a function of temperature and pressure, typical operation values for BWR, PWR and SCWR are placed in the schema (left). The changes of different H₂O properties across the SC-point (right).

To study the metal – fluid interaction and corrosion phenomenon and water chemistry issues under SC-conditions a test programme has been started in Euratom HPLWR Phase 2 project (High Performance Light Water Reactor) where four European partners are collaborating in the Materials and Water Chemistry work package: VTT, CEA, Areva and NRI, Table 3.

Targets of the HPLWR Phase 2 project are to study the degradation mechanisms of the potential materials and the effects of water chemistry and temperature on the material properties. A materials database will be made for the SCWR concept uses. To be able to carry out this program specific testing facilities will be designed and realized. An in-pile loop will be designed and developed for irradiation tests at NRI. A supercritical autoclave with a water loop is needed for metal-coolant interaction studies, Fig. 4 shows the facility built at VTT in 2003 with maximum operating temperature of 700°C and pressure of 42 MPa.

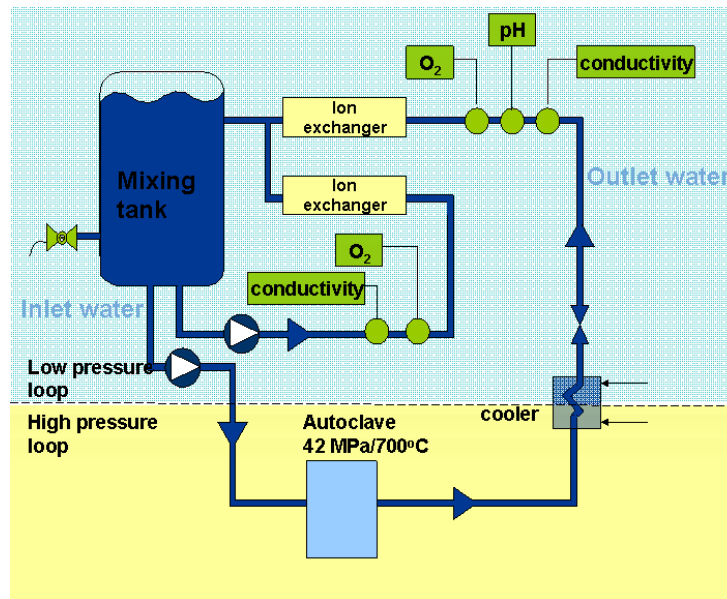


Figure 4. The SC autoclave equipment with a water loop designed and constructed at VTT [6].

Understanding the SC-water chemistry and corrosion phenomenon means that development of monitoring technologies is essential. At VTT both contact electric resistance (CER) and impedance (CEI) methods have been successfully used up to 650°C under SC fluid environment [6].

The structural strength and creep strength are essential to all of the SCWR components. A summary of the creep properties of the candidate materials (Stainless steels and Ni-based alloys) is presented in Fig. 5. The general corrosion characteristics for potential alloys for SCWR RPV and internals are shown in Fig. 6 [7].

Stress corrosion cracking results have been reported by G. Was & al. under simulated SCW conditions for alloy 625 at 400–550°C, Fig. 7 [7].

The oxidation behaviour depends highly on the alloy composition and temperature. Typical features for the oxide growth on austenitic steel AISI 316 at 500 to 700°C are shown in Fig. 8 [6].

Table 3. The experimental programme for SCWR materials in Euratom HPLWR Phase 2 project.

Partner	Test/activity type	Material and environment	Potential component
CEA	<u>Materials performance studies (review)</u> : Provider for a SC-materials database including all tests and literature data	Austenitic stainless steels Ni-based alloys Simulated irradiated materials	Fuel Cladding RPV internals
VTT	<u>Corrosion and creep studies</u> : - Oxidation and general corrosion with coupons - SCC with U-bend and 3-point bend specimens - Creep-oxidation using bellow loading (500–600°C) for controlled slow tensile loading	Ferritic steels Ferritic and austenitic stainless steels Ni-based alloys at 300°C -> 600°C H ₂ & O ₂ water chemistry	Fuel Cladding RPV Internals Out of core components
AREVA	<u>Expert contribution</u> : specifications, evaluation of results and water chemistry concept	-	Fuel Cladding Internal support Out of core components
UJV	<u>Supercritical Water Loop construction</u> and qualification out-of-pile. Preparation of the loop for future in-pile tests.	Varying water chemistry (H ₂ content optimisation to suppress radiolysis)	Fuel Cladding Internal support Out of core components

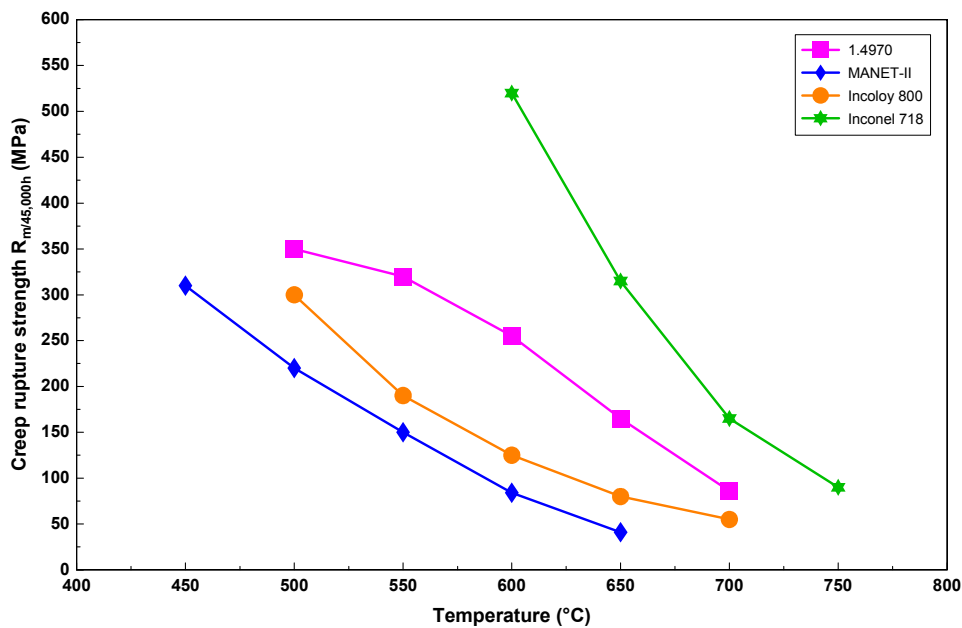


Figure 5. Creep rupture strength of candidate materials for RPV, externals and cladding by Ehrlich et al. 2003 [4].

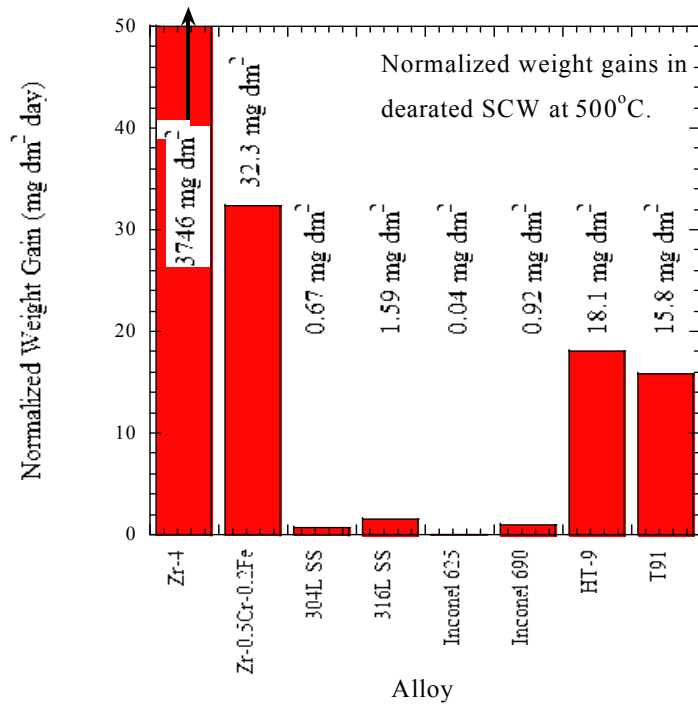


Figure 6. General Corrosion Experiments for candidate materials at 500°C by G. Was 2005 [7].

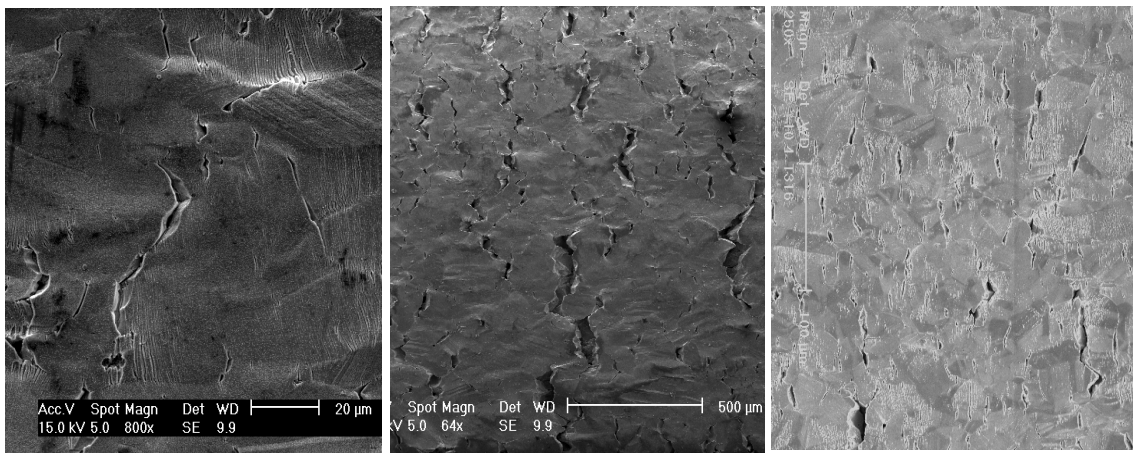


Figure 7. Gage surfaces after SCC tests on alloy 625 in SCW: G. Was, University of Michigan, 2005 (400, 500 and 550°C from the left) [7].

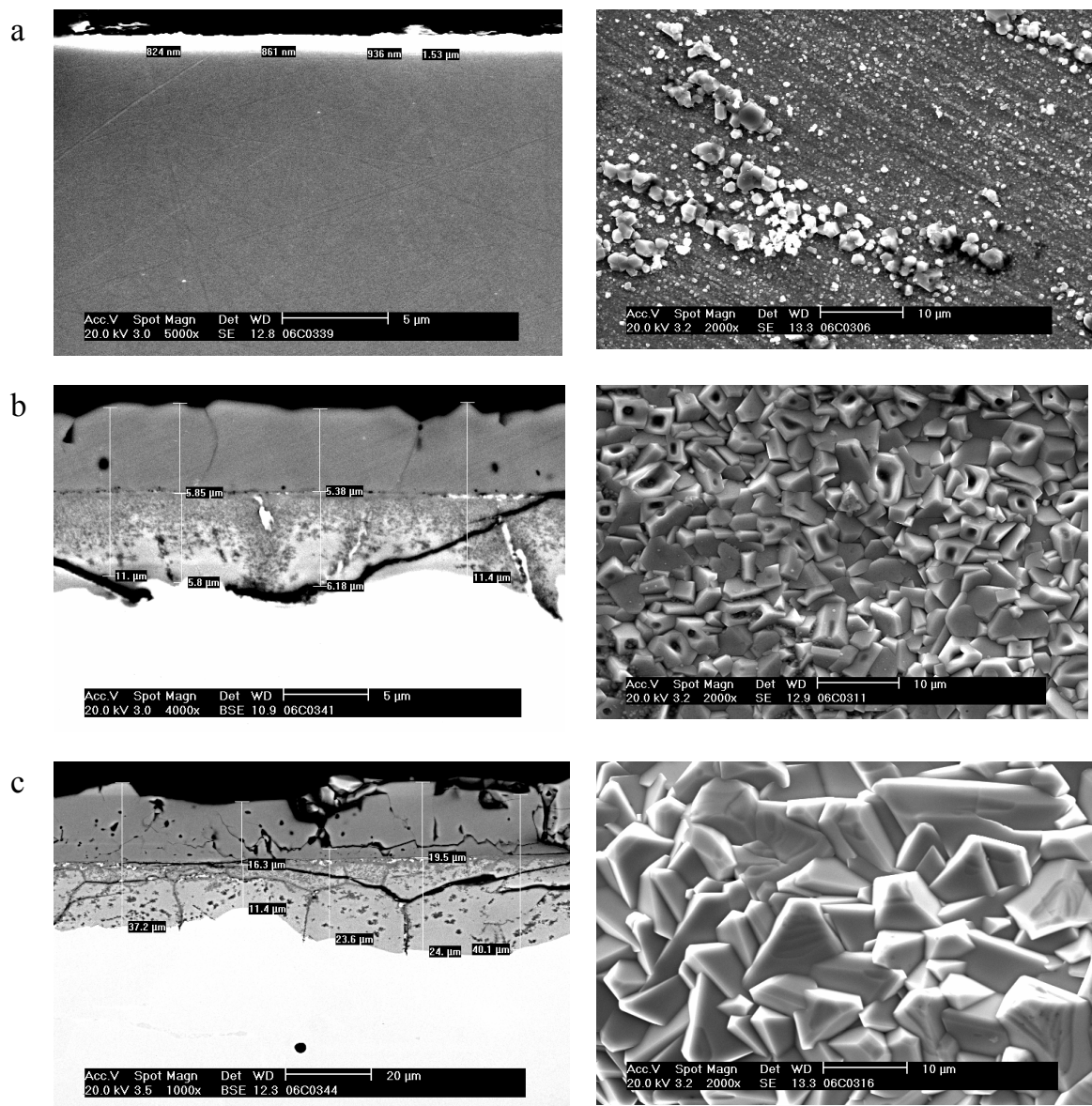


Figure 8. The oxide cross sections, left, and the surface morphologies, right, of oxide films on AISI316 – exposure for 100 h under 30 MPa: a) 500°C (total oxide thickness < 1 μm), b) 600°C (total oxide thickness 6 μm) and c) 700°C (total oxide thickness 20 μm) [6].

3.3 Materials research status and further needs

Gen IV materials research approach starts from the application of commercial alloys and is extended with modified alloys, e.g. stainless steels for nuclear purposes. Special development is carried out to develop fuel materials for pebble bed reactors and for some of the heat exchangers needed for the high temperature solutions. The present status of materials development and verification for Gen IV concepts:

- Commercial alloys: α - (9–12% Cr), γ - steels and Ni-based alloys are widely studied for most of the concepts and components.
- Modified commercial alloys: mod. α - and γ -alloys, ODS alloys, Zr-alloys (up to 500°C corrosion rate of a Zr-0.4Fe-0.2Cr is 0.5 x that of α -steel), are studied for fuel cladding alloys.
- Fusion Technology development: results on γ -steels, ODS-alloys and graphite are exploited directly in the R&D of GenIV materials.
- New development (ongoing): VHTR Fuel, SiC-SiC and graphite materials.
- Refractory metals for various fuel concepts and/or heat exchangers are an option for ceramics and ODS materials.
- Need to study radiation damage at GenIV operational temperatures is a future challenge.
- Need to study materials performance in specific corrosion loops that enable the material-coolant studies under irradiation. This is a future challenge in order to verify material choices for GenIV design and demonstration phases.

4. Summary

The materials issues are critical in developing new energy concepts with high operating temperatures and especially when neutron flux is involved. Part of the materials issues in GenIV development are concept specific but many are still cross cutting and, therefore, a common ground for GenIV materials research can be established.

There are many technologies and facilities to be developed besides the new material development itself in order to meet the GenIV requirements and also to make these concepts possible. Especially the development of test loops for the materials performance testing and carrying out irradiation tests at relevant environmental conditions would be necessary. Research and development of the welding and weldability and manufacturing issues are needed for the realisation of structural components. Later on the development of suitable NDE technologies will be required to verify the acceptance criteria for the components and to demonstrate the plant life management concepts for the new processes.

Modelling of materials properties and performance is needed for the efficient use of experimental results and to overcome the limitations in the data achievable. To get a sound data basis also experimental technology and devices should be developed further to meet all the critical requirements of GenIV concepts. Modelling in general improves the understanding and the usability of the knowledge, but it is needed also to interact with the other actors in the design process. This means also improved communication and understanding of knowledge between different

diciplines. The GenIV research gives an opportunity to collaboration between physicists, experimentalists, material scientists and designers.

References

- 1 Charit, I. and Murthy, K.L. Structural materials for the next generation nuclear materials – an overview. Proc. of ICAPP 2007, Nice, France May 13–18, 2007. Paper 7315.
- 2 Cebel, C. et al. Benchmark CEA-Areva-EdF of the corrosion facilities for VHTR material testing. Proc. of ICAPP 2007, Nice, France May 13–18, 2007. Paper 7195.
- 3 Kimura, A. et al. Super ODS steels R&D for cladding of highly efficient nuclear plants. Proc. of ICAPP 2007, Nice, France May 13–18, 2007. Paper 7374.
- 4 Schulenberg, T., Starflinger, J., Aksan, N., Bittermann, D. and Heikinheimo, L. Supercritical water reactor research in the GIF context: Current status and future prospects with emphasis on European activities. Proceedings of FISA 2006 EU Research and Training in Nuclear Systems, Luxembourg, 13–16 March 2006, EUR 21231. Pp. 287–304.
- 5 Saito, N. et al. SCC Properties of candidate alloys for SCWR core components. Proc. IAPP 2006, Reno, NV USA, June 4–8, 2006. Paper 6137.
- 6 Saario, T. et al. Surface film electrochemistry of AISI316 Stainless Steel and its constituents in supercritical water. Proc. of ICAPP 2007, Nice, France May 13–18, 2007. Paper 7123.
- 7 Was, G. et al. Corrosion and stress corrosion cracking of iron- and nickel-base austenitic alloys in supercritical water, Corrosion 2004, Paper 04492, March 28 – April 1, 2004 New Orleans USA, NACE (2004).

Oxyfuel concept development

Toni Pikkarainen, Antti Tourunen and Jouni Hämäläinen

VTT Technical Research Centre of Finland, Jyväskylä, Finland

Abstract

Reduction of greenhouse gas emissions and replacement of fossil fuels by renewable energy sources are important national and international targets. Oxyfuel (oxygen combustion technology) is one of the most promising technologies enabling carbon capture and storage (CCS) from flue gases. Aim of oxyfuel concept development is to study different oxygen production technologies, combustion processes, CO₂ capture methods and integrate those to optimised concept. Goal is to create technical readiness for demonstration of oxygen combustion by using state-of-the-art knowledge, experiments, modelling and simulation. Demonstration plan for oxygen combustion for an existing power plant(s) in Finland will be prepared. Main results will be an evaluation of oxygen combustion business potential for implementation in existing and new power plants, and improvement of competitiveness of Finnish companies in energy sector by developing CO₂-free power production technologies.

Before oxygen combustion can be demonstrated in full-scale, small-scale testing and model development must be done. Material exposure conditions in oxygen combustion will differ from any present day environment. Current high temperature steel grades have been not developed nor tested for such aggressive conditions. VTT (Technical Research Centre of Finland) has in Jyväskylä unique small-scale combustors applicable for oxygen combustion research.

1. Introduction

Reduction of greenhouse gas emissions has become a major challenge for the energy producers and technology suppliers. The main approaches to emission reduction in the energy production are as follows (Fig. 1):

- Increase of efficiency provides emission cuts proportional to the rise in efficiency. When combined with other solutions, it has a direct impact on the consumption of natural resources, generation of waste matter and economics of production.

- Co-firing of solid fossil fuels with CO₂-neutral fuels in fuel-flexible CFB boilers provides a technically and economically feasible solution for CO₂ reduction up to certain degree.
- When bigger emission cuts are required, CCS (Carbon Capture and Storage) offers potential for near zero emission power production from fossil fuels, though at the expense of efficiency and costs.

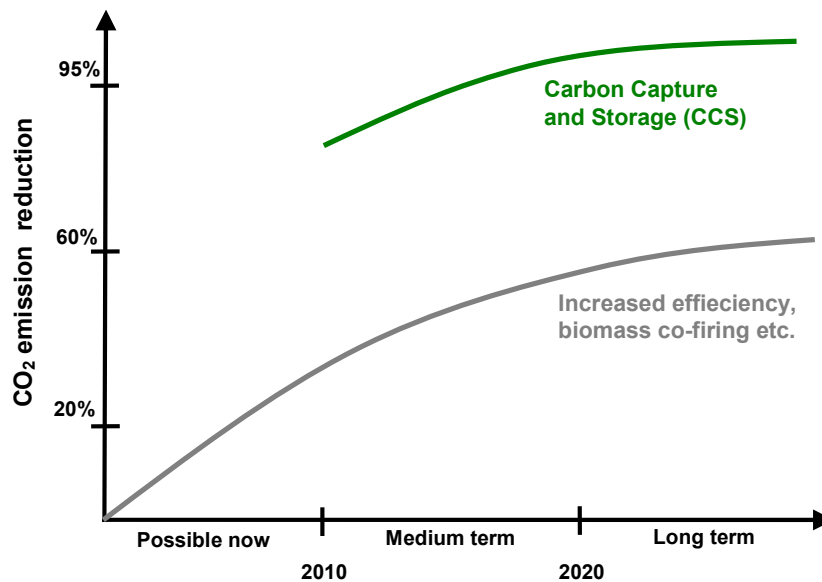


Figure 1. Two main approaches to CO₂ emission reduction in the energy production.

Post-combustion capture of CO₂ from power station flue gases is considered technically feasible for CFB boilers, even as retrofit. However, the flue gas volumes are large and CO₂ is very much diluted with N₂ in conventional combustion with air. Separation of CO₂ from such a stream is costly with the existing technologies, and other options are being explored. [1]

Fig. 2 shows a simplified process flow scheme of an oxygen combustion power plant, which consists of an air separation unit (ASU), a power plant with O₂-blown combustion, and a CO₂ treatment unit. Oxygen is mixed with recirculated flue gases, which creates a mixture of primarily O₂, CO₂ and H₂O used as oxidant in combustion instead of air. The absence of air nitrogen produces a flue gas stream with a high concentration of CO₂, making it more favourable to separate the CO₂ [2].

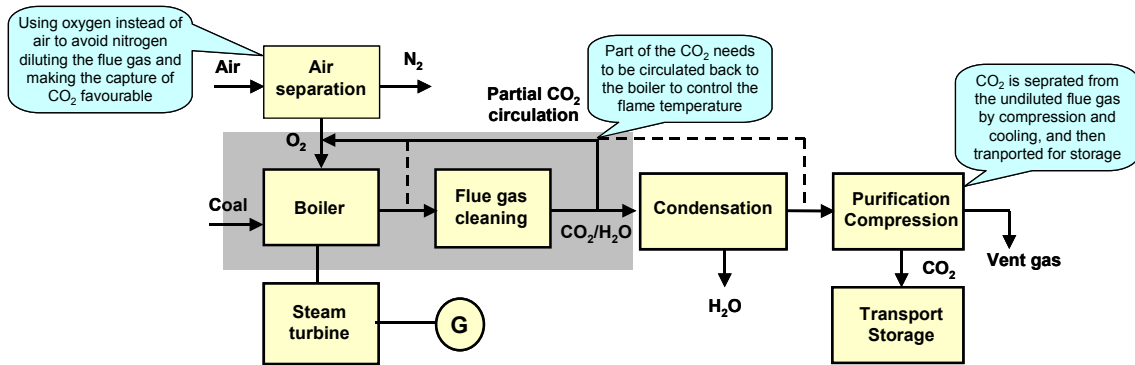


Figure 2. Schematic of an oxygen combustion power plant [1].

2. Oxygen combustion experimental

VTT (Technical Research Centre of Finland) has in Jyväskylä unique small-scale fluidized bed combustors applicable for oxygen combustion research. A pilot-scale (30–100 kW) CFB reactor can be operated in air firing and O₂ combustion modes. The reactor is equipped with O₂ and CO₂ feed from gas tanks and also with flue gas recirculation for demonstrating real oxygen combustion conditions. In addition, a smaller bubbling fluidized bed (BFB) /CFB reactor (< 1 kW), which can be operated at batch and continuous combustion modes, is suitable for phenomena studies of oxygen combustion.

Small-scale tests will be linked to modeling tools and experimental data will be utilized in the validation of various sub-models for oxygen combustion conditions (Fig. 3).

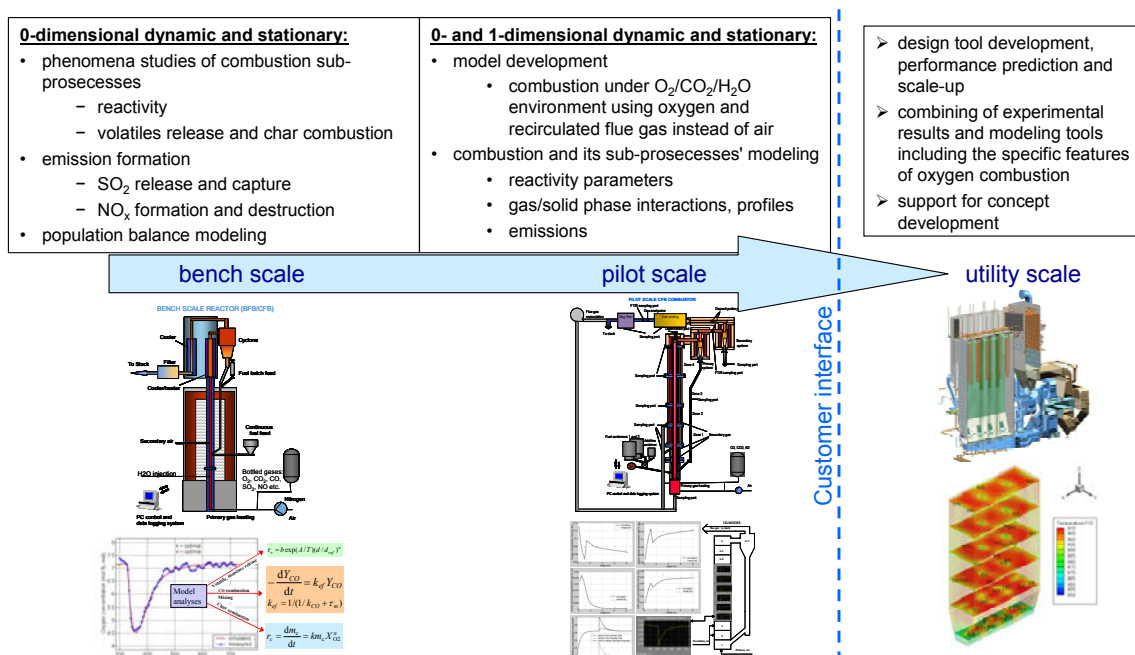


Figure 3. Linking of small-scale tests and modelling with full-scale design tools.

2.1 Bench scale tests

A bench scale BFB/CFB (bubbling/circulating fluidised bed) reactor with fuel/additive batch and continuous feed is illustrated in Fig. 4. Height of the riser tube is 1.52 meters and inner diameter 32.8 mm (at 850°C). Pre-heated primary gas is fed into the reactor through a perforated grid and also secondary gas feed point could be used. Different kind of gas mixtures can be used e.g. O₂, CO₂, SO₂, CO in addition to air and nitrogen. Water vapour can be injected under the grid to simulate wet flue gas recirculation. Fuel or limestone batch can be fed into solids circulation tube returning the solids into the reactor. Fuel or mixture of fuel and additives can be fed into reactor continuously by different screws. Temperature and pressure profiles along the riser are measured from four points. Temperature is controlled with surrounding electric heaters.

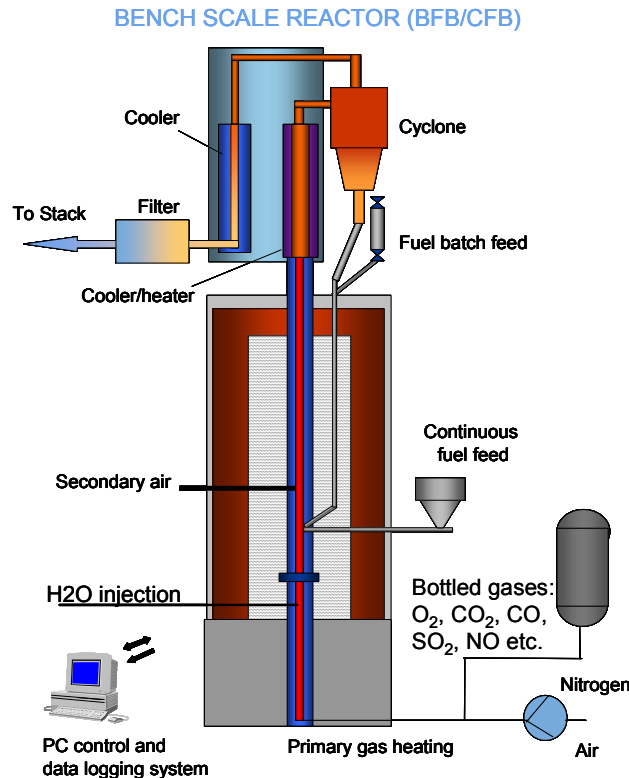


Figure 4. Bench scale BFB/CFB reactor.

Continuous fuel feed tests carried out by bench scale CFB reactor with the Polish bituminous coal. Three different temperature levels – 800°C, 850°C and 900°C – with CO₂ based and air atmospheres were tested. Gas feed was adjusted so that fluidization velocity was kept at about 1.5 m/s. Fuel feed was adjusted so that excess air factor (or excess oxygen factor) was kept constant. Aim of the continuous fuel feed tests was to compare emission formation at oxygen combustion conditions between emission formation at air firing conditions.

SO₂ and NO emissions expressed as ppms at 6% dry oxygen and as mg/MJ as a function of reactor temperature at oxygen and air combustion modes are presented in Fig. 5. Comparing emissions on mg/MJ basis eliminates the diluting effect of nitrogen in air firing. SO₂ emissions were quite independent on reactor temperature, moderate minimum can be seen between temperatures 800–840°C. NO emissions increased with increasing temperature. SO₂ and NO emissions were quite similar at oxygen combustion and at air combustion modes expressed as mg/MJ.

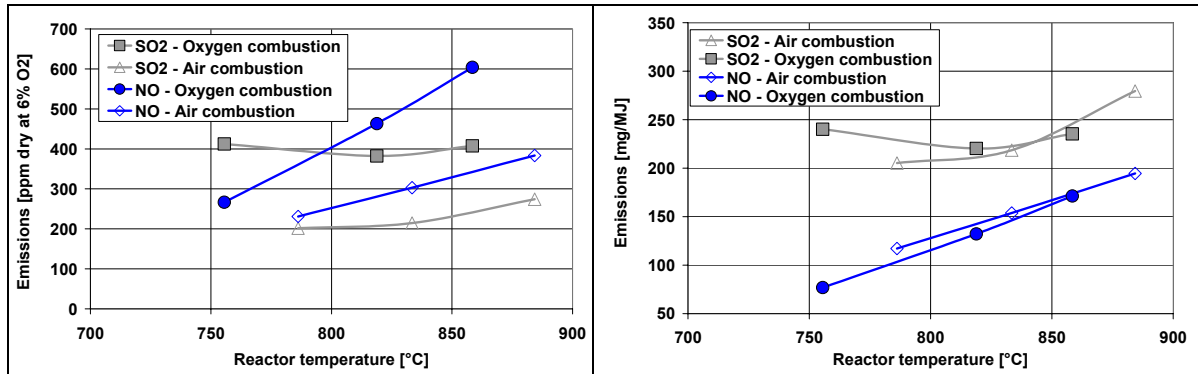


Figure 5. Bench scale continuous fuel feed tests' SO₂ and NO emissions expressed as ppms and mg/MJ as a function of reactor average temperature.

2.2 Pilot scale CFB tests

The riser of the CFB pilot reactor is 8 metres high and the inner diameter is 16.7 cm (Fig. 6). The reactor is equipped with several separately controlled electrically heated and water/air cooled zones in order to control the process conditions (for example O₂ level, temperature and load) almost independently.

A flue gas recirculation system has been built to demonstrate real oxygen combustion at the pilot unit, while, in earlier studies bottled O₂/CO₂ gases have been used. The recirculation gas system contains a fan, a gas pipeline divided into primary and secondary lines after the fan, flow measurement (in the primary line) and control valves.

The combustion gas can consist of air, N₂, O₂, CO₂, recirculated flue gas, or mixtures of these. It is divided into primary gas fed through the grid and secondary gases fed to up to three different levels of the reactor. The gas compositions can be adjusted independently.

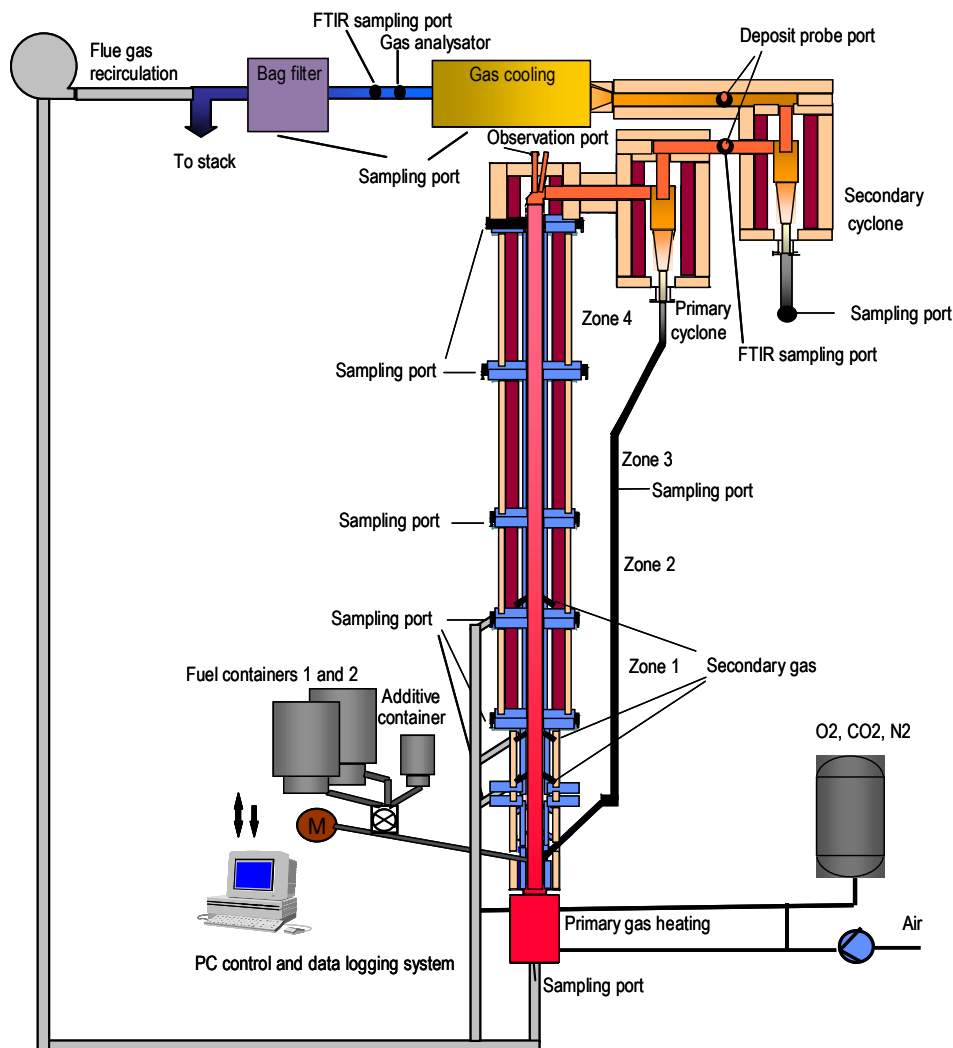


Figure 6. CFB combustor pilot.

A test campaign was carried out under oxygen combustion and normal air combustion conditions with the Polish bituminous coal and commercial limestone (Table 1). One test (Balance 2) was carried out with bottled O₂/CO₂ feed and three tests (Balances 3–5) with pure O₂ feed and flue gas recirculation. Probably this was the first time in the world, when real oxygen combustion was demonstrated successfully in the CFB conditions. Balances 0, 1 and 6 are reference air combustion tests.

Table 1. Pilot scale CFB test matrix.

Balance code	Fuel type	Load kW	Ca/S, lime mol/mol	Feed gas O ₂ %, wet	Prim. gas O ₂ %, wet	Sec. gas O ₂ %, wet	Prim. O ₂ share %	Prim. gas share %	FG RC ratio %
0	Bituminous coal	49.1	0.0	20.8	20.8	20.8	59.0	59.0	-
1		49.6	2.5	20.8	20.8	20.8	61.0	61.0	-
2		46.2	1.5	20.8	20.8	20.8	49.9	50.0	-
3		95.4	1.0	30.7	30.7	30.8	49.9	50.0	67.5
4		86.4	1.0	28.6	28.7	28.5	59.9	59.8	70.2
5		87.2	1.0	39.8	43.2	34.9	64.9	59.4	57.2
6		48.2	1.0	20.8	20.8	20.8	60.0	60.0	-

SO₂ emissions and limestone calcium utilisation of air combustion balances 1 and 6 and oxygen combustion with flue gas recirculation (balances 3–5) are illustrated as a function of bed temperature in Fig. 7. Calcium utilisation was calculated as:

$$Ca_utilisation = \frac{RET}{Ca/S} \quad (1)$$

where RET is sulphur retention [%]
 Ca/S is limestone calcium to fuel sulphur feed ratio [mol/mol].

At oxygen combustion, SO₂ emission decreased and calcium utilisation increased with increasing bed temperature in the temperature range 750–900°C. At about 860–875°C bed temperatures, SO₂ emission was about 270 mg/MJ for air combustion when corresponding emission for oxygen combustion (feed gas O₂ = 40%-wet) was about 46 mg/MJ. That remarkable increase in limestone sulphur capture could be explained by extended reaction time between flue gas SO₂ and calcium when about 60% of flue gas is recirculated. Also sulphur capture mechanism could change when CO₂ partial pressure increases [3–5].

The effect of flue gas recirculation on sulphur capture could be studied by comparing balances 2 and 3. Balance 2 was an oxygen combustion test with bottled O₂/CO₂ gas feed whereas Balance 3 was an oxygen combustion test with about 67% flue gas recirculation (i.e. 33% fresh combustion flue gas to stack). Bed temperature was around 800°C during both of the tests. Calcium utilisation rate increased from 63% to 76% with flue gas recirculation. It must be noted that freeboard temperature was about 900°C during the Balance 3, when it was about 800°C during the Balance 2. Probably high freeboard temperature deteriorates sulphur capture.

NO emissions of tests in Table 1 were compared with the earlier results from air firing tests with the same bituminous coal. Fig. 7 presents NO emissions versus bed temperatures at oxygen and air combustion tests. NO emissions seem to be in the same level at both oxygen and air combustion modes, and about one third compared to the bench scale tests.

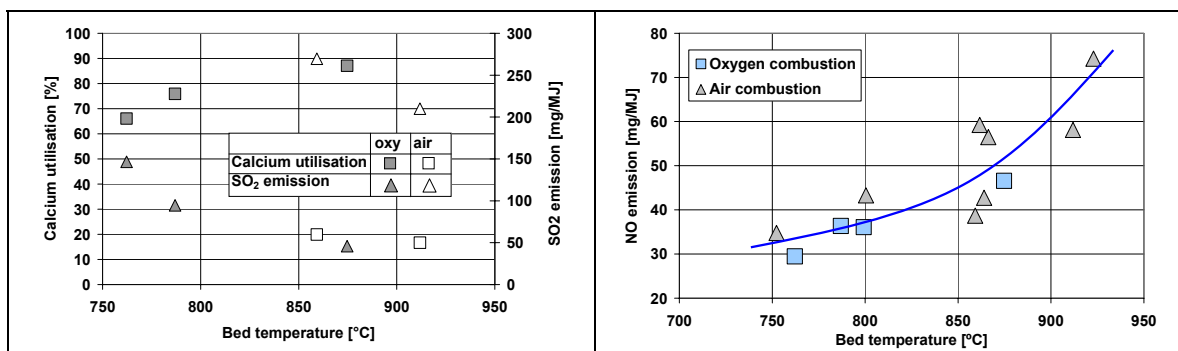


Figure 7. Pilot scale CFB tests' SO₂ emissions and calcium utilization as a function of bed temperature (on left) and NO emissions as a function of bed temperature.

3. Oxyfuel concept development

3.1 Ongoing projects

VTT is coordinating joint financed Tekes (the Finnish Funding Agency for Technology and Innovation) project called Oxyconcepts in Climbus-program (Business Opportunities in Mitigating Climate Change). Main goals of the project are as follows:

- to evaluate technically and economically different oxygen production techniques, combustion and CO₂ capture processes, and the integration of these to overall concepts
- to create technical readiness for demonstration of oxygen combustion by using state-of-the-art knowledge, experiments, modelling and simulation
- to create demonstration plan for oxygen combustion for an existing power plant(s) in Finland
- to evaluate oxygen enriched combustion for power boosting of a power plant.

Main results of the project will be:

- an evaluation of oxygen combustion business potential for implementation in existing and new power plants, and
- an improvement of competitiveness of Finnish companies in energy sector by developing CO₂-free power production technologies.

Project started 06/2006 and ends 12/2008. The structure and participants of the project are illustrated in Fig. 8.

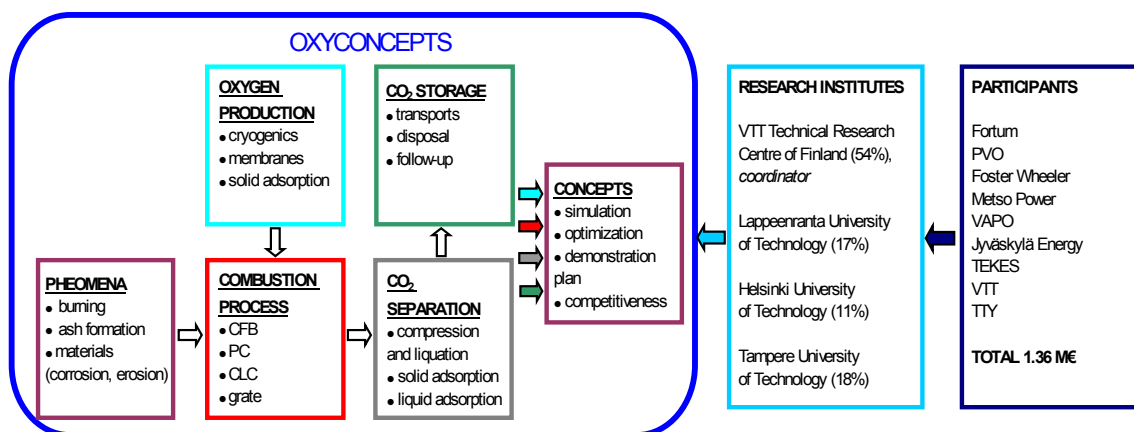


Figure 8. The structure and participants of the project Oxyconcepts.

3.2 Future projects

Material exposure conditions in oxygen combustion of coal will differ from any present day coal combustion environment in terms of higher temperature, higher concentration of O_2 , H_2O and CO_2 in flue gases, as well as in terms of activities of corrosive species such as SO_3 and Cl in the deposits. Current high temperature steel grades have been not developed nor tested for such aggressive conditions. Available data indicates that the corrosion performances of the high temperature steel grades as well as of nickel alloys currently in use can be in some cases insufficient for use in oxyfuel combustion plants.

The rationale of the planned project is to enable steel manufacturers to identify the most potential steel grades and to develop new steels for zero emission plant. The project aims to advance step by step from laboratory scale corrosion screening tests with standardised methods up to detailed explanations and models of prevailing corrosion mechanisms of steels under the targeted process conditions.

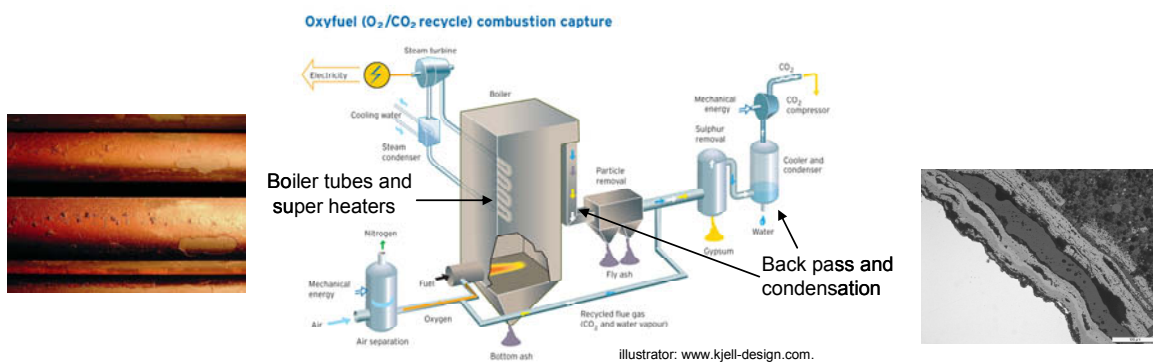


Figure 9. Critical points for materials in oxyfuel process.

During the Oxyconcepts-project a plan for oxygen combustion demonstration at Tornio CFB-boiler will be prepared in co-operation with project partners, Etelä-Pohjanmaan Voima Oy, Outokumpu Oyj and Oy AGA Ab. If circumstances remains good, a new project will be launched to carry out world's first oxygen combustion CFB demonstration (Fig. 10).

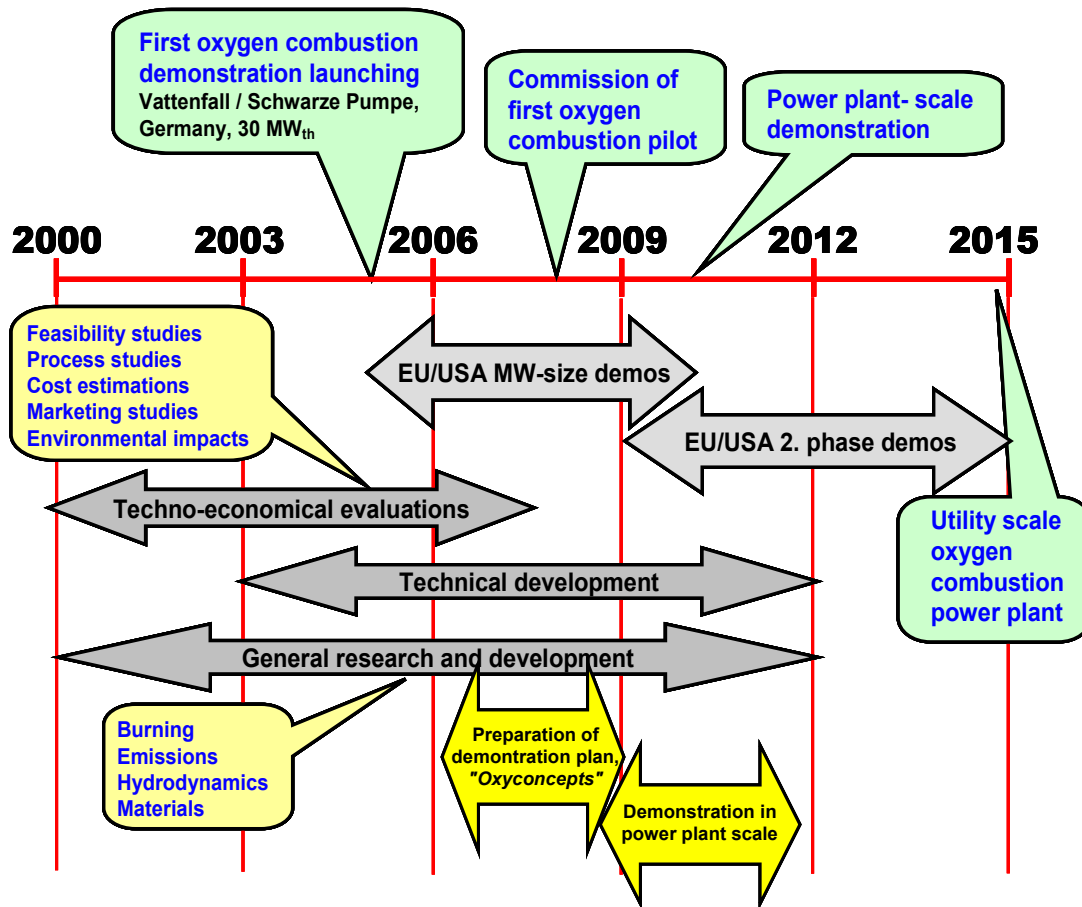


Figure 10. Target schedule for oxyfuel commercialization.

4. Conclusions

Results of the bench scale tests showed that SO₂ and NO emission were around the same level for air and oxygen combustion (with dry bottled O₂/CO₂ gas feed) expressed as mg/MJ. Also at pilot scale tests with pure oxygen feed and wet flue gas recirculation NO emissions were about the same as in air combustion, and about one third compared to the bench scale tests. But SO₂ emissions of pilot scale air combustion tests were clearly higher than that of oxygen combustion with flue gas recirculation. Flue gas recirculation makes SO₂ capture clearly better by prolonging the reaction time between sulphur and calcium. In addition to flue gas recirculation, also different scale of pilot CFB makes flue gas residence time longer. In pilot scale tests flue gas contains water vapour, which also could have effect on emission formation.

Oxyfuel (oxygen combustion technology) is one of the most promising technologies enabling carbon capture and storage (CCS) from flue gases. The aim of the oxyfuel concept development is to study different oxygen production technologies, combustion processes, CO₂ capture methods and design tools, and

integrate the process components to an optimised concept. Goal is to create technical readiness for demonstration of oxygen combustion by using state-of-the-art knowledge, experiments, modelling and simulation. Demonstration plan for oxygen combustion for existing power plants will be prepared. In near future, target is to realise demonstration plan by launching a project to carry out world's first oxygen combustion CFB demonstration.

Before oxygen combustion can be demonstrated in full-scale, small-scale testing and model development must be done. Material exposure conditions in oxygen combustion will differ from any present day environment. Current high temperature steel grades have been not developed nor tested for such aggressive conditions. VTT (Technical Research Centre of Finland) has in Jyväskylä unique small-scale combustors applicable for oxygen combustion research.

References

1. Eriksson T., Sippu O., Hotta A., Fan Z., Myöhänen K., Hyppänen T. and Pikkarainen T. "Oxyfuel CFB Boiler as a Route to Near Zero CO₂ Emission Coal Firing", POWER-GEN Europe 2007, June 26–28, 2007, Feria de Madrid, Spain.
2. Jäntti T., Eriksson T., Hotta A., Hyppänen T. and Nuortimo K. "Circulating Fluidized-bed Technology – toward Zero CO₂ Emissions", POWER-GEN Europe 2006, May 30 – June 1 2006, Cologne, Germany.
3. Liu H., Katagiri S., Kaneko U. and Okazaki K. Sulfation behavior of limestone under high CO₂ concentration in O₂/CO₂ coal combustion. *Fuel* 79 (2000), pp. 945–953.
4. Hajaligol M.R., Longwell J.P. and Sarofin, A.F. Analysis and modeling of the direct sulfation of CaCO₃. *Ind. Eng. Chem. Res.* 1988, 27, pp. 2203–2210.
5. Pikkarainen T., Tourunen A., Nevalainen H., Leino T., Saastamoinen J. and Eriksson T. "Small scale fluidized bed experiments under oxygen combustion conditions", 2007 International Conference on Coal Science and Technology, August 28–31 2007, Nottingham, U.K.

Modelling of supercritical conditions in the safety analysis codes

T. Vanttola, M. Hänninen and A. Daavittila

VTT Technical Research Centre of Finland, Espoo, Finland

Abstract

Thermal hydraulic modelling is needed for describing processes that use water for cooling. Simulator codes solve conservation equations of coolant mass, momentum and energy using numerical methods. Additionally, correlation based models are needed for describing, among others, heat transfer and friction between the structures and the coolant. In two-phase flow the correlations for interfacial heat transfer and friction are used for exchanging of mass, momentum and energy between liquid and gas phases. Typical applications are various boiler processes and nuclear reactors. Some modern boilers operate in supercritical water conditions as well as a new nuclear reactor concept SCWR (Super Critical Water Cooled Reactor). Water properties change fast around the critical point (220.64 bar, 374.15°C) and heat transfer in supercritical state is not fully understood, which makes modelling challenging and is typically beyond normal operation regime of the analysis codes.

At the moment VTT is modifying two of its code packages, APROS and TRAB-SMABRE to adapt for supercritical conditions. APROS is a general purpose simulation code both for nuclear and non-nuclear applications, while TRAB-SMABRE is used solely for nuclear reactor analysis. The models for water properties, such as density, specific heat capacity and heat conductivity, have already been developed. The homogeneous water model of APROS (3 conservation equations) has already been tested in supercritical boiler conditions and operates in principle. The more sophisticated operation mode of APROS (6 conservation equations) operates in supercritical state but the transition from supercritical to subcritical two-phase state has not yet been tested. The correlation package of heat transfer and friction has to be tested and possibly modified in supercritical conditions. The testing of the TRAB-SMABRE code (5 conservation equations) is to be started soon.

TRAB-SMABRE and possibly also APROS are to be applied for reactivity transient analysis of the European development version of the supercritical water reactor in the Euratom 6th Framework Programme project High Performance Light Water Reactor, HPLWR Phase 2.

NULIFE – Network of excellence for harmonised nuclear plant life management methods

Rauno Rintamaa and Irina Aho-Mantila

VTT Technical Research Centre of Finland, Espoo, Finland

Nigel Taylor

European Commission Joint Research Centre, Institute for Energy
Petten, The Netherlands

Abstract

The EU's Network of Excellence NULIFE (Nuclear plant life prediction) has been launched under the EURATOM FP6 Program. NULIFE will help provide a better common understanding of the factors affecting the lifetime of nuclear power plants which, together with associated management methods, will help facilitate extensions to the safe and economic lifetime of existing nuclear power plants. In addition, NULIFE will help in the development of design criteria for future generations of nuclear power plant. Led by VTT, the five-year project has a total budget in excess of EUR 8 millions, with partners drawn from leading research institutions, technical support organisations, power companies and manufacturers throughout Europe.

1. Introduction

NULIFE (Nuclear plant life prediction) is a European network of excellence funded by the European Commission's 6th Framework Programme together with in-kind contributions of the participants. The network is made up of 10 Work Package leader organisations (Contractors) and about 30 Associate Contributors and Collaborators. NULIFE was kicked-off in October 2006 and will work over a 5-year period to create a single organisation structure, capable of providing harmonised R&D at European level to the nuclear power industry and the related safety authorities in the area of lifetime evaluation methods for structural components. While over half are from the research sector, NULIFE also involves many industrial organizations and, in addition to their R&D contributions, these take part in a dedicated End User Group.

Key organisations, Contractors of NULIFE are

- VTT, Technical Research Centre of Finland, a Coordinator of NULIFE
- Studiecentrum voor Kernenergie – Centre d’Etude de l’Energie Nucléaire, SCK•CEN from Belgium
- Ustav jaderného výzkumu Rez a.s., Nuclear Research Institute Rez plc, NRI from Czech Republic
- Commissariat à l’Energie Atomique, CEA and Electricité de France, EDF from France
- AREVA NP GmbH from Germany
- European Commission Directorate General Joint Research Centre, JRC, from EC
- British Energy Generation Ltd and Serco Ltd from UK and
- Forsmark Kraftgrupp AB from Sweden.

NULIFE (Nuclear Plant Life Prediction) has been launched with a clear focus on integrating safety-oriented research on materials, structures and systems and exploiting the results of this integration through the production of harmonised lifetime assessment methods.

1.1 Vision of NULIFE

NULIFE’s vision is to create a virtual institute with

- An integrated RTD platform embracing all European stakeholders (Table 1), with improved and efficient use of public and private RTD funding
- Sustainable forum for realising harmonised technical procedures for the nuclear energy industry and European regulators
- Service provider and source of qualified expertise.

Table 1. The impact for different stakeholders.

Stakeholder	NULIFE Impact
Regulatory bodies TSOs	Source of qualified “best practice” technology for addressing ageing issues in safety-critical NPP structures.
Utilities	Stable resource of operational RTD expertise to support implementation of effective life management programmes.
Manufacturing industry Vendors	Harmonised procedures for design and maintenance of new or refurbished components.
Service organizations Research organizations Universities	Efficient use of RTD resources Improved exploitation of results Stable environment for development of excellence Training services

A multi-phase planning and integration process (Fig. 1) has been developed to realize the NULIFE Institute:

- Integration plan (creation of viable expert groups, a coherent structure and communication methods)
- Preparation of business plan, (funding model, links with national programmes, updated structure, policy for training, knowledge management and communication)
- Consolidation of integration plan (launch of new RTD projects, development and application of procedures and best practices)
- Creation of the Virtual Institute (structure with permanent entity features, joint use of facilities, coordinated investment policy)
- Transition plan to a permanent entity (management structure, long-term business plan, recognition as a solution provider).

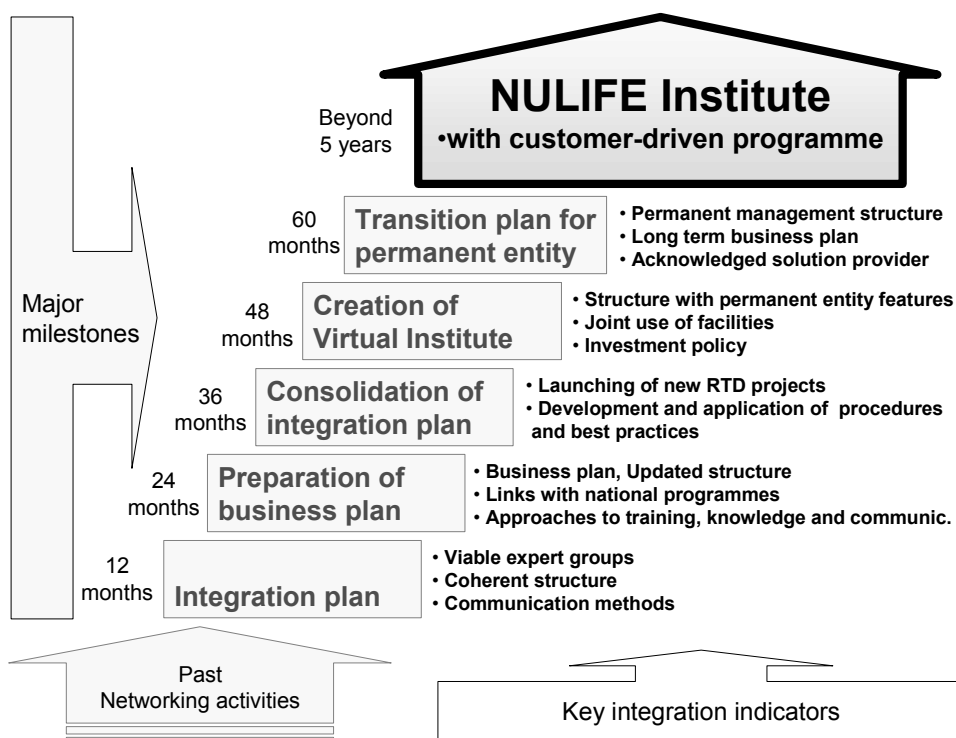


Figure 1. Planned organizational evolution during the five phases of NULIFE (2006–2011).

2. Mapping of expertise and expert group activities

The network will bring together a broad range of scientific and technical competences relevant to effective RTD. The themes covered by the Expert Groups are materials and materials ageing, integrity assessment, lifetime evaluation and

safety, risk information & reliability. In addition to the scientific competence, other skills, experience and data are necessary for efficient plant life management (Fig. 2). In the expertise mapping also knowledge of available facilities, management and spreading excellence skills, design, manufacturing and operating expertise are collected. As a result of the mapping process, complementary and overlapping resources will be identified, together with any ‘gaps’ that have to be addressed.

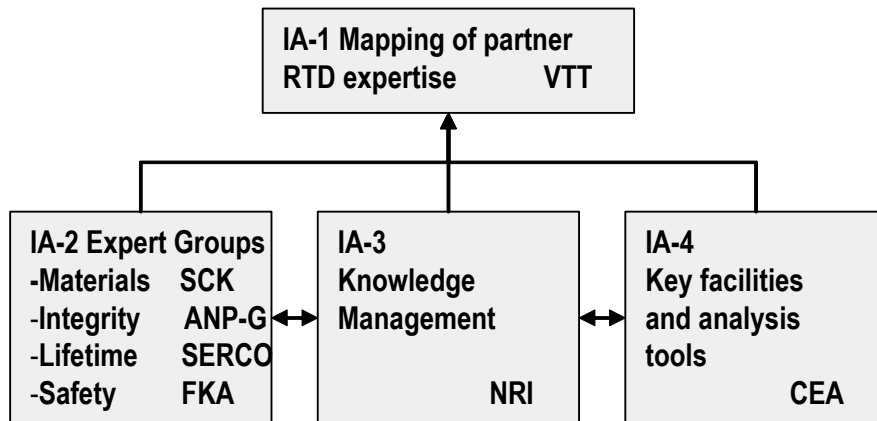


Figure 2. Integrating Activities (IA) for the development of expertise, facility and knowledge clusters for the lifetime management.

The NULIFE questionnaire for mapping expertise has already been launched. Research organizations and service providers will define the current expertise, and end users and vendors are asked to define strategic needs. The strategic views of research organizations and service providers will also be outlined. With the questionnaire, expertise related to different reactor types, experimental conditions, system and component types as well as material types will be outlined. Lifetime management expertise will be defined through detailed list concerning degradation modes, load effects, condition monitoring, inspection, integrity assessment and safety management. Testing facilities, organization/process related expertise, spreading excellence as well as design, manufacturing, operation expertise will also be reviewed.

A key element in the Network structure will be the four Expert Group activities, which will cluster “centres of expertise” and provide a focus for activities. The scope of the individual Expert Group WPs is defined as follows:

- IA-2-1 deals with the material property issues, in particular the mechanisms of materials degradation (EAC, thermal ageing, irradiation embrittlement) and characterization of the properties of aged materials, i.e. as a function of in-service conditions.
- IA-2-2 is concerned with establishing state-of-the-art in methods of defect and loading assessment. It deals not only with fracture mechanics methods such as those used in the assessment of PTS and LBB, but includes also a consideration of existing Codes and Procedures, NDE, failure modes, safety factors and

certain special topics (effects of load history, crack arrest, secondary and residual stresses, WPS).

- In IA-2-3, the knowledge gaps identified by the other expert groups will be assessed in terms of their implications for through-life structural integrity. In addition, an assessment will be made of the potential for, and possible implications of, knowledge gaps outside the scope of the other expert groups. IA-2-3 will take a long-term perspective of component integrity, in particular the safety justification of components over the whole of their foreseen operational life, where the demonstration of safety margins becomes dominated by considerations of fatigue (including thermal fatigue and corrosion fatigue), irradiation embrittlement and other ageing processes (including creep and creep-fatigue).
- IA-2-4 will add to IA-2-1, 2-2 and 2-3 to support the Network by providing advice on identification, characterisation and management of uncertainties in lifetime evaluation, through modelling structural reliability and performing risk assessments to provide added insights into the assessment of safety margins.

3. Research and development planning

The planning of the R&D programme has already been started by a dedicated End-User Group (Table 2). The topics of preliminary interest and chosen for pilot projects are a) Stress corrosion cracking and b) Thermal fatigue. Other preliminary interesting topics are 1) Welds and weld repairs, 2) Clad properties and ageing, 3) Safety factors/uncertainties in damage evaluation, 4) Stress classification. Governing Board of NULIFE has later on emphasized the importance of concrete structures and cables, as well as e.g. instrument systems.

Table 2. Preliminary research topics and application areas identified by the End User Group.

Preliminary research topics proposed by end-users	Application areas:			
	Reactor pressure vessel and internals	Coolant system and lines	Steam generators	Other components
Thermal fatigue	X	X	X	
Stress corrosion cracking	X	X	X	
Welds and weld repairs	X	X		
Clad properties and ageing	X			
Safety factors/uncertainties in damage evaluation	X	X	X	
Stress classification		X		
Other ageing issues				X

Stress corrosion cracking has been identified as one of the more mature areas for action in the pre-proposal activities of the End User Group. This pilot project will bring the results from national programmes on stress corrosion cracking of reactor materials into the Network, in the form of information sharing between the contractors and third parties. The deliverables will be an integrated database on EAC of reactor materials, together with best practice guidelines on EAC testing.

Thermal fatigue has also been identified by the NULIFE end-users as a priority area, exploiting previous R&D in NESC and other European projects. The main tasks include:

- Complete the validation database for thermal stratification and thermal striping type damage
- Extend the knowledge base on thermal hydraulic boundary conditions for high frequency loading in mixing zones of piping including probabilistic aspects
- Extend the assessment procedure and review the best practice in predicting fatigue damage accumulation using both phenomenological criteria and proper material modelling and also provide recommendations for fatigue crack growth
- Provide recommendation on fatigue curves, including implicit or explicit consideration of environmental effects.

A step-wise prioritisation process for joint research and development is foreseen (Fig. 3):

1. Identification of needs, gaps and derived research topics for achieving the NULIFE objectives: The pre-selection of topics or areas for consideration will essentially be defined by the needs of the End User Group. This does not preclude proposals arising from groups or individuals within the NULIFE or as responses to external requests.
2. Evaluation process: This aims to assess and prioritise the research topics following a clear set of criteria. Examples of criteria are: existing level of understanding and need for improvement, cost-benefit, safety consequences, need for harmonisation, the prevalence and extent of the potential application, etc.
3. Feasibility of project realisation: For each selected topic a document covering the following aspects will be prepared: definition of the issue to be addressed; scope of the proposed activity and basic tasks; justification (including cost/benefit and confidence in achieving the task objectives); assessment of resources required (labour, experimental, computing etc); schedule for the activity; deliverables.
4. Decision on prioritisation for NULIFE implementation: The Executive Group will have the responsibility to allocate NULIFE funding or other resources for its implementation. It may also agree to seek other contributions, for

instance in-kind contributions from the NULIFE contractors and third parties, from external sponsors or from national and European programmes. Internal competition mechanisms shall be used to ensure that optimum price/performance is obtained. Once a project is accepted, it becomes a Joint Research Activity Work Package in the NULIFE programme.

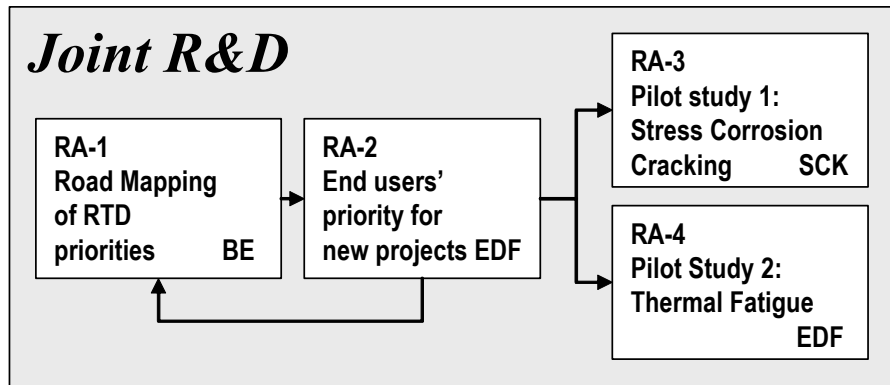


Figure 3. Joint research and development activity prioritisation and first pilot projects.

By providing research excellence and fostering common approaches in nuclear power plant lifetime prediction, NULIFE will contribute to the Electric Power Utilities' decision making in terms of plant operation and investments. Safety Authorities will also benefit from the knowledge in their duties to grant plant licenses for the continued operation of plants.

The ability of the network to deliver procedures and best practices documents on ageing issues will be an important measure of the network's impact. At the highest level, NULIFE will support the development of a European Common Safety Justification Framework. Since lifetime management tools are only one element in such a framework, its development will require support from other stakeholders. The broad composition of the network is a major advantage in this respect.

4. Future trends

The main technical issues that are likely to be important for lifetime management in the future are to gain a better physical understanding of ageing related damage mechanisms, to develop qualified methods for detection, surveillance and control of degradation and to develop predictive models and analysis tools based on the actual damage mechanisms at microstructural which allow more reliable extrapolation to the behaviour of components and structures.

For plant life management, analyses must show that the plant will continue to operate within its design basis. Where a change in operation is desired there will be a need for safety analyses to cover the new operational conditions. The future challenges need to have an adequate knowledge of the current design basis of the

plant, to have a correct picture of the actual state of the plant and to define the analyses needed to support long-term operation within its design basis. This requires relevant and qualified generally accepted data bases and methodologies.

Risk-informed and PSA methods will be increasingly used, e.g. to identify any excessive risk contributors, to evaluate relative significance of safety issues arising from deterministic reviews, to help prioritise corrective actions and to evaluate the effect of proposed plant or procedural modifications. Current ISI programmes are based on experience feedback and engineering judgements through a deterministic analysis. In future, more use of probabilistic safety analysis (PSA) is needed for planning of ageing management programmes. In addition, studies are underway for development of alternative methodologies for proposing an ISI programme which is in compliance with the required safety level. PSR will play an important role in future in reviewing the viability of R&D and industrial infrastructure to support safe NPP operation.

Due to the current boundary conditions in the educational system, there is concern that in the future there will be less possibilities to recruit qualified personnel with knowledge from specialised vocational education. At the European level a well defined structure for training should be established. Further development of the so-called Eurocourse, offered by a consortium of organisations and covering all safety related aspects for pressure-retaining components during operation of nuclear power plants, should be continued.

Lifetime management, being a multidisciplinary process, creates a strong need to navigate, share and integrate the existing knowledge as well as to co-ordinate the initiation of new R&D activities in the international level. Future form of networking need to exploit the experience of the running networks which provide an excellent forum for specific areas. In addition to such present activities, more emphasis is needed on qualification in all relevant technical disciplines and on effective knowledge management important to PLIM.

5. Conclusions

NULIFE's goal of creating a single organisational structure represents a new initiative for an integrated RTD platform embracing all stakeholders at European level.

NULIFE aims to improve the delivery to end-users of best-practice life assessment methods to support optimized ageing management programmes for existing nuclear power plants.

NULIFE intends to use of public and private RTD funding in an optimized way to launch new projects.

High temperature oxidation and corrosion of boiler materials

Satu Tuurna, Sanni Yli-Olli, Stefan Holmström and Liisa Heikinheimo

VTT Technical Research Centre of Finland, Espoo, Finland

Abstract

The study aims to the development of methods and models for the assessment of material performance in boilers and use of mixed fuels with combustion gas species like H₂O, HCl or SO₂. Gas phase oxidation tests at elevated temperatures under different atmospheres were carried out for selected steels. Formed oxide scales were characterised using EDS/SEM, and mass changes were measured for the exposed samples. Thermodynamic stability calculations simulating oxidation correspond quite well to the oxide structures formed in laboratory exposures for specified steel compositions. The results from laboratory exposures were also used to model the oxidation kinetics. The results show that oxidation kinetics and mechanism are strongly dependent on temperature and gas species like H₂O, HCl and SO₂. A further goal is to combine thermodynamic calculations and kinetic measurements for oxidation simulation to get an efficient tool for prediction of corrosion for specific steel types and combustion conditions.

1. Introduction

Traditional material design criteria for high temperature service has been primarily based on mechanical properties, but nowadays with growing combustion temperatures and case of mixed fuels with species like H₂O, HCl or SO₂ the lifetime is limited also by oxidation and consequently by metal wastage. It is now necessary to control high temperature oxidation and therefore investigate the oxidation kinetics and oxide layer growth.

Analyses of field exposure tests and failure cases have provided valuable information on high temperature behaviour of power plant components. This information could be used in prediction of the components remaining lifetime. However, since the conditions in energy conversion systems are very complex and several parameters have synergetic effects, the exact reason for a failure is difficult to identify. Severe metal loss in combustion occurs mainly due to gaseous corrosion (oxidation, chloridation and sulphidation), hot corrosion and corrosion beneath deposits [1–4]. Combustion of fuels containing sulphur produces SO₂, which can partially be oxidised to SO₃. Alkali and heavy metal impurities in the fuel react with SO₂ at the combustion temperature forming different sulphates that are highly

corrosive. Even in small amounts, sulphur in various forms accelerates corrosion at high temperatures. Sulphur together with oxygen forms a much more aggressive environment than oxygen alone [5–7]. The presence of chlorine in combustion atmospheres may cause accelerated corrosion of metallic materials. The formation of volatile chlorides and low temperature eutectics lead to the consumption of metal and to porous non-protective oxide layers [8–9]. Metal chlorides are less stable than oxides and no protective oxide layers are formed. Chlorides accelerate the oxidation of metal surfaces and cause cracking and spallation of the oxide layers [10–11]. Water vapour present in combustion environments plays an important role in oxidation process. Alloys that form protective oxide scales in dry atmospheres, will suffer a detrimental breakaway oxidation in moist gases [5, 12].

In this study, the influence of different gas species on oxidation of two low-alloyed steels and austenitic steel was investigated. The obtained experimental data is used for the development of modelling databases.

2. Experimental

The paper presents the oxidation behaviour of two low alloyed steels and an austenitic steel under different simulating combustion conditions. The results were used for the development of modelling databases. The nominal compositions of the studied materials are presented in Table 1. Exposure temperatures were 420, 550 and 600°C, and times varied from 72 h up to 360 h. Table 2 presents the different gas compositions used in the tests. The fourth gas containing both HCl and SO₂ was used only in tests at 600°C. The details of the high temperature oxidation furnace system and experimental procedures have been reported with earlier work [10, 13]. Surface morphologies and cross-sections of the formed oxide scales were examined by optical, scanning electron microscopy (SEM) and electron dispersive spectroscopy (EDS). To monitor the corrosion phenomena mass change measurements were carried out before and after testing.

Table 1. Nominal composition of the studied materials (wt-%).

Steel	Fe	Cr	C	Si	Ni	Mn	Mo	Al	Cu
71518	bal	0.55	0.07	0.36	0.21	1.01		0.04	0.39
2.25Cr1Mo	bal	2.25	0.09	0.23	0.44	0.59	0.96	0.01	0.15
TP347H	bal	17.6	0.05	1.2	10.7	1.8			

Table 2. Gases used in exposure tests (vol-%).

Gas 1	8% O ₂ - 15% H ₂ O - N ₂
Gas 2	200 ppm SO ₂ - 8% O ₂ - 15% H ₂ O - N ₂
Gas 3	2000 ppm HCl - 8% O ₂ - 15% H ₂ O - N ₂
Gas 4	200 ppm SO ₂ - 2000 ppm HCl - 8% O ₂ - 15% H ₂ O - N ₂

3. Results and Discussions

3.1 Oxide Layer Morphology

SEM/EDS analysis of cross-sections revealed that oxide scales formed on the ferritic steels had a triple layer structure. The inner scale consists of magnetite type oxide, partly an iron-chromium spinel, probably mixture of $\text{Fe}_3\text{O}_4 - (\text{FeCr}_2)\text{O}_4$, with small amounts of alloying elements like Si and Mo near the original metal surface. The middle scale consisted of magnetite. The outermost thin layer composition corresponds to hematite. The EDS line-scan across the oxide scale, Fig. 1, shows how the chromium content changes from the inner layer to the outer layer. Some silicon enrichment was detected on the outer surface. The composition and morphology of the oxide layers formed on the low-alloyed steels did not change in different temperatures. However, there have been some changes between the exposure atmospheres at 550 and 600°C. The most obvious change could be seen in atmosphere containing HCl, where the formed oxide was formed as a repeating layered structure, while the oxide layers formed under moist gas or gas containing SO_2 were mainly uniform. In particular, the oxide layer formed on the 2.25Cr1Mo steel had a clear repeating structure consisting of the inner iron-chromium oxide and the outer iron oxide layers, Fig. 2. This structure indicates active oxidation enhanced by chlorine [1, 10, 14]. The adhesion of the oxide layer is relatively poor and the critical oxide thickness for detachment and/or spallation is reached quickly. The growth of the layer starts over after the detachment or total spallation of the old oxide. In SO_2 containing atmosphere the morphologies of the scales are similar to that found in moist air, but at metal/scale interfaces sulphur was found in the form of sulphides.

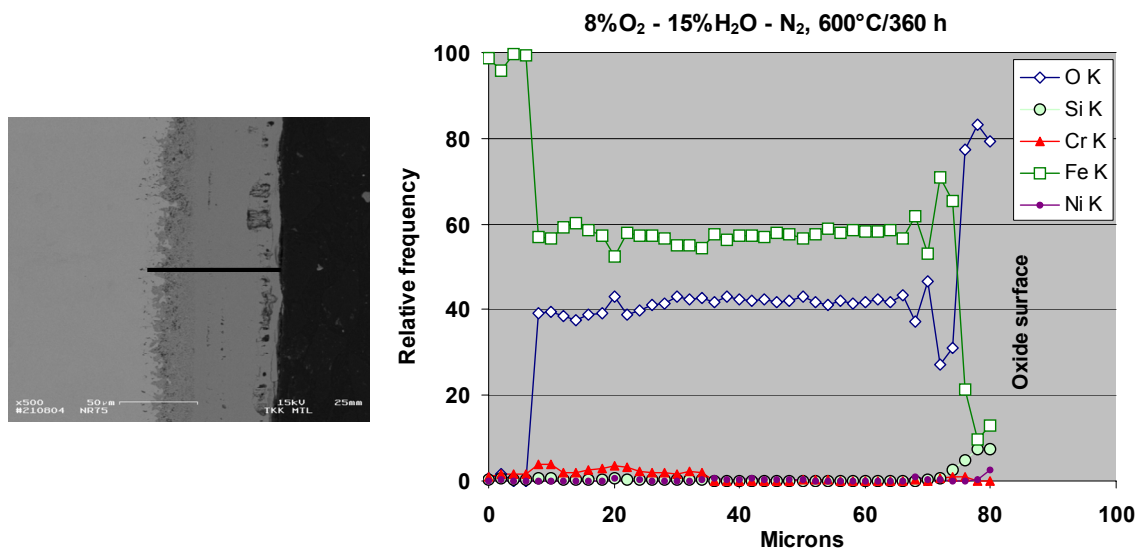
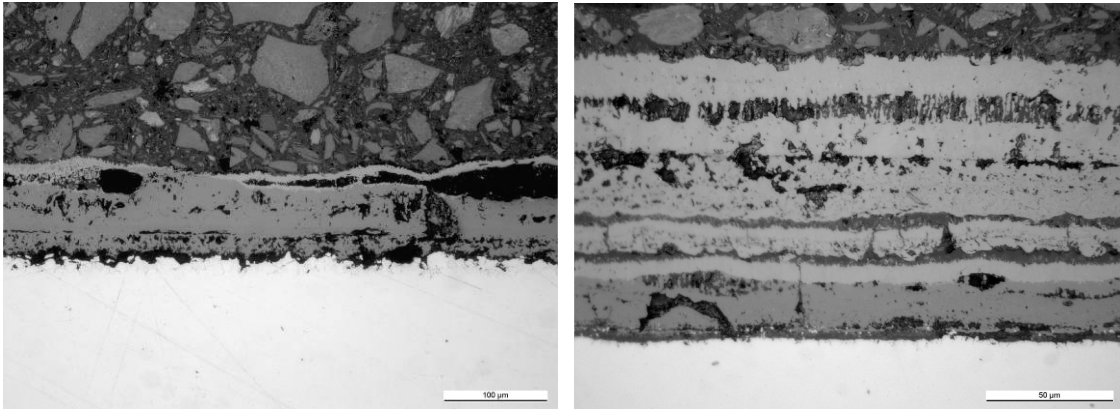


Figure 1. EDS line-scan across the oxide layer of low chromium steel after 360 h exposure at 600°C in moist air (8%O₂ - 15%H₂O - N₂).



a)

b)

Figure 2. Oxide layers after exposure at 600°C in 2000 ppm HCl - 8% O₂ - 15% H₂O - N₂ for 360 h on the surface of a) 71518 and b) 2.25Cr1Mo.

The oxidation behaviour of TP347H is also different under the HCl atmosphere than under the other exposure atmospheres. Chlorine accelerates the oxidation and a thin oxide layer formed on the material surface. At 600°C under moist air some small oxide nodules were found (Fig. 3). These could not be detected at lower temperatures. Nodule formation began from the grain boundaries and with longer exposure times the nodules grow together forming a continuous layer.

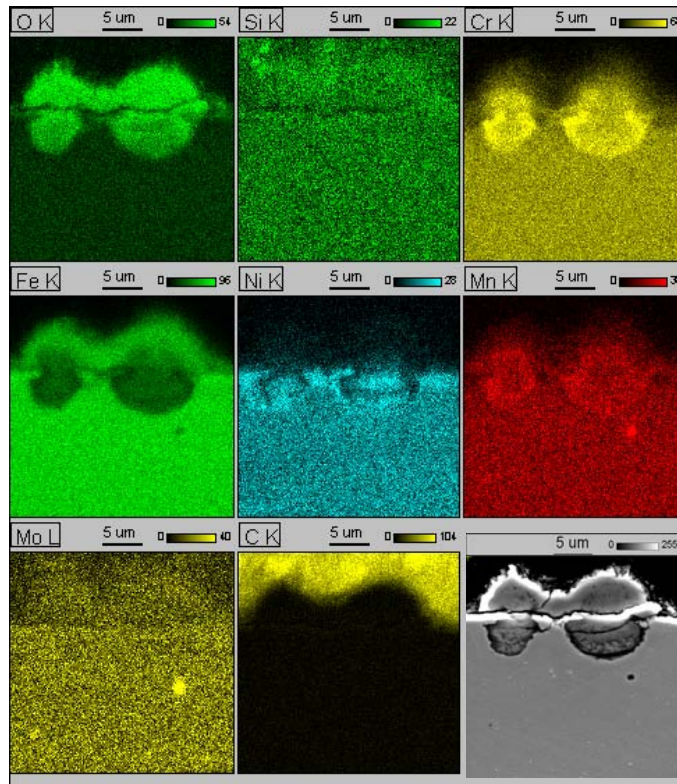


Figure 3. EDS mapping of the oxide nodules formed on the surface of T347H after 360 h exposure under 8%O₂-15%H₂O-N₂ gas.

3.2 Oxidation rate

The oxide layer could be split in to two main sections. The inner layer grows inwards by diffusion of oxygen through the cracks and pores in the oxide. The outer magnetite layer grows by outwards diffusion of iron through the inner layer. The growth of the inner and outer layers is controlled by the reaction kinetics and the oxygen potential in the gas. At 420°C, where oxidation rate is still quite slow, it seems that the inward and outward growing layers are rather equal in thickness. After 360 h of exposure the formed oxide layers on the ferritic steels were thin, less than 10 µm. At higher exposure temperatures it seems that the outer layers are growing faster than inner ones. An example of the oxide thickness increasing with exposure temperature is shown in Fig. 4.

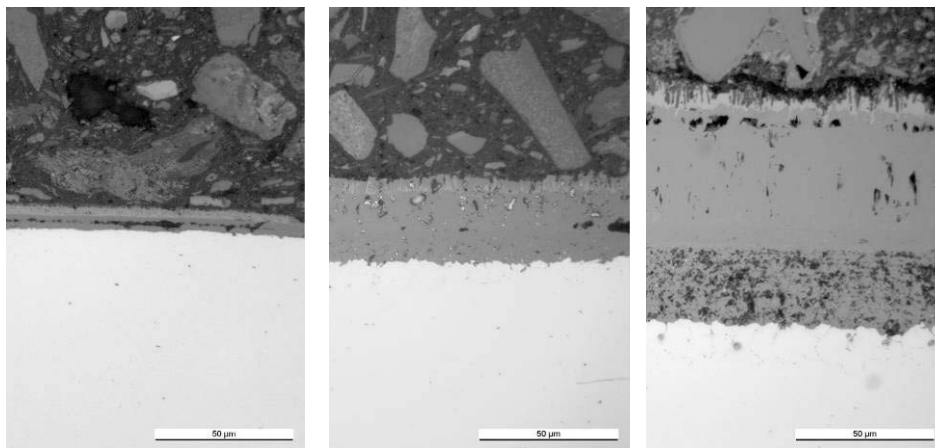


Figure 4. Oxide scale growth in different exposure temperatures (420, 550 and 600°C) for 71518 steel under SO₂ containing gas.

Fig. 5 shows the mass change per unit area values for the samples exposed for 360 h in different simulated combustion atmospheres. The mass change of the samples at 420°C was very low. Under SO₂ containing gas the detachment of formed oxides occurred, and the mass gain was negative. The reason for this negative mass gain was partially on detached powdery oxides, which could not be traced back to some particular sample. Increasing exposure temperature up to 600°C accelerates the oxidation remarkably. At 550°C the oxidation rate of 71518 after 360 h was the lowest under moist air and highest under HCl containing gas as was expected. SO₂ gas seemed to suppress the oxidation rate compared to moist air exposure in the case of 2.25Cr1Mo. At 600°C the same suppressing effect of SO₂ on the oxidation of both ferritic steels could be seen. In these cases sulphur accumulates in the metal-oxide interface and no trace of sulphur can be found inside the oxide layer. The addition of SO₂ to HCl containing gas seems to reduce the detrimental effect of HCl in the gas phase corrosion. Järnäs et al. have reported similar effects of SO₂ on the oxidation of low-alloyed steels in the temperature range 500–600°C [15, 16]. They suggest that small amounts of sulphate formed on the surface slow down the oxidation by suppressing oxygen reduction reactions or

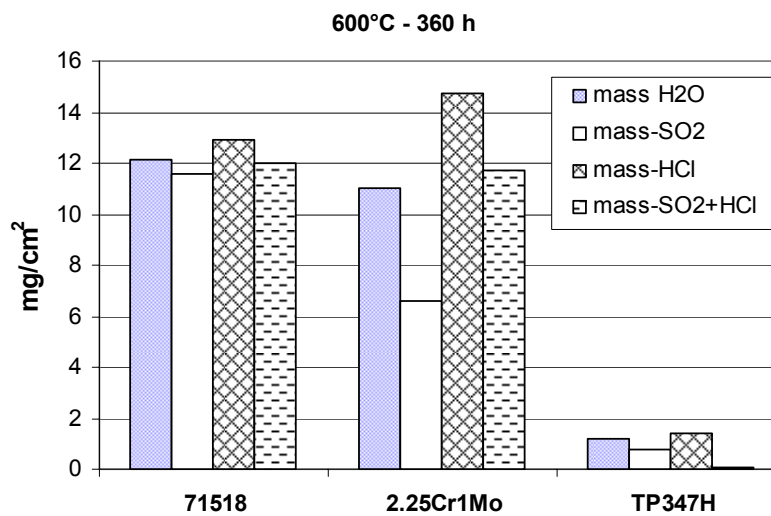
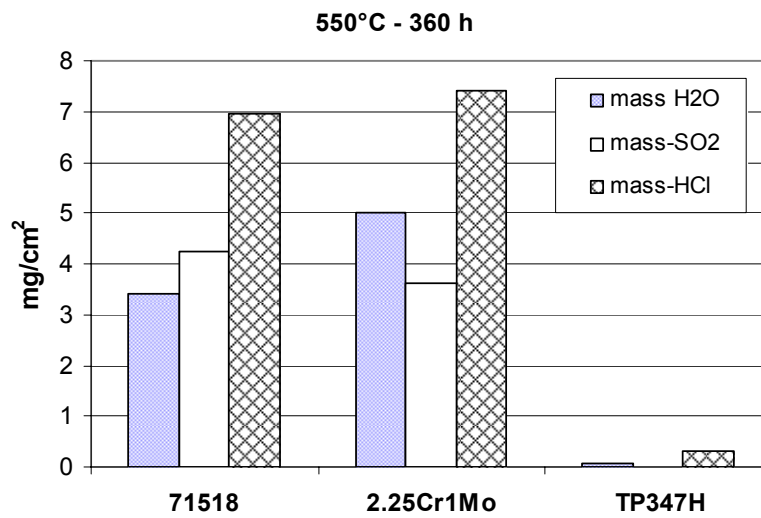
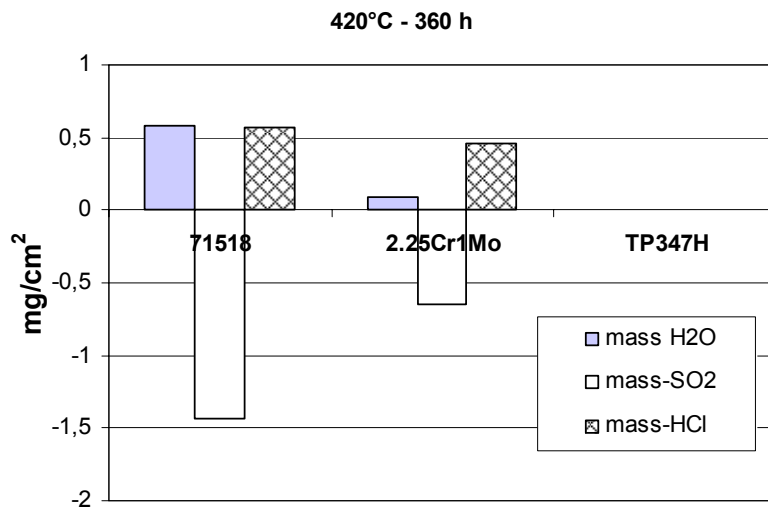


Figure 5. Mass changes per unit area in different exposure atmospheres and temperatures.

by decreasing ion grain boundary transport through the oxide layer. It is a well known fact that SO_2 contributes to the behaviour of chlorine in the combustion. Theoretically a S/Cl ratio of 0.5 is sufficient for sulphate alkali chlorides. However there are many competing reactions that suppress the effect of sulphur in combustion. A S/Cl ratio near 2 is considered sufficient to retard corrosion rates and a ratio of 4 would result in negligible corrosion rates.

The oxidation of alloy TP347H was very slow at least with the used exposure times, although some mass gain and mostly discontinuous thin oxide layers were observed.

Figs. 6 and 7 summarise the mass change and oxide thickness measurements at 550 and 600°C for 71518 and 2.25Cr1Mo steels. The mass gain is fitted using Origin 7.5 programme and equation type $\Delta m = at^b$, relevant for oxidation kinetics. Kinetic constants are summarised in Table 3. The mass gain and mean oxide thickness values follow each other quite well though there is some scatter in the results. The reason for this could be the oxide thickness changes across the sample surface and scale spallation. The discrepancy between mass change and thickness in some results under HCl indicates the layered oxide structure. The oxides contain more cracks and porosity, which increases the oxide thickness values. More measurement points would give less uncertainty. Results also indicate that oxidation of low alloyed steels does not follow parabolic law so well anymore at these temperatures – oxidation accelerates with longer exposure times that correspond to linear behaviour typical for spallation and non-protective oxide formation. In some cases especially the oxidation of 71518 steel follows slightly better linear behaviour, $\Delta m = at + c$, than parabolic oxidation behaviour. Oxidation kinetic is strongly dependent on temperature and gas species.

Fig. 8 presents the overall composition and sequence of the growing oxide layers on low alloyed steel with time. At the gas-oxide interface where the oxygen potential is high a thin hematite layer is formed, and magnetite and spinel are formed with lower oxygen potentials near metal surface. Chlorine accelerates oxidation and volatile MCl_x changes the forming oxide structure as seen in Fig. 2.

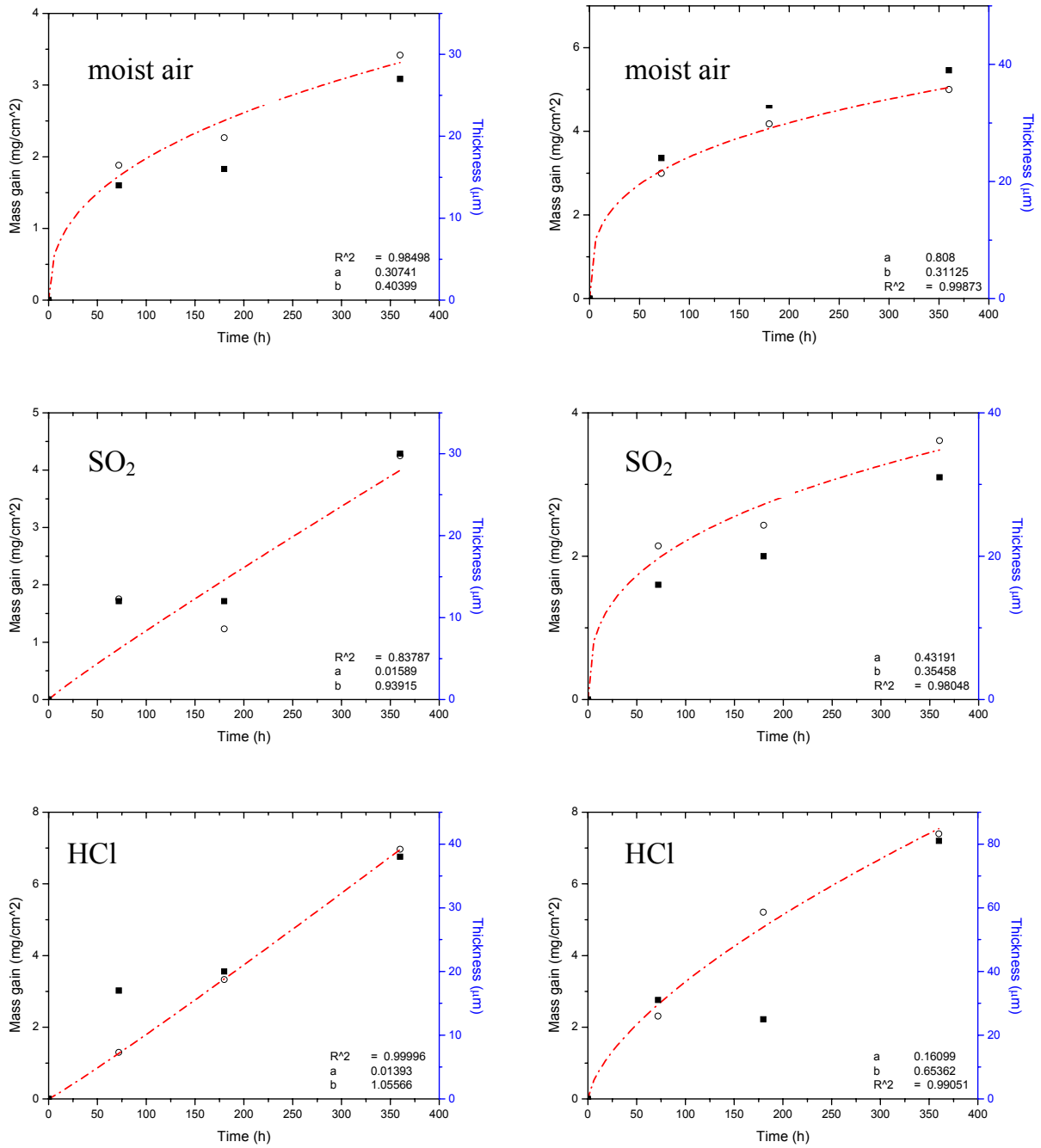


Figure 6. Overview of the exposure results at 550°C for the low alloyed steels. Steel 71518 left – 2.25Cr1Mo right; white mark – mass gain, black – thickness.

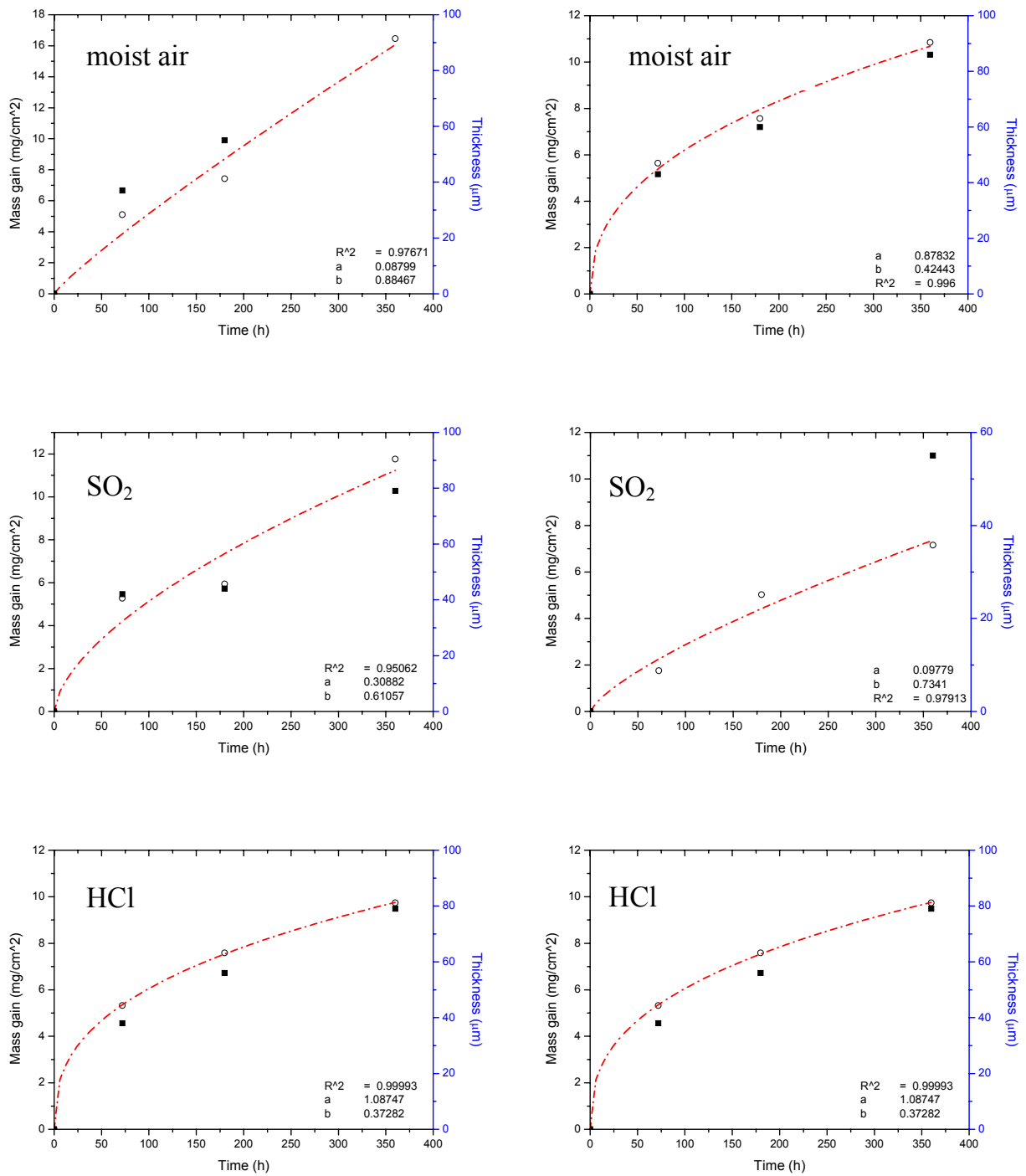


Figure 7. Overview of the exposure results at 600°C the low alloyed steels. Steel 71518 left – 2.25Cr1Mo right; white mark – mass gain, black – thickness.

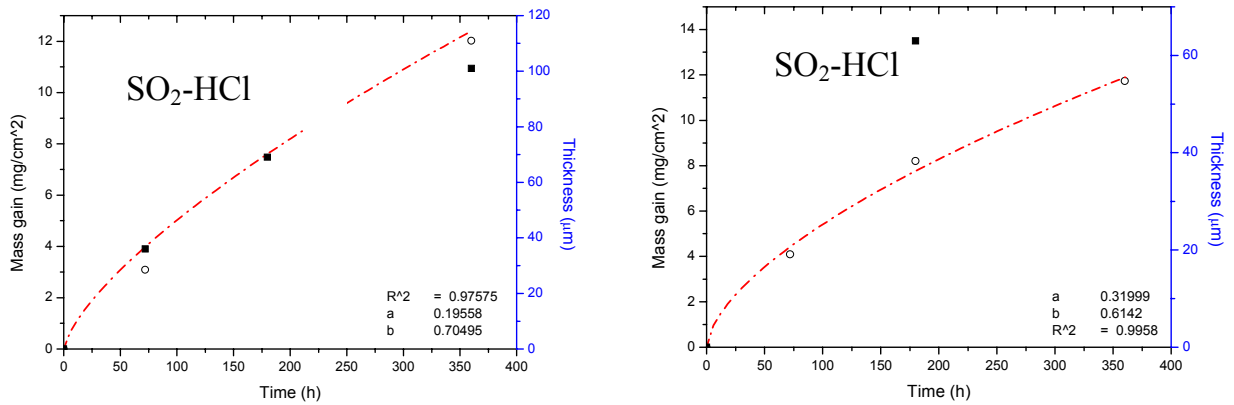


Figure 7. continues...

Table 3. Mass gain versus exposure time follows the equation $\Delta m = at^b$ in Figs. 6 and 7. Oxidation kinetic constants for different steel types at 550 and 600°C.

550				
Steel type	Atmosphere	a	b	R ²
71518	moist air	0.3074	0.0439	0.9849
	200 ppm SO ₂	0.0159	0.9391	0.8378
	2000 ppm HCl	0.0139	1.0556	0.9999
2.25Cr1Mo	moist air	0.808	0.3112	0.9987
	200 ppm SO ₂	0.4319	0.3546	0.9805
	2000 ppm HCl	0.1609	0.6536	0.9905
600				
71518	moist air	0.0879	0.0879	0.9767
	200 ppm SO ₂	0.3088	0.6106	0.9506
	2000 ppm HCl	1.0874	0.3728	0.9999
	200 SO ₂ + 2000 HCl	0.1956	0.7049	0.9757
2.25Cr1Mo	moist air	0.8783	0.4244	0.9960
	200 ppm SO ₂	0.0977	0.7341	0.9791
	2000 ppm HCl	0.6109	0.5155	0.9912
	200 SO ₂ + 2000 HCl	0.3199	0.6142	0.9956

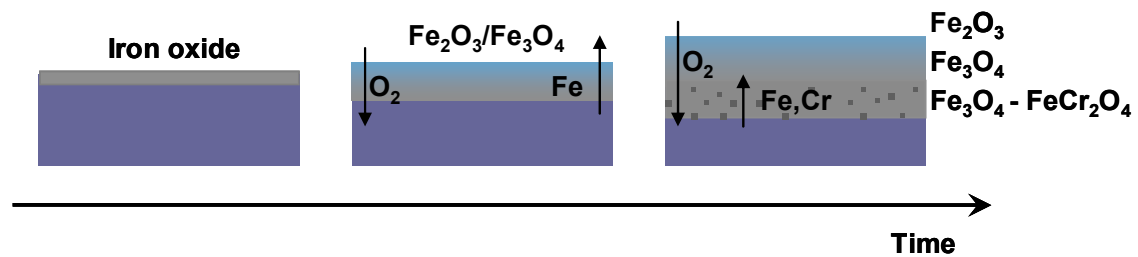


Figure 8. Development of an oxide layer with exposure time. Oxygen diffuses inwards, and iron and chromium move towards the higher oxygen potentials.

3.3 Thermodynamic calculations

Thermodynamic calculations using Factsage programme [17] were carried out. Oxide structures formed in laboratory exposures correspond to thermodynamic stability calculations. The layered structure of the oxide scale can be predicted from the calculated phase diagrams, Figs. 9 and 10. With high oxygen potentials at gas-oxide interface hematite, Fe_2O_3 , is formed. With low oxygen potentials, typical of inner metal-oxide interfaces magnetite, Fe_3O_4 , and spinel, FeCr_2O_4 , are predicted. These diagrams can be used for the assessment of microstructural characterisation of corrosion product layers. Thermodynamic calculations can be also used as a supporting tool in choosing proper ranges of test parameters and gas atmospheres for the experiments in the future.

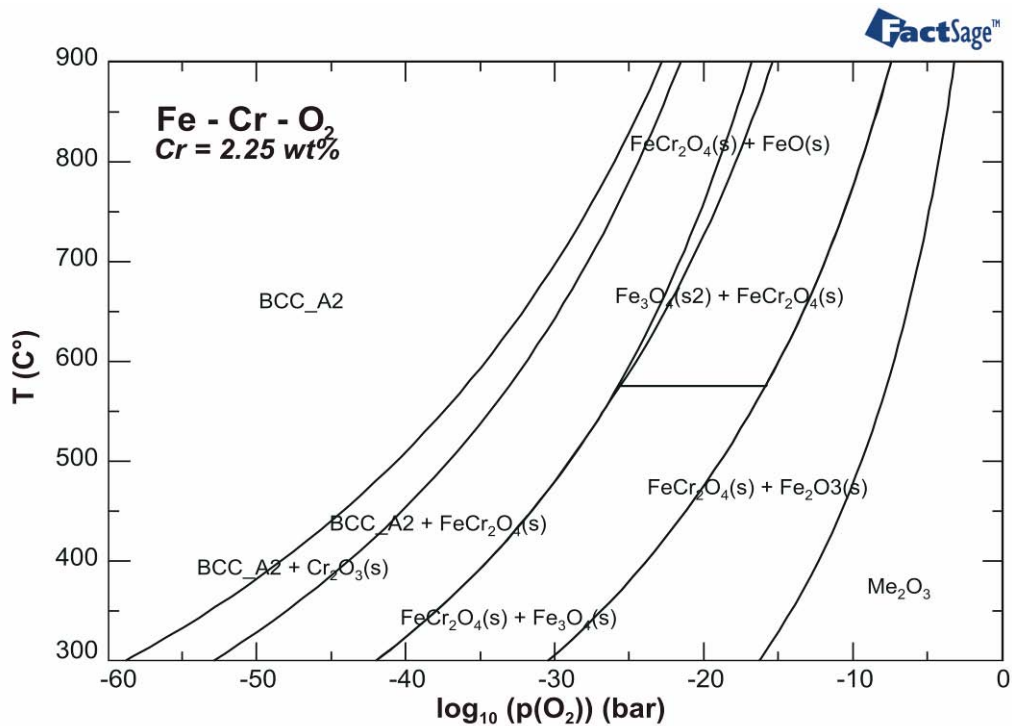


Figure 9. Fe-Cr-O phase diagram showing forming oxide layers at different temperatures.

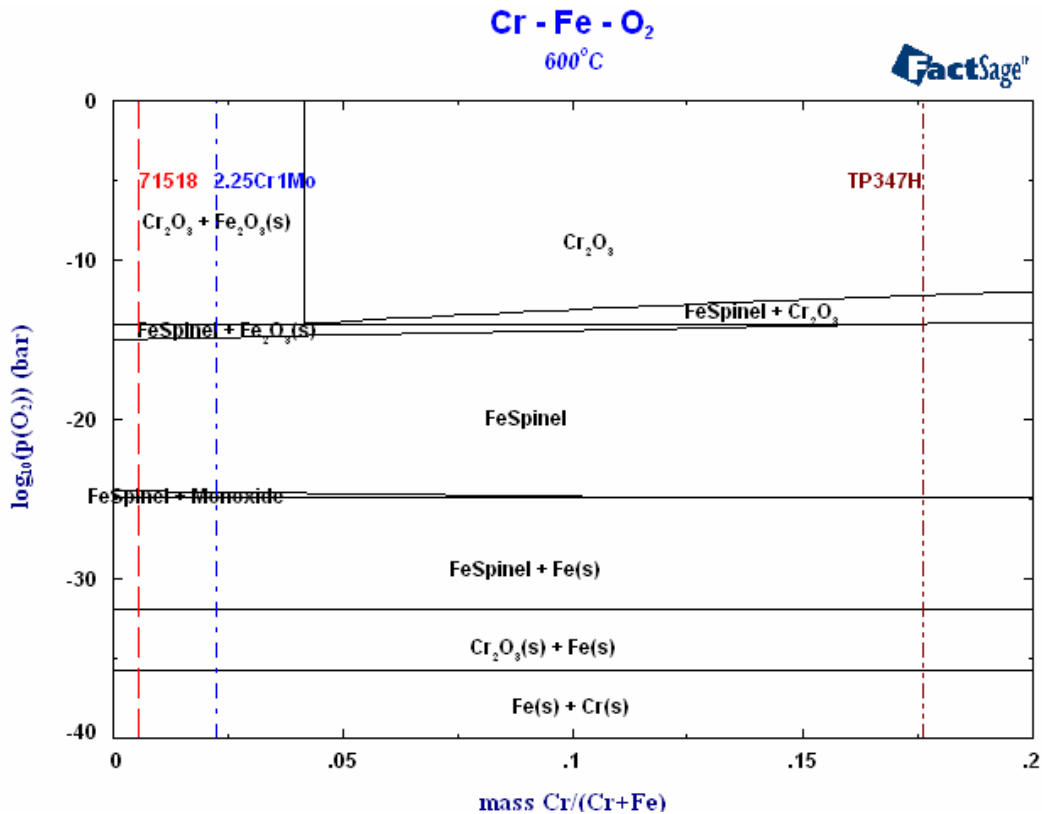


Figure 10. Fe-Cr-O stability diagram for $T = 600^\circ\text{C}$.

4. Conclusions

The temperature and gas composition have a significant influence on the morphology and the growth rate of the oxide scale. Oxide layers formed on low-alloyed steels have a multi-layer structure. The outer scale consists of hematite (Fe_2O_3) at the oxide/gas interface followed by magnetite (Fe_3O_4). For the inner scale a more complex structure was observed: Fe-Cr spinel with Fe_3O_4 and some amount of Cr_2O_3 . At 420°C this structure is not so obvious. HCl containing atmosphere is most detrimental for studied steels. There is a tendency for oxide cracking and spallation, therefore no protective oxide can be formed. In many cases the presence of SO_2 suppresses the oxidation rate of the tested materials. The suppressing tendency increases with increasing temperature and is attained first with higher chromium contents.

Mass changes, thickness of oxide layers and their morphologies can be used as parameters for lifetime prediction. Further, these can be used for the development of lifetime prediction models as well. In order to build models to simulate corrosion processes, data of adequate corrosion kinetics from laboratory tests and also data from real plants are needed.

Thermodynamic calculations using Factsage supported the experimental observations on oxide species. The layered structure of the oxide scale can be reliably predicted from the calculated phase diagrams. It is clear that these diagrams can not give the full picture of the real cases due to the fact that the kinetic factor is missing. However, they can anyway be used as assistance in screen testing, life assessment and in analysing the results. More kinetic data and knowledge of oxidation and corrosion mechanisms are still needed before accurate corrosion rates and thereby lifetime predictions can be made.

References

1. Grabke, H.J., Reese, E. and Spiegel, M. Corrosion Science Vol. 37, No. 7 (1995), pp. 1023–1043.
2. Pyykönen, J. and Jokiniemi, J. Vol. 80 (2003), pp. 225–262.
3. Bryers, R.W. Prog. Energy Combust. Sci. Vol. 22 (1996), pp. 29–120.
4. Zahs, A., Spiegel, M., Grabke, H.J. Corrosion Science 42 (2000), pp. 1093–1122
5. Kofstad, P. High Temperature Corrosion, Elsevier Applied Science, 1988, 558 p.
6. Srivastava, S. and Godiwalla, K. Journal of Materials Science 32 (1997), pp. 835–849.
7. Bakker, W. Materials at High Temperatures, Vol. 20 (2003), pp. 161–169.
8. Spiegel, M., Zahs, A. and Grabke, H.J. Materials at High Temperatures 20 (2003), pp. 153–159.
9. Liu, X., Maier, J. and Hein, K.R.G. 15th International Corrosion Conference (ICC) – Frontiers in Corrosion Science and Technology, Granada Spain, 22.–27.9.2002.
10. Sroda, S., Tuurna, S., Penttilä, K. and Heikinheimo, L. Materials Science Forum Vol. 461–464 (2004), pp. 981–988.
11. Kim, A.S. and McNellan, M.J. Corrosion, Vol. 46 (1990), pp. 746–755.
12. Nickel, H., Wouters, Y., Thiele, M. and Quadackers, W.J. Fresenius Journal of Analytical Chemistry (1998) 361, pp. 540–544.
13. Sroda, S. and Tuurna, S. Materials and Corrosion, Vol. 57 (2006), pp. 244–251.

14. Kawahara, Y. Corrosion Science 44 (2002), pp. 223–245.
15. Järtnäs, A., Svensson, J.-E. and Johansson, L.-G. Materials Science Forum Vol. 369–372 (2001), pp. 173–180.
16. Järtnäs, A., Svensson, J.-E. and Johansson, L.-G. Oxidation of Metals Vol. 60 (2003), pp. 427–445.
17. FactSage™ – Interactive Programs for Computational Thermochemistry. GTT Technologies.



Series title, number and report
code of publication

VTT Symposium 246
VTT-SYMP-246

Author(s) Veivo, Juha & Auerkari, Pertti (eds.)		
Title BALTICA VII Life Management and Maintenance for Power Plants. Vol. 1		
Abstract BALTICA VII. International Conference on Life Management and Main-tenance for Power Plants, Helsinki–Stockholm–Helsinki, June 12–14, 2007. This is one of the two volumes of the proceedings of the BALTICA VII Conference. The Conference aims to review recent experience, new technology and views on future developments for supporting successful, safe and productive operation of power plants.		
ISBN 978-951-38-6315-9 (soft back ed.) 978-951-38-6316-6 (URL: http://www.vtt.fi/publications/index.jsp)		
Series title and ISSN VTT Symposium 0357-9387 (soft back ed.) 1455-0873 (URL: http://www.vtt.fi/publications/index.jsp)	Project number	
Date June 2007	Language English	Pages 257 p.
Name of project BALTICA VII	Commissioned by	
Keywords power plant, maintenance, boilers, machinery, equipment, inspection, monitoring, condition, life, performance, risk, reliability	Publisher VTT Technical Research Centre of Finland P.O. Box 1000, FI-02044 VTT, Finland Phone internat. +358 20 722 4404 Fax +358 20 722 4374	

BALTICA VII. International Conference on Life Management and Maintenance for Power Plants, Helsinki-Stockholm-Helsinki, June 12-14, 2007.

This is one of the two volumes of the proceedings of the BALTICA VII Conference. The Conference aims to review recent experience, new technology and views on future developments for supporting successful, safe and productive operation of power plants.

The BALTICA events:

BALTICA I. Materials Aspects in Life Extension of Power Plants, Helsinki-Stockholm-Helsinki, September 19-22, 1988.

BALTICA II. International Conference on Plant Life Management & Extension, Helsinki-Stockholm-Helsinki, October 5-6, together with the International Symposium on Life and Performance of High Temperature Materials and Structures, Tallinn, Estonia, October 7-8, 1992.

BALTICA III. International Conference on Plant Condition & Life Management, Helsinki-Stockholm-Helsinki, June 6-8, 1995.

BALTICA IV. Plant Maintenance for Managing Life & Performance, Helsinki-Stockholm-Helsinki, September 7-9, 1998.

BALTICA V. International Conference on Condition and Life Management for Power Plants, Porvoo, Finland, June 6-8, 2001.

BALTICA VI. International Conference on Life Management and Maintenance for Power Plants, Helsinki-Stockholm-Helsinki, June 8-10, 2004.

BALTICA VII. International Conference on Life Management and Maintenance for Power Plants, Helsinki-Stockholm-Helsinki, June 12-14, 2007.

Julkaisu on saatavana

VTT
PL 1000
02044 VTT
Puh. 020 722 4404
Faksi 020 722 4374

Publikationen distribueras av

VTT
PB 1000
02044 VTT
Tel. 020 722 4404
Fax 020 722 4374

This publication is available from

VTT
P.O. Box 1000
FI-02044 VTT, Finland
Phone internat. + 358 20 722 4404
Fax + 358 20 722 4374
